Investigating meiotic chromosome structure during meiotic prophase in *C. elegans*

a thesis submitted for the degree of

Doctor of Philosophy

2018

ANGEL LUIS JASO TAMAME

Imperial College London

MRC London Institute of Medical Sciences

DECLARATION OF ORIGINALITY

I, Angel Luis Jaso Tamame, hereby declare that the work presented in this thesis is my own and has not been submitted in any form for another degree or diploma at any other university. Information derived from the published work of others has been acknowledged in the text and a list of references is given.

COPYRIGHT DECLARATION

ACKNOWLEDGEMENTS

First and foremost, I would like to thank my supervisor Fadri Martinez-Perez for giving me the opportunity to pursue this PhD. Your encouragement, enthusiasm and constructive criticism throughout my PhD has been critical to finish this huge book called thesis. Thanks for your support specially in the last months, I will always be grateful.

Secondly, I would like to thank former and current members of the Meiosis Group for supporting me both scientifically and morally. Consu, Maikel, Sarai, Nan, Jocelyn, George, Oana and Daimona. Thank you all, it has been fun.

I would like to acknowledge Chad Whilding for his work helping me with the SRM. Without him, this project would have been even more challenging. I would also like to thank Amalia who has been patiently listening to me for the last 4 years in a non-scientific way.

Finally, I would like to thank my parents and my sister Diana for supporting through my PhD, especially during the last year. I would also want to thank my friends, particularly Fran and Laura for always been there supporting me.

Abstract

Meiosis is the specialised cell division program that allows the formation of haploid gametes from diploid germ cells, playing an essential role in the life cycle of sexually-reproducing organisms. Meiosis involves dramatic changes in chromosome structure during the long prophase that precedes the first meiotic division. At the onset of meiosis axial elements (AE) containing cohesin, the complex that provides sister chromatid cohesion (SCC), are established along each chromosome. Following AE assembly, homologous chromosomes pair with one another and crossover (CO) recombination events are formed between them. COs, together with SCC, provide the basis of chiasmata: temporary physical attachments between homologous chromosomes that ensure their correct orientation on the first meiotic spindle. Therefore, COs play an essential role during meiosis and their number and position appear to be highly regulated. However, the functional interplay between chromosome structure and CO formation and distribution remains poorly understood. In this project, I have combined the experimental advantages of the *C. elegans* germ line with super resolution microscopy (SRM) techniques to study the structural changes that chromosomes undergo during meiotic prophase. I develop methods to image three-dimensionally intact meiotic nuclei using structural illumination microscopy (SIM) and Imaris image software analysis, making it possible to measure structural features of individual meiotic chromosomes, including CO sites. When combined with the extensive genetic resources available in *C. elegans*, this method provides a powerful tool to investigate the functional regulation of meiotic chromosome structure by different protein complexes such as cohesin. I also describe that a mutation in MEI-2, a component of the microtubule severing complex katanin, results in altered CO distribution, likely by affecting early steps of meiotic recombination. This finding reveals an unexpected role for katanin during meiotic prophase and suggests that the microtubule network plays an important role in the regulation of CO distribution.

TABLE OF CONTENTS

LIST OF ABBREVIATIONS

AE	Axial element
ATP	Adenosine 5'-triphosphate
BSA	Bovine serum albumin
CE	Central element
CGC	Caenorhabditis Genetics Centre
cM	CentiMorgan
CO	Crossover
D-loop	displacement loop
DAPI	(4', 6-diamidino-2-phenylindole)
DNA	deoxyribonucleic acid
dHJ	Double Holliday junction
DSB	double strand break
dsDNA	Double stranded DNA
dsRNA	Double stranded RNA
dpy	Dumpy
EDTA	Ethylenediaminetetraacetic acid
FISH	Fluorescence in situ hybridization
g	Grams
GFP	Green fluorescent protein
Him	High incidence of males
HR	Homologous recombination
L4	Larval moult 4
l	Litres
LB	Lysogeny broth
LE	Lateral element
M9	Salt buffer

min	Minutes
ml	Millitres
mm	Millimetre
mM	Millimolar
mRNA	Messenger RNA
NCO	Non-crossover
NE	Nuclear envelope
ng	Nanogramme
NGM	Nematode growth media
NHEJ	Non-homologous end-joining
OP50	Attenuated E. coli strain
PBS	Phosphate buffered saline
PBST	Phosphate buffered saline Tween
PC	Pairing Centre
PCR	Polymerase chain reaction
PFA	Paraformaldehyde
rDNA	Ribosomal DNA
RNA	Ribonucleic acid
RNAi	RNA interference
rpm	Revolutions per minute
RT	Room temperature
SC	Synaptonemal complex
SCC	Sister chromatid cohesion
sec	Seconds
s	Seconds
SMC	Structural maintenance of chromosomes
SNP	Single nucleotide polymorphism
ssDNA	Single stranded DNA

Tm	Melting temperature
TZ	Transition zone
unc	Uncoordinated
ZMM	Zip1-Zip2-Zip3-Zip4-Msh4-Msh5-Mer3 complex
µg	Microgram
µl	Microlitres
µm	Micrometres
µM	Micromolar
°C	Degree centigrade

CHAPTER 1:

INTRODUCTION

1.1 General background

The genome of eukaryotes is organised into structures of DNA and proteins known as chromosomes, which are located within the nucleus. These molecular entities encode the information required to perform all the processes that allow organisms to grow and reproduce. Therefore, this information must be carefully maintained and faithfully transmitted during cell division. In mitotic cells, chromosomes are replicated from end to end to generate two copies of identical sequence, known as sister chromatids, which are then segregated into the two daughter cells generated at the end of mitosis.

Sexually reproducing organisms carry two copies of each chromosome, one inherited from the mother and the other from the father, which are known as homologues or homologous chromosomes. In order to maintain the total chromosome number constant across generations, homologous chromosomes must be separated during gamete production. Meiosis is the special type of cell division that produces haploid gametes from diploid germ cells. This reduction in chromosome number is achieved by a single round of DNA replication, which produces two identical sister chromatids, followed by two rounds of chromosome segregation. Meiosis involves dramatic changes in chromosome structure during the long prophase that precedes the first meiotic division, and most prophase is dedicated to ensure pairing and recombination between homologous chromosomes to ensure their proper orientation on the first meiotic spindle.

1.2 Meiosis

Meiosis is a multi-step specialised cell division programme that allows diploid germ cells to produce haploid gametes. Meiosis starts with one single round of DNA replication followed by two rounds of chromosome segregation, thus halving the total number of chromosomes. During meiosis I (the reductional division), homologous chromosomes

are separated into two daughter cells, while during meiosis II (the equational division), sister chromatids are separated into two daughter cells (Petronczki et al., 2003). A crucial aspect of meiotic prophase is the pairing of homologous chromosomes that takes place during meiotic prophase, a process marked by several changes in chromosome structure. Firstly, a proteinaceous axial element containing cohesin, the complex that provides sister chromatid cohesion (SCC), is formed along the length of each chromosome. In addition, axial elements contain meiosis-specific proteins, including a conserved group of HORMA-domain proteins. Secondly, once homologous chromosomes have recognised each other, these early pairing interactions are stabilised by the synaptonemal complex (SC), a proteinaceous structure that links together the axial elements of paired homologues (Cahoon and Hawley, 2016). Pachytene begins once the SC is stablished between homologues. These first steps are crucial for CO formation/recombination, which is initiated prior to SC assembly. Recombination begins with the regulated formation of DNA double strand breaks (DSBs). Moreover, in most organisms pairing and synapsis are dependent on the formation of these programmed DSBs. Several DSBs are made along each chromosome, and crucially some of these are repaired as inter-homologue crossover (CO) events, while others are repaired as non-CO events. The formation of inter-homologue CO events is an essential part of the meiotic program, due to the fact that COs, together with SCC, provide the basis of chiasmata: temporary physical attachments between homologous chromosomes that ensure their correct orientation on the first meiotic spindle. Therefore, CO formation must be regulated properly to ensure that each homologue pair has at least one CO at the end of meiotic prophase. Nevertheless, the molecular mechanisms that control the distribution and number of COs along meiotic chromosomes are not fully understood (Berchowitz and Copenhaver, 2010; Yanowitz, 2010). After COs are stablished, the SC is disassembled and homologues are only linked by chiasmata, forming structures known as bivalents. Chiasmata promote the biorentation of the kinetochores from homologous chromosomes on the meiosis I spindle, and then the selective release of SCC from chromosome arms allows the orderly partition of homologous chromosomes into two different daughter cells. SCC that remains on centromeric regions allows the biorentation of sister kinetochores on meiosis II spindle, and then full removal of cohesin

results in sister chromatid separation during anaphase II. All these events involve large changes in chromosome structure, which are not completely understood.

The initial goal of this project was to shed light on the intrinsic relationship between CO formation and chromosome structure. On the one hand, acquisition of proper chromosome structure during early prophase is needed to promote CO formation, while on the other CO formation is known to induce structural changes on chromosomes. To achieve this, I focused on a *C. elegans* meiotic mutant that displayed altered CO distribution and in developing super resolution microscopy methods to measure features of meiotic chromosomes in three-dimensionally intact nuclei.

1.2.1 Importance of meiosis

1.2.1.1 Clinical relevance of meiosis

Problems in meiotic chromosome segregation are especially frequent in human oocytes, with studies estimating that between 10-30% of fertilised eggs carry one chromosome more than the normal number (trisomy) or one less (monosomy). It is thought that at least one-third of miscarriages are a direct cause of aneuploidy originated during meiosis, making this a main cause of pregnancy loss (Hassold and Hunt, 2001). The incidence of aneuploidy is 0.3% among liveborns and 4% among stillbirths (fetal deaths taking place between 20 weeks of gestation and term). However, this percentage increases to 35% among spontaneous abortions (fetal deaths taking place between 6-8 weeks of gestation). In vitro fertilization studies have shown that most aneuploid embryos, although morphologically normal, experience implantation failure in the uterus or miscarriage during the first weeks of pregnancy (Hassold and Hunt, 2001). Interestingly, multiple studies have shown a correlation between maternal age and aneuploidy, demonstrating that the level of aneuploidy in oocytes of women increases from 5% in women under 25 years, to 10-25% in women in their 30s, and finally rising over 50% in women in their 40s (Kuliev et al., 2003; Pellestor et al., 2003; Sandalinas et al., 2000). Although the causes of this maternal age effect remain poorly understood, premature loss of SCC is thought to be an important contributor (Herbert et al., 2015). This has been shown to be the case in several mouse models (Nagaoka et al., 2012).

Furthermore, it has been demonstrated that there is no cohesin turnover during oocyte growth in mice, implying that this could be an essential mechanism for premature loss of SCC (Tachibana-Konwalski et al., 2010).

Most aneuploidies are not compatible with life in humans, but among the ones that are, the most common are: Down's syndrome (47 chromosomes, trisomy 21), Klinefelter's syndrome (47, XXY) and Turner's syndrome (45, X0). People affected by these syndromes can develop into adulthood but show mental, physical and fertility impairment (Hassold and Jacobs, 1984). On the other hand, there are other autosomal trisomy syndromes which are less frequent than the previous ones. Patau's syndrome (47, trisomy 13) and Edward's syndrome (47, trisomy 18) have a more difficult prognosis. Individuals that have these syndromes show multiple birth defects and most of them do not survive the first six months (Taylor, 1968).

More research needs to be done to understand why aneuploidy levels are so high in human beings and to discover and comprehend the molecular mechanisms affected in patients who suffer from infertility, developing possible treatments for them.

1.2.1.2 Importance of meiosis in crop breading

Food demand is currently growing and crop productivity needs to be improved to cope with it (Ray et al., 2012, 2013). An increase of 60-110% in crop productivity will be required to feed nine billion of people, which is the expected population by 2050 (Alexandratos and Bruinsma, 2012). One way of improving crop productivity is by crop breading, which increases genetic diversity while conserving natural resources and ensuring food security. The objective of crop breading is to generate new varieties of plants that combine the desired alleles of the parental strains. To do this, the reshuffling of the genome that occurs during meiosis is essential as it creates new allele combinations in the gametes. This reshuffling is controlled by the position and the number of COs within the chromosomes during meiosis (Moose and Mumm, 2008). CO numbers and their distribution are highly constrained (see section 1.2.7.8) and this limits the possibilities of crop breading. The manipulation of these CO patterns could increase the efficiency of breeding programs (Blary and Jenczewski, 2019).

1.2.2 *Caenorhabditis elegans* as a model organism to study meiosis

Caenorhabditis elegans has several features that make this nematode an excellent model for the study of meiosis. First, each adult germ line contains a complete time course of meiosis with nuclei organised in a spatial/temporal gradient in which specific meiotic stages can be easily identified (figure 1). The distal region of the germline, known as mitotic tip, contains mitotically-replicating nuclei and nuclei undergoing meiotic S-phase (Fox et al., 2011; Jaramillo-Lambert et al., 2007). This region is followed by the transition zone (TZ), which contains nuclei displaying a polarized organization that correspond to the leptotene and zygotene stages of meiotic prophase. In this region, homology search takes places, leading to initial pairing interactions and the start of SC assembly, and recombination is initiated (Colaiácovo et al., 2003; Dernburg et al., 1998; MacQueen et al., 2002). The onset of the third region of the germline is marked by full synapsis between homologues and this stage is known as pachytene. Recombination is completed during late stages of this phase, resulting in the formation a single CO per homologue pair (Hillers and Villeneuve, 2003). The fourth region of the germline is diplotene, where remodelling, including SC disassembly, and condensation of homologous chromosomes occur. Finally, at diakinesis (the last stage of meiotic prophase), six pairs of homologous chromosomes attached by a single chiasma (bivalent) can be observed.

An advantage of using *C. elegans* as a meiotic model is relatively easy to understand what problems a meiotic mutant might have. For example, mutants with defects in CO formation can be easily identified because their diakinesis oocytes contain between 7 and 12 DAPI-stained bodies, depending on the severity of the CO failure, with 12 DAPI-stained bodies indicating a complete failure in CO formation.

Another feature of *C. elegans* genetics that is extremely useful for meiotic studies is its mode of sex determination: hermaphrodites have two X chromosomes (XX), while males have a single X chromosome (X0), therefore, mutants that display X chromosome missegregation during meiosis display a high incidence of males (him phenotype) among their progeny (Hodgkin et al., 1979). Similarly, autosomal missegregation during meiosis results in high levels of embryo lethality among the progeny.

Another important feature of *C. elegans* is that the extraction of the germ line for imaging is relatively simple and worms can be genetically modified to express transgenic fluorophore-tagged versions of proteins (Frøkjær-Jensen et al., 2008, 2012), which can then be combined with antibody staining to analyse protein localization. Moreover*, C. elegans* germ line extraction allows the study of meiotic processes by microscopy in three-dimensional nuclei. Recently, CRISPR methods have been developed in *C. elegans*. This approach is based on the homologous recombination machinery, and it uses the Cas-9 endonuclease to create a DSB at a specific genetic location that allows a targeted insertion or the replacement of genetic information at the desired location (Arribere et al., 2014; Friedland et al., 2013). Moreover, since the cuticle is transparent, in vivo imaging of meiotic nuclei is possible in transgenic/CRISPR strains expressing fluorescently tagged proteins.

The next sections will outline our current understanding of the molecular mechanisms that control key meiotic events, focusing on the structure of meiotic chromosomes and on how this structure interacts with CO formation and taking into consideration the different particularities of *C. elegans* meiosis.

1.2.3 Meiosis initiation

The beginning of meiosis in multicellular organisms starts with the transition of a mitotic germ cell towards meiotic S-phase, a highly regulated step which details vary across organisms. In mice, there is an important difference between females and males. During female development, primordial germ cells (PGCs) colonise the primordial gonads and enter meiosis, progressing until metaphase I and staying arrested until puberty. Then, those germ cells, located in the ovary, produce mature oocytes. In males, PGCs are arrested at G1/G0 once they colonise the primordial gonads. At puberty, they develop into spermatogonial stem cells, producing sperm and self-renewing themselves (Kimble, 2007; Nel-Themaat et al., 2010). The signal that drives mitotic germ cells to enter meiosis is retinoic acid in both female fetal gonads and mature testis, and meiotic entrance is mediated by the STRA8 transcription factor (Anderson et al., 2008; Baltus et al., 2006; Oulad-Abdelghani et al., 1996). Interestingly, degradation of retinoic acid by Cyp26b1

protein prevents fetal testis from entering meiosis (Bowles et al., 2006). In *C. elegans*, a single stem cell, known as the distal tip cell (DTC), is able to promote the proliferation of adjacent mitotic germ cells by GLP-1/Notch signalling (Crittenden et al., 2003). The DTC establishes a Notch signal gradient where mitotic cells close to the tip are inhibited from entering meiosis, and as mitotic cells move away from the tip, they express meiosis-triggering factors GLD-1 and GLD-2 to enter meiosis (Fox et al., 2011).

1.2.4 Meiotic S-phase

Historically, this stage was considered the last step prior meiosis, also known as premeiotic S-phase. Nevertheless, studies have shown that meiotic S-phase is coupled with meiosis and that specific processes take place during meiotic replication (Baltus et al., 2006; Forsburg, 2002; Watanabe et al., 2001). Whereas the machinery for mitotic and meiotic replication seem to be the same, the regulation for both meiotic and mitotic S-phase appears to be different (Hollingsworth and Sclafani, 1993; Simchen and Hirschberg, 1977; Williamson et al., 1983). For example, cdc4 mutation blocks DNA replication in mitosis, whereas in meiosis they can complete replication at permissive temperature (25°C) and progress until the first meiotic division in yeast (Simchen and Hirschberg, 1977).

Moreover, several studies have shown that meiotic S-phase takes longer than mitotic S-phase in *Mus musculus, C. elegans,* and *Saccharomyces cerevisiae* among other organisms (Callan, 1973; Jaramillo-Lambert et al., 2007; Sung et al., 1986; Williamson et al., 1983). Although it is unclear why meiotic S-phase lasts longer, it appears to be coupled with meiotic prophase and is important for the events that undergo meiotic cells later during meiotic prophase. For example, deletion of SPO11, which is necessary for DSB formation and recombination, reduces the length of meiotic S-phase by 25% in yeast (Cha et al., 2000) and blocking meiotic replication impedes DSB formation in *S. cerevisiae* (Borde et al., 2000), suggesting that both meiotic S-phase and recombination are coupled in *S. cerevisiae*. Nevertheless, this feature does not seem to be universal, meiotic S-phase is not affected in mutants with defects in DSB formation in *S. pombe* (Murakami and Nurse, 2001). In *C. elegans*, DNA replication is regulated in a

temporal/spatial manner, with autosomal chromosomes replicated earlier than the X chromosomes, which show a heterochromatic state during meiosis (Jaramillo-Lambert et al., 2007). This late replication of heterochromatin has been observed in other organisms during mitotic S-phase (Dutrillaux et al., 1976; Holmquist et al., 1982; Stambrook and Flickinger, 1970).

1.2.4.1 Morphogenesis of meiotic chromosomes

Similar to mitosis, sister chromatid cohesion (SCC) needs to be established during S-phase to allow proper chromosome segregation when cohesin is removed during the meiotic divisions. The cohesin complex forms a ring structure that is highly conserved across organisms. The core cohesin complex is formed of two structural maintenance of chromosomes (SMC) proteins, Smc1 and Smc3, which are connected by a hinge domain, while the ATPase heads of Smc1 and Smc3 are bridged by a kleisin subunit, Scc1/RAD21 in mitosis and Rec8 in meiosis. The accessory protein Scc3/STAG binds to the kleisin and is key for the functionality of the complex. Mitotic and meiotic cohesin differ in the kleisin subunit, which is essential and defines the different roles the cohesin ring carries (Nasmyth and Haering, 2009). Studies in yeast identified Rec8 as the meiosis-specific kleisin that substitutes Scc1 in meiosis (Klein et al., 1999). Rec8 is widely conserved, playing key meiotic roles in most organisms, including *C. elegans* (Pasierbek et al., 2001). In addition to Rec8, higher eukaryotes carry additional meiotic kleisins that have specialised roles within meiosis. In mammals, RAD21L and REC8 coexist within the same nucleus during early prophase but seem to have different roles. RAD21L, which loads after S-phase and is present until mid-pachytene, promotes homologue pairing, meiotic recombination and synapsis initiation, (Herrán et al., 2011; Ishiguro et al., 2014; Lee and Hirano, 2011), whereas REC8 is responsible for the SCC (Burkhardt et al., 2016). In *A. thaliana*, there are four meiotic kleisins: REC8, SYN2, SYN3 and SYN4. SYN2 and SYN4 kleisins participate in DNA repair while SYN3 has a role in the nucleolus of both mitotic and meiotic nuclei (Bolaños-Villegas et al., 2017; Cai, 2003; Dong et al., 2001; Jiang et al., 2007; Zhao et al., 2006). *C. elegans* also has two meiotic kleisins in addition to REC-8: COH-3 and COH-4, which are highly similarly and functionally redundant, participating in CO formation, SC assembly and meiotic chromosome structure (Crawley et al., 2016;

Pasierbek et al., 2001; Severson and Meyer, 2014; Severson et al., 2009). Similar to mouse, only REC-8 is loaded during meiotic S-phase, while COH-3/4 load following completion of replication (Severson and Meyer, 2014). Moreover, COH-3/4 cohesin complexes are targeted by WAPL-1, a cohesin removal factor, during meiotic prophase, while REC-8 complexes are not (Crawley et al., 2016). Importantly, both REC-8 and COH-3/4 cohesin promote axis assembly, as the assembly of the axial elements only fails when no cohesin associates with chromosomes (Lightfoot et al., 2011; Severson et al., 2009).

Another crucial player in regulating meiotic and mitotic chromosome structure is the condensin complex, which is structurally similar to cohesin and conserved across eukaryotes, participating in chromosome organization, condensation and segregation (Hirano, 2016) (figure 5). Condensin structure ring is composed of two SMC proteins, SMC2 and SMC4, forming a heterodimer which is associated to a kleisin subunit and two other regulatory proteins, known as Chromosome Associated Proteins (CAPs) (figure 4). There are two types of condensin, condensin I and condensin II, which differ in the CAP proteins and in their timing of location to chromosomes (Csankovszki et al., 2009a; Hirano, 2016; Ono et al., 2004). *C. elegans* has another subtype of condensin I (condensin I^{DC}) that participates in gene regulation of the X chromosome in hermaphrodites (Csankovszki et al., 2009b), but this complex is not involved in meiosis. Interestingly, in *C. elegans* condensin and cohesin display functional interplay as condensin I promotes cohesin stabilization by antagonising WAPL-1 activity (Hernandez et al., 2018).

1.2.5 Homologous pairing

Before homologous chromosomes recombine, they need to identify and pair with one another, distinguishing their homologous partner from all other chromosomes within the nucleus. This process starts at leptotene, the first stage of meiotic prophase, and the way that homology search occurs varies across organisms.

Most organisms (including mammalians, plants and some fungi) use a largely recombination-dependent mechanism, where DSBs generated by Spo11 and resected

by other factors (see below) produce “homology searching tentacles” that help identify homologous DNA sequences in the nucleus (Hunter, 2015). This process coincides with a clustering of telomeres on a small region of the nuclear envelope (NE), forming a special organisation known as bouquet configuration. This consists in both telomeres of each chromosome associating with the NE and then gathering them in a small area on the NE, whereas the rest of the chromosome is located into the nucleus (Zickler and Kleckner, 1998). Then, chromosome movements are thought to promote homologue pairing by both facilitating interactions between chromosomes and driving them apart when homology is not satisfied. As mentioned above, DSBs play a key role in this process as their repair involves a search for homologous sequences (Harper, 2004; Hiraoka, 1998; Scherthan, 2001; Yancey-Wrona and Camerini-Otero, 1995). However, a recent study has shown that there is a certain level of homolog pairing before DSB are made by SPO11 in mice (Boateng et al., 2013), suggesting the presence of DSB-independent pairing mechanisms.

In *C. elegans*, pairing is independent of recombination and a single end of each chromosome is attached to the NE through the pairing centers (PCs), also known as Homolog Recognition Regions (HHRs). At this stage chromosomes cluster on one side of the nucleus, forming a bouquet-like structure that facilitates homology search. These PCs are repetitive DNA sequences located at the end of the chromosomes and they recruit specifically four different zinc-finger proteins: ZIM-1 (chromosome II and III), ZIM-2 (chromosome V), ZIM-3 (chromosome I and IV) and HIM-8 (chromosome X) (Phillips and Dernburg, 2006; Phillips et al., 2005, 2009; Sanford and Perry, 2001). Interestingly, ZIM mutants show defects in pairing of the specific chromosome they bind to (MacQueen et al., 2005; Phillips et al., 2005). Regulation of HIM-8 differs from the rest of PC-binding proteins as HIM-8 binds to the X chromosome PCs from leptotene-zygotene until late pachytene, whereas autosomal ZIM proteins are linked to autosomal PCs from leptotene-zygotene to early pachytene (Phillips and Dernburg, 2006; Phillips et al., 2005).

In *C. elegans*, the CHK-2 kinase acts as a master regulator of early meiotic events involved, promoting DSB formation and homology search (MacQueen and Villeneuve, 2001). Polo-like kinase 2 (PLK-2) also participates in synapsis and pairing during early

prophase (Harper et al., 2011; Labella et al., 2011). At the beginning of meiotic prophase, CHK-2 phosphorylates HIM-8/ZIM proteins, promoting the association of ZIMs with PCs. Then, PLK-2 can associate with PC-binding proteins through S-pS/T-P motifs phosphorylated by CHK-2, triggering the formation of SUN-1/ZYG-12 aggregates on the NE on areas where PCs are placed on the NE, promoting cytoskeleton-driven chromosome movement (Harper et al., 2011; Penkner et al., 2009; Sato et al., 2009). SUN-1 is located in the inner membrane of the NE and binds to ZYG-12, a transmembrane KASH protein (Starr and Han, 2002), which interacts with cytoplasmic dynein (Malone et al., 2003) (figure 6B and C). *sun-1* or *zyg-12* mutants display abnormal synapsis between nonhomologous chromosomes (Penkner et al., 2007; Sato et al., 2009). This SUN/KASH complex is conserved across eukaryotes (Fridkin et al., 2004; Malone et al., 2003; Minn et al., 2009; Penkner et al., 2007) and connects chromosomes with the cytoskeleton network. Fascinatingly, as result of this molecular system, chromosome movements are originated by cytoskeletal forces located outside the nucleus.

1.2.6 Synapsis

Once homologous chromosomes recognise one another, the SC is assembled linking together the axial elements of the homologues along their entire lengths. The SC is a landmark of meiotic prophase, with this structure observed in most species, including budding yeast, plants, worms and mammals (Cahoon and Hawley, 2016; Moses, 1969). The SC shows a tripartite configuration composed of two main components, the two axial elements (AEs) that are established along each homologue and the central elements (CEs) that holds together the two AEs (figure 2). This “zipper-like” proteinaceous complex was observed using electron microscopy (Moses, 1969) and the distance between the homologues seems to be constant across organisms, being between 90-150 nm (Cahoon and Hawley, 2016; Colaiácovo et al., 2003; De Muyt et al., 2014; Ortiz et al., 2016). While this highly organised proteinaceous complex is crucial to stabilise interactions between homologous chromosomes and to promote crossover formation, the specific roles of the SC and its different components are not completely understood (Cahoon and Hawley, 2016).

AEs are proteinaceous structures assembled along the length of each homologue and contain cohesin and meiosis-specific proteins containing HORMA domains (Aravind and Koonin, 1998). Hop1 was the first HORMA domain protein discovered in *S. cerevisiae*. Mutants in *hop1* have problems with loading the SC and in forming DSBs (Hollingsworth et al., 1990; Smith and Roeder, 1997). In *M. musculus*, HORMAD1 and HORMAD2 are Hop1 homologues and these proteins are also involved in loading and maintenance of the SC and CO formation (Daniel et al., 2011; Kogo et al., 2012; Shin et al., 2010; Wojtasz et al., 2009). In *C. elegans*, HIM-3 is the homologue of Hop1, but along with this protein, there are three HIM-3 paralogues: HTP-1, HTP-2 and HTP-3 (Couteau and Zetka, 2005; Martinez-Perez and Villeneuve, 2005; Martinez-Perez et al., 2008; Severson et al., 2009)). These HORMA domain proteins participate in the regulation of key events through meiosis, such as homolog recognition, CO formation or release of sister chromatid cohesion. HTP-3 acts as the backbone of the rest of axial element, being required for DSB formation (Goodyer et al., 2008) and to load REC-8-containing cohesin complexes (Severson et al., 2009). On the other hand, HTP-1 and HIM-3 participate in homolog recognition, promoting faithful SC assembly (Couteau and Zetka, 2005; Martinez-Perez and Villeneuve, 2005)**.**

HORMA domain proteins also play roles in the quality control mechanisms that monitor the progression of SC assembly and recombination between the homologues (Subramanian and Hochwagen, 2014). In *C. elegans,* defects in SC assembly, even between a single pair of homologues (*him-8* mutants), trigger a clear delay in meiotic progression that is evident by the persistence of nuclei with clustered chromosomes beyond the transition zone of the germline. This delay is also exemplified by the persistence of markers of chromosome movement, such as PLK-2 aggregates on PCs, into the pachytene region (Harper et al., 2011; Penkner et al., 2009; Sato et al., 2009). Moreover, mutants that display impaired CO formation due to defects in DSB formation or repair, but that display normal synapsis, display prolonged activity of DSB-promoting mechanisms (Rosu et al., 2013; Stamper et al., 2013). In both cases, defects in SC assembly or CO formation, HORMA domain proteins are required for the feedback mechanisms that prevent exit from meiotic stages competent for DSB formation and chromosome movement ((Harper et al., 2011; Silva et al., 2014).

The central element (CE) of the SC is required to stabilise interactions between homologues, creating a zipper-like structure between AEs. *S. cerevisiae* only presents a single CE component known as Zip1 (Sym et al., 1993), whereas in *M. musculus* there are five proteins with this role: SYCP1, SYCP2, SYCP3, SYCE1 and TEX12 (Fraune et al., 2012). In *C. elegans* four proteins have been described: SYP-1, SYP-2, SYP-3 and SYP-4, which are interdependent for their loading onto chromosomes: if any of them is absent, the SC fails to assemble (Colaiácovo et al., 2003; MacQueen et al., 2002; Smolikov et al., 2007, 2009). Another particularity of *C. elegans* is that synapsis starts from the chromosome end containing the pairing center, and progresses along chromosomes regardless of homology, leading to non-homologous synapsis when homology search mechanisms fail (Couteau and Zetka, 2005; Dernburg et al., 1998; MacQueen et al., 2005; Martinez-Perez and Villeneuve, 2005). In most organisms, but not in *C. elegans* and *D. melanogaster*, synapsis and recombination are coupled and synapsis fails in the absence of DSBs (Dernburg et al., 1998; MacQueen et al., 2002; Zickler and Kleckner, 1999). This represents an experimental advantage as *C. elegans* allows the study of recombination and synapsis independently, which has facilitated the identification of the main players in each process. Finally, mutants with defects in SC assembly display severe defects in CO formation (Lui and Colaiácovo, 2013).

1.2.7 Recombination

Proper meiotic chromosome segregation requires the formation of at least one crossover event between each homologue pair. COs, together with the SCC, provide the basis of chiasmata, temporary physical attachments between homologous chromosomes that ensure their correct orientation on the first meiotic spindle. Moreover, COs contribute to genetic variability by reshuffling the paternal and maternal genomes.

1.2.7.1 DSB formation

Recombination is initiated by Spo11, a topoisomerase-like enzyme that is highly conserved across organisms (Bergerat et al., 1997; Keeney et al., 1997; Sun et al., 1989)

(figure 3). Spo11 was proposed as the enzyme that catalyses DSB formation as dimers since its similarity with the catalytic A subunit of TopoVI, which is a member of the type II DNA topoisomerase family (Bergerat et al., 1997). TopoVI is formed by a heterotetramer composed of two different homodimers (TopoVIA and TopoVIB). The TopoVIA homodimer is composed of two catalytic A subunits, whereas the TopoVIB homodimer is composed of two b subunits, which contain ATP binding domains. ATP hydrolysis is required for the catalytic activity and conformational changes of the complex (Robert et al., 2016a).

Nevertheless, recent studies have shown that the core of the DSB machinery is more similar to TopoVI topoisomerase than expected. Spo11 has been found to form heterotetramers with TopoVIB-like proteins in mice (TOP6BL), *S. cerevisiae* (Rec102), *S. pombe* (Rec6), and *D. melanogaster* (MEI-P22)(Robert et al., 2016b; Vrielynck et al., 2016). No TopoVIB-like protein has been found in *C. elegans* yet. This complex would cleave both DNA strands of a double-stranded DNA molecule and form a covalent union between each strand of DNA and a tyrosine residue on Spo11 (Bergerat et al., 1997; Keeney et al., 1997).

Furthermore, Spo11 needs to work with several auxiliary proteins to be able to function properly and these cofactors vary across organisms. In *S. cerevisiae*, phosphorylation of Mer2 by cell cycle kinases is necessary to start programmed DSB formation (Henderson et al., 2006; Wan et al., 2008). In *C. elegans*, *spo-11* mutants and other mutants which have defects in DSB formation, such as DSB-1 (Stamper et al., 2013)and DSB-2 (Rosu et al., 2013)**,** display 12 univalent chromosomes in diakinesis as consequence of a global failure in CO formation.

Determining where DSBs occur in the genome is the first step to regulate CO distribution. DSB formation is tightly regulated across the genome (Baudat and Nicolas, 1997; Gerton et al., 2000), with some areas of the genome being more prone to DSB formation than others. The regions of the genome which are more favourable to DSBs are known as DSB hot spots, and the distribution of these hot spots varies across species. In *S. cerevisiae*, hot spots have a tendency to be near transcriptional start sites and do not have a recognisable DNA motif, whilst in other species like *M. musculus* and *H. sapiens*, DSB hot spots tend to avoid those regions and they seem to have a DNA motif

(Myers et al., 2006, 2008). Moreover, regions of the genome that contain high levels of trimethylation of histone H3 on lysine 4 (H3K4me3) correlate with hot spots in *M. musculus*, *H. sapiens* and yeast (Borde et al., 2009; Buard et al., 2009). In *C. elegans*, it has been shown that condensin DPY-28 affects DSB distribution and CO distribution (Mets and Meyer, 2009; Tsai et al., 2008), suggesting that condensin has a role regulating both by altering chromosome structure.

1.2.7.2 DSB resection

Once the dimer of Spo11 has carried out its function by producing a DSB, Spo11 remains covalently bound to the DNA (Bergerat et al., 1997; Keeney et al., 1997). This molecular intermediate is cleaved by the Mre11-Rad50-Xrs2/Nbs1 (MRX/N) exonuclease complex together with the endonuclease Com-1/Sae2/Ctp1, releasing two Spo-11-oligonucleotides (Hartsuiker et al., 2009; Neale et al., 2005). Then, the 5'-3' exonuclease EXO-1 resects the ssDNA end on either side of the break, producing two long overhanging 3' single-stranded DNA (ssDNA) (Tsubouchi and Ogawa, 2000; Zakharyevich et al., 2010). In *C. elegans*, MRN/X complex is conserved but MRE-11 also shows an important role for DSB formation. *mre-11* and *rad-50* mutants cannot process DSBs and show oocytes containing chromatin aggregates at diakinesis (Chin and Villeneuve, 2001; Hayashi et al., 2007; Yin and Smolikove, 2013). These aggregates occur as a result of repairing DSBs by non-homologous end joining (NHEJ) instead of using homologous recombination (HR).

1.2.7.3 Strand invasion

Following resection, several RPA (replication factor A) molecules bind to the ssDNA tails to protect and stabilise them from creating secondary structures. After this, RPA is replaced by two recombinases: Rad51 and the meiosis-specific DMC1 (Bishop et al., 1992; Sehorn et al., 2004; Shinohara et al., 1992). These RAD51-DMC1-ssDNA complexes, together with other chromatin remodelling proteins, can invade other double strand DNA (dsDNA) templates searching for homology. As a result of this, the complementary strand of the invaded dsDNA template is displaced creating a

displacement loop (D-loop) (Szostak et al., 1983). *C. elegans* does not have Dmc1 homologue, so it is thought that RAD-51 recombinase can perform this activity alone. Moreover, RAD-51 foci peaks appear in wild type worms between early pachytene and mid pachytene, in contrast with the majority of species which have these peaks between leptotene and zygotene. This is because synapsis and DSB formation are independent in *C. elegans* (Alpi et al., 2003).

1.2.7.4 Repair bias and partner choice

Proper chromosome segregation requires DSBs to be repaired as COs using one of chromatids of the homologue as a repair template. Consequently, a repair bias mechanism is generated in meiosis by promoting inter-homologue (IH) strand invasion and inhibiting inter-sister (IS) recombination. This bias has been empirically observed in *S. cerevisiae*, where the ratio between IH:IS is 5:1, whereas if there was not any bias, the expected ratio would be 2:1 (Bzymek et al., 2010; Kadyk and Hartwell, 1992; Schwacha and Kleckner, 1994). This is achieved by the Hop2-Mnd1 heterodimer which promotes IH recombination by Dmc1 (Tsubouchi and Roeder, 2002; Zierhut et al., 2004). In yeast, it has also been shown that Mek1 signalling, a paralog of CHK-2 in *C. elegans* limits IS recombination (Goldfarb and Lichten, 2010). Moreover, Hop1, an axial element (HORMA-domain) protein in *S. cerevisiae*, is involved in an IH repair checkpoint where Hop1 is phosphorylated by Mec1/Tel1 to promote IH recombination (Niu et al., 2005; Wan et al., 2004). HORMA-domain protein HTP-1 appears to play an analogous role in preventing IS repair during meiosis in *C. elegans* (Martinez-Perez and Villeneuve, 2005).

1.2.7.5 ZMM-dependent crossover pathways

After D-loop formation, DNA polymerases extend the ssDNA using the invaded double strand as a template, spreading the D-loop as well. Then, the extended D-loop is taken by the opposite strand of the DSB, a process known as second end capture, forming a joint molecule (JM) between the two recombining chromatids (Szostak et al., 1983). Normally, this JM is not resolved by endonucleases, favouring this molecule becomes a double Holliday junction (dHJ) (Bzymek et al., 2010; Holliday, 1964). ZMM proteins

stabilise this dHJ intermediate, allowing it to be either repaired as a crossover event (resolution) or as a noncrossover event (dissolution) by resolvases (Wyatt and West, 2014). Nevertheless, studies in *S. cerevisiae* have shown that dHJs are mostly repaired as COs (Bishop and Zickler, 2004; Lynn et al., 2007). Members of this ZMM family are: Mer3 helicase which helps to extend D-loops, Msh4-Msh5 heterodimer (known as MutSγ) which stabilises dHJs (Hollingsworth et al., 1995; De los Santos et al., 2003). Zip2, Zip3, Zip4 and Hei10 which modify protein interactions by SUMOylation and/or ubiquitination (Cheng et al., 2006; De Muyt et al., 2014; Perry et al., 2005). This ZMM-dependent pathway is responsible for most crossovers in yeast, plants, mammals and for virtually all crossovers in the case of *C. elegans* (Guillon et al., 2005). ZMM-dependent crossovers are known as class I crossovers.

1.2.7.6 ZMM-independent crossover pathways

Joint molecules can also be resolved as COs or non-crossovers (NCOs) by Mus81-Mms4 and Slx-1-Slx4 endonucleases before they become dHJ (Cromie et al., 2006; Gaillard et al., 2003; Interthal and Heyer, 2000; Zakharyevich et al., 2012). These COs are known as class II crossovers, and in contrast to class I they do not show CO interference (see section 1.2.7.8.3 below) and are responsible for a small fraction of the total number of COs in most species. In *M. musculus*, this pathway contributes with 5-10% of COs (Holloway et al., 2008), 5% in *Arabidopsis thaliana* (Higgins et al., 2012) and 15-35% in budding yeast (Wan et al., 2004). However, *S. pombe* relies on this pathway almost completely, depending on Mus-81-Emei1 endonucleases to form 80-95% of its COs, which do not show CO interference (Smith et al., 2003). Although *C. elegans* does not use this pathway to form COs in normal conditions, MUS-81 with SLX-1 and SLX1-SLX4 can create class II crossovers if there is an artificial increase of DSBs that come from gamma-irradiation or a mutation in the helicase *rtel-1* (Agostinho et al., 2013; Saito et al., 2013; Youds et al., 2010).

1.2.7.7 Crossover vs non-crossover pathway

The number of DSBs greatly exceeds the number of COs, implying that most DSBs are repaired as NCO events. The majority of NCOs are generated by the synthesis-dependent strand annealing (SDSA) pathway in *S. cerevisiae* (McMahill et al., 2007). In this pathway, the D-loop of the JM is disrupted because ZMM proteins are not protecting the dHJ. Then, the invading 3' ssDNA is able to reanneal with the other side of the DSB and DNA synthesis in both strands occurs (Morrical, 2015). Surprisingly, *S. cerevisiae* could also generate NCOs by the dissolution of dHJs by the Sgs1 (BLM in mammals) helicase working together with TopoIIIα topoisomerase (Martini et al., 2011). In *C. elegans*, the conserved anti-recombinase RTEL-1 promotes NCO formation by disrupting D-loops and promoting SDSA (Barber et al., 2008; Youds et al., 2010).

On the other hand, only a subset of CO intermediates will transform into COs. The process of determining which CO intermediates will become mature COs is known as CO designation. In *C. elegans*, several MutS foci (class I component) per chromosome can be monitored at mid pachytene, when DSB repair is taking place. By late pachytene, these foci are restricted to the final CO site. Furthermore, COSA-1, an essential cyclin-like protein for CO formation, reinforces CO designation, forming a single focus per homologue pair at late pachytene that indicates the position of the CO (Woglar and Villeneuve, 2018; Yokoo et al., 2012). Mutations in *cosa-1*, *msh-4* or *msh-5* genes lead to total defects in CO formation (Kelly et al., 2000; Yokoo et al., 2012; Zalevsky et al., 1999). In mouse, CNTD1, an ortholog of COSA-1, has shown that it is also crucial for CO formation (Holloway et al., 2014), demonstrating conservation of this protein in CO formation.

1.2.7.8 CO regulation

The number and distribution of COs are highly regulated in all organisms. Although the regulation governing these two features is not completely understood, there are three different features of meiotic recombination that shape CO numbers and distribution. First, each pair of homologous chromosomes should receive at least one CO, which is known as CO assurance. Second, COs are more spread out than it would be expected

from a random distribution, which is known as CO interference. Finally, CO homeostasis maintains constant the number of COs despite increments or reductions in DSB numbers. Whether these properties are independently regulated or whether they are controlled by the same molecular mechanisms remains to be addressed. In this section, I will review the different processes that regulate crossover formation, mostly focusing on *C. elegans*.

1.2.7.8.1 DSB distribution

As recombination is initiated by the formation of SPO11-dependent DSBs, the number and location of DSBs has crucial impact on the location of the final product of recombination, which is the CO. Moreover, meiotic chromosome organization is essential for recombination, as chromosomes axes play key roles in the regulation of DSB formation and repair (Borde and de Massy, 2013).

Similar to CO interference, the formation of nearby DSBs is disfavoured during early meiosis in *S. cerevisiae*, a process known as DSB interference and that requires the Tel1 (ATM) (Garcia et al., 2015). In mammals, the ATM kinase also diminishes the frequency of DSB formation expected across 70-100kb, thus preventing clustering of DSBs and shaping the DSB landscape (Mohibullah and Keeney, 2017). Interestingly, a study in *S. cerevisiae* showed that the addition of a non-natural DSB hotspot produces a decrement of DSBs and recombination around that zone (Ohta et al., 1999). Given this, it has been hypothesized that DSB hotspots compete among each other for essential DSB formation factors to form COs.

In mice and humans, PRDM9, a histone methyltransferase with a specific DNA-binding domain, determines the distribution of the majority of DSBs and, consequently, DSB "hotspots" (Baudat et al., 2010; Parvanov et al., 2010). PRDM9 binds its DNA targets and catalyses histone H3 lysine 4 trimethylation (H3K4me3) on the closest nucleosomes, recruiting and activating SPO11 in a direct or indirect fashion. Moreover, H3K4me3 is not sufficient to promote DSB formation, as other regions of the genome enriched with H3K4me3, such as enhancers or transcription start sites, are not DSB hot spots (Brick et al., 2012; Myers et al., 2008).

In *C. elegans* the regulation of the DSB landscape is poorly understood, but it has been shown that condensin I has a crucial role controlling DSB distribution by modifying chromosome structure (Mets and Meyer, 2009). Spo11-oligonucleotide techniques have not been implemented in *C. elegans* yet, but ChIP-seq studies have showed that wild type chromosome arms are enriched with RAD-51, an essential early recombination intermediate, compared to chromosome centres, mirroring the CO distribution and suggesting that DSBs might form more frequently in chromosome arms (Yu et al., 2016). Nevertheless, RAD-51 was also detected in chromosome subtelomeric regions while COs are not present in these regions, showing a discrepancy between the RAD-51 intermediates map and CO distribution, and implicating that DSBs are preferably repaired as non-crossovers in these regions (Ho et al., 2014; Yu et al., 2016). However, when DSBs are induced by ionizing radiation in *spo-11* mutants, producing randomly placed artificial DSBs along the entire length of chromosomes, this increases the percentage of COs located in the central region chromosomes (JS and AM, 1987).

1.2.7.8.2 CO assurance

Crossover assurance refers to the process that ensures the formation of at least one CO, the obligate CO, between each pair of homologues, which is essential for correct chromosome segregation at meiosis I. This phenomenon is present in most animals, however, an exception for this is the chromosome 4 of *D. melanogaster*, in which crossover formation does not occur (Hartmann and Sekelsky, 2017). Whether the same mechanisms governing CO interference are also responsible for CO assurance is uncertain. In *S. cerevisiae*, most *zmm* mutants, such as *zip1* or *msh5*, have defects in SC formation and a decrease in the number of CO events, affecting both CO interference and CO assurance and indicating that these two properties could share molecular mechanisms (Börner et al., 2004). On the other hand, *spo16* mutant, another ZMM component that promotes Zip1 polymerization from recombination sites, also shows defects in SC and a reduced number of COs, making only 33-50% of COs compared to wild type levels and these residual COs retain CO interference, indicating that the molecular mechanisms that regulate CO assurance and CO interference could be different (Shinohara et al., 2008).

C. elegans displays strong crossover assurance, with a single artificially induced DSB per homologue pair being sufficient to form a crossover (Rosu et al., 2013). A feedback mechanism to ensure CO formation, by promoting DSB formation, takes place when cells have difficulties making CO-fated intermediates. Most mutants with defects in CO formation induce a crossover assurance checkpoint that prolongs CHK-2 activity, extending the leptotene/zygotene stage and maintaining active DSB-1 and DSB-2, two proteins thought to indicate a permissive DSB formation state (Rosu et al., 2013; Stamper et al., 2013). Doing this, these cells attempt to stimulate the formation of DSBs to ensure that each bivalent obtains a CO-fated intermediate, which exact nature remains unknown. Interestingly, these new DSBs are placed in different regions of the genome, altering the DSB map, and consequently, the CO distribution. A good example of this situation is the *him-8* mutant. HIM-8 binds to the pairing center of the X chromosome and is essential to promote chromosome movement, synapsis, pairing and, therefore, CO formation within the X chromosome. *him-8* mutants do not have any problem at making COs on the autosomes, however, they also show an alteration in autosomal genetic distances, demonstrating that this feedback mechanism is indirectly affecting the CO distribution in these autosomes (Herman and Kari, 1989; Yu et al., 2016).

1.2.7.8.3 Crossover interference

The formation of one CO at one position disfavours the event of another CO event nearby, generating spaces between COs, which as a consequence follow a gamma distribution. This property, which was discovered more than 100 years ago in *Drosophila melanogaster* (Sturtevant, 1915), has been found in most organisms: *S. cerevisiae* (Sym et al., 1993), *M. musculus* (Broman et al., 2002), *H. sapiens* (Rasmussen and Holm, 1984) and *C. elegans* (Meneely et al., 2002). Only class I COs are affected by interference (Berchowitz et al., 2007; Holloway et al., 2008; De los Santos et al., 2003). Organisms such as *Schizosaccharomyces pombe*, in which 80-95% of its COs are formed by Mus81-Eme1 (class II CO pathway), do not show CO interference (Cromie et al., 2006; Smith et al., 2003). Interestingly, *Mus81* mutants in mice, which lack class II COs, have supplementary class I COs that are not subject to interference, implicating that there is

a temporal difference between the timing when interference acts and the formation of these new subset of class I COs which replace the COs formed by MUS81 in mice (Holloway et al., 2008).

C. elegans exhibits strong CO interference, showing one single CO event per homologue pair in most cases, this displaying complete crossover interference. However, genetic studies have shown that a second CO can rarely occur, and this second CO is normally far apart from the first CO. Moreover, studies with strains carrying chromosomes fusions involving two (*mnT12* (X;IV) or three chromosomes (*meT7* (III;X;IV)) have shown that a single CO is what it happens in most occasions, demonstrating that CO interference is powerful enough to limit the number of COs in a context where the length of the chromosome is three times longer in worms with a wild-type karyotype (Hillers and Villeneuve, 2003; Libuda et al., 2013; Lim et al., 2008). Although the signal that transmits interference remain unknown (see below), worms with partial depletion of a central region SC component displayed reduced interference, suggesting that an intact SC is important for interference (Libuda et al., 2013).

1.2.7.8.3.1 Models of CO interference

One question that remains elusive is how the signal responsible for interference is transmitted along chromosomes, with three main interference models having been proposed. The first model is the “mechanical stress model”, also known as Beam-Film model, which proposes chromosomes are under stress as they compress and expand continuously. In this model, CO designation reliefs the stress generated within the chromosome locally, creating a signal that could expand to the rest of the chromosome in both directions, dissipating with distance (Kleckner et al., 2004). If another CO event is needed to relief remaining stress, this will happen in a region where stress was not released by the first CO. In this model, the transmission of mechanical stress would be the signal responsible for CO interference. However this model would not explain why class II crossovers do not relieve stress as class I crossovers do (Berchowitz and Copenhaver, 2010; Kleckner et al., 2004; Zhang et al., 2014). The second model is the “polymerization model” which proposes that early recombination events begin

simultaneously within different locations along the chromosome in an independent fashion and they would have the same probability of developing a polymerization event (Berchowitz and Copenhaver, 2010; King and Mortimer, 1990). This polymerization event could propagate bidirectionally to the rest of the chromosome, acting as the interference signal that blocks nearby events to become COs. Nevertheless, this polymer has never been found, but it is possible that cohesin or a histone modification, such as acetylation, phosphorylation or methylation, could be the signal that acts as a polymer. The third model is the "counting model" which is a mathematical model that predicts that contiguous COs are widely spaced by a fixed number of intervening NCOs. The original counting model predicted CO data from *Drosophila* and *N. crassa* well, whereas it was not able to do the same with CO data from humans and *S. cerevisiae*. To explain these CO distributions, a new version of the counting model was adapted. This version admitted several non-interfering CO, fitting data from humans, *S. cerevisiae* and *A. thaliana*. However, no specific CO interference mechanism has been proposed for this model (Berchowitz and Copenhaver, 2010; Foss et al., 1993; Zhang et al., 2014).

1.2.7.8.4 CO Homeostasis

Meiotic DSBs outnumber CO events in all studied organisms and the ratio between CO/DSB depends on the organism. However, if the number of DSBs is altered, a phenomenon called CO homeostasis maintains the number of COs constant despite of increasing or decreasing numbers of DSBs, which is achieved by modulating the number of NCO events. This property has been observed in *S. cerevisiae*, *M. musculus*, *C. elegans* and *A. thaliana* (Cole et al., 2012; Martini et al., 2006; Varas et al., 2015; Yokoo et al., 2012).

Similar to CO assurance, *C. elegans* shows robust CO homeostasis. As previously mentioned, a single DSB produced by transposon excision is sufficient to form a CO in C. elegans (Rosu et al., 2013). However, the study which demonstrated better CO homeostasis in *C. elegans* was performed by Yokoo and colleagues. In this study, *spo-11* mutants were irradiated with different amounts of gamma irradiation. At lower amounts of irradiation, these artificial DSBs were proficiently transformed into one CO

per homolog; at higher amounts of irradiation, these worms kept making only one CO per homolog despite much higher numbers of DSBs, demonstrating that CO homeostasis is present in *C. elegans* (Yokoo et al., 2012).

Finally, CO homeostasis could be considered as a consequence of both CO assurance and CO interference. Firstly, CO assurance stablishes the minimum number of CO per pair of homologous and, simultaneously, CO interference defines the maximum number of CO per homolog. Given this, to distinguish whether these three phenomena share molecular mechanisms or not is a question that remains to be clarified.

1.2.7.8.5 CO distribution

CO distribution results from the interplay between all the regulatory phenomena mentioned above, and is also known to be variable across organisms and even between the sexes of the same species (Mézard et al., 2015). Nevertheless, the molecular mechanisms that regulate CO distribution are vastly unknown. There are some patterns that are generally found among species, for example, centromeres and telomeres are usually depleted of COs, as COs in these regions are thought to increase the probability of meiotic chromosome missegregation (Ottolini et al., 2015; Ren et al., 2016; Saito and Colaiácovo, 2017). COs can affect kinetochore orientation and cohesion around the pericentric region when they are placed at centromeres, inducing high levels of chromosome missegregation during meiosis I in *S. cerevisiae* (Sears et al., 1995). This was known as the "centromere effect" and it was firstly described in *D. melanogaster* (Beadle and Ker, 1931) but it has also been found in other organisms. In plants, this centromere effect is achieved by methylation of centromeric regions by *met1* (Yelina et al., 2012).

In *C. elegans*, even though this nematode has holocentric chromosomes (lacking localized centromeres), COs tend to be avoided around the centre of chromosomes by a mechanisms that requires the SLX-1 endonuclease (Saito et al., 2013). High resolution recombination mapping has shown that the *C. elegans* genome does not contain apparent CO hotspots regions and that COs are also excluded at telomeres (Barnes et al., 1995; Kaur and Rockman, 2014; Rockman and Kruglyak, 2009; Yu et al., 2016).

1.2.8 Chromosome Remodelling

Following the formation of COs between the homologues, the SC is disassembled, and chromosomes start to condense during diplotene in preparation for the meiotic divisions. SC disassembly is a highly regulated and kinase-dependent process in which the timing between CO formation and SC disassembly is crucial. In *S. cerevisiae*, SC disassembly depends on Cdc5 (Polo-like kinase) and Ipl1 (Aurora B) kinases (Jordan et al., 2009; Sourirajan and Lichten, 2008). Similar to *S. cerevisiae*, PLK1 and INCENP, a protein cofactor which regulates Aurora B localization and activation, participate in SC disassembly in *M. musculus*, and they are both located to the SC during pachytene (Jordan et al., 2012; Parra, 2003). SC components SYCP1 and TEX12 are phosphorylated by PLK1, promoting the disassembly of the central region of the SC at diplotene (Parra, 2003). This affects INCENP localization which disappears from the chromosome arms and stays at the centromeric regions recruiting Aurora B (Parra, 2003). SYCP3 and SYCP2 vanish from the lateral elements by Aurora B activity, and they are only maintained at the heterochromatic centromeres until metaphase I (Parra, 2003; Sun and Handel, 2008). In *C. elegans*, chromosomes are holocentric, so the strategy must be different. CO formation triggers the asymmetrical disassembly of the SC around the CO site, with the SC being depleted between the CO and the furthest telomere, and retained between the CO and the closest telomere (Nabeshima et al., 2005). COs also produce a redistribution of axial element components: while HIM-3 and HTP-3 remain located along the whole length of chromosomes (Goodyer et al., 2008; Zetka et al., 1999), while HTP-1/2 and LAB-1 are only retained between the CO and the furthest telomere (SC depleted region) (figure 7) (De Carvalho et al., 2008; Martinez-Perez et al., 2008). The region retaining SC components until late diakinesis is known as the short arm of bivalents, while the region containing HTP-1/2 and LAB-1 is known as the long arm of bivalent diakinesis. This CO-triggered remodelling is crucial for chromosome segregation as regions containing HTP-1/2 and LAB-1 are protected from cohesin removal during the first meiotic division (De Carvalho et al., 2008; Ferrandiz et al., 2018; Martinez-Perez et al., 2008).

1.2.9 The Meiotic divisions

Chiasma formation during meiotic prophase is crucial for the meiotic divisions, as this structure, provided by a CO together with SCC, is essential for the correct orientation of bivalents on the metaphase I plate. Key to this process is the mono-orientation of sister centromeres so that their kinetochores attach together to microtubules from the same spindle pole. In organisms with monocentric chromosomes, such as mammals or budding yeast, the kinetochore is located in the predetermined centromere position. In organism with holocentric chromosomes, such as *C. elegans* or some plants, the kinetochores decorate the whole length of the chromosome (Biggins and Walczak, 2003; Hauf and Watanabe, 2004; Kitagawa and Hieter, 2001). Once all bivalents are correctly aligned on the metaphase plate, the onset of anaphase I triggers the activation of separase, which induces cohesin cleavage along chromosome arms to allow the separation of homologous to opposite poles of the cell. Crucially, cohesin on centromeric regions is protected from separase cleavage during the first meiotic division, so that these regions remain tethered until the second meiotic division. As mentioned above, in *C. elegans* HTP-1/2 and LAB-1 determine the regions in which cohesin must be protected during the first meiotic division. They achieve this by promoting recruitment of the PP1 phosphatase, which antagonizes Aurora B recruitment and thus REC-8 phosphorylation, which promotes cohesin removal (De Carvalho et al., 2008; Ferrandiz et al., 2018; Martinez-Perez et al., 2008). Finally, during the second meiotic division, sister kinetochores are bi-orientated, attaching to microtubules from opposite spindle poles, and complete removal of cohesin by separase allows the segregation of sister chromatids to opposite spindle poles, generating haploid gametes.

The goal of this project was to improve our understanding on the interplay between chromosome structure and CO formation. Particularly, I wanted to understand how subtle differences in chromosome structure could alter CO properties, and, at the same time, how these COs could promote changes in chromosome structure.

1.3 Aims of this thesis

The original aims of this study were:

1. To use super resolution microscopy (SRM) to investigate the structural changes that meiotic chromosomes undergo during meiosis, focusing on the process of crossover formation during meiotic prophase.

2. To elucidate how the *him-13* mutation affects crossover distribution and/or chromosome morphology.

To achieve aim 1, the first experimental goal of this study was to develop protocols to image three-dimensionally intact meiotic nuclei from the *C. elegans* germline using different SRM techniques. Chapter 3 contains a brief introduction to SRM and a detailed description of the methods that I developed to implement SIM and STED microscopy to image meiotic chromosomes.

The first goal for aim 2 was to identify the molecular identity of the *him-13* mutation, which previous studies in the lab had demonstrated to induce an altered CO distribution without affecting CO numbers. Moreover, these studies also suggested that diakinesis bivalents displayed altered chromosome structure, despite the presence of chiasmata. These features made this mutant an attractive candidate to investigate the functional interplay between meiotic chromosome structure and the mechanisms that determine CO distribution. Chapter 4 shows the multiple genetic approaches that I took to determine the molecular identity of the *him-13* mutation, while chapter 5 is dedicated to the functional characterisation of this mutant, including the use of SRM to investigate CO distribution in *him-13* mutants.

Finally, in chapter 6, I exploit SRM methods described in chapter 3 to perform a detailed analysis of the morphological features of specific chromosomes at different meiotic

stages, and I start investigating how different known regulators of meiotic chromosome structure affect these features.

Figure 1. *C. elegans* is an excellent model to study meiosis

A - Schematic diagram of C. elegans germ line showing all the stages of meiosis. Each germ line contains a complete time course of meiosis with nuclei organised in a spatial/temporal gradient in which specific meiotic stages can be easily identified. The main events of meiotic prophase can be easily distinguished by the specific morphology of the nucleus in each stage. In TZ, nuclei form a distinct crescent moon shape, which indicates the clustering of homologues as they look for each other. In pachytene, the SC is established between the homologs, forming parallel tracks. Following this, CO formation in late pachytene triggers the disassembly of the SC, leading to the distinct chromosomal morphology of the diplotene stage, where chromosomes condense and undergo remodelling. Finally, in diakinesis, 6 bivalents, which are only linked by the chiasmata and SCC, can be visualised.

B - Dissected *C. elegans* germ line stained with DAPI.

Diagram adapted from my colleague Sarah Testori.

A

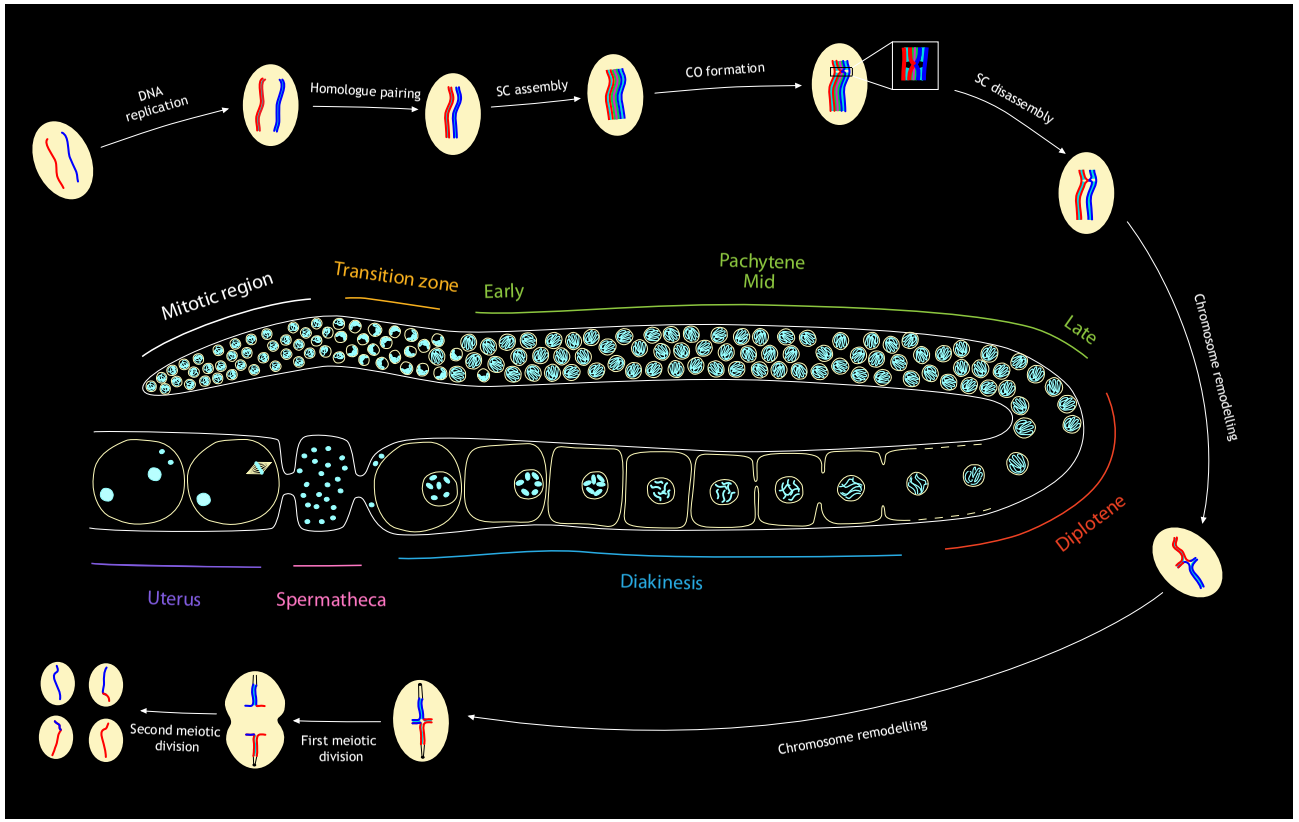
DNA replication
Homologue pairing
SC assembly
CO formation
SC disassembly
Chromosome remodelling
Mitotic region
Transition zone
Early
Pachytene
Mid
Late
Diplotene
Diakinesis
Uterus
Spermatheca
Second meiotic division
First meiotic division
Chromosome remodelling

B

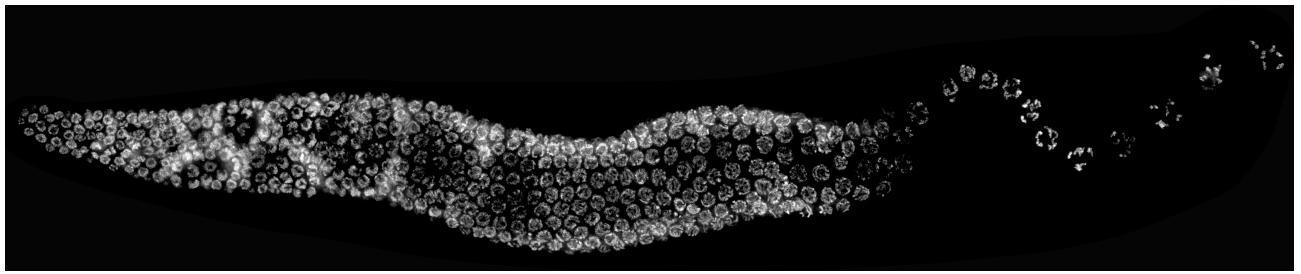

Figure 2. Synaptonemal complex structure and chromosome organization is highly conserved across organisms

The synaptonemal complex (SC) is a dynamic zipper-like tripartite proteinaceous structure that holds together the homologous chromosomes during meiotic prophase before the first meiotic division. Cohesin complexes and HORMA proteins are loaded onto the homologous chromosomes forming the axial elements (AEs). Central element (CE) are loaded along the midline of the homologous chromosomes stabilising synapsis. At pachytene stage, synapsis is completed, and SC is fully formed between homologous chromosomes. The SC is disassembled again during diplotene and diakinesis stages. The separation between the axial elements is around 120 nm in *C. elegans*.

Diagram adapted from Sarah Testori.

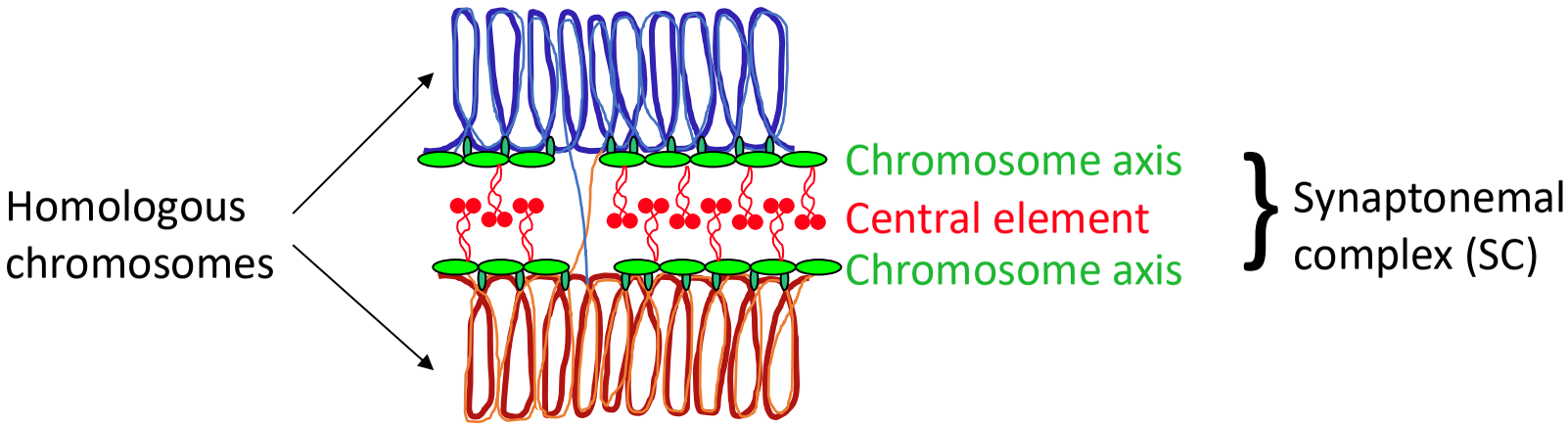
Homologous
chromosomes
Chromosome axis
Central element
Chromosome axis
Synaptonemal
complex (SC)

Figure 3. Diagram showing the main events of meiotic recombination in *C. elegans*

Homologues are represented in red and blue, while the sister chromatids of each homolog are represented by two lines of the same colour. Enzymes required for specific events are indicated on the right side of each specific step. Recombination is initiated with the formation of a DSB in a single chromatid by SPO-11. MRE-11/RAD-50 exonuclease complex together with the endonuclease COM-1 cleave this intermediate, releasing two SPO-11-oligonucleotides. Then, the 5'- 3' EXO-1 exonuclease completes the resection, creating two overhanging 3' ssDNA. After this, RAD-51 is loaded onto the ssDNA and promotes the invasion of another chromatid from the other homologous chromosome, creating a D-loop by DNA synthesis. RTEL-1 can destabilise this structure, producing a NCO event. However, when this structure is stabilised by ZMM proteins (MSH-4, MSH-5), a dHJ is formed. This dHJ is repaired as a CO event (resolution) or as a NCO event (dissolution). Interestingly, *C. elegans* RAD-51 is enough to promote the strand invasion, whereas in most organisms the meiosis-specific DMC1 recombinase is also required. Moreover, Class I COs are responsible for virtually all crossovers in the case of *C. elegans.*

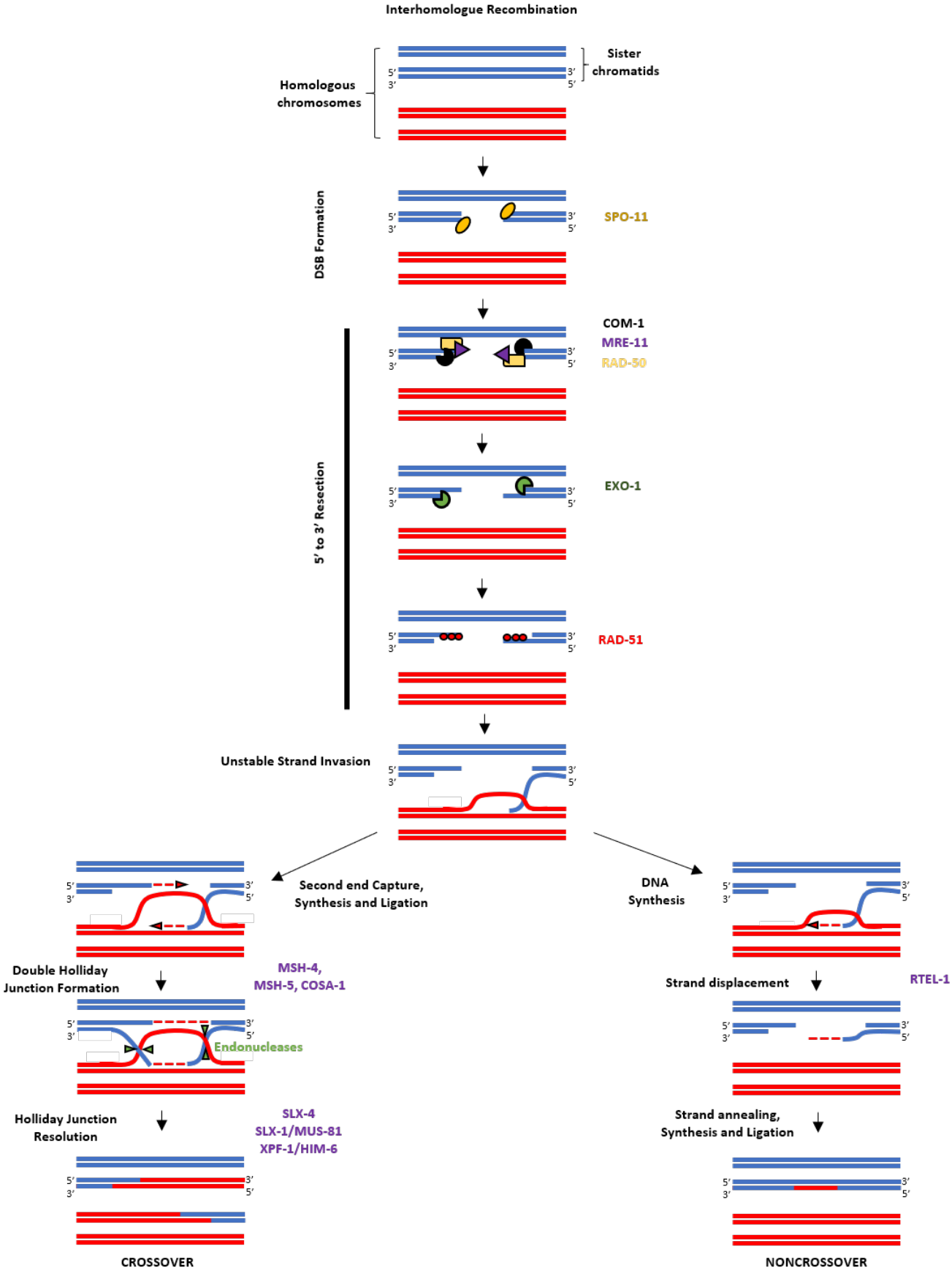
Interhomologue Recombination
Homologous chromosomes
Sister chromatids
5′
3′
3′
5′
DSB Formation
SPO-11
COM-1
MRE-11
RAD-50
5′ to 3′ Resection
EXO-1
RAD-51
Unstable Strand Invasion
Second end Capture, Synthesis and Ligation
DNA Synthesis
Double Holliday Junction Formation
MSH-4, MSH-5, COSA-1
Endonucleases
Holliday Junction Resolution
SLX-4
SLX-1/MUS-81
XPF-1/HIM-6
CROSSOVER
Strand displacement
RTEL-1
Strand annealing, Synthesis and Ligation
NONCROSSOVER

Figure 4. Cohesin complexes in *C. elegans*

The core cohesin complex is formed by two SMC proteins, SMC-1 and SMC-3, which are linked by a hinge domain, plus a kleisin subunit (SCC-1, REC-8 or COH-3/4) that bridges the ATPase heads of SMC-1 and SMC-3, completing the cohesin ring. The SCC-3 subunit associates with the kleisin and is essential for cohesin function. Mitotic and meiotic cohesin differ in the kleisin subunit, which defines the different roles of the cohesin ring carries. During meiosis, the mitotic kleisin SCC-1 is substituted by the meiosis-specific kleisins REC-8 or COH-3/4.

Mitotic Cohesin

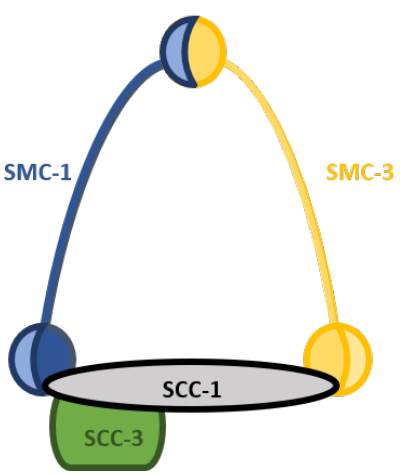

Meiotic Cohesin

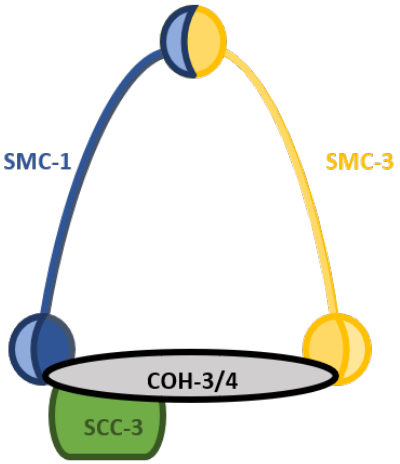

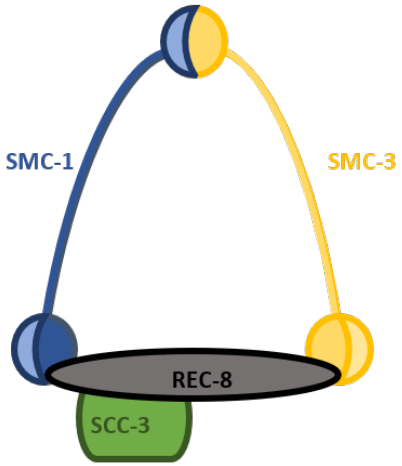

Figure 5. Condensin complexes in *C. elegans*

Condensin complexes consist of two SMC proteins, linked by a hinge domain, and three non-SMC proteins. Condensin I and the dosage-compensation condensin complex (condensin I^{DC}) share the same non-SMC proteins (DPY-28, DPY26 and CAPG-1) and one SMC protein (MIX-1), whereas they differ in one SMC subunit (SMC-4 in condensin I and DYP-27 in condensin I^{DC}). Condensin II shares the SMC proteins with condensin I (SMC-4 and MIX-1), while differing in the three non-SMC proteins (CAPG-2, HCP-6 and KLE-2).

Condensin I

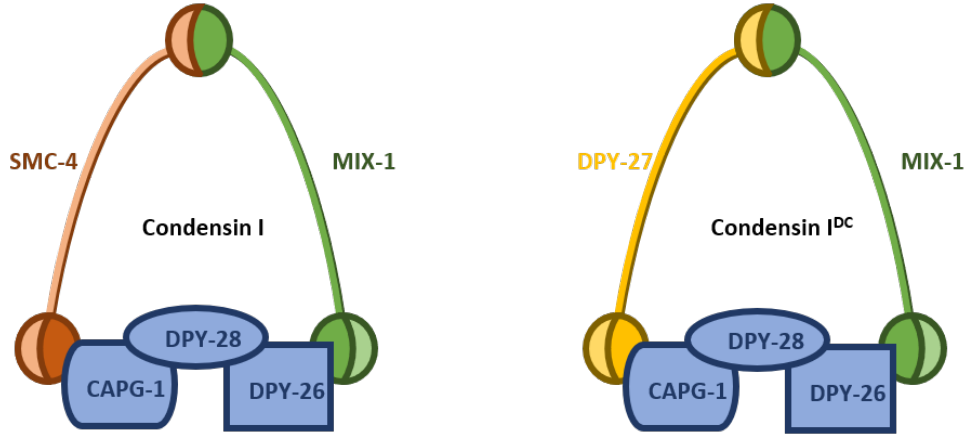

Condensin II

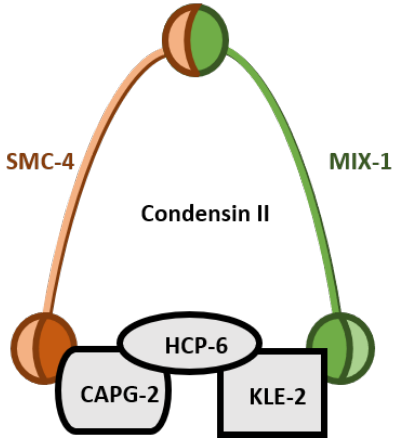

Figure 6. Chromosome movement is generated by cytoskeletal forces generated outside the nucleus

A - Microtubule structure. α-β-tubulin dimers are assembled into protofilaments. A microtubule is composed of 13 of these protofilaments, forming a 25-nm-wide cylinder. Each microtubule contains a stable and slow-growing minus end, and an unstable and fast-growing plus end.

B - Diagram of SUN-1/KASH-12 machinery transferring cytoskeletal forces into meiotic chromosomes. At the onset of meiosis, chromosomes are connected to the nuclear membrane through the chromosomal end containing the PC, which is bound by PC-binding proteins that are phosphorylated by CHK-2 to induce PLK-2 recruitment. Then, PLK-2 promotes the formation of SUN-1/ZYG-12 aggregates. ZYG-12 is a transmembrane KASH protein that interacts with cytoplasmic dynein, which associates with the microtubule network. This molecular machinery promotes the generation of chromosomes movement by cytoskeletal forces located outside the nucleus.

C – Schematic representation of chromosome movement at leptotene-zygotene stages. The model shows two pairs of homologous chromosomes (the first pair in black and second pair in pink) connected to the nuclear membrane through the SUN-1/ZYG-12 machinery. Chromosome movement is generated outside the nucleus and transmitted by SUN/KASH complexes.

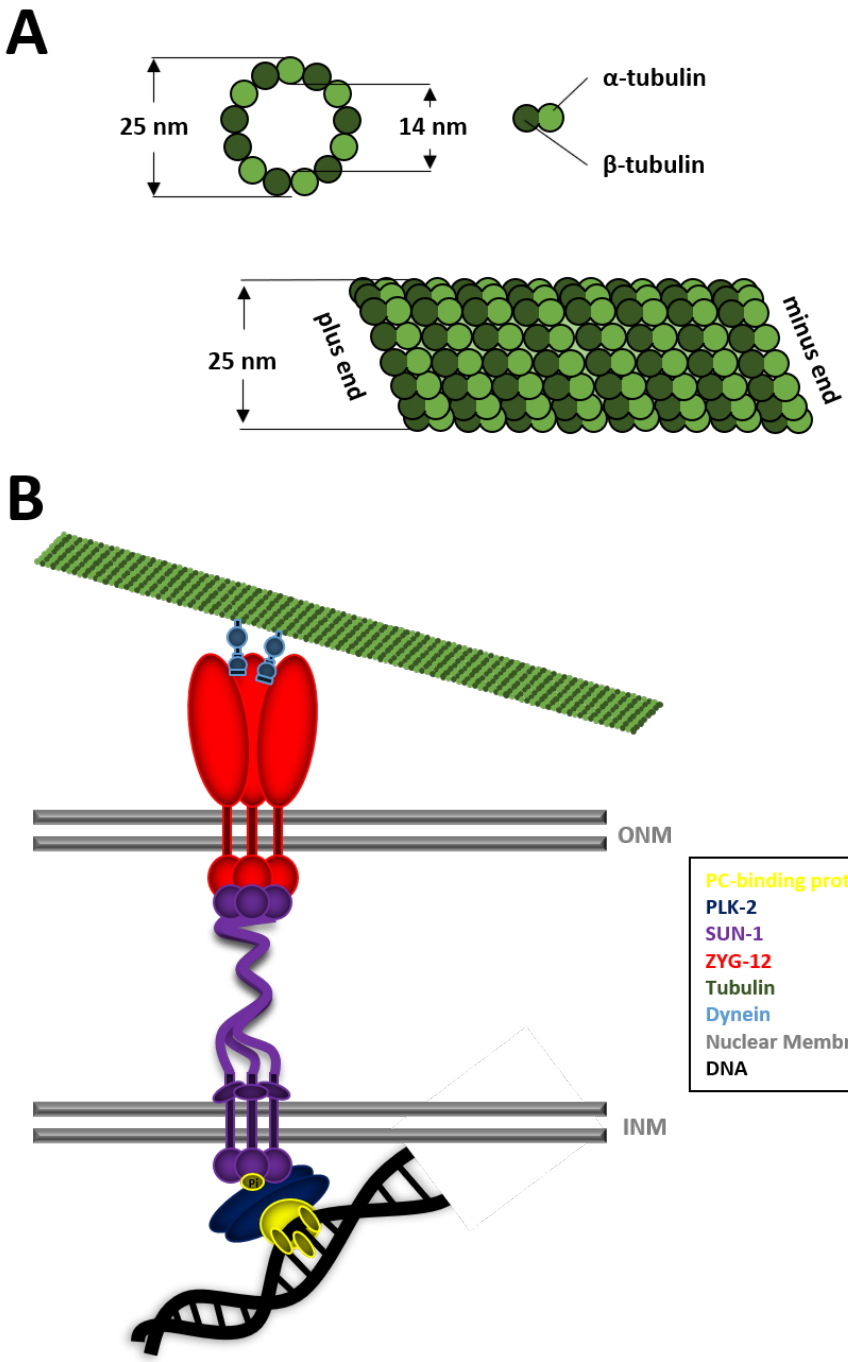
A
25 nm
14 nm
α-tubulin
β-tubulin
25 nm
plus end
minus end
B
ONM
INM
PC-binding proteins
PLK-2
SUN-1
ZYG-12
Tubulin
Dynein
Nuclear Membranes
DNA
C
PC-binding proteins
PLK-2
SUN-1
ZYG-12
Tubulin
Dynein
Nuclear Membranes
Homologues 1
Homologues 2

Figure 7. **Diagram of chromosome remodelling triggered by crossovers during meiotic prophase**

Top - Simplified diagram of chromosomal structural changes during crossover formation, homologous chromosomes are represented in blue and light brown. The red arrow marks the separation of sister chromatids around crossover sites.

Bottom - Images of a single pair of homologous chromosomes as they undergo reorganisation of HTP-1 to the long arm and SYP-1 to the short arm of the late prophase bivalent.

Adapted from Martinez-Perez *et al*. 2008.

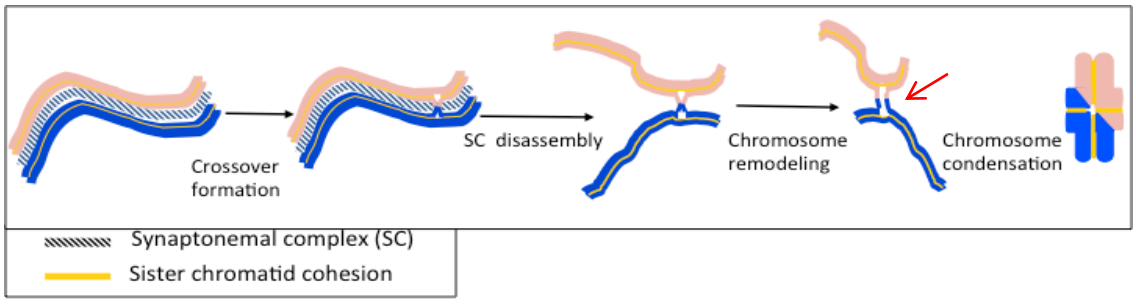

Early prophase I Mid-prophase I Late-prophase I – Metaphase I

Crossover-triggered chromosome remodeling imaged with Delta vision

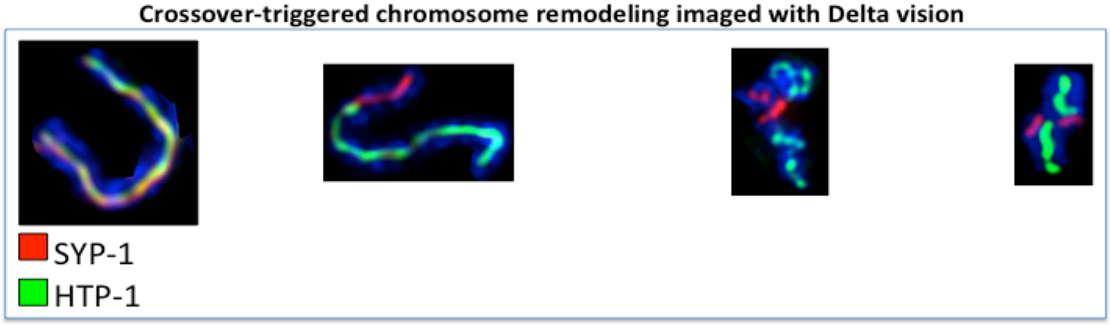

CHAPTER 2:
MATERIALS AND METHODS

2.1 *C. elegans* general methods

2.1.1 *C. elegans* growth conditions

C. elegans strains were maintained on Nematode Growth Media (NGM) plates seeded with OP50 *Escherichia coli* (Brenner, 1974). Solutions and media are described in Table 5. *C. elegans* Bristol strain (N2) was used as wild type control and all strains were maintained at 20 °C, unless otherwise stated. Worms were transferred to new seeded plates every 2-3 days to prevent them from starving and to provide a constant source of animals from all stages of the life cycle. Starved strains were wrapped in parafilm to prevent them from becoming dehydrated. A full list of strains used in this project can be found in Table 3.

2.1.2 Handling and observation of *C. elegans*

Animals were manipulated using a fine-crafted pick made from platinum wire (Sigma-Aldrich platinum wire diameter 0.25 mm, product number: 373265) welded onto the end of a glass Pasteur pipette. Worms were visualised using a Leica MZ75 bench stereoscope or with a Leica MZ16F fluorescence stereoscope for transgenic worms carrying fluorescence markers.

2.1.3 Maintenance of male stocks

C. elegans males were maintained by picking 6 male wild type worms and putting them on NGM plates along with 3 L4 stage hermaphrodites to ensuring that mating occurred while hermaphrodites were young adults, resulting in the production of up to 50% of males in the F1 progeny.

2.1.4 Genetic crosses

Genetic crosses were performed by picking 3-6 males from N2 plates and putting them on NGM plates together with 1 hermaphrodite carrying the desired CRISPR allele,

transgene or mutation. Then, the F1 male progeny was used for subsequent crosses until the final strain containing all the required alleles was generated. Because of the random assortment and heterozygosity of alleles, excess crosses and progeny were picked at all steps to ensure that the desired combination of alleles was achieved (Brenner, 1974). Worms were screened by PCR, making sure they had the desired genotype.

2.1.5 Maintenance of meiotic mutants

Maintenance of *C. elegans* homozygous meiotic mutants is problematic because of the high levels of embryonic lethality observed among their progeny. Moreover, meiotic mutants have frequently compromised genomic integrity which allows the generation of novel mutations into the genome when strains are preserved as homozygous stocks. Given this, meiotic strains must be maintained in heterozygosity by using genetic balancers, which are reciprocal translocations that carry visible markers, such as GFP or *unc* mutations, to balance meiotic mutations. Homozygous worms of the desired mutation can be easily obtained from these balanced strains as they can be easily identified on the plates by the absence of GFP or/and *unc* phenotype.

2.1.6 Cleaning of *C. elegans* strains

C. elegans strains can be contaminated by moulds or bacteria, which could affect the usual growth of the animals. Contaminated strains were restored by washing the plates with Bleach Solution (Table 5). Contaminated worms and eggs were washed using 2 ml of Bleaching Solution per plate and then pipetted in a Falcon tube, using a final volume of 10 ml of Bleaching Solution for each wash. Falcon tubes were left on a nutator for around 10-15 minutes until the worms had dissolved, leaving no carcasses visible. The worm eggs were pelleted by centrifuging for 1 min at 900 x g in a bench top centrifuge at room-temperature (RT) and washed 3 times with 10 ml of dH_2O. Finally, the egg pellet was resuspended in 500 µl of M9 and transferred onto fresh OP50 seeded NGM plates. After 12-18 hours the eggs hatched to produce a clean culture of worms.

2.1.7 Freezing of *C. elegans* strains

C. elegans can be frozen and stored in -80°C freezers or liquid nitrogen for many years, this is one of the most practical properties of this animal model (Brenner, 1974). L1 and

L2 early larval stages of the life cycle endure the freezing process best, consequently plates containing large amounts of L1 and L2 were used to create strain stocks. Worms from 3 plates were washed off using 1.5 ml of M9 and placed onto a 15 ml falcon tube. Then, this solution was mixed with freezing solution (Table 5) in a 1:1 ratio, pipetting 0.5 ml of this mixture into 2 ml cryotube (Fisher), producing 6 vials in total. After this, they were immediately transferred to a -80°C, one of these vials was thawed the next day to check if the strain had survived the freezing process.

2.2 DNA methods

2.2.1 Single worm lysis for DNA extraction

C. elegans genomic DNA was obtained from a single worm by placing it in a 0.2 ml PCR tube containing 10 µl of 1x Polymerase Chain Reaction (PCR) Lysis Buffer with 1 µg/µl of Proteinase K (Table 5). The tube was frozen in liquid nitrogen and then transferred to a PCR thermocycler, running the following lysis program:

- 70 min at 60°C
- 15 min at 95°C

The resulting DNA was used as a template for PCR reaction or stored at -20 °C until needed. The same protocol could be used to extract DNA from a population of animals by placing multiple animals in the same PCR tube.

2.2.2 Single worm PCR

Using 2-4 µl of extracted DNA as template, a 25 µl PCR reaction was set up as follows:

- 12.5 µl of Taq PCR Master Mix (Qiagen)
- 1 µ of the required primer pair [10µM]
- dH_2O up to 25 µl

The annealing temperature was established based on the melting temperature (T_m) of each primer pair and the duration of the elongation step was chosen depending on the amplicon size, assuming and extension rate of 1 Kbp per minute. 10 µl of the reaction

product was run on agarose gels by standard electrophoresis procedures. The following PCR program was used:

	5 min at 95°C
Denaturalization	30 sec at 95°C
Annealing	30 sec at Tm
Elongation	X sec at 72°C
	10 min at 72°C for 1 cycle

2.2.3 PCR amplicon sequencing

For sequencing, DNA amplicon products were purified using the Qiagen MinElute PCR purification kit. 50 µl of PCR reaction volume was used to obtain sufficient purified DNA for sequencing. 10 µl of sterile H_2O was used for the last step of the kit protocol. DNA was quantified using Qubit Fluorometer from Thermo Fischer Scientific. Sample tubes for sequencing were made with the purified PCR product at approximately 10 ng per 100 bp of sequence and primer tubes were made at 2.5pmole. Both sample tubes and primer tubes were given to GeneWiz, an external sequencing company.

2.2.4 Whole plate DNA extraction

To collect the worms from starved plates from genetic mapping crosses (figure 20A and 32), plates were washed 3 times with M9 + 0.1 % Triton X-100 and placed in 15 ml tube balanced up to 10 ml. Animals were centrifuged at 2000 rpm for 2 min and supernatant was removed, the worm pellet was washed 3 times with dH_2O and stored at -80 °C O/N. The Gentra Puregene Tissue Kit (QIAGEN) was used for the DNA extraction using an adapted protocol for worms. The following protocol relates to an extraction of 75 µl worm pellet:

The worm pellet was placed to a 1.5 ml tube and 600 µl of Cell Lysis Solution + 5 µl of Proteinase K were added, mixing the tube by inverting 25 times. After this, the samples were incubated at 55 °C in a shaking block for 4 h at 500 rpm. Once the sample was clear, 3 µl of RNAse A were added and the sample was mixed by inverting 25 times. The samples were incubated again at 55 °C in a shaking block for 1 h at 500 rpm, then

incubated on ice for 1 min. 200 µl of Protein Precipitation Solution were added and the samples were vortexed for 20 s and incubated on ice for 5 min. The samples were centrifuged at 16,200 x g for 3 min at 4 °C.

600 µl of isopropanol were placed to a clean 1.5 ml Eppendorf tube and the supernatant, from the previous centrifugation was carefully added. The tubes were mixed by inverting 50 times and centrifuged at 16,200 x g for 15 min at 4° C. The supernatant was removed by pouring carefully and the pellet was left to dry on a clean piece of filter paper. Then, the pellet was washed 3 times with 70% ethanol and centrifuged at 16,200 x g for 15 min at 4 °C. In the last wash, the supernatant was discarded by pouring and left to dry on a clean piece of filter paper. Finally, the DNA was resuspended in 100 µl of dH_2O. The DNA concentration was measured using both Qubit Fluorometer (Thermo Fisher Scientific) and NanoDrop (Thermo Fisher Scientific).

2.2.5 Whole genome sequencing

DNA libraries for WGS were prepared by the LMS Genomics Facility and analysis of the dataset was carried out by the LMS Computing and Bioinformatics Facility.

2.2.6 Pyrosequencer

To check the status of each SNP, PyroMark Q96 ID instrument was used (Biotage) (Luis Royo et al., 2007). 30 ng of genomic DNA was added to 50 µl of PCR mix composed of 25 µl of Taq PCR Master Mix (Qiagen), 0.8 µl of the universal biotinylated forward primer (biotin-cgccagggttttcccagtcacgac) at 10 mM, 0.2 µl of the specific forward primer at 10 mM and 1 µl of specific reverse primer at 10 mM. PCR product was purified and pyrosequenced by following the manufacturer's instructions and using the proper sequencing primer for each SNP.

2.3 Transgenic methods

To generate transgenic worms, Mos1-mediated single-copy insertion (MosSCI) technique was used in this study (Frøkjær-Jensen et al., 2008). To use this method, the chosen gene needs to be cloned into a vector which contains a wild type copy of *unc-*

119 gene. These two genes are flanked by two homologous sequences which are identical to the chromosomal locus with the Mos1 site. The Mos1 transposon is excised by the Mos1 transposase, generating a DSB, and the chosen gene is inserted by homologous recombination using the homologous sequences within the vector. Depending on which chromosome we want to insert our gene of interest, we need to choose the appropriate strain and vector combination. I generated two alleles using this method, *fqSi1* (*mei-2*^{WT}) and *fqSi2 (mei-2*^{E131K}*)*, inserting the transgenes of interest in a Chromosome II locus (ttTi5605, EG4322 strain) using the pCFJ151 plasmid. The rest of the transgenes used in this study had been generated by members of our lab or had been ordered from the *Caenorhabditis* genetics center (CGC).

2.3.1 Preparation of worms for injection

EG4322 strain was microinjected to generate the transgenic strain. These worms carried an *unc-119* mutation that made them "uncoordinated", affecting the movement of the worms and acting as a visible marker. Because the transgene carried a wild type copy of *unc-119* gene, after insertion, positive worms recovered wild type movement, making it easy to identify. These strains were kept in an incubator at 15 °C on NGM plates seeded with HB101, because this strain of *E. coli* improves viability of microinjected worms. To microinject young adult worms, L4 worms were picked to new NGM plates seeded with bacteria 24 hours before microinjection.

2.3.2 Generation of plasmids for injection

The plasmids used for injection were generated by gene synthesis and cloned into the MosSCI vector by GeneScript, an external cloning company.

2.3.3 Generation of transgenic strains by microinjection

Worms were microinjected with the transgene construct into their germline. To differentiate worms that had been properly microinjected from those that had not, and those which had the insert integrated and those in which it was expressed from an extra-chromosomal array, several positive and negative markers were used. Positive injected worms were identified by the presence of *non-unc* progeny, as the *unc-119* phenotype was only rescued by the insertion of the wild type copy carried in the transgene vector.

Furthermore, three other markers were co-injected with the transgene vectors. These have mCherry expression driven by pharyngeal, neural and muscle promoters and as a consequence, the progeny which has been correctly microinjected will exhibit mCherry expression. To eliminate worms which had extrachromosomal arrays, a plasmid containing the *peel-1* negative selection marker was also co-injected. After a heat-shock at 34 °C for 2 hrs, *peel-1* expression causes the presence of extra chromosomal arrays to become toxic for worms, therefore surviving *non-unc* worms must have an insertion event and no extra chromosomal array. To check for occasional survivors from heat-shock that were array positive, worms were checked for the absence of mCherry makers. Afterwards, worms were checked by PCR (see below).

2.3.4 Preparation of the injection mix

Plasmid constructs from GeneScript were suspended in 20 µl of water, using 1 µl of this to transform chemically competent DH115a *E. coli* cells, following the manufacturer's instructions. After the transformation, 100 µl of bacteria were spread on LB plates with ampicillin (50mg/ml). Then, a liquid culture using a single colony was performed to isolate enough plasmid DNA by using the Invitrogen Miniprep Kit. Afterwards, Qubit Fluorometer was used to quantify the amount of DNA.

Table 1: 10X Injection mix

Plasmid	Description	Final concentration
pCFJ601	Peft-3::transposase	500ng/µl
pGH8	Prab-3::mCherry (panneuronal)	100ng/µl
pCFJ90	Pmyo-2::mCherry (pharynx muscle)	25ng/µl
pCFJ104	Pmyo-3::mCherry (body muscle)	50ng/µl
pMA122 1	Phsp::peel-	100ng/µl

2.3.5 Worm handling

Worms are immobilised by putting them onto 2% agarose pads, which had been pre-warned at 37° C. Halocarbon oil 700 (Sigma-Aldrich) was used to immerse to avoid worms dehydration. Borosilicate glass (OD 1.9 mm, ID 0.78 mm from Stutter Instrument) was used to make needles by pulling them with the Flaming/brown Micropipette Puller (model P97, Sutter Instrument). These needles were used to microinject worms in the gonad. Microinjected animals were recovered from the pads by washing them with a drop of M9 to transfer them onto individual NGM plates seeded with bacteria for recovery. Worms were left to recover at 20 °C for a few hours and then were transferred to 25 °C until they were starved.

2.3.6 Screening for full insertion events

Starved plates were left in an incubator at 34 °C for 3 hours for heat-shock and then transferred to an incubator at 20 °C to recover until the next day. This gave time to peel-1 toxin to act before screening for MosSCI insertion. Animals with the inserted transgene were found at the L1 stage with a wild type phenotype, not expressing any of the mCherry markers that were co-injected with the transgene. Several of these worms were transferred to individual plates and let them to lay progeny. The mother was lysed and checked for the insertion by PCR using "Chromosome II insert positive" primers (see below). After confirming that the gene had been inserted, homozygous worms were isolated by picking 16 worms into separate plates and then checked that their progeny was not *unc.* Moreover, "Chromosome II insert homozygous" primers (see below), in which one primer is over the Mos excision, were also used to ensure that gave a blank result. Then, the strain carrying the transgene was crossed in the desired mutant background.

Chromosome II insert positive	F: TCTGGCTCTGCTTCTTCGTT
	R: CAATTCATCCCGGTTTCTGT
Chromosome II insert homozygous	F: CGCTACTTACCGGAAACCAA
	R: CCCGGGTTTGTCTAGATATGA

Table 2: Transgenic plasmids used

Vector	Transgene	Regulatory sequence	Description
pCFJ151	*mei-2*^{WT}	*mei-2* 5' and 3' UTR	Wild type *mei-2* sequence
pCFJ151	*mei-2*^{E131K}	*mei-2* 5' and 3' UTR	mei-2 with *him-13* mutation (amino acid change from glutamic acid to lysine at position 131)

2.4 Co-CRISPR method

Wild type young adult worms (N2) were microinjected to create CRISPR alleles. Cas9 nuclease needs two small RNAs to function. The first RNA, CRISPR RNA (crRNA), guides the nuclease to the target sequence, whereas the second one, trans-activating crRNA (tracrRNA), associates with Cas9 and crRNA, forming the ribonucleoprotein complex that can cut the DNA at the targeted location (Paix et al., 2015). A *dpy-10* co-CRISPR strategy (Arribere et al., 2014) was used for all CRISPR-generated strains.

First, tracrRNA and specific crRNAs (Integrated DNA Technologies (IDT)) were incubated at 95˚C for 5 minutes, and then they were left to cool at RT. Ultramer oligonucleotides (IDT) were used as ssDNA repair templates. The initial mix contained: 2 µl of specific crRNA:trDNA duplex [100 µM], 0.2 µl of *dpy-10* crRNA:trRNA duplex [100 µM], 2.95 µl of Alt-R™ S.p. Cas9 Nuclease 3NLS [61 µM] (IDT) and 0.21 µl of H_2O. This mixture was incubated for 5 minutes at RT. After the incubation, 2.85 µl of H_2O, 1.6 µl of specific ssDNA repair template and 0.5 µl of *dpy-10* ssDNA were added to the initial mix, being this final injection mix used to microinject the germ line of young adult worms. Injected worms were picked to individual plates and left at 25˚C. After 4 days, F_1 rollers and dumpy worms were transferred to individual plates and left to lay eggs. Then, F_1 hermaphrodites were screened by PCR using specific primers.

2.5 *C. elegans* strains used

Table 3: List of strains used in this study

	Strain	Genotype
Wild type	**N2**	**Wild type (Bristol).**
	CB4856	**Wild type (Hawaiian).**
CGC strains	**BW1102**	***dpy-6(e61), mei-2(ct102), unc-29(e1072) I; sDp2 (I;f).***
	CB3234	***him-13(e1742).***
	JK1743	***gld-2(q497)/dpy-5(e61) unc-13(e51) I***
	SP646	***mnT12 (IV;X).***
	EG7522	**syIs46 II; *unc-119(ed3) oxTi467 III***
	EG7529	**syIs46 II; *unc-119(ed3) III; oxTi474 V***
	EG7530	**syIs46 II; *unc-119(ed3) III; oxTi475 V***
	EG7531	**syIs46 II; *unc-119(ed3) III; oxTi476 V***
	EG7539	**syIs46 II*; unc-119(ed3) III; oxTi486 V***
Lab generated	**ATG56**	***him-13(e1742) I*. Outcrossed 3 times with Hawaiian strain**
	ATG228	***smc-1 (fq20 [smc-1::gfp])***
	ATG398	***dpy-26 (fq62 [dpy-26::degron::MYC]), eSi38 [sun-1p::TIR1::mRuby::sun-1 3'UTR + Cbr-unc-119(+)] IV.***
Generated for this project	**ATGSi484**	***[Pmei-2 mei-2 3' UTRmei-2] II; unc-119(ed3) III***
	ATGSi509	***[Pmei-2 mei-2 3' UTRmei-2] II; dpy-5(e61), mei-2(ct102), unc-29(e1072) I.***
	ATGSi510	***[Pmei-2 mei-2 E131K 3' UTRmei-2] II; dpy-5(e61), mei-2(ct102), unc-29(e1072) I.***
	ATGSi540	***[Pmei-2 mei-2 3' UTRmei-2] II, him-13(e1742) I.***
	ATG332	***cosa-1(fq42 [cosa-1::HA]) III.***

	ATG335	***mei-2 (fq37 [mei-2^{E131K}]) I; cosa-1 (fq42 [cosa-1::HA]) III.***
	ATG337	***mei-2(fq37 [E131K]) I.***
	ATG344	***mei-2 (fq45[mei-2::degron]) I; ieSi38 [sun-1p::TIR1::mRuby::sun-1 3'UTR + Cbr-unc-119(+)] IV.***
	ATG350	***mei-2 (fq45[mei-2::degron]) I; cosa-1 (fq42 [cosa-1::HA]), oxTi467 III; ieSi38 [sun-1p::TIR1::mRuby::sun-1 3'UTR + Cbr-unc-119(+)] IV.***
	ATG380	***him-13(e1742) I; cosa-1 (fq42 [cosa-1::HA]) III.***
	ATG395	***mei-2 (fq45[mei-2::degron]) I; cosa-1 (fq42 [cosa-1::HA]) III; ieSi38 [sun-1p::TIR1::mRuby::sun-1 3'UTR + Cbr-unc-119(+)] IV; mnT12(IV;X).***
	ATG401	***cosa-1 (fq42 [cosa-1::HA]), oxTi467 III; oxTi475, oxTi486, oxTi476, oxTi474 V.***
	ATG442	***cosa-1 (fq42 [cosa-1::HA]), oxTi467 III; dpy-26 (fq62 [dpy-26::degrin::MYC]), eSi38 [sun-1p::TIR1::mRuby::sun-1 3'UTR + Cbr-unc-119(+)] IV; oxTi475, oxTi486, oxTi476, oxTi474 V.***
	ATG455	***mei-2 (fq45[mei-2::degron]) I; cosa-1 (fq42 [cosa-1::HA]), oxTi467 III; ieSi38 [sun-1p::TIR1::mRuby::sun-1 3'UTR + Cbr-unc-119(+)] IV; oxTi475, oxTi486, oxTi476, oxTi474 V.***
	ATG442	***cosa-1 (fq42 [cosa-1::HA]), oxTi467 III; dpy-26 (fq62 [dpy-26::degron::MYC]), eSi38 [sun-1p::TIR1::mRuby::sun-1***

[redacted]		***3'UTR + Cbr-unc-119(+)] IV; oxTi475, oxTi486, oxTi476, oxTi474 V.***

2.6 Cytological methods

2.6.1 Ethanol Fixation

Ethanol fixation followed by DAPI staining is a quick and simple method to visualise *C. elegans* chromosomes cytologically. 20-25 worms were picked to a 8 µl drop of M9 buffer on a superfrost charged slide (VWR scientific). As much liquid as possible was removed from the slide using a filter paper until the worms were left in a small volume of M9. 10 µl of 95 % ethanol was added to the slide and air-dried. This was repeated up to 3 times to ensure that the worms were fully dehydrated. Then, 10 µl of 2 µg/ml DAPI was added to the slide and a 22 x 22 glass cover slip was placed on top of the worms. Worms were observed on a Leica DMRB microscope using 20X, 40X, or 63X lenses and imaged with a Leica DFC300 FX camera.

2.6.2 Immunostaining of *C. elegans* germ lines

A slightly modified protocol for immunostaining was carried out as described in Martinez Perez & Villeneuve (Martinez-Perez and Villeneuve, 2005). Worms were synchronised by picking L4s to a fresh NGM plate and allowing them to mature for 20 h until they reach the young adult stage.

Between 20-25 young adults from synchronised plates were picked in 15 µl EGG buffer (see Table 5) with 0.1 Tween on a 22 x 22 cover slip. Worms were dissected behind the pharynx using a fine needle in order to achieve optimum gonad extraction. Germ lines were fixed by adding 15 µl of 2 % paraformaldehyde (PFA) in EGG buffer and 0.1 % Tween. Pipetting gently ensured that PFA was equally distributed and aided in extruding the gonads. 15 µl of the solution was removed using the pipette and the remaining solution was covered with a superfrost charged slide (VWR scientific). The slides were then fixed for 5 minutes from the addition of the PFA and then were immersed in liquid nitrogen. After this, the coverslip was removed and the slide placed in a Coplin jar containing methanol at -20 °C. Although slides could be kept in -20 °C in methanol up to

24 hours, 5 minutes was sufficient for fixing the germ lines. The slides were washed 3 x 5 min in PBST (see Table 5) in Coplin jars before being blocked for 1 hour in 0.7 % BSA in PSBT. 50 µl of primary antibody diluted in PBST was added to each slide and covered with a parafilm cover slip. Slides were incubated in a dark humid chamber at room temperature (RT) O/N. The next day, the primary antibody was washed 3 x 10 mins in PBST in Coplin jars. 50 µl of the proper secondary antibody (Invitrogen) diluted in PBST was added at a concentration of 1:500, placing another parafilm cover slip over the slides. The slides were again incubated for 2-3 hr RT in the dark in a humid chamber. After this, the secondary antibody was also washed for 3 x 10 mins in PBST in Coplin jars. 80 µl of 2 mg/ml DAPI was added to the slides and incubated for 5 min. This was washed for 30 min in PBST and the slides mounted by the addition of 15 µl of Vectashield (Vector labs). A 22 x 22 cover-slip was used to seal the immunostaining. SRM slides were mounted by the addition of 10 µl of SlowFade (Vector labs).

2.6.3 LacO staining

LacO arrays were labelled using LacI::6His::GFP protein (Checchi et al., 2014). First, between 20-25 young adults from synchronised plates were picked to 15 µl of Sperm salts buffer (see Table 5) on a 22 x 22 cover slip. Worms were dissected behind the pharynx using a fine needle in order to achieve optimum gonad extraction. Germ lines were fixed by adding 15 µl of 5 % PFA in Sperm salts buffer. Pipetting gently ensured that PFA was equally distributed and aided in extruding the gonads. 15 µl of the solution was removed using the pipette and the remaining solution was covered with a superfrost charged slide (VWR scientific). The slides were then fixed for 5 minutes from the addition of the PFA and then were immersed in liquid nitrogen and then left in dry ice for at least 10 minutes. After this, the coverslip was removed and the slide placed in a Coplin jar containing methanol at -20 °C for a minute.

The slides were washed 3 x 5 min in PBSTR (see Table 5) in Coplin jars before being blocked for 1 hour in 0.7% BSA in PSBTR. LacI::6his::GFP at a concentration of 1:200 and 100 µl of primary antibodies diluted in PBSTR were added to each slide and covered with a parafilm cover slip. Slides were incubated in a dark humid chamber at 4 °C O/N. The next day, slides were washed 3 x 10 mins in PBSTR in Coplin jars. 100 µl of the proper

secondary antibodies (Invitrogen) diluted in PBSTR were added at a concentration of 1:500, placing another parafilm cover slip over the slides. The slides were again incubated for 2-3 hr RT in the dark in a humid chamber. After this, the secondary antibody was also washed for 3 x 10 mins in PBSTR in Coplin jars. 80 µl of 2 mg/ml DAPI was added to the slides and incubated for 5 min. This was washed for 30 min in PBSTR and the slides mounted by the addition of 10 µl of SlowFade (Vector labs). A 18 x 18 high performance cover-slip (Zeiss) was used to seal the immunostaining.

Table 4: List of antibodies used in this thesis

Antibody	Host	Dilution	Source
HTP-1 (Q4421)	Rabbit	1:400	Lab generated.
SYP-1	Guinea pig	1:200	(MacQueen et al., 2002).
SYP-1	Chicken	1:400	Lab generated (Crawley et al., 2016).
RAD-51	Rabbit	1:200	Novus Biologicals (discontinued).
HIM-8	Rabbit	1:1000	Novus Biologicals.
DSB-2	Rabbit	1:3000	(Rosu et al., 2013).
GFP-488	Rabbit	1:200	InvitroGen.
GFP-FITC	Goat	1:250	Abcam.
HA	Mouse	1:250	Cell Signaling
HTP-3	Guinea pig	1:500	(Goodyer et al., 2008)
HIM-3^{S13P}	Rabbit	1:500	Lab generated.
HIM-8^{T64P}	Rabbit	1:500	Lab generated (Kim et al., 2015).
PLK-2	Rabbit	1:500	(Labella et al., 2011).

2.6.4 Widefield Microscopy

Immunostained germ lines were acquired using a Deltavision Deconvolution microscope developed by Applied Precision (DeltaVision system core, Olympus 1X70 microscope, CoolSNAP$_{HQ}^2$ Monochrome camera). Germ lines were imaged in a series of Z-stacks that required to be deconvoluted to reverse the optical distortion. Z-stacks were processed

and analysed using the Softworks software and were subsequently flattened into a 2D projection (maximum intensity projection). A whole *C. elegans* germ line cannot be imaged in a single field because of its large size, requiring several fields to image the whole structure. Reconstruction of the whole image germ line was done using Photoshop (Adobe).

2.6.5 Structure illumination microscopy (SIM)

Slides were prepared as described above (2.6.2) but using SlowFade Diamond Antifade Mountant (ThermoFisher) and high-performance coverslips (D = 0.170±0.005 mm) (Zeiss). SR stacks were acquired by using Zeiss Elyra S1 (SR-SIM) microscope. Channel alignment, deconvolution and SIM processing of 3D stacks were performed by using ZEN software (Zeiss). 3D stacks were projected using maximum intensity projection in ImageJ and Images were edited in Photoshop (Adobe). IMARIS (Bitplane) was used to analyse SIM stacks in a three-dimensional fashion.

2.6.6 Stimulation Depletion Microscopy (STED)

Slides were prepared as described above (2.6.2) but using SlowFade Diamond Antifade Mountant (ThermoFisher) and high-performance coverslips (D = 0.170±0.005 mm) (Zeiss). DAPI was not used to label DNA because STED lasers excite it generating background. SR stacks were acquired by using Leica TCS SP8 STED 3X microscope. 3D stacks were projected using maximum intensity projection in ImageJ and Images were edited in Photoshop (Adobe).

2.6.7 Auxin-degron system

Worms were treated with auxin to deplete degron-tagged proteins in a strain expressing $P_{sun\text{-}1}$*::TIR1::mcherry* (Zhang et al., 2015). Worms were put on NGM plates seeded with concentrated OP50 *E. coli* containing 1-4 mM auxin. Depending on the tagged-protein, the duration of the treatment was different, and worms were left on auxin plates accordingly. Control experiments were performed by using the same strain without auxin treatment. Moreover, this approach allows to study situations where degron-tagged proteins are depleted in a temporal and germ line specific fashion.

Table 5. List of buffers and solutions used

Name	Composition	Use
NGM	3 g NaCl 2.5 g Bactopeptone 20 g Agar H2O up to 1 l 1 ml 1M $MgSO_4$ 1 ml 1M $CaCl_2$ 1 ml 1M Cholesterol (5 mg/ml in EtOH) Autoclave and add 25 ml Potassium Phosphate (1M, ph &.0) Dispense into 60 mm petri dishes	Growth media for *C. elegans* strains
B-Broth	10 g Bactotryptone 5 g NaCl dH_2O up to 1 l	Growth media for OP50 bacteria primary inoculum
M9	5.8 g Na_2HPO_4 3.0 KH_2PO_4 0.5 NaCl 1.0 g NH_4Cl dH_2O up to 1 liter Autoclave	Short-term preservation of *C. elegans* in liquid
Bleaching Solution	5.5 ml H_2O 2.5 ml 2M NaOH 2 ml Bleach	Cleaning of contaminated *C. elegans* strains
Freezing Solution	5.85 g NaCl 6.8 g KH_2PO_4 300 g Glycerol 5.6 ml 1M NaOH dH_2O up to 1 l	Cryopreservation of *C. elegans* strains

	Autoclave and add 300 µl of 1 M $MgSO_4$	
LB	1% Tryptone	Growth media for *E. coli*
	0.5% Yeast extract	
	10mM NaCl	
	2.5mM KCl	
	10mM $MgCl_2$	
	10mM $MgSO_4$	
	20mM glucose	
SOC	2% Tryptone	Growth media for *E. coli* indicated for transformations
	0.5% Yeast Extract	
	10mM NaCl	
	2.5mM KCl	
	10mM $MgCl_2$	
	10mM $MgSO_4$	
	20mM glucose	
10X PCR Lysis Buffer	100mM Tris	DNA extraction
	500mM KCl	
	15mM $MgCl_2$	
	pH 8.3	
	Add Proteinase K to 1X PCR lysis buffer before use – final concentration of 1 mg/ml	
10X EGG buffer	118mM NaCl	Immunostaining
	48mM KCl_2	
	2mM $CaCl_2$	
	2mM $MgCl_2$	
	5mM HEPES	
	pH 7.4	
10X PBS	0.2M Na_2HPO_4	Immunostaining

	1.5M NaCl	
	pH 7.4	
1X PBST	1X PBS	Immunostaining washes
	0.1% Tween 20	
1X PBSTR	1X PBS	Immunostaining washes
	0.5% Triton	
1X Sperm Salts	50mM PIPES, pH 7.0	Immunostaining
	25mM KCl	
	1mM $MgSO_4$	
	45mM NaCl	
	2mM $CaCl_2$	
10x TBS	24g Tris-Base	Western Blot
	88g NaCl	
	ddH_2O up 1l	
	pH 8.0	
1X TBST	10X TBS	Western Blot Washes
	0.1% Tween 20	
Transfer Buffer	1X Tris-Glycine	Western Blot
	20% Methanol	
TRIS/AS	50mM TRIS/HCl pH 8.0	Wash Buffer used for Binding Assay
	10mM MgAc	
	50uM ZnAc	
	5% Glycerol	
	0.1% Triton	
	200mM AS	
	5mM DTT	
	3mM ATP	
	2X Protease inhibitor cocktail (PIC) from Sigma	

	ddH2O	
Running Buffer	1X Tris-Glycine 0.10% SDS ddH_2O	Used for running denaturation gels
Blocking Solution	1% BSA PBST	Immunostaining

CHAPTER 3

SETTING UP SRM TECHNIQUES TO INVESTIGATE EARLY MEIOTIC CHROMOSOME STRUCTURE

3.1 Objectives and Background

One of the main objectives of this project was to use super resolution microscopy techniques to investigate meiotic chromosome structure in pachytene, when the axial elements of homologous chromosomes are separated by a distance of about 100 nm. Given that the lateral resolution limit of widefield microscopy is around 200 nm, this type of microscopy does not allow the visualisation of the axial elements of homologous chromosomes as separate structures. For this reason, I decided to start imaging three-dimensionally intact pachytene nuclei using both STED and SIM systems to validate the use of these systems in the *C. elegans* germ line.

3.1.1 Meiotic chromosomes and the SC

As previously described (see section 1.2.6), the SC is an essential proteinaceous complex for homologue pairing and recombination that is established between homologous chromosomes during leptotene-zygotene and pachytene. The SC has a tripartite structure composed of two AEs that are established along each homolog and the CEs, which bridge the AEs (figure 2). As shown by electron microscopy (EM), the width of the SC when it is fully paired is around 90-150 nm (Moses, 1969). In *C. elegans*, a study using immuno-electron microscopy proposed a model of how CE proteins (SYP-1, SYP-2, SYP-3 and SYP-4) are organised among themselves and linked to the AEs in the SC (Schild-Prüfert et al., 2011). Later, another study using PALM and STORM microscopy has proposed another model of how AE proteins (HTP-1/2, HTP-3, HIM-3 and cohesin complexes) are organised among themselves along homologous chromosomes in *C. elegans* (Köhler et al., 2017). More studies to integrate how both AEs and CEs are organised within the SC and how the SC associates with the chromatin will be required

(Carlton, 2013). Moreover, several remaining questions about the SC need to be addressed, including how the progression of recombination changes the properties of the SC.

Nonetheless, there are several limitations to study the SC with conventional wide-field optical microscopy and other non-optical methods such as electron microscopy or X-ray crystallography. Firstly, the major limitation to investigate the SC with widefield microscopy is that the limit of resolution (200 nm) is bigger than the width of the SC (90-150 nm), making it virtually impossible to study the SC ultrastructure by this method. Secondly, both X-ray crystallography and electron microscopy cannot label and image multiple specific molecules within the same sample, and they are extremely difficult to use. For these reasons, super resolution microscopy techniques have started to be successfully applied to study the structure of meiotic chromosomes (Carlton, 2008, 2013).

3.1.2 Super Resolution Microscopy (SRM)

As mentioned above, the resolution limit of widefield and confocal microscopes is around 200 nm of lateral resolution and 700 nm of axial resolution. This limit was calculated by Ernest Abbe by using the formula: $d = \lambda/2NA$ (where λ represents the wavelength of emitted light and NA the numerical aperture of the objective) (Abbe, 1873). Two structures closer than the distance calculated by this formula cannot be visualised as separate structures by a traditional microscope. Nevertheless, in the last decades several optical methods have gone beyond this optical limit. These microscopy methods have achieved this by using different strategies. Stimulation Emission Depletion (STED) microscopy achieves this by exciting fluorophores within a constrained area, whereas in Structure Illumination Microscopy (SIM), this is achieved by using patterns of interference, modulating the excitation of fluorophores. Finally, Single Molecule Localisation Microscopy (SMLM) improves resolution by only activating a small population of fluorophores for each image and then combining these to give greater resolution (Huang et al., 2010).

3.1.3 STED microscopy

STED microscopes increase the resolution by exciting fluorophores in a small region of the sample. This is achieved by taking advantage of the properties of fluorochromes. When a fluorochrome is excited by an excitation laser, an electron goes from the ground state of energy into an excited electronic state. After this, the electron becomes relaxed, coming back to the ground state and emitting fluorescence. In STED microscopy, the depletion laser is able to relax electrons which are on an excited electronic state into a higher vibrational state than the ground state, but without emitting fluorescence (Müller et al., 2012).

The STED microscopy technique consist of using two synchronised lasers. The first laser is a conventional laser used in confocal microscopy which excites the sample. Then, the STED laser depletes the previously excited fluorochromes by projecting a donut-shape pulse of a longer wavelength. The STED laser deactivates the fluorophores by bringing back the fluorophores to the ground state without emitting fluorescence, leaving only a central spot where the excited fluorophores can emit fluorescence. The size of the central spot defines the resolution of the image, which is dependent on the power of the depletion laser (Wegel et al., 2016).

3.1.4 SIM microscopy

In widefield microscopy, the sample is illuminated with a uniform field, whereas in SIM microscopy, the sample is illuminated and imaged with different light patterns by using a grating. This process generates images with moiré patterns between the sample and the patterns that were used. High frequency information is encoded in these moiré pattern images, and it can be transformed into low frequency information, which can be resolved by the microscope. The final super resolution image is computationally reconstructed from multiple snapshots with different rotations and light patterns. SIM microscopes improve lateral resolution from 200 nm to 100 nm, whereas axial resolution is improved from 700 nm to 350 nm (Carlton, 2008; Dan et al., 2014).

3.1.5 SMLM: Photo Activated Localization Microscopy/ Stochastic Optical Reconstruction Microscopy (PALM/STORM)

PALM and STORM microscopy go beyond the diffraction limit by localising the position of individual fluorochromes. In conventional widefield microscopy, most fluorochromes are simultaneously activated within the sample, being impossible to distinguish the fluorescence signal from fluorochromes that are closer than the diffraction limit. In SMLM microscopy, a small number of fluorochromes are stochastically activated in each acquired frame, localising specific fluorochromes each time. Importantly, activated individual fluorochromes emit a characteristic fluorescence signal that is known as the point spread function (PSF). This PSF can be visualised as an intensity distribution with a Gaussian shape. In SMLM, lateral position of each individual fluorochrome is mathematically determined by a Gaussian fit. Single fluorochrome positions of thousands of frames are combined, creating a super resolution image. On the other hand, the main difference between PALM and STORM microscopy is the fluorescent label. In PALM microscopy, fluorescent proteins are used, whereas in STORM microscopy, photoswitchable organic dyes are utilised (Baddeley and Bewersdorf, 2017; Huang et al., 2010; Schermelleh et al., 2010).

3.2 Setting up conditions to use SR microscopes to image *C. elegans* germlines

To use Zeiss Elyra S1 SR-SIM microscope, several aspects of sample preparation needed to be considered. First, this microscope is equipped with 405, 488, 561, and 637 laser lines and conventional fluorochromes can be used (GFP, Alexa488, Alexa555, Alexa647, DAPI, etc). Another important aspect is the use of an antifade mounting media to avoid photobleaching. This is quite important since this technique requires the acquisition of 15 images (5 rotations x 3 grating positions) per focal plane within a stack. Ideally, the refractive index of the sample should be as close as possible to that of the coverslip (1.52). Initially, Prolong Diamond (Thermofisher) was used as mounting media because of its refractive index (1.46) and this requires to be cured for 3 days to achieve the best possible performance in terms of super resolution. However, this mounting media compresses the samples when curing, so I decided to stop using it as this reagent

compromises the three-dimensional structure of chromosomes. Given this, I started using SlowFade Diamond (Thermofisher), which is a non-curing mounting media suitable for SR imaging which also has a good refractive index (1.42). High-performance coverslips were also used for sample preparation. Imaging at depths deeper than 10 microns into the sample can be problematic for SIM microscopes. Due to this reason and given that pachytene nuclei are about 5-6 µm in diameter and are radially organised in a cross section of the germline localising immediately under the thin germ line sheath, only the nuclei that were close to the coverslip were acquired.

To use the Leica TCS SP8 STED 3X system, the same mounting media and coverslips that were chosen for the SIM sample preparation were used for STED microscopy. However, some aspects in terms of sample preparation were changed for STED microscopy. First, DAPI cannot be used in this system since STED depletion lasers excites DAPI and therefore generates background. Since labelling DNA is crucial to study meiotic chromosome structure, other DNA-dyes were tried. First, I tried PicoGreen, a DNA fluorescent marker comparable with DAPI. Unfortunately, this dye did not work in *C. elegans* germ lines. Then, I tried a new dye called SiR–Hoechst (Lukinavičius et al., 2015), which is a far-red DNA dye compatible with STED microscopy, that worked well to label DNA in dissected germ lines.

On the other hand, STED systems require photostable fluorophores that can resist the high intensity of STED lasers and, subsequently, the second conventional laser. Moreover, these fluorophores need to be simultaneously compatible with the depletion and excitation lasers. The antibodies that I tried that worked well were Alexa 488 (ThermoFisher), Alexa 594 (ThermoFisher), Alexa 647 (ThermoFisher), Abberior STAR 580 (Abberior Instruments), and Abberior STAR 635P (Abberior Instruments).

3.3 SR Microscopy allows visualization of homologous axial elements in pachytene

I first started using the Zeiss Elyra SIM system to investigate the structure of meiotic chromosomes. This system provides twice the resolution of widefield or confocal systems, enabling the visualisation of structures that could not be resolved before. I imaged germ lines of *smc-1 (fq20 [smc-1::gfp])* worms (a core component of cohesin

present in mitotic and meiotic nuclei) to visualize the loading of the cohesin complex onto chromosomes at the onset of meiosis (figure 9A). These experiments revealed clear changes in SMC-1::GFP localization as mitotic nuclei differentiated and entered meiotic prophase in the transition zone of the germ line (corresponding to the stages of leptotene and zygotene). SMC-1::GFP has a dispersed pattern in mitotic nuclei, while in transition zone nuclei SMC-1::GFP is found forming linear structures corresponding to axial elements (figure 9B). I also used the SIM microscope to observe these axial elements (labelled by SMC-1::GFP) during the pachytene stage of meiotic prophase, when the SC is fully assembled and the axial elements of homologous chromosomes are thought to be separated by around 120 nm (Smolikov et al., 2008). Crucially, these images demonstrate separate SMC-1::GFP tracks corresponding to paired homologous chromosomes (red arrows in figure 10), suggesting that a resolution of at least 120 nm is achieved with the SIM system. Moreover, the SIM system can also be used to resolve other structures in the germ line. For example, in collaboration with Oliver Crawley and other members of my laboratory, I participated in a project that investigated the roles of the cohesin removal factor WAPL-1 during meiosis (Crawley et al., 2016). I used the SIM microscope to visualise changes in chromosome-associated cohesin in diakinesis oocytes of *wapl-1* mutants and wild-type controls expressing SMC-1::GFP. I found that *wapl-1* mutants showed a reduction in the amount of soluble cohesin at diakinesis, consistent with WAPL-1 restricting cohesin binding at this stage (figure 11). Surprisingly, I also found that both *wapl-1* mutants and wild-type controls displayed a reduction in the amount of chromosome-associated cohesin between the most proximal oocyte, which is about to enter Metaphase I, and the second most proximal oocyte (figure 12). As the most proximal diakinesis oocyte is undergoing maturation due to CDK-1 activation, this data suggests that WAPL-1-independent mechanism promotes cohesin removal at this stage.

Despite the success of the SIM in separating the axial elements of homologous chromosomes, the SIM system is unlikely to give sufficient resolution to observe events such as the predicted separation of sister chromatids around CO sites, which may require resolution beyond 50 nm. Due to this, I started imaging pachytene nuclei of the SMC-1::GFP strain using a Leica TCS SP8 STED 3X system. Using this system, I was also

able to visualize the separation of axial elements from homologous chromosomes in pachytene nuclei (red arrows in figure 13). Although both SIM and STED systems can resolve the separation between the axial elements from homologous chromosomes (figure 10 and 13), the SIM system was more consistent than the STED system, not showing any photobleaching. Moreover, in collaboration with Prof. Paul French laboratory, we published an article describing a method for correcting optical aberrations by using a single spatial modulator, increasing the acquisition speed by using multibeam excitation and depletion (Görlitz et al., 2018)(figure 14). In summary, these results demonstrated that I successfully implemented SIM and STED methods to visualise meiotic chromosomes from three-dimensionally intact nuclei, providing a valuable tool to study changes in the structure of meiotic chromosomes.

3.4 Studying CO distribution by three-dimensional tracking of chromosomes

Genetic CO mapping has always been the classical way of studying CO distribution. Although precise, this method has several problems. Firstly, to perform a regular experiment can take between 2 or 3 months in *C. elegans*, which is time-consuming and expensive. Secondly, these experiments depend on the SNPs that are used to distinguish the parental genotypes, which limits the ability to detect some COs, for example close to the telomeres. Thirdly, genetic CO mapping requires the presence of F1 progeny in which recombination events that occur in the paternal or maternal meiosis can be determined. This can be difficult in many meiotic mutants due to the high levels of embryonic lethality caused by defects in chromosome segregation. For these reasons, I started to look for other alternative ways of investigating CO distribution. In mammals, CO distribution can be investigated by studying the location of MLH1 foci, which labels CO sites (Anderson et al., 1999), on SCs of pachytene nuclei. In plants and mammals, after the appearance of MSH4-MSH5 heterodimer (MutSγ), MLH1-MLH3 heterodimer (MutLγ) associates with pachytene nuclei to form class I COs (Gray and Cohen, 2016). This protocol involves measuring the total length of SC and the position of MLH1 foci along the SC, to calculate the relative distance of MLH1 foci to chromosome ends. However, this protocol requires the spreading of meiotic cells, which could potentially affect chromosome structure and alter SC length. A similar approach has been achieved

in *C. elegans* by labelling the axial elements of pachytene chromosomes from dissected germlines (Mets and Meyer, 2009), and subsequently this was combined with imaging of CO sites at late pachytene using GFP::COSA-1 (Libuda et al., 2013; Yokoo et al., 2012). Although this method did not imply any aggressive treatment of the germ line before the staining and allowed tracking of chromosome in three-dimensionally intact pachytene nuclei, it required to straighten chromosomes computationally, a highly time-consuming process. Because of this, I decided to develop a new method to measure CO distribution combining 3D visualisation of nuclei and Super Resolution Microscopy (SRM).

3.4.1 Three-dimensional tracking of chromosomes

To track chromosomes in a three-dimensional fashion, I used Imaris software (BitPlane AG), which allows the reconstruction of 3D stacks. Although this programme was initially created to study neurons, it had some functions to track dendrites that could potentially be used to trace chromosomes. I attempted to track chromosomes using Deltavision files, however, it was not possible because the axial resolution (~600 nm) obtained by this method was not sufficient to properly reconstruct these nuclei (figure 16A). As a consequence of this, I tried to repeat this process but this time using SIM stacks from Zeiss ELYRA S1, in which the axial resolution is approximately 300 nm instead of the 600 nm obtained in the Deltavision. This increase in axial resolution seemed to be crucial to be able to track chromosomes in intact pachytene nuclei (figure 16B). Then, I established the staining conditions to use this method to measure CO distribution. Firstly, I created a *cosa-1::HA* CRISPR strain so that HA antibodies could be used to visualise COs in pachytene nuclei, as the COSA-1 proteins forms clear foci a CO sites (Yokoo et al., 2012). Secondly, αHTP-3 antibodies were used to mark the axial elements in order to visualise the total length of chromosomes, as this HORMA-domain protein binds to the whole length of axial elements throughout meiotic prophase (Goodyer et al., 2008). Finally, αHIM-8 antibodies were used to visualise the left end of the X chromosomes, which contain the binding sites for this pairing center-binding protein (Phillips et al., 2005). Importantly, visualization of HIM-8 allowed me to determine the orientation of the X chromosome in every imaged nucleus (figure 15 and 17A) (See video figure 17B).

Following image acquisition of pachytene nuclei labelled with the markers mentioned above, I tracked X chromosomes by first identifying the single HIM-8 signal within the nucleus and identifying the HTP-3 track associated with the HIM-8 focus. This provided the orientation of the X paired chromosomes and allowed me to calculate the whole length of the axial elements of the X chromosomes. Then, the CO site was assigned by identifying where the HTP-3 signal overlapped with the COSA-1::HA foci (figure 15). This divided the HTP-3 track associated with the X chromosomes in two parts, and allowed me to calculate the distance between the HIM-8 and the COSA-1::HA focus. Finally, the distance between the COSA-1::HA foci and the pairing center was divided between the total length of the chromosome, obtaining the relative position of the CO within the chromosome.

3.5 Summary of results

In this chapter, I have set up the conditions to use the SIM and the STED systems to visualise different structural features of meiotic chromosomes at all stages of meiotic prophase. To achieve this, I needed to try a range of antibodies, antifade mounting solutions and different acquisition conditions. After setting the conditions for SRM, I demonstrated the separation between axial elements of paired homologous chromosomes in pachytene nuclei, which is around 120 nm in *C. elegans*. Importantly, I was able to observe this separation with both SIM and STED, suggesting that I achieved an axial resolution of at least 120 nm in both cases. The SIM method was used to visualise the pattern of cohesin binding in diakinesis oocytes of *wapl-1* mutants, and these data was used in a publication describing how WAPL-1 regulates cohesin binding during meiosis (Crawley et al, 2016). The STED method was developed in collaboration with the group of Prof. Paul French and described in Görlitz et al. (2018). Finally, I developed a method to map CO distribution using Imaris and the SIM system together, allowing me to track specific chromosomes and to localise CO sites in three-dimensionally intact pachytene nuclei. This method was also used to measure other properties of chromosomes, as it will be explained in the following chapters.

Figure 8. The principles of SIM, STEM and SMLM microscopy

A – SIM microscopy. In SIM microscopy, the sample is illuminated by using different light patterns. This is achieved by passing light through a grating, generating moiré fringes between the structures of the sample and the light patterns. 15 images per slice are acquired (3 rotations x 5 translations) to mathematically reconstruct a super resolution image with twice the resolution compared to widefield microscopy.

B – STED microscopy. In STED microscopy, the sample is excited by using two laser. First, the excitation pulse excites the fluorochromes. Then, the STED laser depletes the previously activated fluorochromes by projecting a donut-shape pulse of a longer wavelength. The lasers scans the sample in a raster pattern This process reduces the size of the effective point spread function (PSF), improving the resolution of the image.

C – Single molecule localization (SMLM) microscopy. In SMLM, the sample is excited by activating only a few fluorophores in each frame. The localisation of the fluorochrome is done by assuming the PSF to be of Gaussian. Then, the position of the fluorochromes of each frame are used to mathematically reconstruct a super resolution image. To achieved this, between hundreds and thousands of frames need to be acquired.

A **Structure Illumination Microscopy (SIM)**

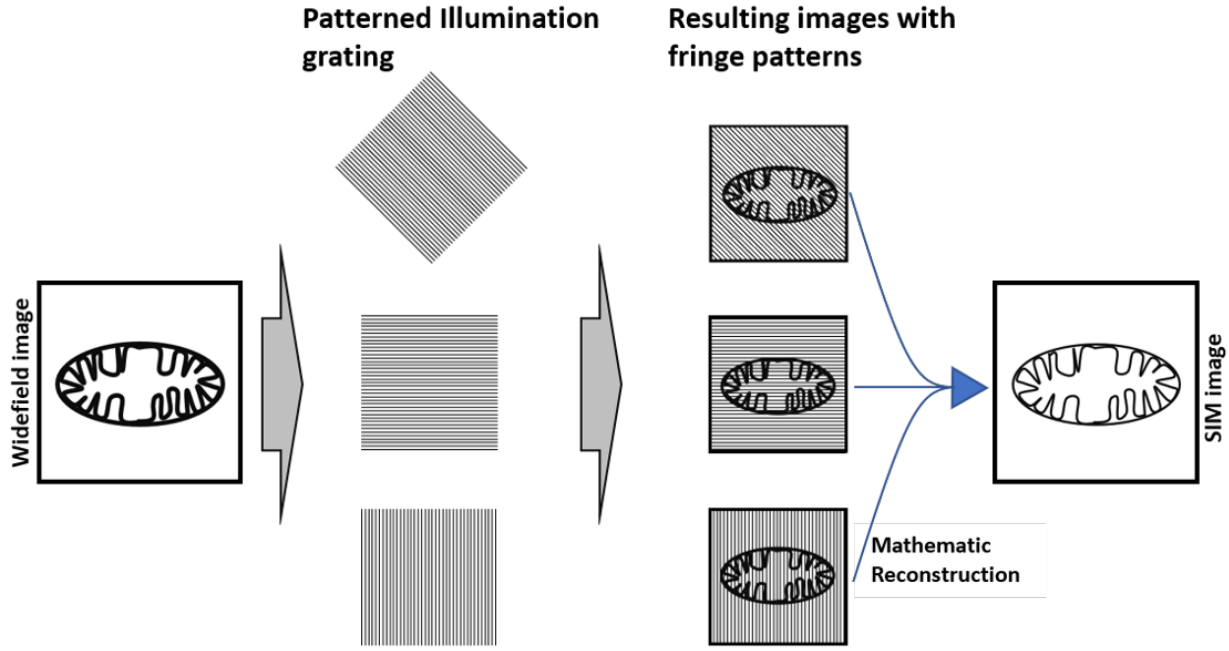

B **Stimulated Emission Depletion (STED) Microscopy**

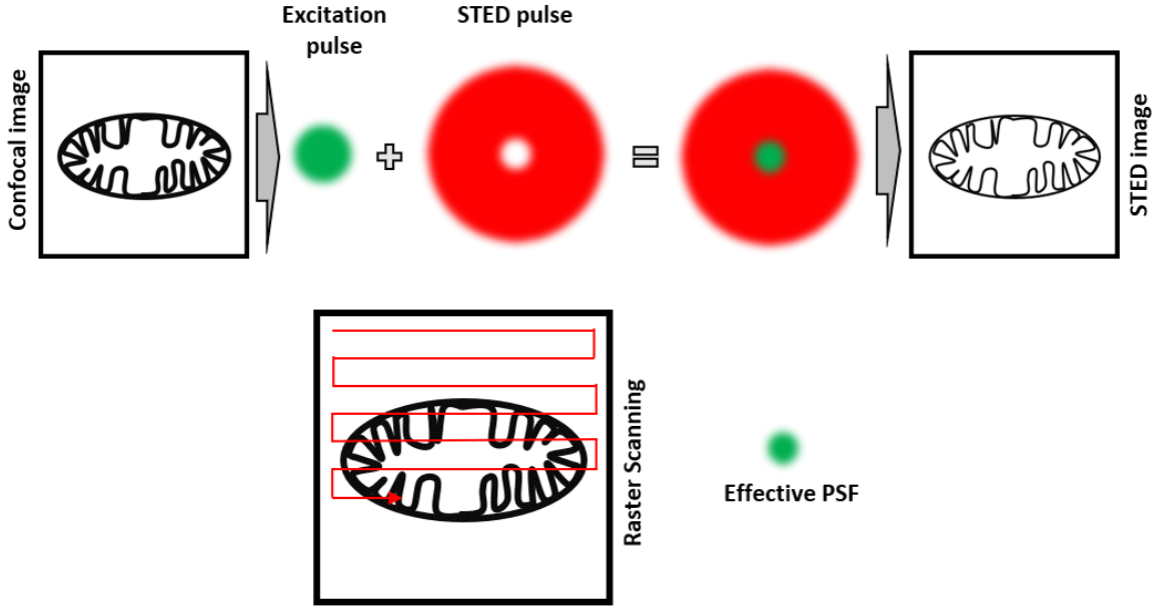

C **Single Molecule Localization Microscopy (PALM/STORM)**

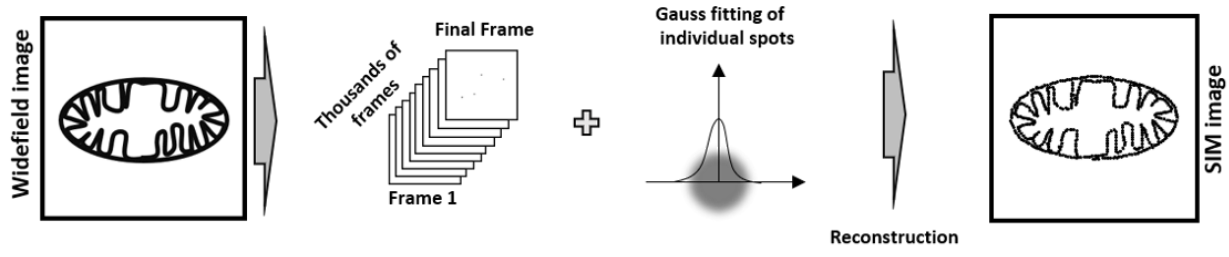

Figure 9. Imaging axial element morphogenesis at the onset of meiosis using SIM

A - Projection of nuclei from mitotic and transition zone of the germ line from worms expressing SMC-1::GFP. DNA was stained by DAPI (blue) and SMC-1::GFP (a protein that is present in all versions of meiotic cohesin complexes) was stained with anti-GFP antibodies conjugated with 488 (green). Images were taken using the Zeiss ELYRA S1 system. Note that as mitotic nuclei enter meiotic prophase SMC-1::GFP changes it distribution from a diffused staining to strong localization on axial elements. Scale bar = 5 µm.

B - Comparison of SMC-1::GFP location between mitotic and early meiosis (leptotene-zygotene) nuclei. DNA was stained by DAPI and SMC-1::GFP was stained by anti-GFP antibodies conjugated with 488. Images were taken using the Zeiss ELYRA S1 system. Scale bar = 5 µm.

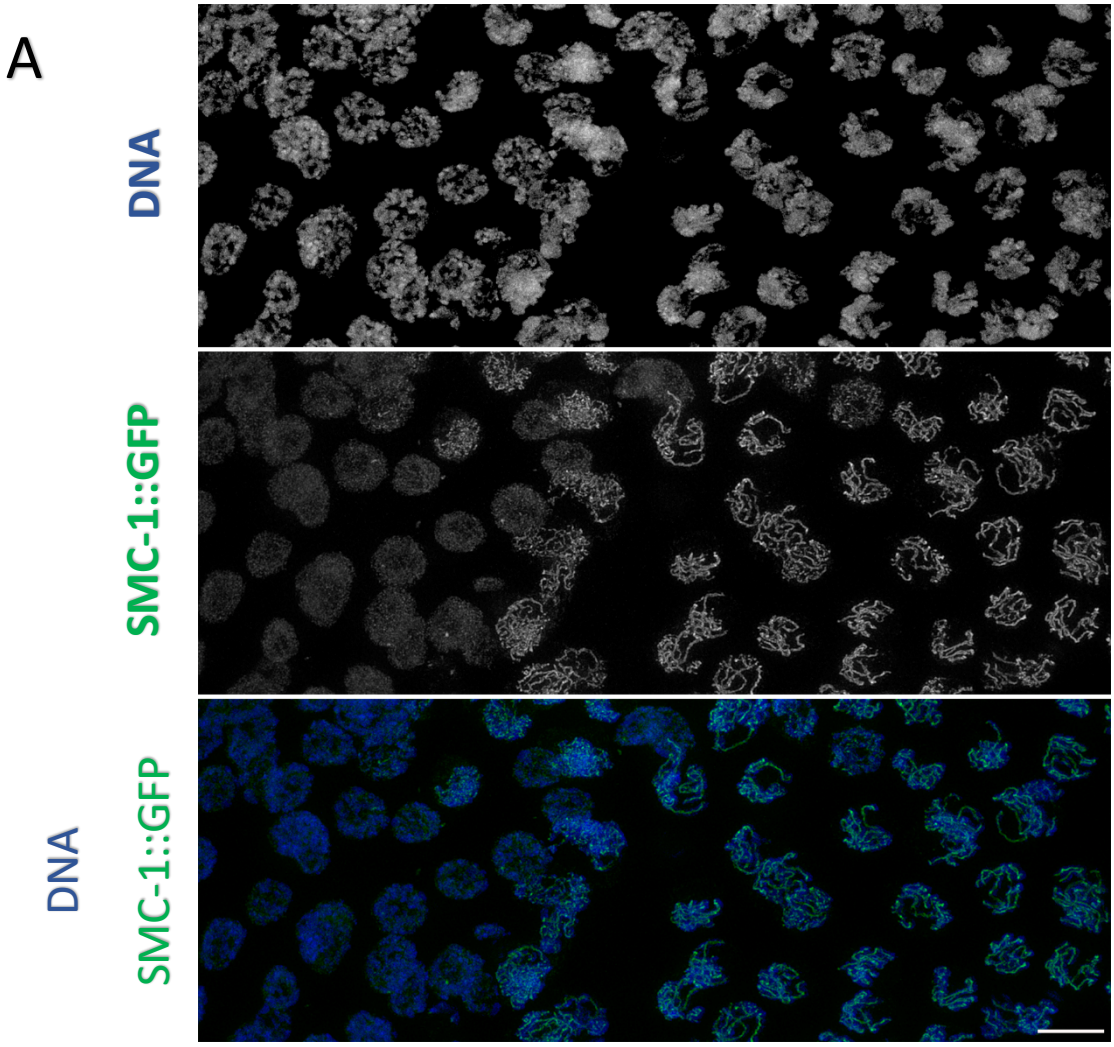
A
DNA
SMC-1::GFP
DNA
SMC-1::GFP

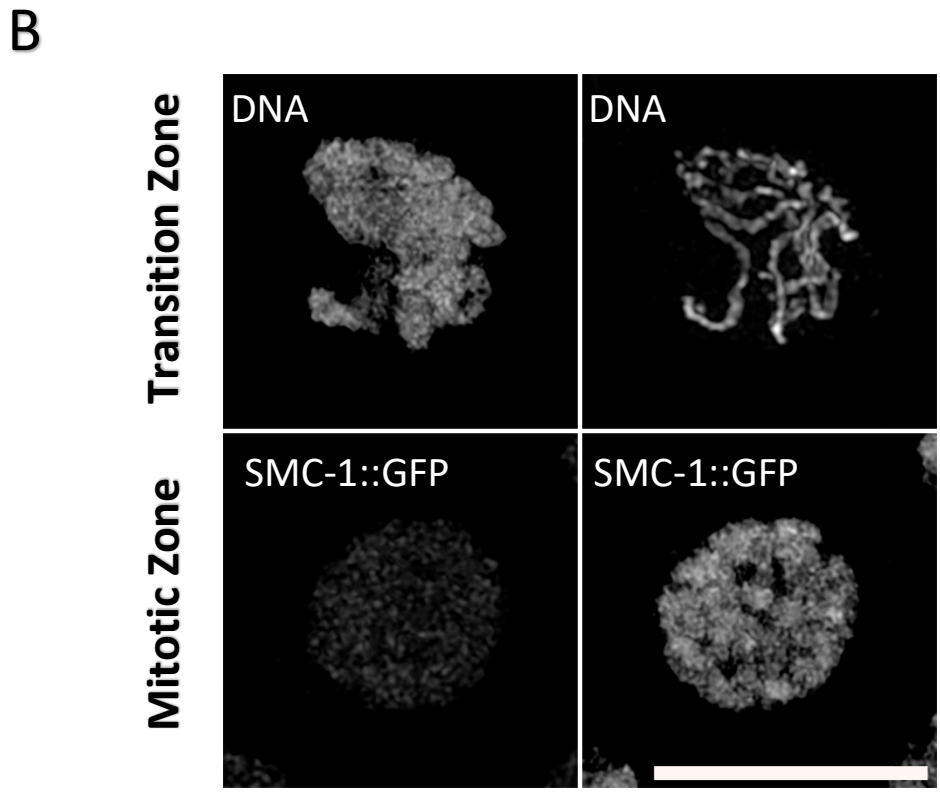
B
Transition Zone
Mitotic Zone
DNA
DNA
SMC-1::GFP
SMC-1::GFP

Figure 10. Imaging of axial elements during late meiotic prophase using SIM

Projections of late pachytene nuclei from worms expressing SMC-1::GFP. DNA was stained by DAPI (blue) and SMC-1::GFP (a protein that is present in all versions of meiotic cohesin complexes) was stained with anti-GFP antibodies conjugated with 488 (green). Images were taken using the Zeiss ELYRA S1 system. Note that axial elements from homologous chromosomes can be visualised as separate linear structures in many regions (red arrows). Scale bar = 5 µm.

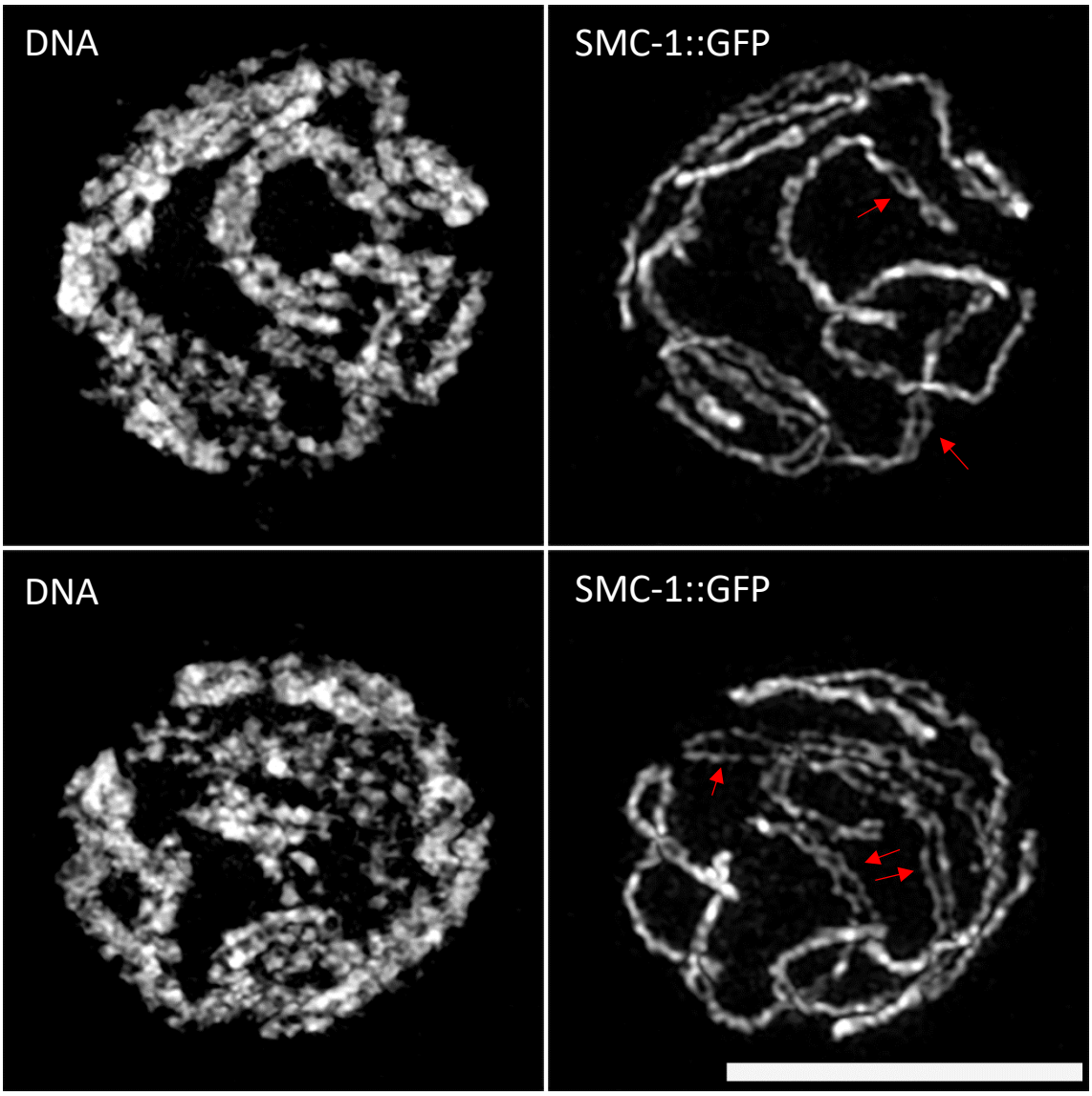
DNA
SMC-1::GFP
DNA
SMC-1::GFP

Figure 11. Projections of diakinesis oocytes from worms expressing SMC-1::GFP

DNA was stained by DAPI (blue) and SMC-1::GFP (a protein that is present in all versions of meiotic cohesin complexes) was stained with anti-GFP antibodies conjugated with 488 (green). Images were taken using the Zeiss ELYRA S1 system. Note the absence of nuclear soluble SMC-1::GFP signal in *wapl-1* mutant oocytes and that chromosome associated SMC-1::GFP signal decreases between the -2 and -1 oocytes in both wild type and *wapl-1* mutant oocytes. Scale bar = 5 μm.

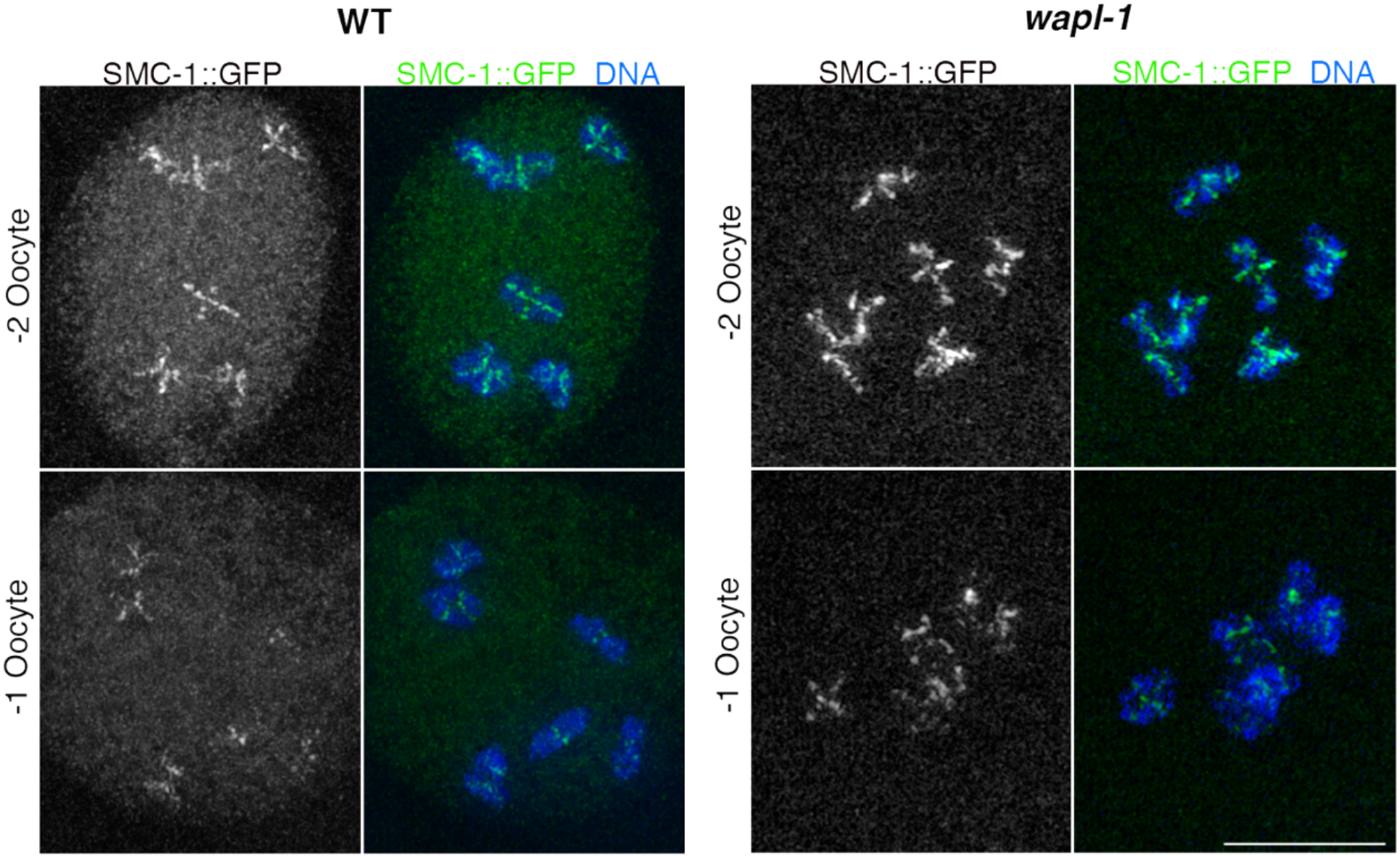
WT
wapl-1
SMC-1::GFP
SMC-1::GFP DNA
SMC-1::GFP
SMC-1::GFP DNA
-2 Oocyte
-1 Oocyte
-2 Oocyte
-1 Oocyte

Figure 12. Chromosome associated SMC-1::GFP staining decreases during diakinesis in a WAPL-1 independent manner

Projection of *wapl-1* mutant diakinesis. Germ lines were stained with DAPI and αGFP primary antibody conjugated with Alexa488 to amplify the SMC-1::GFP signal. The position of the oocytes is indicated by the numbers at the top, being the -1 oocyte the next to start metaphase I. There is a decrease in the amount of SMC-1::GFP associated to chromosomes from -3 to -2. Scale bar = 5 μm.

-1 oocyte
-2 oocyte
-3 oocyte
DNA
SMC-1::GFP
DNA SMC-1::GFP

Figure 13. Comparison between confocal and STED images of axial elements during meiotic prophase

Both images show projections of the same pachytene nuclei from worms expressing SMC-1::GFP. DNA was stained by DAPI (blue) and SMC-1::GFP (a protein that is present in all versions of meiotic cohesin complexes) was stained with anti-GFP antibodies conjugated with 488 (green). Image on the left was acquired using confocal microscopy, while the image on the right was acquired using STED. Red arrows show places were homologs are clearly separated, only visible in the STED image. Images were taken using the Leica TCS SP8 STED 3X system. Scale bar= 2.5 µm.

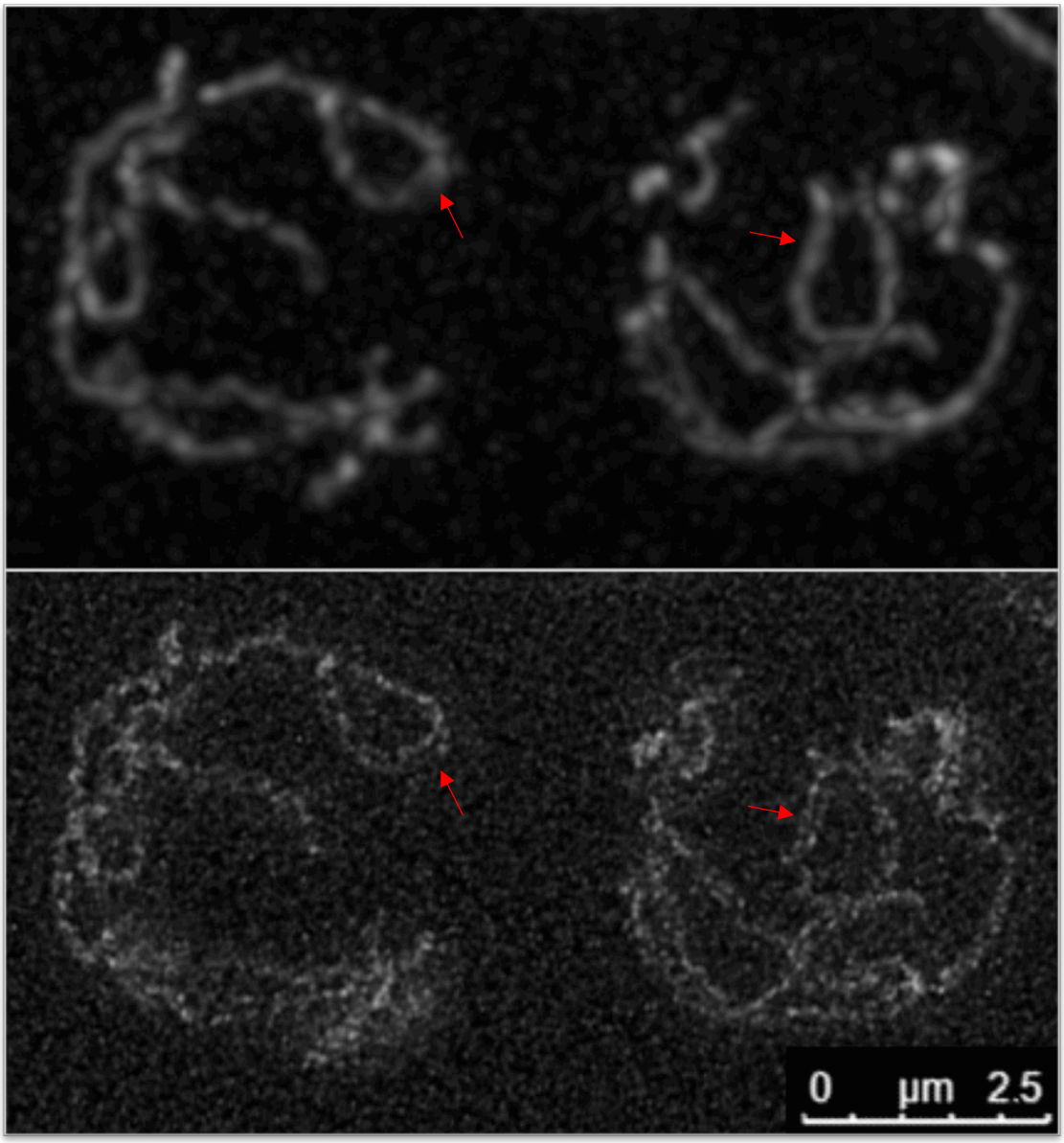
0 µm 2.5

Figure 14. Comparison between confocal and easySLM-STED images of axial elements during late pachytene

Axial elements were labelled by using αHTP-1 antibody with Alexa-488. Whereas easySLM-STED can resolve separation between axial elements (B), confocal cannot (A), as it can been observed in the line profiles. Scale bar = 2 μm.

I performed the preparation of the samples for this figure, while Frederik Görlitz acquired the images and made this figure.

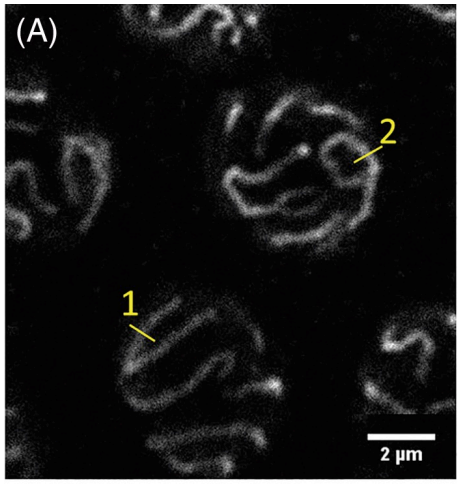
(A)
2
1
2 µm

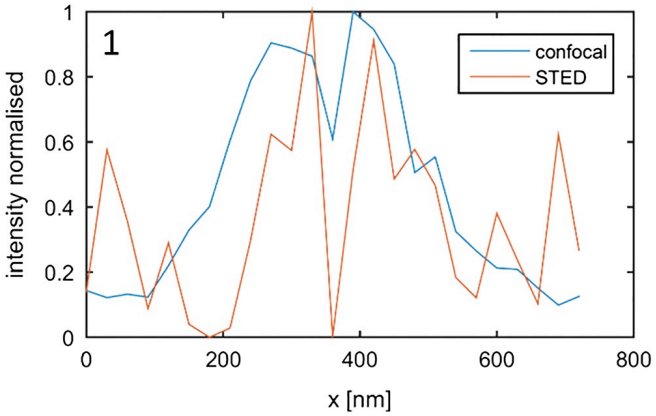
1
confocal
STED
intensity normalised
x [nm]
0
0.2
0.4
0.6
0.8
1
0
200
400
600
800

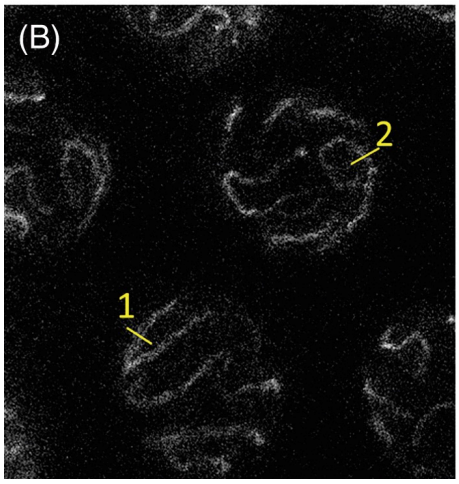
(B)
2
1

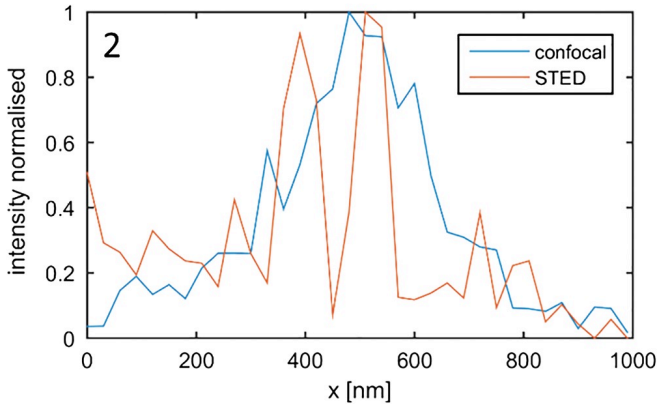
2
confocal
STED
intensity normalised
x [nm]
0
0.2
0.4
0.6
0.8
1
0
200
400
600
800
1000

Figure 15. *cosa-1::HA* 6 foci at late pachytene

Deconvolved projections from late pachytene nuclei from the *cosa-1::HA* strain stained with αHIM-8, αHTP-3, and αHA antibodies. Note that six COSA-1::HA foci can be observed in all nuclei and that all COSA-1 foci localize to different HTP-3 tracks. Scale bar = 5 μm.

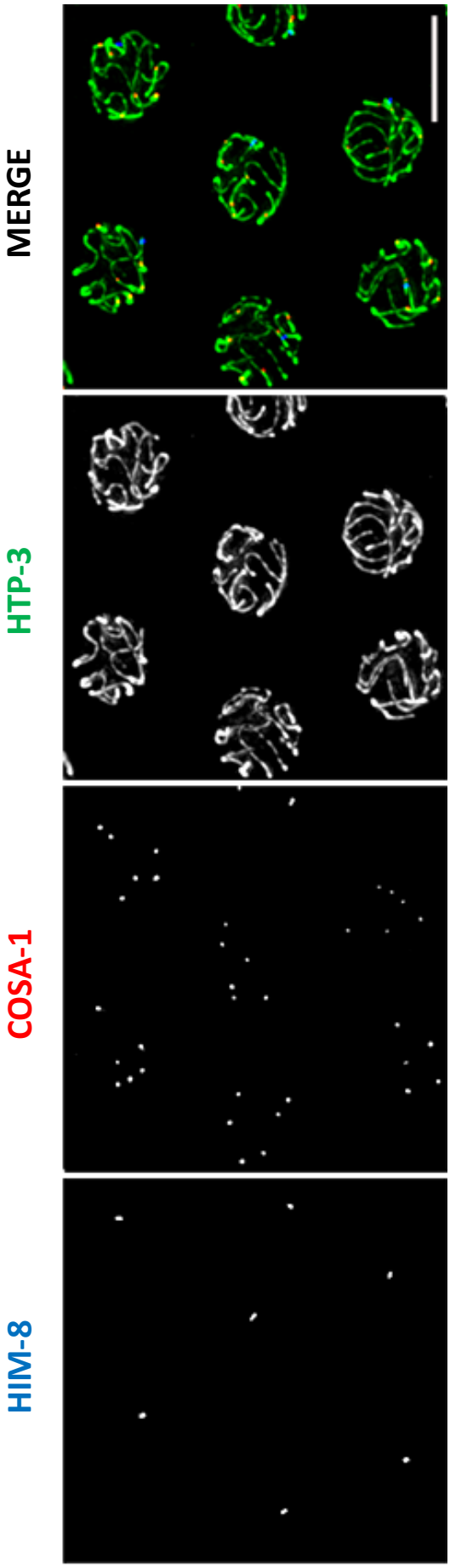
MERGE
HTP-3
COSA-1
HIM-8

Figure 16. Comparison of Delta vision and SIM 3D stacks analysed with Imaris software

Both 3D reconstructions were rotated to display the Z axis.

A - Visualization of widefield stacks on Imaris. Images were acquired with Deltavision microscope. Z axis resolution (600 nm) does not allow chromosome tracking in a three-dimensional fashion using IMARIS software. Axial elements were labelled with αHTP-3 (green), CO sites were labelled with αHA antibody against COSA-1::HA (pink) and the pairing center of chromosome X was labelled by using αHIM-8 (red). Scale bar = 2 µm.

B - Visualization of SIM stacks on Imaris. Images were acquired with Zeiss Elyra S1. Z axis resolution (300 nm) allows the tracking of the chromosomes in a three-dimensional fashion using IMARIS software. Scale bar = 2 µm.

A

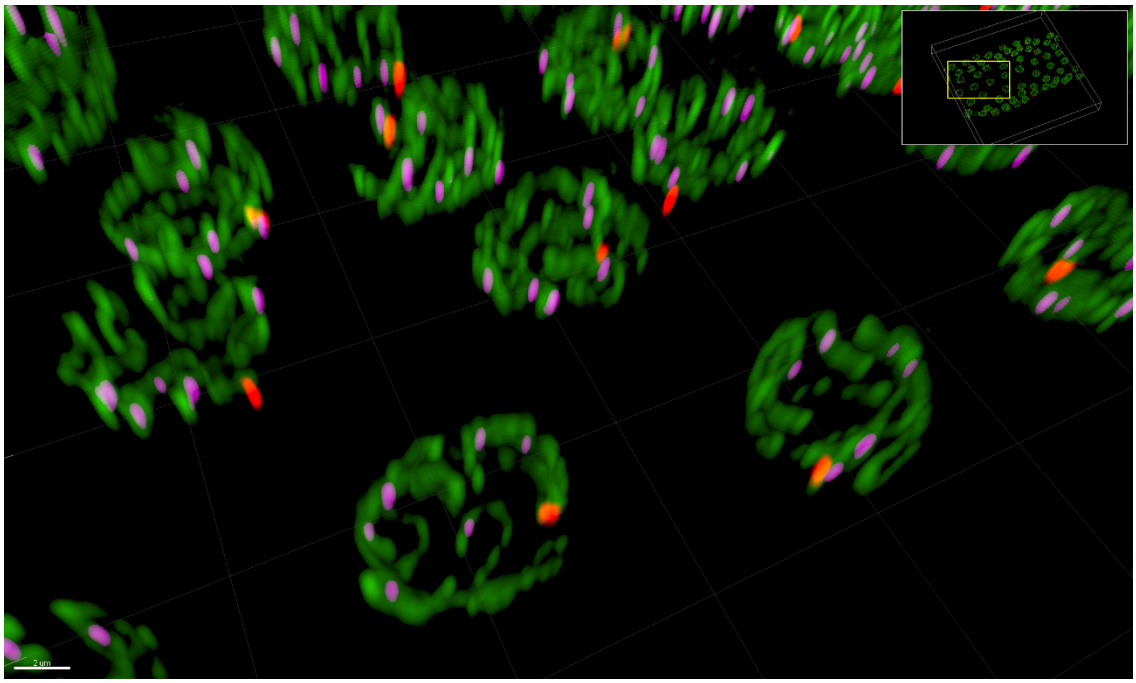

B

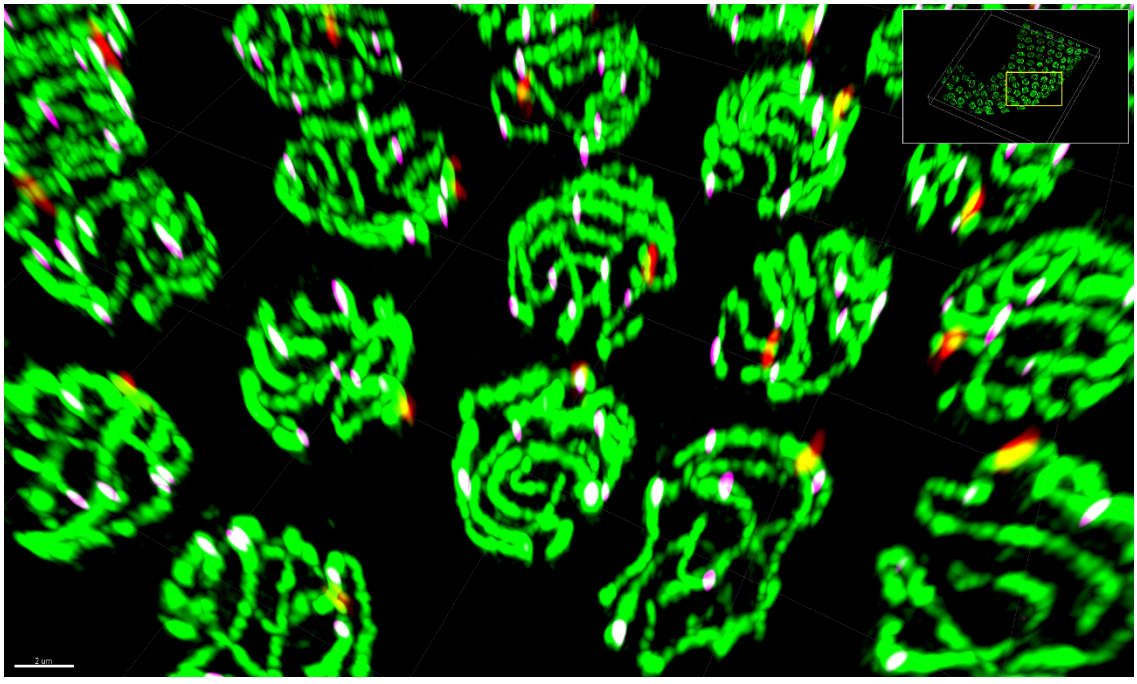

Figure 17. Imaris allows three-dimensional tracking of chromosomes

A - Reconstructions of 5 late pachytene nuclei from the *cosa-1::HA* strain using Imaris. Axial elements were labelled using αHTP-3 (green), COSA-1::HA was labelled using αHA (pink), HIM-8 was labelled by using αHIM-8 (red) and DAPI (blue). Note that X chromosomes can be easily tracked and oriented, and the position of the CO (COSA-1::HA foci). All these features can be captured in a 3D model of the X chromosomes (2nd column). Scale bar = 2 µm.

B - Video1

https://imperiallondon-my.sharepoint.com/:f:/g/personal/alj14_ic_ac_uk/ErttqDYL_QlAiRfQHSsJavQB-e_xiismsvmGgg6yFCTbTQ?e=h90huI

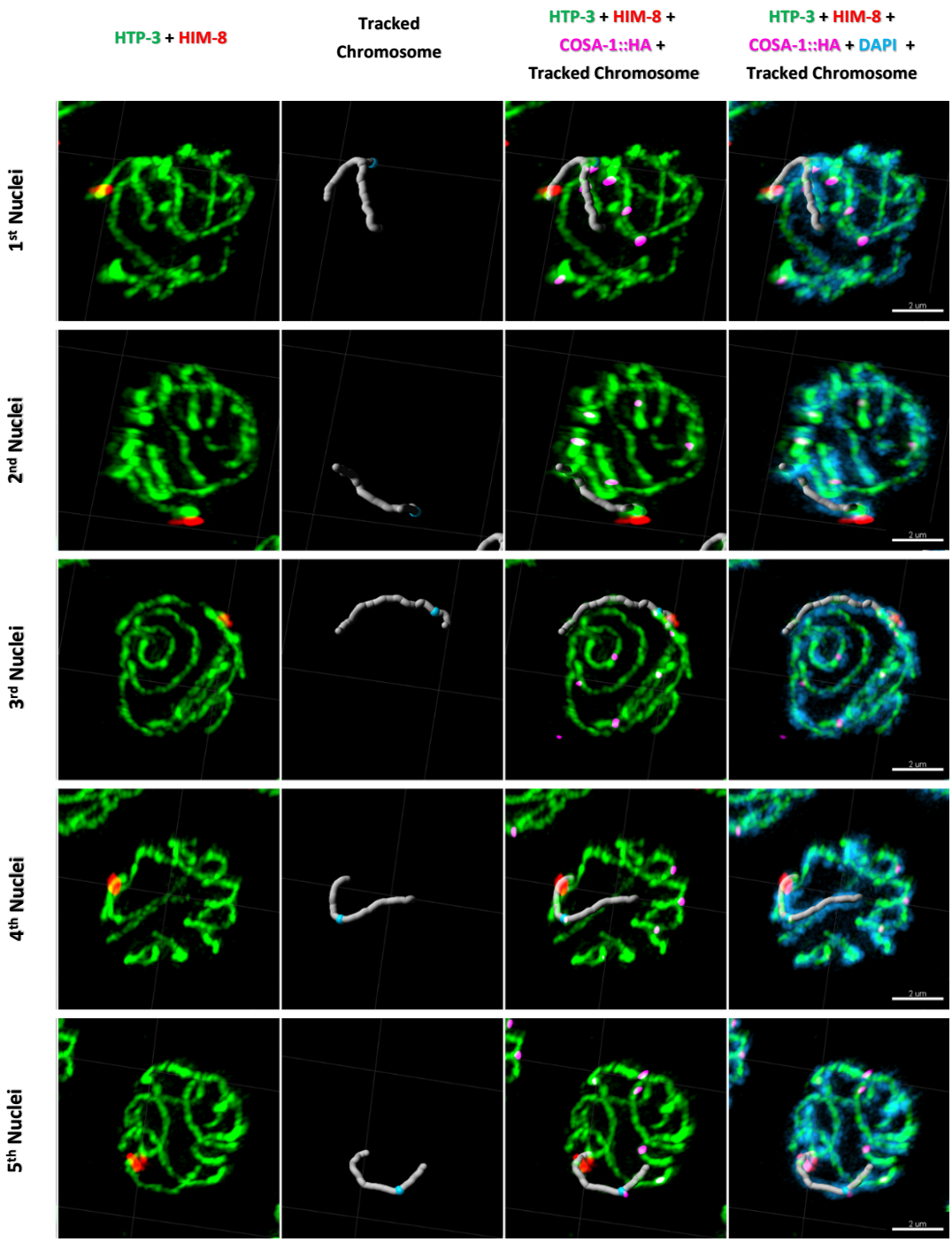
HTP-3 + HIM-8
Tracked Chromosome
HTP-3 + HIM-8 + COSA-1::HA + Tracked Chromosome
HTP-3 + HIM-8 + COSA-1::HA + DAPI + Tracked Chromosome
1st Nuclei
2nd Nuclei
3rd Nuclei
4th Nuclei
5th Nuclei
2 um

CHAPTER 4: RESULTS

MAPPING THE *him-13(e1742)* MUTATION

4.1 Objectives and background

Over the last two decades, research in *C. elegans* has contributed to demonstrate the intrinsic relationship between CO formation and chromosome structure. For example, partial impairment in condensin function alters CO numbers and distribution by affecting DSB formation during early prophase, while during late pachytene COs trigger a dramatic remodelling of axial elements and SC components as well as inducing a local elongation of axial elements (Libuda et al., 2013; Martinez-Perez et al., 2008; Mets and Meyer, 2009). In fact, most models of CO interference imply a transmission along chromosome axes of a signal generated by CO-designated events (Saito and Colaiácovo, 2017). Despite these observations, our understanding of the interplay between the processes of CO-formation (including DSB formation and CO-designation) and chromosome organization remains limited. Previous studies in our laboratory demonstrated that a meiotic mutant called *him-13*, which was isolated over 30 years ago by Jonathan Hodgkin due to the high incidence of male (him phenotype) progeny, which is normally caused by non-disjunction of the X chromosomes during meiosis, displayed changes in CO distribution. *him-13* hermaphrodites (XX) produce 5% males (X0) self-progeny (compared to 0.2% for wild type) and they also have a high frequency of dead embryos (29.7%) (figure 18A), suggesting impaired segregation of both autosomes and X chromosomes during meiosis. Moreover, preliminary CO mapping experiments performed by previous members of our laboratory showed that *him-13* mutants display altered CO distribution along autosomal chromosomes, but that CO numbers remain unaltered at 1 per homologue pair (Figure 18C and D). In agreement with this genetic mapping experiments, diakinesis oocytes of *him-13* mutants always contain six bivalents, demonstrating normal chiasma formation. However, some bivalents of *him-13* mutants display an unusual morphology, appearing much more cross-shaped than the bivalents of wild type oocytes (figure 18B). These observations suggested that *him-13 mutants* may be deficient in the chromosome remodelling

triggered by COs, or that altered chromosome organization induces changes in CO distribution that ultimately cause changes in diakinesis bivalents. All these experiments were performed using the *him-13(e1742)* allele, however the molecular identity of the gene carrying this mutation remained unknown. Previous mapping and whole-genome sequencing (WGS) of *him-13* mutants conducted in the lab showed that the *him-13(e1742)* mutation is located on chromosome I (figure 18E and 18F) in a 2 Mb genetic interval defined by *dpy-5* (I: 0.0 cM*)* (physical map 5.43 Mbp) and *unc-13* (I: 2.07 cM) (physical map 7.42 Mbp) (figure 19). Given the potential role of *him-13* as a factor that regulates the interplay between chromosome structure and CO formation, I set up to determine the molecular identity of *him-13(e1742)* with the ultimate goal of understanding the molecular processes affected by this mutation.

4.2 Strategies followed to identify *him-13* mutation

4.2.1 Genetic mapping of *him-13* using visual markers

To map the *him-13(e1742)* mutation, I measured the recombination frequency between the *him-13* locus and mutations in two flanking genes, whose mutation induces visible phenotypes. I crossed the *him-13* mutant with a strain carrying mutations in the dumpy-5 (*dpy-5*) and uncoordinated-13 (*unc-13*) genes, which are separated by a 2.0 cM genetic interval containing the *him-13* mutation (figure 20A). Then, the recombination frequency between the *him-13(e1742)* mutation and these visible markers was analysed (figure 20B). This experiment demonstrated that the distance between *him-13* locus and *dpy-5* was 0.70 cM; meanwhile the distance between *him-13* locus and *unc-13* was 1.3 cM, suggesting that *him-13* must be located around genetic position 1.3 on chromosome I (figure 20C).

After this, I looked at the WGS data of *him-13* mutants to identify mutations near the predicted genetic position of the *him-13(e1742)* mutation based on the above genetic mapping experiment. Gene *T23B3.1* is exactly located on position 1.3 on chromosome I, and carries a mutation predicted to induce an amino acid change from proline to leucine at position 225 of the T23B3.1 protein. Importantly, Sanger sequencing of *T23B3.1* in different strains homozygous for the *him-13(e1742)* mutation confirmed that the

mutation is only found in *him-13* mutants, but not in wild type controls (figure 20D). Moreover, expression of the *T23B3.1* gene is upregulated in the germ line (Kim, 2001), as expected for genes involved in meiosis.

4.2.2 CRISPR-generated alleles of *T23B3.1* demonstrate that *T23B3.1* gene is not him-*13*

In order to validate if a mutation in *T23B3.1* is responsible for the *him-13* phenotypes, I attempted to knock down *T23B3.1* using the technique of feeding RNAi, however, no embryonic lethality or male progeny was observed among the progeny of worms fed on bacteria expressing *T23B3.1* dsRNA. Although RNAi by feeding is a useful method for the analysis of gene function in *C. elegans*, it is not the best method to obtain phenotypes for genes involved in meiosis, since RNAi by feeding shows limited penetrance in the germ line. Hence, I created four mutant alleles of *T23B3.1* using a co-CRISPR approach (figure 21A and methods). All four alleles had a deletion/insertion at the beginning of the gene, inducing frameshifts predicted to result in null alleles (figure 21B). Nevertheless, homozygous worms for these four mutations did not show any embryo lethality nor high incidence of males, indicating that *T23B3.1* gene could not be responsible for the *him-13* phenotype. To confirm this, I performed a complementation test between the *him-13(e1742)* mutation and the *T23B3.1* CRISPR alleles. A complementation test is an assay where a candidate gene could be identified as the gene carrying a specific mutation. First, I crossed *him-13* homozygous mutant males with hermaphrodite worms homozygous for each one of the four *T23B3.1* CRISPR alleles, to produce heterozygous worms between *him-13* and the *T23B3.1* alleles. Then, I picked 10 of these heterozygous worms of each cross in different plates (figure 21C). Later, I analysed the progeny (percentage of males and embryo lethality) of F1 worms heterozygous for the original *him-13(e1742)* mutation and the different *T23B3.1* CRISPR alleles (figure 21D and E). Embryonic lethality and incidence of males were similar to the heterozygous wild type/ *him-13(e1742)* worms in all heterozygous *T23B3.1* CRISPR mutants/ *him-13(e1742)*, confirming that a mutation in the *T23B3.1* gene is not responsible for the *him- 13* phenotypes.

4.2.3 Whole genome sequencing of *him-13* recombinants

After ruling out that *him-13(e1742)* corresponded to *T23B3.1*, I decided to take a different strategy to identify the molecular identity of *him-13*. Because the original WGS data of *him-13(e1742)* demonstrated that there are several genes carrying mutations in the *dpy-5* - *unc-13* interval, I decided to sequence two *dpy-5; him-13* recombinants and two *him-13; unc-13* recombinants. In this way, if a CO is made close to the *him-13(e1742)* mutation in these recombinants, some candidates defined by mutations identified on the original WGS experiment could be discarded (figure 22A). I also sequenced two wild type and two *him-13* strains as controls (figure 22B). In this way, a new WGS list was obtained where fourteen genes with point mutations were common among all sequenced *him-13* strains (figure 22C). Insertions and deletions were also analysed, but no common candidates to all *him-13* strains were found. Although, analysis of the new WGS experiments did not discard any candidate genes, because COs occurred close to the *dpy-5* and *unc-13* markers in the sequenced recombinants, this experiment confirmed that *him-13(e1742)* mutation must correspond to one of the fourteen mutations common to all sequenced *him-13* strains (figure 22C).

4.2.3.1 Sanger sequencing of *him-13* recombinants reduced the number of candidates

To further reduce the genetic region containing *him-13(e1742)*, I used Sanger sequencing to sequence the 14 candidate genes in 23 *dpy-5 him-13* and *him-13 unc-13* recombinants using (figure 23A and B). This experiment resulted in a final list containing only four candidates: Two mutations in the coding region of genes *T10E9.3* and *mei-2*, plus two mutations in the intergenic regions between *C17F3.3* and *ckr-1*, and between *T21G5.2* and *T21G5.6* (figure 23C). Therefore, this strategy to find out the gene responsible for the *him-13* phenotype was quite successful, because the list was reduced from 14 candidates to only 4.

4.2.3.2 Complementation tests shows that *him-13* corresponds to *mei*-2

Out of the four mutations left, I first tested if *him-13(e1742)* corresponded to *mei-2* because a strain carrying a mutant allele with a strong phenotype for this gene was available from the *Caenorhabditis Genetics* Center (CGC). The *mei-2(ct102)* mutation is a recessive allele that displays maternal lethal effect, showing 100% of embryo lethality among the progeny of homozygous mothers, which are viable (figure 25A). Embryonic lethality of *mei-2(ct102)* is caused by disorganised meiotic spindles, which prevents proper chromosome segregation during the meiotic divisions (Srayko et al., 2000). MEI-2, together with with MEI-1, constitute the *C. elegans* katanin complex that is known for its role in microtubule severing. Katanin is known to participate in different cellular processes, including the meiotic divisions, as it will be explained in detail in chapter 5. The BW1102 strain contains *mei-2(ct102)* allele flanked by mutations in two visible markers, *dpy-5(e61)* and *unc-29(e1072),* which greatly facilitated following the *mei-2(ct102)* mutation in genetic crosses with *him-13*. A complementation test between *him-13(e1742)* mutation and *dpy-5 mei-2 unc-29* was performed as follows: First, *him-13* homozygous mutant males were crossed with a *dpy-5 mei-2 unc-29* hermaphrodite worm and the hermaphrodite was left to lay eggs. Then, 10 of these hermaphrodites heterozygous for *him-13(e1742)* and *dpy-5 mei-2 unc-29* were picked to individual plates and their progeny was analysed by measuring the percentage of males and embryo lethality. Embryonic lethality (65.3%) and incidence of males (9.5%) of *dpy-5 mei-2 unc-29/him-13(e1742)* were similar to the *him-13* homozygous worms (53.1% and 8.5% respectively) (figure 24A and B). These data strongly suggest that *him-13* corresponds to *mei-2*, and that a point mutation predicted to induce an amino acid change from glutamic acid to lysine at position 131 of the MEI-2 protein is responsible for the embryonic lethality and high incidence of males observed in the original strain containing the *him-13(e1742)* mutation.

4.3 Confirming the identity of *him-13* as *mei-2*

4.3.1 Complementation test between *mei-2* and *mei-2^{E131K}* and *mei-2^{WT}* transgenes

The following step was to confirm that the gene responsible for the *him-13* phenotype was *mei-2* and for this, two transgenic strains carrying a single copy insertion on chromosome II *(ttTi5605* II) of transgenes expressing either a wild-type version of *mei-2* (*fqSi1* transgene) or a version encoding the E131K mutation (*fqSi2* transgene) were created (see Materials and Methods) and then crossed into worms containing the mei-2*(ct102)* mutation at the endogenous *mei-2* locus. Homozygous worms for *fqSi1* (*mei-2^{WT}*) transgene showed wild type phenotype, not producing males or embryo lethality among their progeny (figure 25C and D). Unexpectedly, worms homozygous for the *fqSi2 (mei-2^{E131K})* transgene could not be maintained and therefore the transgene was maintained in heterozygosity.

To determine if these transgenes were able to complement the *mei-2(ct102)* mutation, the transgenes were crossed into a *dpy-5 mei-2 unc-29* background. In this occasion, I was able to isolate worms homozygous for the *fqSi2* (*mei-2^{E131K}*) transgene in the *dpy-5 mei-2 unc-29* mutant background. Whereas the *fqSi1* (*mei-2$^{WT)}$* transgene complemented the *mei-2(ct102)* mutation, showing a 100% of viability compared to 0% of viability of *mei-2(ct102)* mutants; the *fqSi2* (*mei-$^{2E131K)}$* transgene partially rescued the *mei-2* phenotype in the *dpy-5 mei-2 unc-29/ mei-2^{E131K}*, displaying 24.07% of embryonic viability and 2.82% of incidence of males (figure 25A and B). Therefore, expression of the *fqSi2* transgene in a *mei-2(ct102)* background induces a *him-13*-like phenotype, consistent with the E131K mutation being responsible for *him-13* phenotypes.

The next step was to check whether the *fqSi1* (*mei-2$^{WT)}$* transgene was able to complement the *him-13(e1742)* mutation. To do this, *mei-2^{WT}* was crossed into the *him-13* background, generating a strain which was homozygous for both *mei-2^{WT}* transgene and the endogenous mutated *mei-2*. The *mei-2^{WT}* transgene complemented the *him-13(e1742)* mutation, displaying a 100% of viability compared to 72.83% in *him-13* mutants (figure 25C) and a 0% of incidence of males, compared to a 6.90 % in *him-13* mutants (figure 25D).

4.3.2 Creation of a mei2E131K CRISPR strain

The experiments described above clearly indicate that the E131K mutation in *mei-2* is responsible for the phenotypes observed in the original *him-13* strain. To fully confirm this and discard any possible impact of the other 3 mutations in the genetic region containing *him-13(e1742)* (figure 23C), I decided to use CRISPR (Paix et al., 2016) to introduce the E131K mutation in the endogenous *mei-2* locus of a wild type strain (see Materials and Methods). This mutant displayed similar percentages of embryo lethality and incidence of males compared to *him-13* mutants (data not shown). Together the experiments mentioned above confirm that the *him-13(e1742)* allele corresponds to a E131K mutation in *mei-2.*

4.4 Summary of results

The molecular mechanisms that control the interplay between CO formation and chromosome structure are not completely understood. Preliminary studies in our laboratory had shown that the *him-13* mutant displayed abnormal CO distribution without affecting the total number of COs and suggested that the morphology of diakinesis bivalents was affected. Moreover, *him-13* mutants display high incidence of males and high embryo lethality, consistent with problems in meiotic chromosome segregation. These observations suggested that chromosome remodelling triggered by COs might be affected in *him-13* mutants, or that abnormal chromosome organisation could be responsible for changes in CO distribution that would cause an alteration in diakinesis bivalents. Surprisingly, I found that the gene mutated in the *him-13* strain is *mei-2,* a component of the microtubule severing complex katanin. This finding was unexpected as the only known role of katanin during meiosis in *C. elegans* is to organise the spindle during the meiotic divisions and although CO formation and meiotic divisions occur in the germ line, these processes are temporally and spatially separated. These findings suggest that MEI-2 could have an unanticipated role in regulating CO distribution, perhaps by regulating the microtubule network outside the nucleus during meiotic prophase when the cytoskeleton plays an important role in promoting pairing and synapsis between homologous chromosomes.

Figure 18. The *him-13* mutation affects crossover distribution

A - *him-13* mutants show embryonic lethality and high incidence of males compared to wild type controls. Both phenotypes are clear indicators of defects in meiotic chromosome segregation.

B - Diakinesis oocytes stained with DAPI. Note that wild type bivalents have an elongated appearance, while some *him-13* mutant bivalents have a more cruciform shape.

C - Number of crossovers in *him-13* mutants and wild type controls on chromosome III. Note that *him-13* and wild type controls have the same number of crossovers.

D - Graph showing the distribution of crossovers in four genetic intervals along chromosome III in wild type vs. *him-13* mutants (indicate genetic intervals -position of markers-). Note that crossover distribution is shifted towards the left end of chromosome III in *him-13* mutants.

E - *him-13(e1742)* mutant Comparative Genomic Hybridization (CGH) array results. *him-13* mutant (Bristonian background) was crossed with Hawaiian wild type strain to obtain *him-13* recombinants with mixed background that were used for mapping. Y-axis represents the log2 of the ratio between the two signals (Hawaiian/Bristonian) for all SNPs plotted versus genome position. The higher the signal, the more enriched the proportion of Bristonian SNPs. Colours represent different chromosomes: (I, II, III, IV, V and X respectively). This graph indicates that the *him-13(e1742)* mutation is located in chromosome I.

F - Rainbow plot showing chromosome I result from *him-13(e1742)* mutant CGH array. Each circle represents a ratio for a specific SNP. Y-axis represents the log2 of the ratio between the two signals (Hawaiian/Bristonian) for all SNPs plotted versus the physical position on chromosome I. The black line represents the predicted position for the *him-13(e1742)* mutation, being this at 6.5Mb.

All experiments shown on this figure were performed by lab members or collaborators before I joined the group and they are shown as the provide the basis for investigating the potential role of *him-13* as factor that regulates the interplay between CO distribution and chromosome structure.

A

	him-13	WT (N2)
Embryo lethality (%)	29.3	0.98
Male (%)	4.4	0.08

B

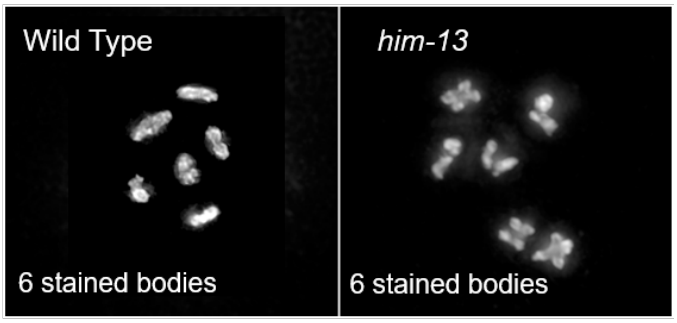

Diakinesis oocytes stained with DAPI

Chromosome III

C

	WT	*him-13*
Number of worms	100	98
Expected COs	45.9	44.98
Observed COs	43	42
COs per meiosis	0.43	0.43

D

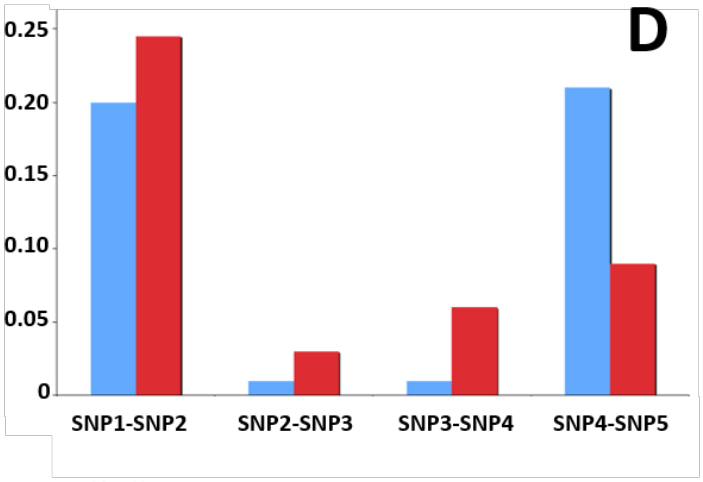

E

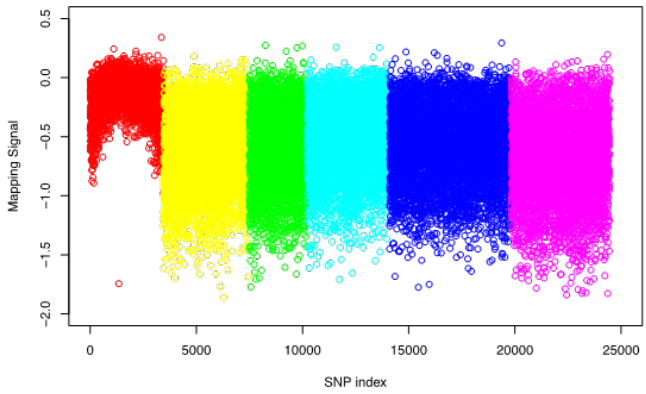

F

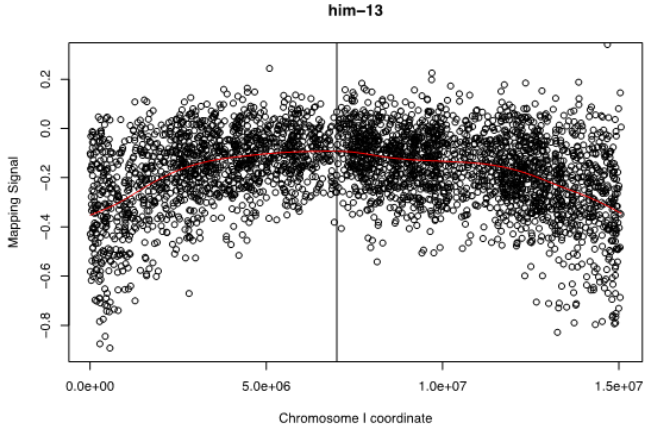

Figure 19. List of mutations in the genetic interval defined by *C27A12.9* (I: 0.74 cM) and *ttx-7* (I: 1.88 cM) locus and identified by whole genome sequencing of *him-13* mutants

The WGS dataset used for this analysis was performed by Oliver Crawley and the LMS bioinformatics facility.

Chromosome	Start	End	Reference	Observed	Zygosity	SNP Quality	ReadDepth	RMS Mapping quality	Genomic region	Gene Name	Exonic function	Aminoacid Change
chrI	*6066253*	*6066253*	-	*TCCAATTACAAT*	*hom*	*214*	*167*	-	*exonic*	*C27A12.9*	*nonframeshift insertion*	*C27A12.9:NM_059*
chrI	6180315	6180315	C	T	hom	222	141	60	exonic	T09B4.9	nonsynonymous SNV	T09B4.9:NM_0593
chrI	6228401	6228401	T	G	het	39	50	37	exonic	T08B2.3	nonsynonymous SNV	T08B2.3:NM_0593
chrI	6228403	6228403	A	G	het	7,8	49	37	exonic	T08B2.3	nonsynonymous SNV	T08B2.3:NM_0593
chrI	6267992	6267992	C	T	hom	222	308	59	exonic	oac-9	nonsynonymous SNV	oac-9:NM_059408
chrI	6377791	6377791	C	T	hom	222	199	59	exonic	gld-2	nonsynonymous SNV	gld-2:NM_059440:
chrI	6537682	6537682	C	T	hom	222	167	58	exonic	T10E9.3	nonsynonymous SNV	T10E9.3:NM_0594
chrI	*6543345*	*6543345*	*C*	*A*	*hom*	*222*	*148*	*58*	*exonic*	*T10E9.2*	*synonymous SNV*	*T10E9.2:NM_0594*
chrI	6565415	6565415	C	T	hom	222	256	59	exonic	mei-2	nonsynonymous SNV	mei-2:NM_059493
chrI	*6621065*	*6621065*	*A*	*C*	*het*	*110*	*256*	*42*	*exonic*	*D2092.8*	*synonymous SNV*	*D2092.8:NM_0595*
chrI	6718694	6718694	C	T	hom	222	189	59	exonic	T23B3.1	nonsynonymous SNV	T23B3.1:NM_0011
chrI	*6728514*	*6728514*	*C*	*T*	*hom*	*222*	*217*	*59*	*exonic*	*lbp-6*	*synonymous SNV*	*lbp-6:NM_059525:*
chrI	7094227	7094227	C	T	hom	222	229	60	exonic	prpf-4	nonsynonymous SNV	prpf-4:NM_05960
chrI	7264490	7264490	C	T	hom	222	250	52	exonic	let-75	nonsynonymous SNV	let-75:NM_059652
chrI	*7301404*	*7301404*	*C*	*G*	*hom*	*222*	*199*	*58*	*exonic*	*ttx-7*	*nonsynonymous SNV*	*ttx-7:NM_0011289*

Figure 20. Genetic mapping of the *him-13(e1742)* mutation using visible markers

A - Diagram of genetic crosses using the *dpy-5* (I: 0.0 cM*)* and *unc-13* (I: 2.07 cM) markers. The *him-13* mutant was crossed with the double mutant strain carrying visible markers CB2167 (*dpy-5; unc-13*). To analyse the frequency of recombination between the *him-13(e1742)* mutation and the two visual markers, 110 F_2 recombinants of each genotype were picked, being either *dpy-5;* non-*unc-13* or *unc-13;* non-*dpy-5*. For the *dpy-5* non-*unc-13* recombinants, plates that did not throw *unc-13* worms were isolated and checked for embryo lethality and males, being the opposite for *unc-13* non-*dpy-5* recombinants. If a plate threw males, that would have meant that a CO event had happened between the *him-13* locus and the opposite marker.

B - Recombination frequency analysis between *him-13* and genetic markers. Distances among genes were calculated based on the genetic position of *dpy-5* and *unc-13* obtained from Wormbase.

C - Genetic map showing the genetic position of *him-13*.

D - Sequencing of *T23B3.1* gene. Different recombinant and original strains were sequenced to validate our candidate gene. N2 (wild type strain), U73 (*unc-13* recombinant number 73) and D20 (*dpy-5* recombinant number 20) had wild type phenotype; meanwhile *him-13*, U57 (*unc-13* recombinant number 57) and D3 (*dpy-5* recombinant number 3) had *him-13* phenotype. Presence of the mutation was confirmed by sequencing both strands (top and bottom panel).

A

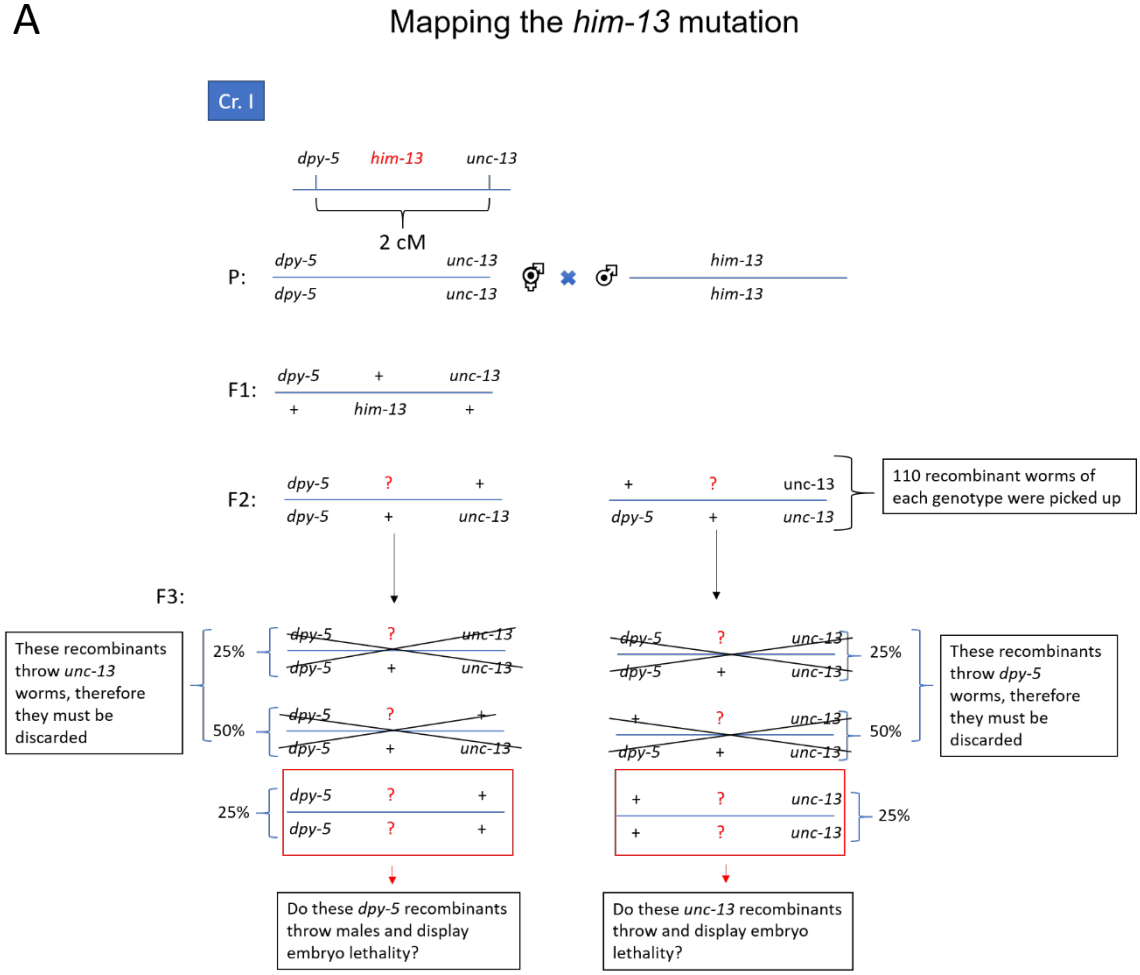

B

unc-13 Recombinants	Total Number	Recombination Frequency	Distance (cM)
him Phenotype	38	0.35	0.70
WT Phenotype	71	0.65	1.30

dpy-5 Recombinants	Total Number	Recombination Frequency	Distance (cM)
him Phenotype	71	0.65	1.29
WT Phenotype	39	0.35	0.71

C

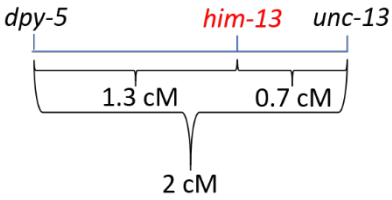

D

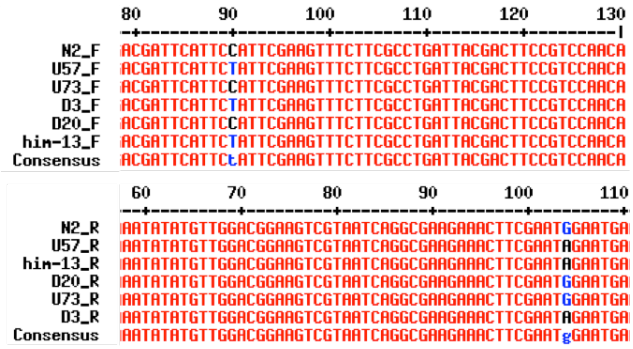

Figure 21. Mutation of the *T23B3.1* gene by CRISPR does not result in *him-13*-like phenotype

A - Alignment of sequences corresponding to the beginning of the *T23B3.1* gene in different CRISPR mutants and wild type controls. The four CRISPR mutants and the wild type strain were sequenced by Sanger sequencing and aligned using MultAlin (http://multalin.toulouse.inra.fr/multalin/).

B - Alignment of predicted amino acid sequence based on the previous DNA sequences. The four mutants are predicted to encode a truncated protein due to early STOP codons.

C - Diagram of complementation test between *T23B3.1* CRISPR alleles and *him-13* mutants.

D - Percentage of males in complementation test. There was no difference in percentage of males among the four heterozygous *him-13*/ *T23B3.1* CRISPR mutants (mut5, mut11, mut17 and mut20) and the *him-13*/WT, indicating that *T23B3.1* is not the gene responsible for the *him-13* phenotype.

E - Percentage of embryo lethality in complementation test. There was no difference in percentage of embryo lethality among the four heterozygous *him-13*/ *T23B3.1* CRISPR mutants (mut5, mut11, mut17 and mut20) and the *him-13*/WT, indicating that *T23B3.1* is not the gene responsible for *him-13* phenotype.

A

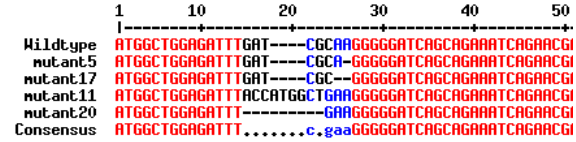
1 10 20 30 40 50
Wildtype ATGGCTGGAGATTTGAT----CGCAAGGGGGATCAGCAGAAATCAGAACG
mutant5 ATGGCTGGAGATTTGAT----CGCA-GGGGGATCAGCAGAAATCAGAACG
mutant17 ATGGCTGGAGATTTGAT----CGC--GGGGGATCAGCAGAAATCAGAACG
mutant11 ATGGCTGGAGATTTACCATGGCTGAAGGGGGATCAGCAGAAATCAGAACG
mutant20 ATGGCTGGAGATTT---------GAAGGGGGATCAGCAGAAATCAGAACG
Consensus ATGGCTGGAGATTT.......c.gaaGGGGGATCAGCAGAAATCAGAACG

B

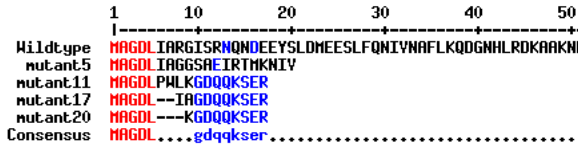
1 10 20 30 40 50
Wildtype MAGDLIARGISRNQNDEEYSLDMEESLFQNIVNAFLKQDGNHLRDKAAKN
mutant5 MAGDLIAGGSAEIRTMKNIV
mutant11 MAGDLPWLKGDQQKSER
mutant17 MAGDL--IAGDQQKSER
mutant20 MAGDL---KGDQQKSER
Consensus MAGDL....gdqqkser.....

C

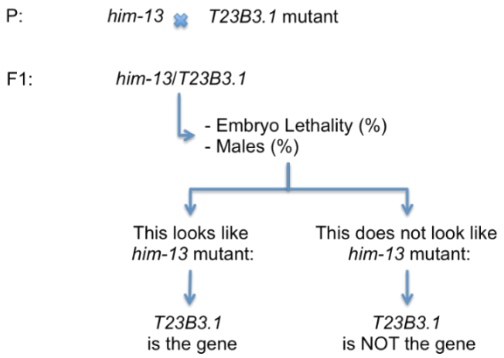
P:
him-13
T23B3.1 mutant
F1:
him-13/T23B3.1
- Embryo Lethality (%)
- Males (%)
This looks like him-13 mutant:
This does not look like him-13 mutant:
T23B3.1 is the gene
T23B3.1 is NOT the gene

D

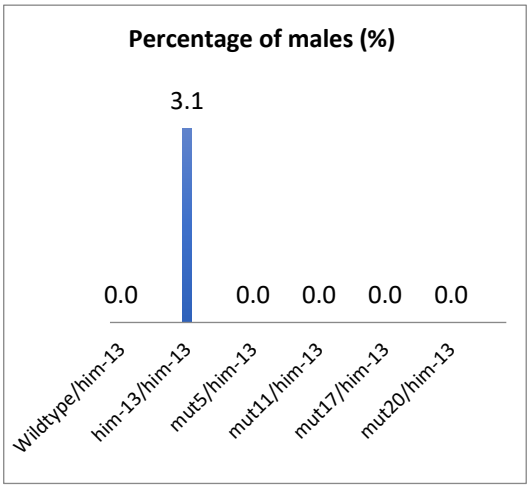
Percentage of males (%)
3.1
0.0
0.0
0.0
0.0
0.0
Wildtype/him-13
him-13/him-13
mut5/him-13
mut11/him-13
mut17/him-13
mut20/him-13

E

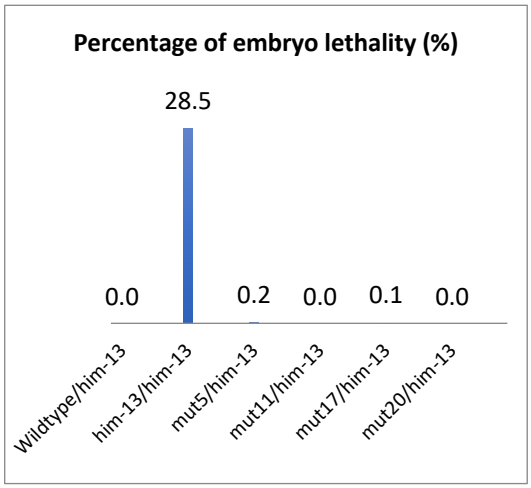
Percentage of embryo lethality (%)
28.5
0.0
0.2
0.0
0.1
0.0
Wildtype/him-13
him-13/him-13
mut5/him-13
mut11/him-13
mut17/him-13
mut20/him-13

Figure 22. Whole genome sequencing of recombinant between *him-13* and *dpy-5* or *unc-13*

A - Diagram of how recombinants were generated depending on where the crossover position is made.

B - List of sequenced strains. Four recombinant strains were sent to sequence (*dpy-5*; *him-13* (1), *dpy-5*; *him-13* (2), *him-13*; *unc-13* (1) and *him-13*; *unc-13* (2)), two control *him-13* strains (CB3234 (original him-13 strain from CGC) and him-13 mutants from the *him-13*/ht2 balanced strain generated in the lab) and two strains not displaying the *him-13* phenotype (CB2167 (*dpy-5*; *unc-13)* and N2).

C - List of the common mutations of the sequenced *him-13* mutants in the genetic interval defined by *T09B4.5* (I: 0.83 cM) and *myo-1* (I: 1.87 cM) locus and identified by whole genome sequencing. The WGS dataset used for this analysis was performed by the LMS bioinformatics facility.

A

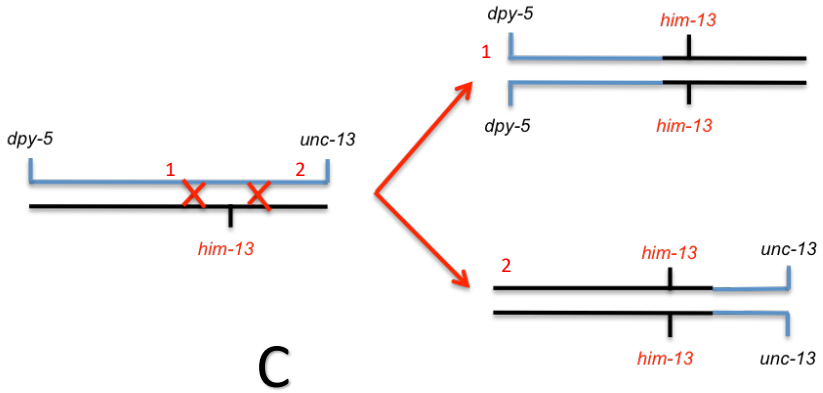

B

Samples to sequence	Phenotype
dpy-5; him-13 (1)	*him-13*
dpy-5; him-13 (2)	*him-13*
him-13; unc-13 (1)	*him-13*
him-13; unc-13 (2)	*him-13*
CB3234	*him-13*
him-13/ht2	*him-13*
N2	wild-type
dpy-5; unc-13	wild-type

C

I	6157217	6157217	C	T	UTR3	T09B4.5
I	6180313	6180313	C	T	exonic	T09B4.9
I	6267990	6267990	C	T	exonic	oac-9
I	6364924	6364924	C	A	UTR5	K04F10.1
I	6462170	6462170	C	T	exonic	knl-2
I	6537681	6537681	C	T	exonic	T10E9.3
I	6565414	6565414	C	T	exonic	mei-2
I	6684931	6684931	T	A	intergenic	C17F3.3, ckr-1
I	6718693	6718693	C	T	exonic	T23B3.1
I	6870458	6870458	A	G	upstream;downstream	T21G5.2, T21G5.6
I	7094228	7094228	C	T	exonic	prpf-4
I	7221913	7221913	C	T	upstream;downstream	C01H6.6, nhr-23
I	7234585	7234585	C	T	UTR5	R06C7.2
I	7264492	7264492	C	T	exonic	myo-1

Figure 23. Sanger sequencing of candidate genes from *dpy-5/him-13 him-13/unc-13* recombinants

A - Sanger sequencing results of *dpy-5; him-13* recombinants. *prpf-4* and *C01H6.6* were discarded because they displayed the wild type sequence in some recombinants showing *him-13* phenotype.

B - Sanger sequencing results of *him-13; unc-13* recombinants. *gld-2* was discarded because it displayed the wild type sequence in one recombinant showing *him-13* phenotype.

C - Final list of candidates. This experiment has resulted in four candidates: Two mutations in the coding region of genes *T10E9.3* and *mei-2*, plus two mutations in the intergenic regions between *C17F3.3* and *ckr-1*, and between *T21G5.2* and *T21G5.6*.

A

	unc-13_8	*unc-13_9*	*unc-13_11*	*unc-13_19*	*unc-13_24*	*unc-13_26*	*unc-13_29*	*unc-13_30*	WT	*him-13*
gld-2	-	-	-	-	-	-	-	-	wt	mut
T10E9.3	-	-	-	-	-	-	-	-	wt	mut
mei-2	-	-	-	-	-	-	-	-	wt	mut
C17F3.3	mut	mut	mut	mut	mut	mut	mut	mut	wt	mut
T21G5.2	mut	mut	mut	mut	mut	mut	mut	mut	wt	mut
prpf-4	mut	wt	mut	wt	mut	mut	wt	mut	wt	mut
C01H6.6	mut	wt	mut	wt	wt	mut	wt	mut	wt	mut

B

	dpy-5_2	*dpy-5_3*	*dpy-5_6*	*dpy-5_7*	*dpy-5_8*	*dpy-5_11*	*dpy-5_12*	*dpy-5_15*	*dpy-5_16*	*dpy-5_18*
gld-2	mut	mut	mut	mut	mut	mut	mut	mut	mut	mut
T10E9.3	mut	mut	mut	mut	mut	mut	mut	mut	mut	mut
mei-2	mut	mut	mut	mut	mut	mut	mut	mut	mut	mut
C17F3.3	mut	mut	mut	mut	mut	mut	mut	mut	mut	mut
T21G5.2	mut	mut	mut	mut	mut	mut	mut	mut	mut	mut
prpf-4	-	-	-	-	-	-	-	-	-	-
C01H6.6	-	-	-	-	-	-	-	-	-	-

	dpy-5_19	*dpy-5_22*	*dpy-5_25*	*dpy-5_26*	*dpy-5_29*	WT	*him-13*
gld-2	mut	mut	mut	mut	wt	wt	mut
T10E9.3	mut	mut	mut	mut	mut	wt	mut
mei-2	mut	mut	mut	mut	mut	wt	mut
C17F3.3	mut	mut	mut	mut	mut	wt	mut
T21G5.2	mut	mut	mut	mut	mut	wt	mut
prpf-4	-	-	-	-	-	wt	mut
C01H6.6	-	-	-	-	-	wt	mut

C

I	6537681	6537681	C	T	exonic	T10E9.3
I	6565414	6565414	C	T	exonic	mei-2
I	6684931	6684931	T	A	intergenic	C17F3.3, ckr-1
I	6718693	6718693	C	T	exonic	T23B3.1
I	6870458	6870458	A	G	upstream;downstream	T21G5.2, T21G5.6

Figure 24. The *mei-2(ct102)* mutant allele does not complement *him-13(e1742)*

A - Percentage of embryo lethality among the progeny of worms of the indicated genotype. *dpy-5* and *unc-29* mutations were in the original *mei-2* mutant strain as visual markers to manipulate the strain, not affecting either viability of incidence of males. There was no difference in the percentage of embryo lethality between WT/*him-13* and *gld-2/him-13*, indicating *gld-2* is not the gene responsible for the *him-13* phenotype as expected from the sanger sequencing data. Meanwhile *dpy-5; mei-2; unc-29/him-13* showed a high percentage of embryo lethality which was comparable to *him-13/him-13*, indicating that *mei-2* is the gene responsible for the *him-13* phenotype.

B - Percentage of males in complementation test. Similar to embryo lethality, while WT/*him-13* and *gld-2/him-13* did not show any incidence of males, *dpy-5; mei-2; dpy-29/him-13* and *him-13/him-13* showed similar percentage of males, suggesting that the gene responsible for the *him-13* phenotype is *mei-2.*

A

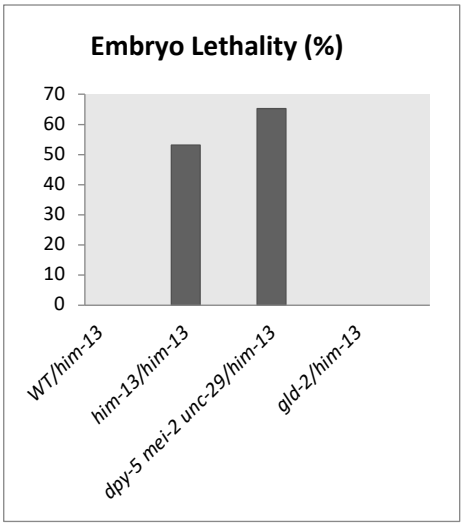
Embryo Lethality (%)
70
60
50
40
30
20
10
0
WT/him-13
him-13/him-13
dpy-5 mei-2 unc-29/him-13
gld-2/him-13

B

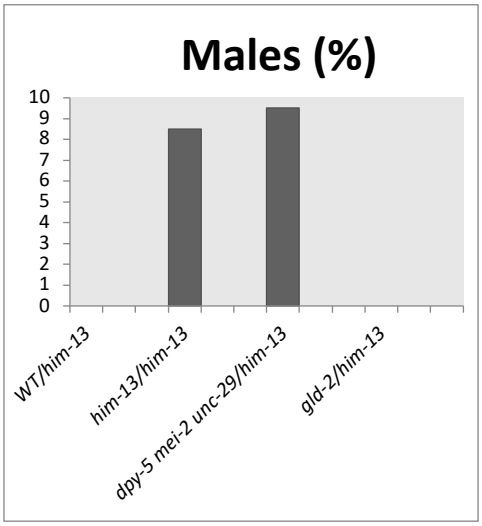
Males (%)
10
9
8
7
6
5
4
3
2
1
0
WT/him-13
him-13/him-13
dpy-5 mei-2 unc-29/him-13
gld-2/him-13

Figure 25. Complementation tests of single copy transgenes expressing *mei-2^{WT}* or *mei-2^{E131K}*

A - Percentage of Viability of *mei-2(ct102)* mutant without any transgene, homozygous for *fqSi1 (mei-2^{WT})* transgene in the *mei-2(ct102)* background and homozygous for *fqSi2 (mei-2^{E131K})* in the *mei-2(ct102)* background. *fqSi1(mei-2^{WT})* transgene complemented *mei-2(ct102)* mutation, whereas fqsi2(mei-2^{E131K}) partially rescued the phenotype of *mei-2(ct102)* mutant with a 24.07% of viability.

B - Incidence of males of *mei-2(ct102)* mutant without any transgene, homozygous for *fqSi1 (mei-2^{WT})* transgene in the *mei-2(ct102)* background and homozygous for *fqSi2 (mei-2^{E131K})* in the *mei-2(ct102)* background. *fqSi1(mei-2^{WT})* transgene complemented *mei-2(ct102)* mutation without producing males, whereas *fqsi2(mei-2^{E131K})* partially rescued the phenotype of *mei-2(ct102)* mutant, although throwing males.

C - Percentage of viability of the *him-13* mutant, the strain homozygous for *fqSi1(mei-2^{WT})* transgene and homozygous *fqSi1(mei-2^{WT})* in the *him-13* background. *fqSi1(mei-2^{WT})* transgene complemented the *him-13(e1742)* mutation, displaying a 99.86% of viability as the control *fqSi1(mei-2^{WT})* control.

D - Incidence of males of the *him-13* mutant, the strain homozygous for *fqSi1(mei-2^{WT})* transgene and homozygous *fqSi1(mei-2^{WT})* in the *him-13* background. *fqSi1(mei-2^{WT})* transgene complemented the *him-13(e1742)* mutation, showing no incidence of males as the *fqSi1(mei-2^{WT})* control. All these data confirm that *mei-2* is mutated in the *him-13* strain.

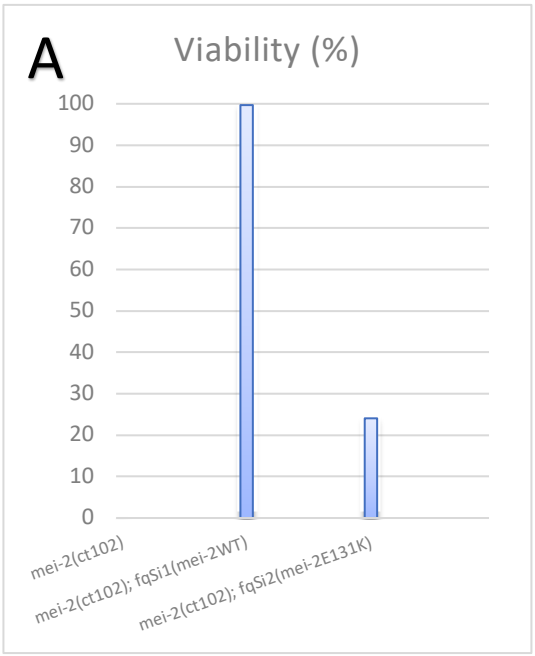
A
Viability (%)
100
90
80
70
60
50
40
30
20
10
0
mei-2(ct102)
mei-2(ct102); fqSi1(mei-2WT)
mei-2(ct102); fqSi2(mei-2E131K)

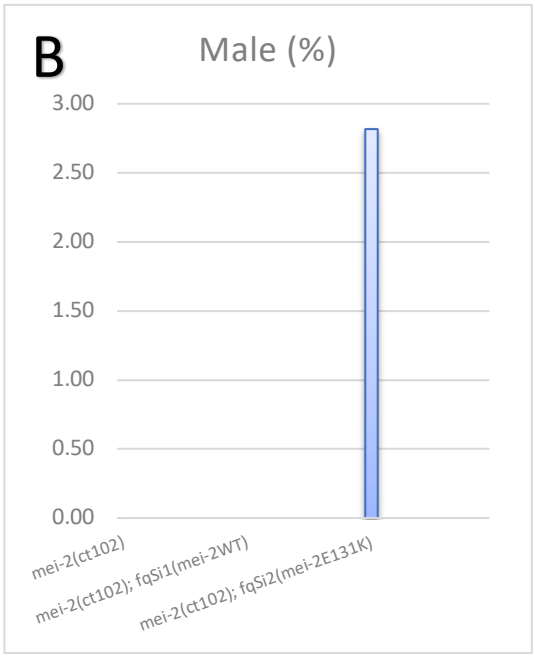
B
Male (%)
3.00
2.50
2.00
1.50
1.00
0.50
0.00
mei-2(ct102)
mei-2(ct102); fqSi1(mei-2WT)
mei-2(ct102); fqSi2(mei-2E131K)

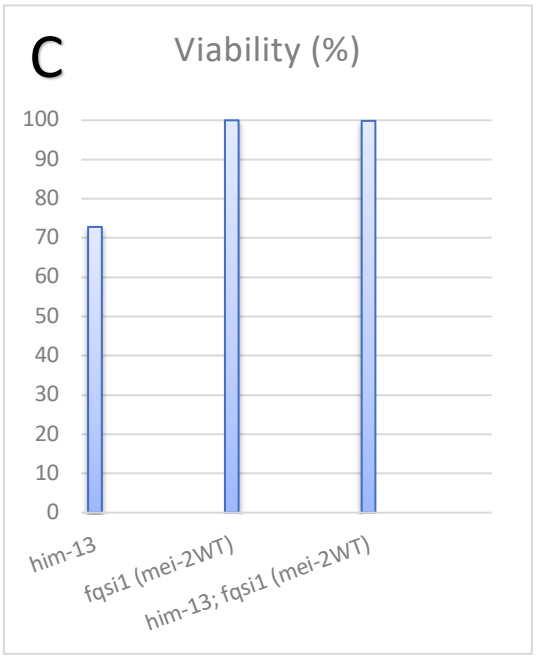
C
Viability (%)
100
90
80
70
60
50
40
30
20
10
0
him-13
fqsi1 (mei-2WT)
him-13; fqsi1 (mei-2WT)

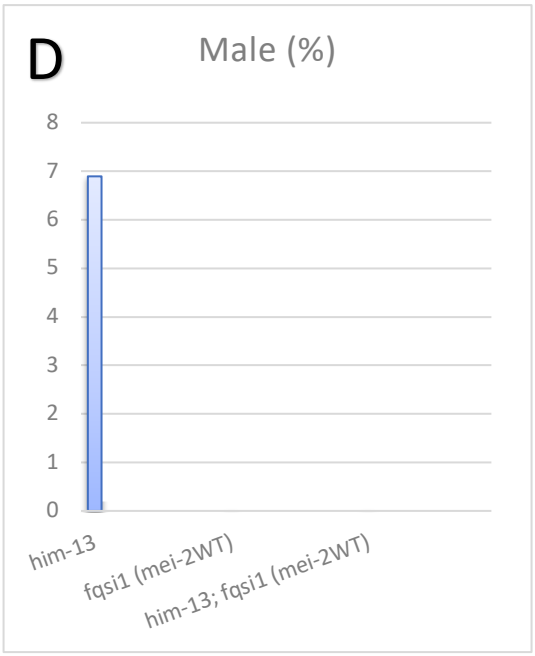
D
Male (%)
8
7
6
5
4
3
2
1
0
him-13
fqsi1 (mei-2WT)
him-13; fqsi1 (mei-2WT)

CHAPTER 5: RESULTS.

FUNCTIONAL ANALYSIS OF *HIM-13* MUTANTS

5.1 Objectives and background

After discovering that a mutation in *mei-2* was responsible for the *him-13* phenotype, as reported in chapter 4, I wanted to understand how a presumed defect in katanin function could be responsible for the apparent changes in CO distribution observed in *him-13* mutants. In principle, an alteration of CO distribution can be caused in several ways, such as by changes in the number and/or location of DSBs, as observed in worms heterozygous for mutations in condensin subunit *dpy-28* that increases DSB numbers (Mets and Meyer, 2009; Tsai et al., 2008), or by affecting the mode of repair of DSBs, as observed in *rtel-1* mutants where more DSBs are repaired as COs because of a defect in the disassembly of strand invasion intermediates (Barber et al., 2008; Youds et al., 2010). Although katanin has a role in organising microtubules during meiotic divisions, there are no previous reports suggesting that katanin could have a role during meiotic prophase. However, previous studies have shown that the cytoskeleton plays important roles during early meiotic prophase, as microtubule motors promote meiotic chromosome movement to achieve homologous pairing and synapsis in a process requiring the nuclear envelope SUN/KASH complexes in *C. elegans* (Sato et al., 2009). In fact, *sun-1* mutants have major defects in chromosome recognition, pairing and CO formation, demonstrating that chromosome movement is essential for these processes (Penkner et al., 2007). These chromosome movements are conserved across species and it has been proposed that they might contribute to eliminate interactions between non-homologous chromosomes, being crucial for homologous pairing (Koszul and Kleckner, 2009).

5.1.1 Microtubules

The cytoskeleton is an intricate network of filaments which is extended through the cytoplasm and the nucleus, participating and coordinating many cellular processes that are essential for eukaryotic cells, including cell division, cell migration or neuronal

development (Sharp and Ross, 2012). Microtubule filaments are made of α/β tubulin heterodimers which then assemble into protofilaments and 13 protofilaments come together to form a microtubule, which is a hollow cylinder with a polarised structure, showing a plus and minus end (figure 6A). This fundamental polarity defines where polymerisation or depolymerisation of the microtubule can occur, taking place in the plus end and being substantial for microtubule dynamics (Müller-Reichert et al., 2010).

Microtube dynamics is a highly regulated process that is vital for the correct function of the cell. To do this, microtubule-associated proteins (MAPs) have a role in controlling the assembly of microtubule filaments promoting nucleation and growth, stabilising microtubules or promoting microtubule catastrophe (switching between a growing state to a shrinkage state or vice versa), (Goodson and Jonasson, 2018). For example, Doublecortin is a MAP that stabilises neuronal microtubules in humans, protecting them against microtubule catastrophe and also promoting microtubule nucleation. Mutations in Doublecortin cause epilepsy and mental retardation (Moores et al., 2006). On the other hand, microtubule severing enzymes, including katanin, spastin, and fidgetin, promote microtubule destabilization. These proteins play major roles in chromosome segregation, morphogenesis, migration or cell wall biosynthesis (Sharp and Ross, 2012).

5.1.2 Katanin and other severing-microtubule enzymes

MAPs are fundamental to control microtubule dynamics and severing-microtubule enzymes are an important subfamily of ATPases associated with diverse cellular activities (or AAA protein superfamily) (Frickey and Lupas, 2004). Three severing-microtubule enzymes have been discovered: katanin, spastin and fidgetin. These AAA proteins contain an AAA domain which consist of 230 amino acids with ATPase activity and they usually work together as hexameric rings or dodecameric rings (Sharp and Ross, 2012). This domain contains the catalytic activity that can hydrolyse ATP and the resulting energy is used to sever microtubules. To do this, the AAA domain contains two Walker motives, a Walker A motif that binds ATP molecules and a Walker B motif that hydrolyses the same ATP molecules (Frickey and Lupas, 2004).

Katanin is widely conserved across eukaryotic species and was the first microtubule-severing enzyme discovered in *Xenopus* egg extracts (Sharp and Ross, 2012; Vale, 1991). Katanin consists of a heterodimer formed by a 60 kDa catalytic subunit (p60/MEI-1/KATNA1) and an 80 kDa regulatory subunit (p80/MEI-2/KATNB1) (McNally and Vale, 1993). In sea urchin the p60 catalytic subunit is sufficient to sever microtubules in vivo, whereas in *C. elegans*, *Chlamydomonas* and *Tetrahymena* both p60 and p80 are needed for katanin activity (Dymek et al., 2004; McNally and Vale, 1993; Sharma et al., 2007). p80 interacts with p60 through its C-terminus, modulating p60 activity and localization, for example by targeting katanin to the centrosome. Katanin can carry out two kind of enzymatic activities, depolymerization of microtubule ends and severing of microtubules, which could contribute to increase microtubule nucleation (Ghosh et al., 2012). Several studies have shown how spastin and katanin can sever microtubules, although this mechanism is not completely understood. To sever microtubules, these enzymes join to the C-terminus tail of tubulin and pulling on it they provoke destabilisation of the microtubule (Roll-Mecak and McNally, 2010; Roll-Mecak and Vale, 2008; White et al., 2007).

Katanin has been described to participate in several molecular processes including spindle organisation during meiosis (Mains et al., 1990), mitosis (Zhang et al., 2007), neuronal processes (Ahmad et al., 2000), and cilia biogenesis (Sharma et al., 2007) among others.

5.1.2.1 Katanin in *C. elegans*

The genes encoding katanin subunits in *C. elegans*, *mei-1* (p60) and *mei-2* (p80), were identified in a screen for meiotic mutants in 1990, before severing-microtubule enzymes were discovered (Mains et al., 1990). *mei-1* and *mei-2* mutants show high embryo lethality and defects in creating a bipolar meiotic spindle, with no additional defects having been reported (Joly et al., 2016; Mains et al., 1990; Srayko et al., 2000). In wild type worms the activity of katanin converts long microtubule polymers into shorter microtubule fragments, some of which might be used as seeds for new microtubules, and also increases the polymer mass. In contrast, mutations in *mei-1* or *mei-2* result in fewer and longer microtubules and also creates defects in microtubule orientation (Roll-

Mecak and Vale, 2006; Srayko et al., 2006). As a consequence of these defects, katanin mutants display defects in meiotic chromosome segregation (McNally et al., 2006; Srayko et al., 2000). Combined in vitro and in vivo analysis of engineered MEI-1 and MEI-2 variants demonstrated that the role of MEI-2 in *C. elegans* Katanin is to promote microtubule binding and that the microtubule severing activity of the complex is essential for its in vivo role in meiotic spindles (Joly et al., 2016). Katanin localises to meiotic chromosomes and spindle poles (Srayko et al., 2000), where katanin has been proposed to have a secondary activity by promoting the assembly of meiotic spindle poles (McNally and McNally, 2011). Interestingly, katanin is not involved in the mitotic divisions of the early embryo, in fact, katanin must be degraded after meiosis as it presence in the early embryo causes lethality due to excess microtubule severing during early cleavages (Beard et al., 2016; Lu and Mains, 2007).

5.2 Characterization of meiotic prophase events in *him-13* mutants

Given the role of katanin as a microtubule severing enzyme and the involvement of cytoskeleton-driven chromosome movement in promoting pairing and recombination, I decided to start the investigation of potential defects in meiotic prophase in *him-13* by using cytological markers of meiotic recombination and chromosome movement.

5.2.1 Recombination intermediates are prolonged in *him-13* mutants

5.2.1.1 DSB-2 is extended in *him-13* mutants

As mentioned before, the *him-13* mutant was initially isolated because of its high embryo lethality and high incidence of males (figure 18A), two phenotypes that are clear indicators of defects in meiotic chromosome segregation. However, *him-13* mutants always showed six DAPI-stained bodies in diakinesis oocytes, demonstrating that *him-13* mutants have no problems in forming crossovers. However, previous analysis in our group suggested that *him-13* mutants display altered crossover distribution, which is expected to be a consequence of difficulties during meiotic recombination. Thus, I decided to investigate whether *him-13* mutants had problems in meiotic recombination. Meiotic recombination is initiated by SPO-11, which needs meiotic cofactors such as DSB-1 and DSB-2, which are thought to promote chromatin structure compatible for DSB

formation in a CHK-2-dependent manner (Rosu et al., 2013; Stamper et al., 2013). Thus, I monitored the pattern of DSB-2 in *him-13(e1742)* mutants by immunostaining. In wild type germ lines, DSB-2 appears at the onset of TZ, being stronger at early pachytene and disappearing at mid-pachytene (Rosu et al., 2013). The same pattern was observed in the wild type control germ lines (figure 26), while in the *him-13* mutant germ lines, DSB-2 signal was slightly more extended than in the wild type, suggesting that the competence for DSB formation was prolonged in *him-13* mutants. This extension of DSB-2 activity could be one of the reasons why CO distribution is altered in the *him-13* mutants. These observations also suggest that early steps of recombination may be compromised in *him-13* mutants, as extension of the zone of DSB-2 activity reflects the activity of a monitoring mechanism that regulates exit from a DSB-competent stage (Rosu et al., 2013; Stamper et al., 2013).

5.2.1.2 RAD-51 foci disappearance is delayed in *him-13* mutants

In order to further investigate whether meiotic recombination is affected in *him-13* mutants, as suggested by the DSB-2 extension, I decided to study the progression of recombination intermediates by analysing the distribution of RAD-51 foci along the germ line (Alpi et al., 2003; Colaiácovo et al., 2003). Following the resection of DSBs previously generated by SPO-11, RAD-51 molecules bind to single stranded DNA to begin homologous repair. These RAD-51 molecules can normally be visualised as chromosome-associated foci in the *C. elegans* germ line. In wild type germ lines, RAD-51 foci start to appear in transition zone nuclei (leptotene-zygotene stage) and peak between early pachytene and mid-pachytene before gradually disappearing by the end of pachytene (Alpi et al., 2003) (figure 27). In *him-13* mutant germ lines, overall RAD-51 numbers seemed to be reduced in comparison to wild-type controls, with the appearance and disappearance of RAD-51 foci in mutants delayed compared to wild-type controls. To analyse RAD-51 foci dynamics germ lines were divided in 7 equal-size regions including nuclei between the tip of the germ line (mitotic nuclei, zones 1 and 2), and late pachytene (zone 7). Whereas RAD-51 foci started to appear at zone 3 (17.3 % of total RAD-51 foci within the germ line) (transition zone), peaked in zone 4 (49.9 %) (early pachytene) and had largely disappeared by zone 6 (8.1 %) of wild-type controls, in *him-13* mutants, RAD-51 foci appeared in zone 4 (23.6 %), peaked at zone 5 (38 %)

and they remained high in zone 6 (23.8 %), disappearing in zone 7 (10.2 %) (figure 28C). Hence, although recombination intermediates are successfully repaired, RAD-51 intermediates are prolonged in *him-13* mutants, suggesting that proper MEI-2 activity is required to maintain recombination intermediate numbers and timely repair of meiotic DSBs.

5.2.2 Early prophase stages are extended in *him-13* mutants

After discovering that RAD-51 foci were delayed in *him-13*, I wondered whether other earlier stages of meiosis, such as homology search or synapsis were also affected. To do this, I first monitored homology search and chromosome movement by analysing PLK-2 presence by immunostaining. PLK-2 (Polo like kinase 2) associates with PC-binding proteins that are phosphorylated by CHK-2, thereby creating a Polo docking motif that promotes the formation of SUN-1/ZYG-12 aggregates on the nuclear envelope regions where PCs are located, ultimately promoting chromosome movement and consequently, pairing and synapsis (Harper et al., 2011; Penkner et al., 2009; Sato et al., 2009). ZYG-12 is a transmembrane KASH protein (Starr and Han, 2002) that interacts with cytoplasmic dynein (Malone et al., 2003), connecting meiotic chromosomes with the microtubule network, thus allowing chromosome movement generated by cytoskeletal forces located outside the nucleus (Sato et al., 2009). The presence of PLK-2 aggregates was extended in *him-13* mutant germ lines in comparison with wild-type controls (48.18% and 28.54% respectively), suggesting that *him-13* mutants undergo delayed meiotic progression during early prophase (figure 29 and 30C). This result suggests that meiotic nuclei in *him-13* mutants spend more time in leptotene-zygotene stages characterised by active chromosome movement and DSB formation.

Given that PLK-2 is activated and phosphorylated by CHK-2 kinase, I wondered if other CHK-2 targets were equally affected in the *him-13* mutant. As mentioned above, CHK-2 participates in several meiotic events such as chromosome pairing, synapsis, and meiotic recombination (MacQueen and Villeneuve, 2001). CHK-2 phosphorylates HIM-8 on threonine 64 residue along with other ZIM proteins during early meiotic prophase to promote PLK-2 recruitment (Kim et al., 2015). HIM-3 phosphorylation on serine 13 was discovered in our laboratory by Sarai Pacheco-Pinol in a phosphoproteomic experiment

comparing wild types, *chk-2* mutants and *syp-2* mutants, in which a failure in SC assembly triggers a dramatic extension of the zone of CHK-2 activity. In order to monitor CHK-2 activity by immunostaining, I used two phosphor-specific antibodies against each HIM-3 pS13 and HIM-8 pT64 (figure 31). The percentage of nuclei positive for HIM-3^{S13P} signal was extended in *him-13* germ lines in comparison with wild-type controls (66.47 % and 33.53 % respectively) (figure 32B), as was also the case for HIM-8^{T64P} signal (43.96 % and 21.76% respectively) (figure 32C). Taken together, these results suggest that meiotic nuclei in *him-13* mutants spend more time at early meiotic stages characterized by active DSB formation and chromosome movement, which could potentially end up affecting the pattern of CO distribution. It has been described that in situations where CO designation is delayed, a feedback mechanism extends the leptotene/zygotene stage, promoting new DSBs by CHK-2 when one of more chromosome pair fails to form a CO-fated intermediate (Kim et al., 2015; Stamper et al., 2013).

5.2.3 Synaptonemal complex and remodelling are not affected in *him-13* mutants

Considering that recombination timing and early stages of prophase were altered in *him-13* mutants, I wondered whether the *him-13(e1742)* mutation was also affected synapsis. To assess synapsis in *him-13* mutants, I did a double immunostaining of two SC proteins, HTP-1 and SYP-1 (figure 33B). HTP-1 is a component of the axial elements of meiotic chromosomes (Martinez-Perez and Villeneuve, 2005), whereas SYP-1 is a component of the central elements (MacQueen et al., 2002). Both proteins colocalized at mid pachytene, suggesting that synapsis was normal in *him-13* mutants (figure 33A).

After visualising synapsis during pachytene, I decided to check whether *him-13* mutants had problems in chromosome remodelling triggered by CO formation. SC disassembly occurs in an asymmetric fashion in *C. elegans*: central elements like SYP-1 are removed between the CO site and furthest telomere, a region that will become the long arm of diakinesis bivalents and in which sister chromatid cohesion will be protected during the first meiotic division, while HTP-1 is retained in these regions, displaying are reciprocal staining pattern with SYP-1 (De Carvalho et al., 2008; Martinez-Perez et al., 2008). This process starts in late pachytene and culminates with the formation of asymmetrical diakinesis bivalents in which the short and long arms contain different SC proteins. There

were no obvious differences in chromosome remodelling between wild type and *him-13* mutant diakinesis oocytes (figure 33C), suggesting that *him-13* mutants do not have problems in either synapsis or chromosome remodelling. This is result was somewhat surprising as the presence of cruciform diakinesis bivalents (in which the "long" and "short" arms cannot be differentiated due to the symmetric shape of these bivalents) that are sometimes observed in *him-13* mutants could have been caused by problems in chromosome remodelling.

5.2.4 Microtubule architecture seems to be normal in *him-13* mutants

Considering that my results indicated that a mutation in katanin was causing an extension of leptotene-zygotene stages and a delay in DSB processing, I hypothesized that these defects could be instigated by changes in the microtubule network outside the nucleus, even though katanin has not been described to have any role in early meiosis (Joly et al., 2016; Mains et al., 1990; Srayko et al., 2000). Microtubule dynamics have been shown to have an essential role during early meiotic stages, participating in the formation of SUN-1/ZYG-12 clusters, pairing, and synapsis (Sato et al., 2009). When colchicine, a microtubule polymerization inhibitor, is microinjected into the germ line, these processes are affected (Sato et al., 2009), showing how fundamental microtubule dynamics are. At the same time, ZYG-12 is crucial to bring dynein to the SUN-1/ZYG-12 clusters, promoting a proper microtubule architecture and organising the nuclei within the syncytium (Zhou et al., 2009). Given that my results showed that katanin could potentially participate in early stages of meiosis, I hypothesised a defect in microtubule severing could alter the microtubule network required for chromosome movement during leptotene and zygotene. To evaluate this hypothesis, I crossed the *him-13* mutant with a strain carrying an *α-tubulin::GFP* transgene, creating a strain homozygous for both *him-13(e1742)* and this transgene. Afterwards, I did an immunostaining using this new *him-13* strain and the strain carrying the *α-tubulin::GFP* transgene as a wild type control. Surprisingly, no obvious differences were observed between the *him-13* mutant and the wild type control (figure 34). However, there were several reasons that could explain why *him-13* mutants did not show obvious defects in microtubule organisation. One possibility would be that these images did not have enough resolution to resolve this

structure or that the staining protocol that I used did not work well enough to visualise any difference. Further experiments need to be performed to determine whether the microtubule network associated with early prophase nuclei is affected in *him-13* mutants.

5.3 Characterisation of *mei-2::degron* and *mei-2^{E131K}* CRISPR strains

The original strain carrying the *him-13(e1742)* mutation also contained additional mutations within the genetic interval defined by *dpy-5* and *unc-13*. Because of the complementation experiments, I already knew that the *e1742* allele generated a E131K substitution in MEI-2 that was responsible for the high embryo lethality and high incidence of males observed in *him-13* mutants. However, I could not exclude the possibility that the non-discarded mutations could be contributing to other *him-13* phenotypes, such as the alteration in CO patterns or the extension in meiotic early stages. To reject this possibility, I created two strains by CRISPR/Cas9 method (see materials and methods).

First, I generated a mei-2^{E131K} mutation by CRISPR strain to replicate the *him-13(e1742)* mutation within the wild type strain. This mutation is referred to as *mei-2(fq37[E131K]).* As mentioned in chapter 4, this mutant had high embryo lethality and high incidence of males as expected. To assess whether homology search and chromosome movement were also extended in this mutant, PLK-2 presence was analysed by immunostaining. PLK-2 aggregates were extended in *mei-2(fq37[E131K])* germ lines in comparison with wild type germ lines (45.88% and 35.23% respectively), suggesting that *mei-2(fq37[E131K])* has a delay in early meiotic progression (figure 35A). This result suggests that *mei-2(fq37[E131K])* has the same phenotype than the original *him-13* strain, implying *him-13(e1742)* mutation in *mei-2* katanin can extend early meiotic progression stages by itself.

Second, to evaluate whether the effect of not having any MEI-2 protein had the same effect than carrying the *him-13(e1742)* mutation, a *mei-2::degron* strain was created by CRISPR/Cas9 system (Paix et al., 2016) . This was achieved by using the auxin-inducible degradation (AID) system, which has been demonstrated to work in *C. elegans* (Zhang

et al., 2015). In this system, TIR1, a F-box protein from plants (Kepinski and Leyser, 2005), is expressed together with the gene of interest carrying a degron sequence. TIR1 protein recognises E3, a subunit of Skp1-Cullin-F-box (SCF) ubiquitin ligase complex, and it only recognises the degron tail of the protein of interest in the presence of auxin (indole-3-acetic acid, or IAA), leading to its degradation by the proteasome (Tan et al., 2007). A strain carrying the $P_{sun\text{-}1}$*::TIR1::mcherry*, which expresses TIR-1 in the germ line was microinjected to introduce the degron sequence in the C-terminus of the endogenous *mei-2* gene by CRISPR/Cas9 system.

Once the double homozygous for TIR1 and *mei-2::degron* was isolated, I observed that this strain looked completely wild type, not showing any meiotic defect. However, when worms were grown in the presence of auxin, they showed 100% of embryo lethality in their progeny as expected from a *mei-2* knockout mutant (due to defects in the meiotic divisions), indicating that the degron system worked well to deplete MEI-2. The next step was to evaluate whether chromosome movement and homology search were also extended in the absence of the MEI-2 protein by studying PLK-2 presence by immunostaining. PLK-2 aggregates were extended in *mei-2::degron* germ lines in the presence of auxin (4 mM) compared with mei-2:: degron control germ lines (49.42% and 34.51% respectively) (figure 35B). This result suggests that absence of MEI-2 protein extends early stages of meiosis, being comparable to what occurs in the *him-13* mutant and the *mei-2*^{E131K} CRISPR mutant.

5.4 Verification of CO distribution is altered in *him-13* mutants

Although previous experiments in our laboratory had suggested that *him-13* mutants had an alteration in CO distribution on chromosome III, these experiments were not conclusive because of the insufficient number of samples. To have a better understanding of how CO distribution was behaving in *him-13* mutants, I decided to perform additional genetic CO mapping experiments. To perform this experiment, a Hawaiian strain of *C. elegans* was used because it carries a large number of SNPs compared to the Bristolian (N2) strain that is conventionally used as the reference wild-type strain (Hillers and Villeneuve, 2003; Lim et al., 2008). *him-13* mutant males were crossed with Hawaiian hermaphrodites several times, until I created a strain which had

the *him-13* phenotype and was homozygous for all the Hawaiian SNPs for the chosen chromosome (Chr. III).

To perform this experiment, homozygous Bristolian *him-13* mutants were crossed with homozygous Hawaiian (chromosome III) *him-13* mutants, and the resulting F_1 progeny, homozygous for the *him-13* mutation and heterozygous for the Hawaiian and Bristolian SNPs on chromosome III, was crossed again with Hawaiian males. Then, F_2 L4 hermaphrodites from this cross were picked to individual plates and they were left to produce F_3 progeny until starvation. Then, the DNA was extracted from the whole plates, as genotyping of the SNPs present in the F_3-F_4 population is representative of the genotype of the single F_2 hermaphrodite used to start each plate (figure 36). Simultaneously, the same experiment was performed with the Bristolian and Hawaiian wild type strains as control. This experiment allowed me to map COs that occurred between Hawaiian and Bristolian markers on chromosome III during oocyte meiosis in F_1 hermaphrodites.

COs position was mapped by checking six SNPs of known physical position that were spread along chromosome III, defining 5 genetic intervals, using the PyroMark Q48 Autoprep (see Materials and Methods). The physical and genetic distance of these SNPs are shown in figure 37A. To determine where a CO was made, a genotypic change between two SNPs must be detected, for example, from N2 (Bristolian strain) to N2/HW (Bristolian/Hawaiian) or vice versa. CO distribution was shifted to the left in *him-13* mutants in comparison with wild type controls, having an increase in CO numbers in the first two intervals, which is where the pairing center is located on chromosome III, whereas there was a reduction in CO numbers in the last two intervals (figure 37D), mirroring the CO distribution previously observed by former members of our laboratory. Chi-squared test was performed to compare *him-13* mutant frequencies against wild type frequencies (figure 37D), showing that both CO distributions were statistically different (0.0012, Chi-square test). Expected COs frequencies were also calculated using the genetic distance between the different SNPs, and Chi-squared tests were also performed to compare the expected CO distribution against both *him-13* and wild type distributions (figure 37B and C). Unexpectedly, the expected CO distribution and the wild type CO distributions were statistically different (Chi-square test, 0.025) (figure

37B), whereas the expected CO distribution and the *him-13* CO distribution were the same (Chi-squared, 0.104) (figure 37C). No double COs were observed in either wild type or *him-13* mutants, suggesting that interference was not affected in *him-13* mutants.

5.5 Studying CO distribution by three-dimensional tracking of chromosomes

After validating that CO distribution was shifted towards the pairing center in *him-13* mutants, I wondered whether the same phenotype was present in *mei-2(fq37[E131K])* mutant and whether depletion of MEI-2 using the auxin degron system will have the same effect. However, to do a genetic mapping experiment with the *mei-2::degron* strain was not possible, considering that once this strain is given auxin, no MEI-2 protein is available, and thus fails to complete meiotic divisions. Furthermore, each genetic mapping experiment was time-consuming. Because of this, I decided to develop a new method to measure CO distribution combining 3D visualisation of nuclei and Super Resolution Microscopy (SRM), as described in chapter 3.

5.5.1 CO distribution is shifted towards the pairing center on Chr. X in *him-13* and *mei-2^{E131K}* mutants

To investigate whether CO distribution was also altered in *mei-2(fq37[E131K])*, the microscopy method described in chapter 3 was used. First, I crossed the strain carrying the *cosa-1::HA* CRISPR marker with the *him-13(e1742)* mutant and *mei-2(fq37[E131K])*. After this, these three strains were used for a triple immunostaining using αHIM-8, αHA and αHTP-3 antibodies together with DAPI. All images these were acquired using a Zeiss ELYRA S1 SIM microscope. Then, the SIM stacks were processed with Imaris, tracking at least 180 chromosomes per genotype, mapping the relative physical position of the CO (COSA-1 focus) within the X chromosome and dividing the total length of each chromosome into four equal-size intervals. The expected CO distribution for the wild type was calculated by choosing physical positions that divided the X chromosome into four equal-size intervals and obtaining the respective genetic distances from Wormbase (figure 38A and B). Strikingly, the CO distribution observed from my chromosome tracking approach in wild type nuclei was very similar to the expected CO distribution

derived from Wormbase (figure 38B and C). A Chi-squared test confirmed that these two distributions were the same (0.7109, chi-square test), confirming that this method was valid to quantify CO distribution. The next step was to check whether CO distribution on the X chromosome was affected in *him-13* mutants using this method. As expected, CO distribution was shifted towards the pairing center end of the *him-13(e1742)* mutant X chromosome (figure 38B and D). Finally, CO distribution was also changed in *mei-2(fq37[E131K])* mutants, with the CO distribution also shifted towards the pairing center end (figure 38B and E). However, the *mei-2(fq37[E131K])* and *him-13(e1742)* CO distributions looked quite different between them. To study if these CO distributions were statistically different, Kolmogorov-Smirnov tests were performed between *him-13(e1742)*, *mei-2(fq37[E131K])* and WT distributions, resulting in all distributions being different from each other (figure 38F, G and H). The reason why CO distribution appear to be different in him-13(e1742) and *mei-2(fq37[E131K])* is not known, but in both cases, there is a clear shift of COs towards the left of the chromosome. Repeating these experiments with higher numbers of tracked nuclei will help to clarify this aspect.

5.5.2 CO distribution is also affected following MEI-2 depletion with the auxin degron

Following the discovery that *mei-2(fq37[E131K])* mutants show a shift of COs towards the pairing center on the X chromosome, I wondered whether in a situation where no MEI-2 protein was available, this would affect the location of COs. To address this question, I crossed the *cosa-1::HA* strain with the *mei-2::degron* strain and then, I did a triple immunostaining using αHIM-8, αHA and αHTP-3 antibodies together with DAPI. To perform this staining, I synchronised *C. elegans* larvae by bleaching adult worms, which kills and dissolve adults but does not affect developing embryos inside the eggs, and the eggs obtained in this step were placed in plates with 4mM of auxin or without auxin and let to grow until young adults. This protocol is expected to induce strong depletion of MEI-2 in the germ line, as worms are grown in the presence of auxin before germ line development starts. As a result of this treatment, all the embryos coming from these auxin plates were dead, indicating that the degron system was properly working. Stained germ lines from these worms were acquired with the Zeiss ELYRA S1. SIM images were processed using Imaris and at least 190 chromosomes were tracked for each

condition, to obtain the relative position of each CO within the chromosome and the expected CO distribution was calculated using the genetic distances from Wormbase. Chi-squared test confirmed that the expected CO distribution and the *mei-2::degron* without auxin CO distribution were statistically similar (0.129, chi-squared test) (figure 39A), confirming that the degron tag in MEI-2 protein was not affecting CO distribution. The next step was to check whether CO distribution on Chr. X was also affected when there was no MEI-2 protein left. Interestingly, CO distribution was shifted towards the pairing center in *mei-2::degron* worms treated with auxin, suggesting that the effect of losing the protein is similar to *him-13(e1742)* mutation. This CO distribution was statistically different from the predicted CO distribution (0.000083, chi-squared test) (figure 39B). To study if both *mei-2::degron* with and without auxin treatment had statistically different CO distributions, a Kolmogorov-Smirnov test was performed (0.02, Kolmogorov-Smirnov test), being the distribution different from each other (figure 39C and D). These results confirmed that the depletion of MEI-2 protein, and therefore katanin, affected CO distribution on Chr. X. These results suggest that katanin plays a role in balancing CO distribution towards both ends.

5.5.3 MEI-2 depletion does not affect CO interference

After confirming that both *mei-2(fq37[E131K])* mutants and auxin-mediated depletion of MEI-2 protein display altered CO distribution, I wondered if katanin could be altering CO distribution by affecting CO interference. *C. elegans* displays "complete" CO interference, making a single CO per homolog pair per meiosis (Hillers and Villeneuve, 2003). However, several studies have described mutants with defects in CO distribution that also had problems with CO interference. For instance, RTEL-1 promotes NCO formation by disassembling D-loop intermediates during recombination and encouraging SDSA (Barber et al., 2008). *rtel-1* mutants have been shown to have an altered CO distribution and interference, showing more than one CO per homolog (Youds et al., 2010). Another mutant in which both CO distribution and interference are affected is *dpy-28* mutant. DPY-28 is a subunit of the condensin I complexes, which controls CO number and distribution by changing DSB distribution (Mets and Meyer, 2009; Tsai et al., 2008). Given that mutants in *mei-2* had defects in CO distribution, I

thought that it would be possible that these mutants could also have problems in CO interference. However, no double COs were observed in the previous genetic mapping experiments or in the imaging mapping experiments, suggesting that CO interference was not affected. Because of *C. elegans* displays complete interference, it would be possible that a slight defect in interference will not result in a dramatic increase in double COs and therefore may be difficult to identify due to the limited number meiosis analysed in CO mapping experiments. To test this hypothesis, I crossed the *cosa-1::HA*, *mei-2::degron,* $P_{sun\text{-}1}$*::TIR1::mcherry* strain with a strain carrying an end-to-end fusion of chromosomes X and IV (*mnT12* chromosome) (Hillers and Villeneuve, 2003) (figure 40A). Worms containing this chromosome fusion are healthy and viable as *C. elegans* chromosomes are holocentric, lacking localised centromeres. Strikingly, the fused *mnt12* chromosome displays a single CO in most meiosis, demonstrating that interference in *C. elegans* regulates CO distribution over very large physical distances (Hillers and Villeneuve, 2003). Then, these worms were grown with 4mM of auxin and without auxin, to be dissected when they were young adults. Afterwards, a triple immunostaining was performed using αHIM-8, αHA and αHTP-3 antibodies together with DAPI. Pachytene nuclei were imaged with the Zeiss ELYRA S1 microscope and SIM images were processed with Imaris, tracking at least 89 chromosomes for each condition and measuring the relative position of the CO or COs within the chromosome. The percentage of double CO on *mnT12* chromosomes was unaffected in treated *mei-2::degron* germ lines in comparison with untreated ones (20.51% and 19.09% respectively) (figure 40B). Although not statistically significant (0.053, Kolmogorov-Smirnov), there was a tendency indicating that single CO distributions of treated and untreated germ could be different (figure 40C and D). Instead, double CO distributions of treated and untreated germ lines were statistically the same (0.968, Kolmogorov-Smirnov) (figure 40E and F). These results indicate that, although CO interference is not affected in depleted MEI-2 germ lines, the distribution of the single COs is different but, at the same time, the distribution of double COs is the same.

5.6 Summary of results

In this chapter, I have demonstrated that early prophase stages are affected in *him-13(e1742)* mutants. First, DSB-2 extension suggested that the period when SPO-11 can make DSBs was extended in *him-13(e1742)* mutants. This hypothesis is also reinforced by the fact that RAD-51 foci are delayed in *him-13(e1742)* mutants, suggesting that DSB formation or their initial processing may be delayed and that a subset of late-generated DSBs could have a different position in comparison with the DSBs generated during leptotene-pachytene. Both results supported the idea that the reason behind the alteration in CO distribution would be difficulties in CO formation or DSB location. Since recombination starts at the onset of meiosis, I studied other early meiosis stages to check whether they were also affected. Homology search and chromosome movement were assessed by analysing PLK-2 presence, which was extended in *him-13(e1742)* mutants. This result also suggested that early meiosis stages are delayed in *him-13(e1742)* mutants. Importantly, this delay in exiting early prophase was also observed in *mei-2(fq37[E131K])* mutants and in auxin treated *mei-2::degron* germ lines. Since PLK-2 recruitment to PCs requires CHK-2, direct targets of CHK-2 were investigated by using phospho-specific antibodies against HIM-3 pS13 and HIM-8 pT64. In both cases staining was extended in *him-13(e1742)* mutant germ lines, confirming delayed meiotic progression. I detected no obvious defects in either synapsis or chromosome remodelling in *him-13(e1742) mutants*. Furthermore, since the *him-13(e1742)* mutation affects mei-2 gene and thereby katanin, I thought that it would be plausible that microtubule network could be affected. However, no obvious defects in microtubule organization were observed in the *him-13(e1742)* mutants. Further research needs to be conducted to clarify if the microtubule network present in early meiotic prophase nuclei is affected when Katanin function is compromised.

To corroborate that MEI-2 has an effect on CO distribution, I performed different CO mapping experiments. First, genetic mapping of CO distribution confirmed that *him-13(e1742)* mutants display alter CO distribution on chromosome III. Afterwards, I developed a new method to map COs using SIM images and Imaris software. This new tool allowed me to study CO distribution in wild type, *mei-2(fq37[E131K])*, and *him-13(e1742)* mutants, corroborating that CO distributions are different among them.

Outstandingly, the predicted CO distribution and wild type CO distribution were statistically the same, indicating that this new method can be used for CO mapping in three-dimensional intact meiotic nuclei. Given that auxin-mediated depletion of MEI-2 also induced delayed exit from early prophase stages, I wondered if depleting MEI-2 could also cause a variation in CO distribution, which I confirmed using the SIM method of CO mapping. Moreover, I also investigated a potential effect of MEI-2 in CO interference by combining the MEI-2::degron system with the *mnT12* fusion chromosome. This analysis evidenced no defects in CO interference following MEI-2 depletion. In summary, results from this chapter suggest that MEI-2 regulates CO distribution, most likely by affecting an early meiotic prophase event, but does not affect CO interference.

Figure 26. DSB-2 staining in the wild type and *him-13* mutant

Whole mounted germ lines from wild type and *him-13* mutants stained with αDSB-2 and DAPI. Upper part shows DAPI staining for wild type germline (top left) and *him-13* germ line (top right). Lower part shows αDSB-2 staining for wild type germ line (bottom left) and *him-13* germ line (bottom right).

Wild Type
him-13(e1742)
Transition Zone
Early Pachytene
Mid Pachytene
Late Pachytene
Transition Zone
Early Pachytene
Mid Pachytene
Late Pachytene
DAPI
αDSB-2

Figure 27. RAD-51 staining in the wild type and *him-13* mutant

Whole mounted germ lines from wild type and *him-13* mutants stained with αRAD-51 and DAPI. Upper part shows DAPI staining for wild type germline (top left) and *him-13* germ line (top right). Lower part shows αRAD-51 staining for wild type germ line (bottom left) and *him-13* germ line (bottom right).

him-13(e1742)
Wild Type
DAPI
αRAD-51

Figure 28. RAD-51 recombination intermediates are delayed in him-13 mutants

A - Projections from transition zone and late pachytene nuclei of indicated genotypes and stained with anti-RAD-51 antibodies and DAPI. RAD-51 foci can be observed at late pachytene in him-13 mutants, whereas in wild type controls these RAD-51 foci are reduced.

B – Diagram of RAD-51 quantification showing how germ lines were equally divided with regions 4 to 7 representing early to late pachytene.

C - Quantification of RAD-51 foci in him-13 and wild type germ lines. Each germ line was divided into 7 equal zones, from the mitotic tip to late pachytene. The Y axis indicates the percentage of nuclei with a given number of RAD-51 foci (this is indicated in the colour key), whereas the X axis indicates the 7 different zones. The tables below the graphs represents the percentage of the total RAD-51 foci within the germ line in each zone. For the quantification, 4 wild type and 5 *him-13* germ lines were used.

A

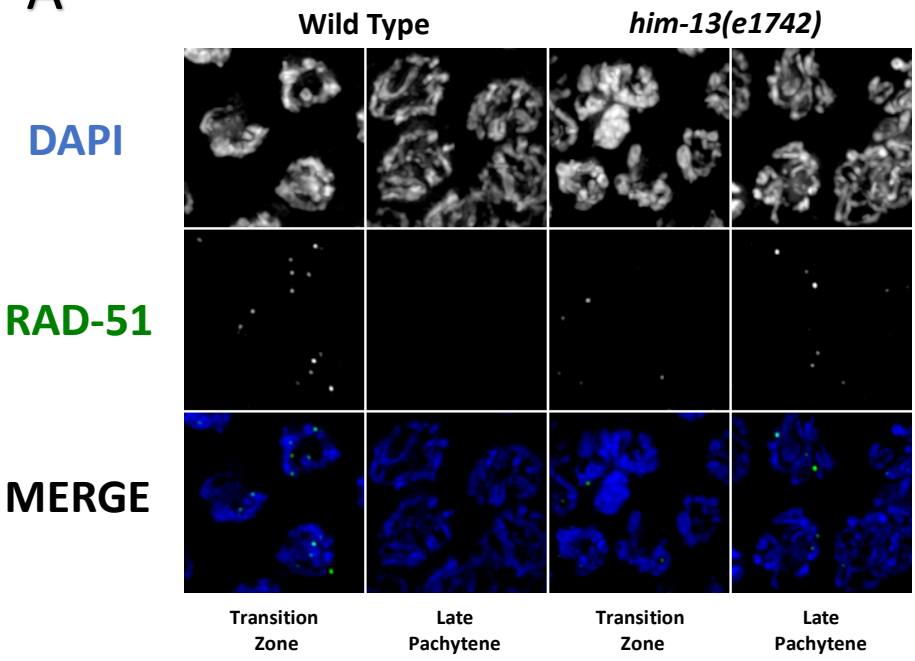

B

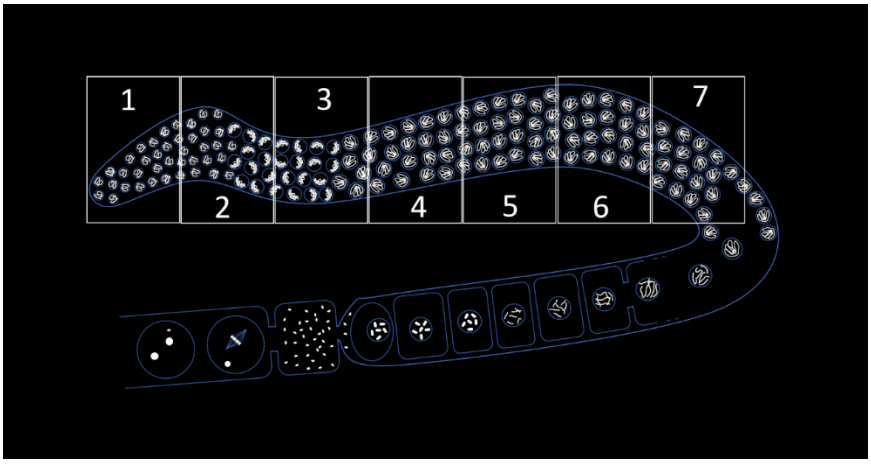

C

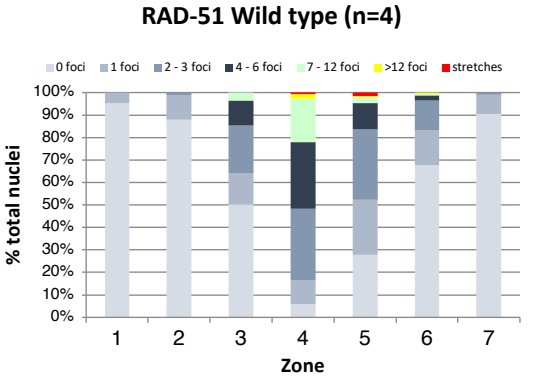

Zone	1	2	3	4	5	6	7
Total RAD-51 foci (%)	0.5	1.5	17.3	49.9	21.3	8.1	1.2

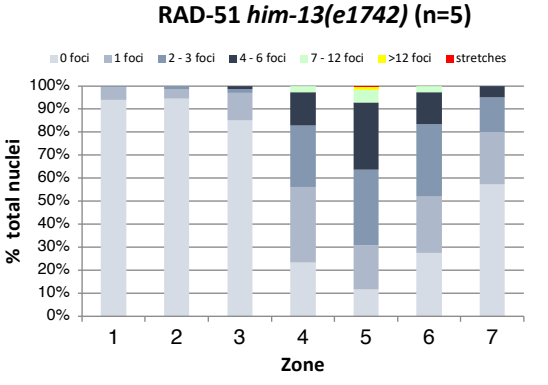

Zone	1	2	3	4	5	6	7
Total RAD-51 foci (%)	0.8	0.9	2.7	23.6	38	23.8	10.2

Figure 29. PLK-2 staining in the wild type and *him-13* mutant

Whole mounted germ lines from wild type and *him-13* mutants stained with αPLK-2 and DAPI. Upper part shows DAPI staining for wild type germline (top left) and *him-13* germ line (top right). Lower part shows αPLK-2 staining for wild type germ line (bottom left) and *him-13* germ line (bottom right).

him-13(e1742)
Wild type
DAPI
αPLK-2

Figure 30. Delayed exit from early meiotic prophase stages in *him-13* mutants

A - Projection of early pachytene nuclei of *him-13* mutant and wild type control stained with α-PLK-2 and counterstained with DAPI. Scale bars, 5 µm.

B - Diagram of PLK-2 quantification. The total number of rows was obtained by counting from the first row of nuclei containing PLK-2 aggregates, which overlaps with the onset of TZ, until the end of late pachytene. To consider a row as positive, more than 50% of nuclei must have 2 or more PLK-2 aggregates. At least three germ lines were scored per genotype.

C - Quantification of the percentage of nuclei in leptotene-zygotene (transition zone). Extension of transition zone (TZ) was measured by the presence of more than one PLK-2 aggregate. TZ was more extended in *him-13* mutant germ lines compared with wild type germ lines (28.54% and 48.18% respectively) (p= 0.0019, t test).

A

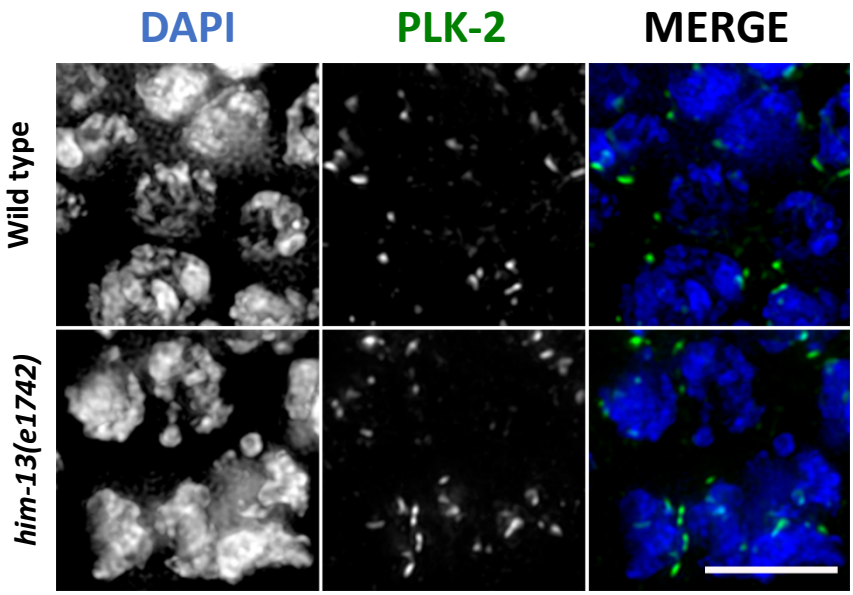
DAPI
PLK-2
MERGE
Wild type
him-13(e1742)

B

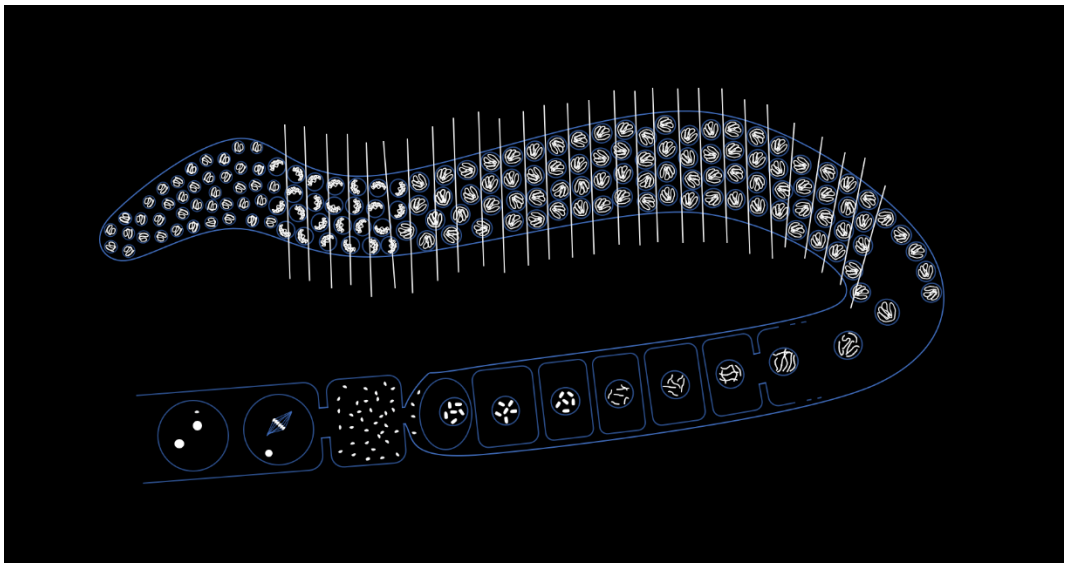

C

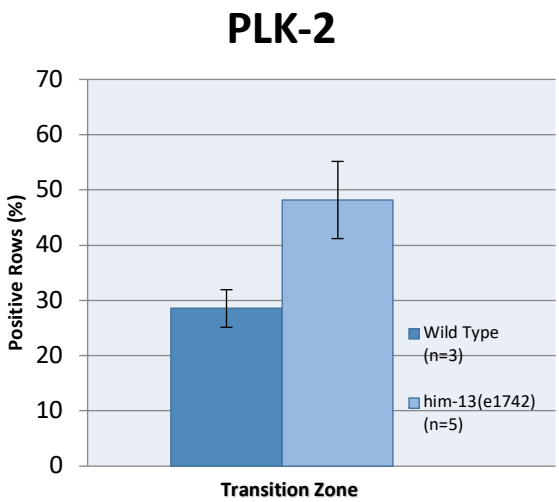
PLK-2
70
60
50
40
30
20
10
0
Positive Rows (%)
Transition Zone
Wild Type (n=3)
him-13(e1742) (n=5)

Figure 31. HIM-3^{S13P} HIM-8^{T64P} staining in wild type and *him-13* mutants

A - Whole mounted germ lines from wild type and *him-13* mutants stained with αHIM-3^{S13P} and DAPI. Upper part shows DAPI staining for wild type germline (top left) and *him-13* germ line (top right). Lower part shows αHIM-3^{S13P} staining for wild type germ line (bottom left) and *him-13* germ line (bottom right). Scale bar, 5 µm.

B - Whole mounted germ lines from wild type and *him-13* mutants stained with αHIM-8^{T64P} and DAPI. Upper part shows DAPI staining for wild type germline (top left) and *him-13* germ line (top right). Lower part shows αHIM-8^{T64P} staining for wild type germ line (bottom left) and *him-13* germ line (bottom right).

A
Wild Type
him-13(e1742)
DAPI
αHIM-3S13P
B
DAPI
αHIM8T64P

Figure 32. CHK-2 readouts are extended in *him-13* mutants

A - Diagram of HIM-3^{S13P} and HIM-8^{T64P} quantification. The total number of rows was obtained by counting from the first row of nuclei showing HIM-3^{S13P} or HIM-8^{T64P} staining. In the case of HIM-3^{S13P}, to consider a row as positive, more than 50% of nuclei must have been stained. In the case of HIM8^{T64P}, similar to PLK-2 quantification, more than 50% of nuclei must have 2 or more HIM-8^{T64P} aggregates in each row to be considered as positive for the marker. At least three germ lines were used for each genotype.

B - Quantification of HIM-3^{S13P} staining in wild type and *him-13* germ lines. CHK-2 activity was measured by the extension of HIM-3^{S13P} presence. HIM-3^{S13P} staining was more extended in the *him-13* germ line compared with the wild type germ line (66.47 % and 33.53 % respectively) (p= 0.0023, t test). Three germ lines were used for each quantification.

C - Quantification of HIM8^{T64P} staining in wild type and *him-13* germ lines. CHK-2 activity was measured by the presence of more than one HIM8^{T64P} aggregates. HIM8^{T64P} staining was more extended in the *him-13* germ line compared with the wild type germ line (43.96 % and 21.76% respectively) (p= 0.0007, t test). At least three germ lines were used for each quantification.

A

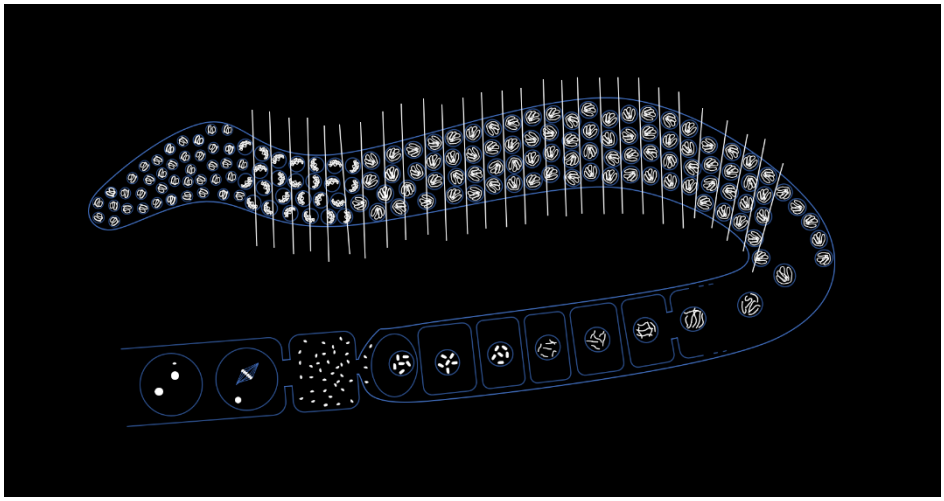

B

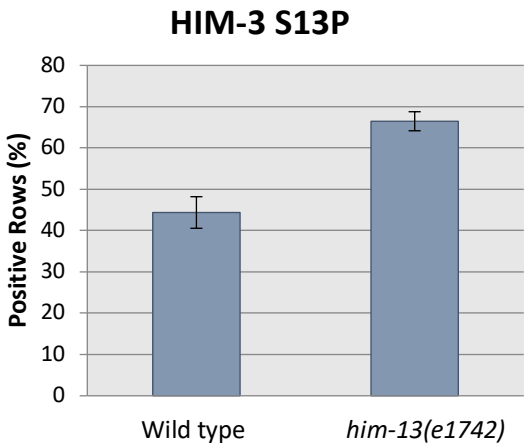
HIM-3 S13P
Positive Rows (%)
80
70
60
50
40
30
20
10
0
Wild type
him-13(e1742)

C

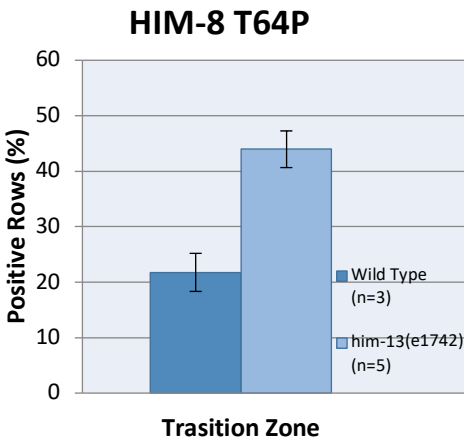
HIM-8 T64P
Positive Rows (%)
60
50
40
30
20
10
0
Wild Type (n=3)
him-13(e1742) (n=5)
Trasition Zone

Figure 33. Characterization of the SC in *him-13* mutants

A- *him-13* mutants do not show any defect in synapsis. Projections from mid pachytene nuclei of wild type and *him-13* mutants stained with α-HTP-1 and α-SYP-1 antibodies and DAPI. Synapsis is normal in *him-13* mutants. Scale bars, 5 mm.

B - Diagram of HTP-1 and SYP-1 localization in the SC. HTP-1 is in green and is located on the axial elements along the meiotic chromosome, whereas SYP-1 is in red and is located between the two axial elements.

C – Remodelling is not affected in *him-13* mutants. Projections from diakinesis nuclei of wild type and *him-13* mutants stained with α-HTP-1 and α-SYP-1 antibodies and DAPI. Remodelling is normal in *him-13* mutants. Scale bars, 5 µm.

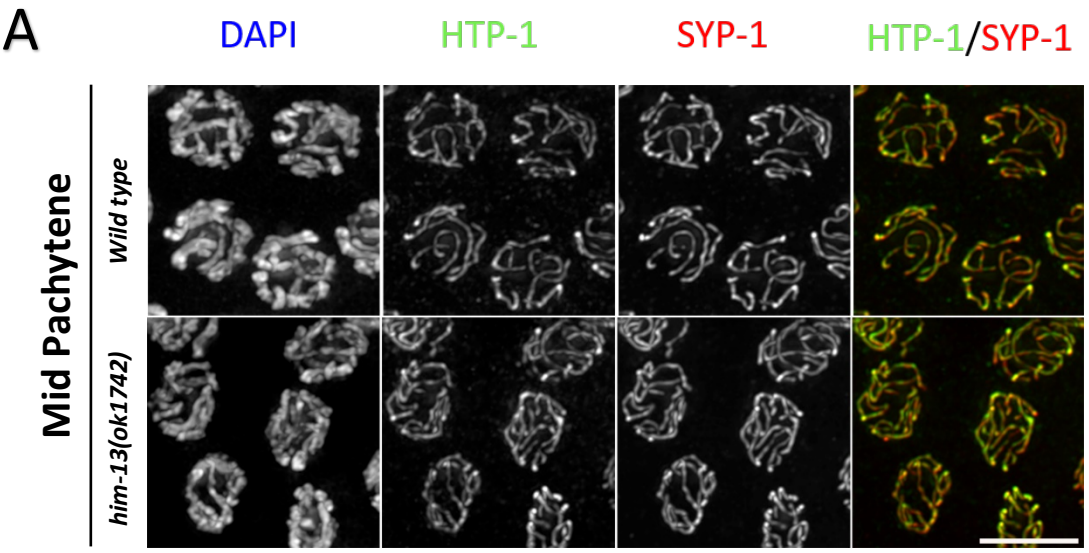
A
DAPI
HTP-1
SYP-1
HTP-1/SYP-1
Mid Pachytene
Wild type
him-13(ok1742)

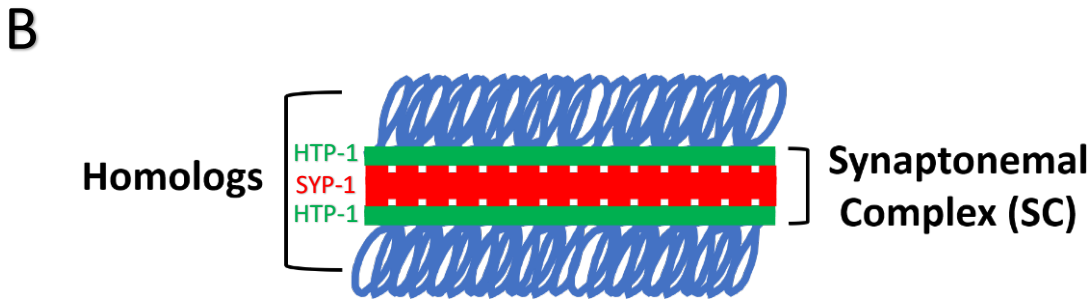
B
Homologs
HTP-1
SYP-1
HTP-1
Synaptonemal
Complex (SC)

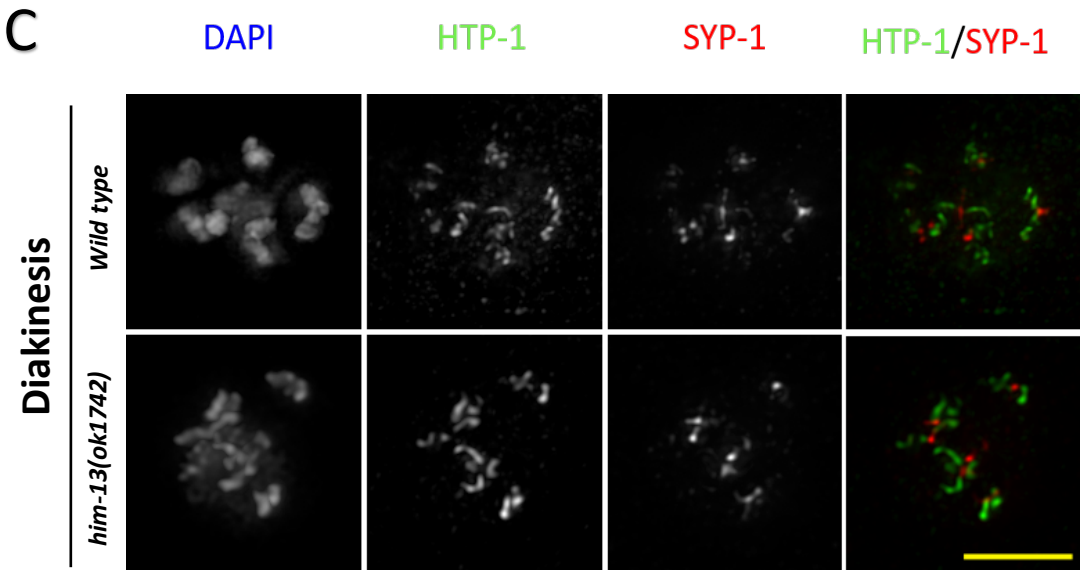
C
DAPI
HTP-1
SYP-1
HTP-1/SYP-1
Diakinesis
Wild type
him-13(ok1742)

Figure 34. Microtubule network appears to be normal in *him-13* mutants

Non-deconvolved projections from TZ, early pachytene and late pachytene nuclei of wild type and *him-13* mutants, expressing both a GFP-α-tubulin transgene and stained with α-GFP primary antibody conjugated with Alexa488 and DAPI. No obvious differences were observed between the *him-13* mutant and the wild type. Scale bars, 5 μm.

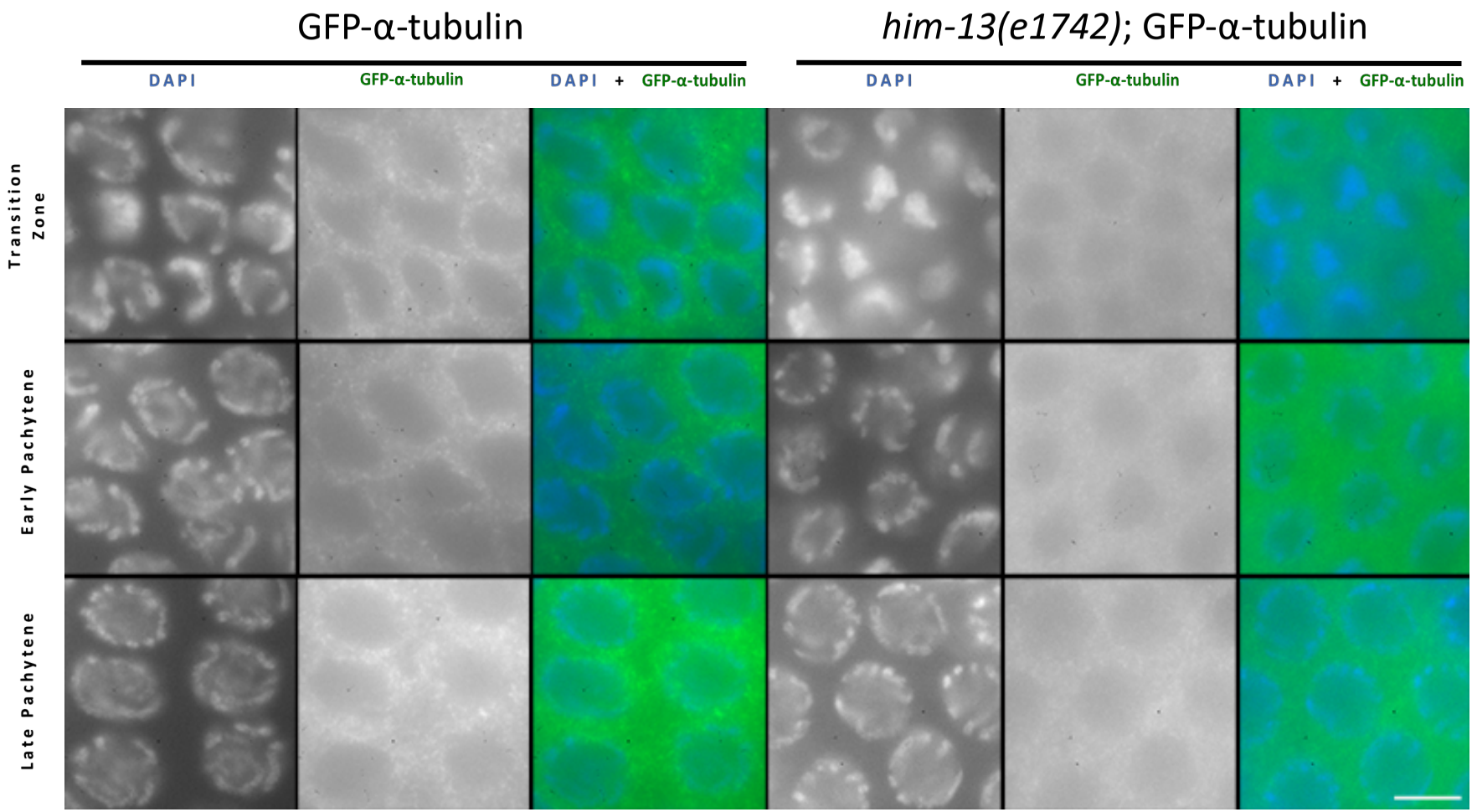
GFP-α-tubulin
him-13(e1742); GFP-α-tubulin
DAPI
GFP-α-tubulin
DAPI + GFP-α-tubulin
DAPI
GFP-α-tubulin
DAPI + GFP-α-tubulin
Transition Zone
Early Pachytene
Late Pachytene

Figure 35. PLK-2 aggregates are extended in *mei-2(fq37[E131K])* mutants and *mei-2::degron* worms treated with auxin

A - Quantification of PLK-2 aggregates in wild type and *mei-2(fq37[E131K])* mutants. Extension of TZ was measured by the presence of more than one PLK-2 aggregate. TZ was more extended in the *mei-2(fq37[E131K])* mutant germ line compared with the wild type germ line (45.88 % and 35.28% respectively) (p= 0.0062, t test). Three germ lines were used for each genotype.

B - Quantification of PLK-2 aggregates in *mei-2::degron* strain . Extension of TZ was measured by the presence of more than one PLK-2 aggregate. TZ was more extended in the germ lines treated with auxin compared with control germ lines (p= 0.0048, t test). Four germ lines were used for each condition.

A

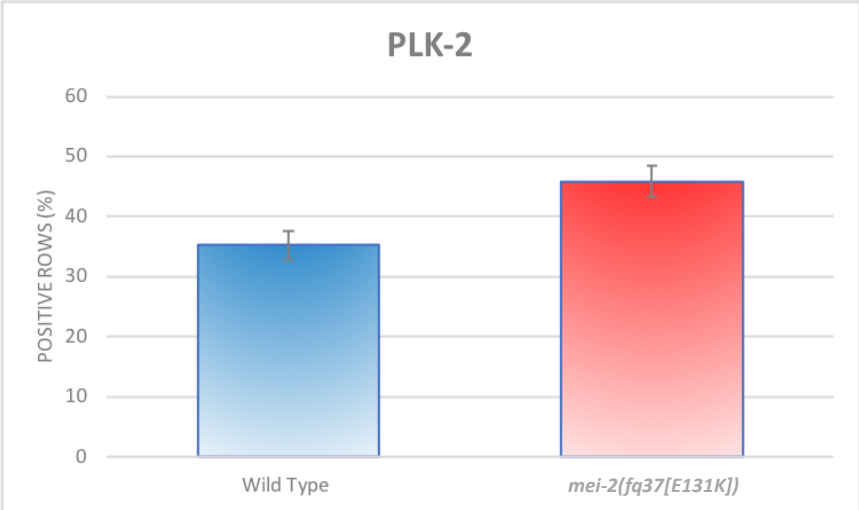
PLK-2
POSITIVE ROWS (%)
60
50
40
30
20
10
0
Wild Type
mei-2(fq37[E131K])

B

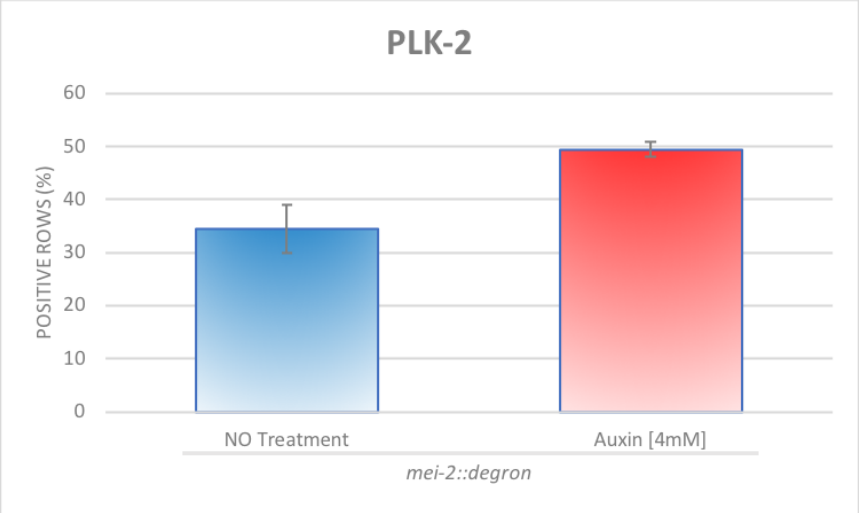
PLK-2
POSITIVE ROWS (%)
60
50
40
30
20
10
0
NO Treatment
Auxin [4mM]
mei-2::degron

Figure 36. Scheme of the CO mapping stages

Red chromosomes contain Hawaiian SNPs, whereas blue chromosomes contain N2 SNPs. *him-13 unc-13* double mutant strain was used to ensure cross progeny. Moreover, the same experiment was repeated using both Hawaiian and N2 wild type strains to obtain the wild type CO distribution.

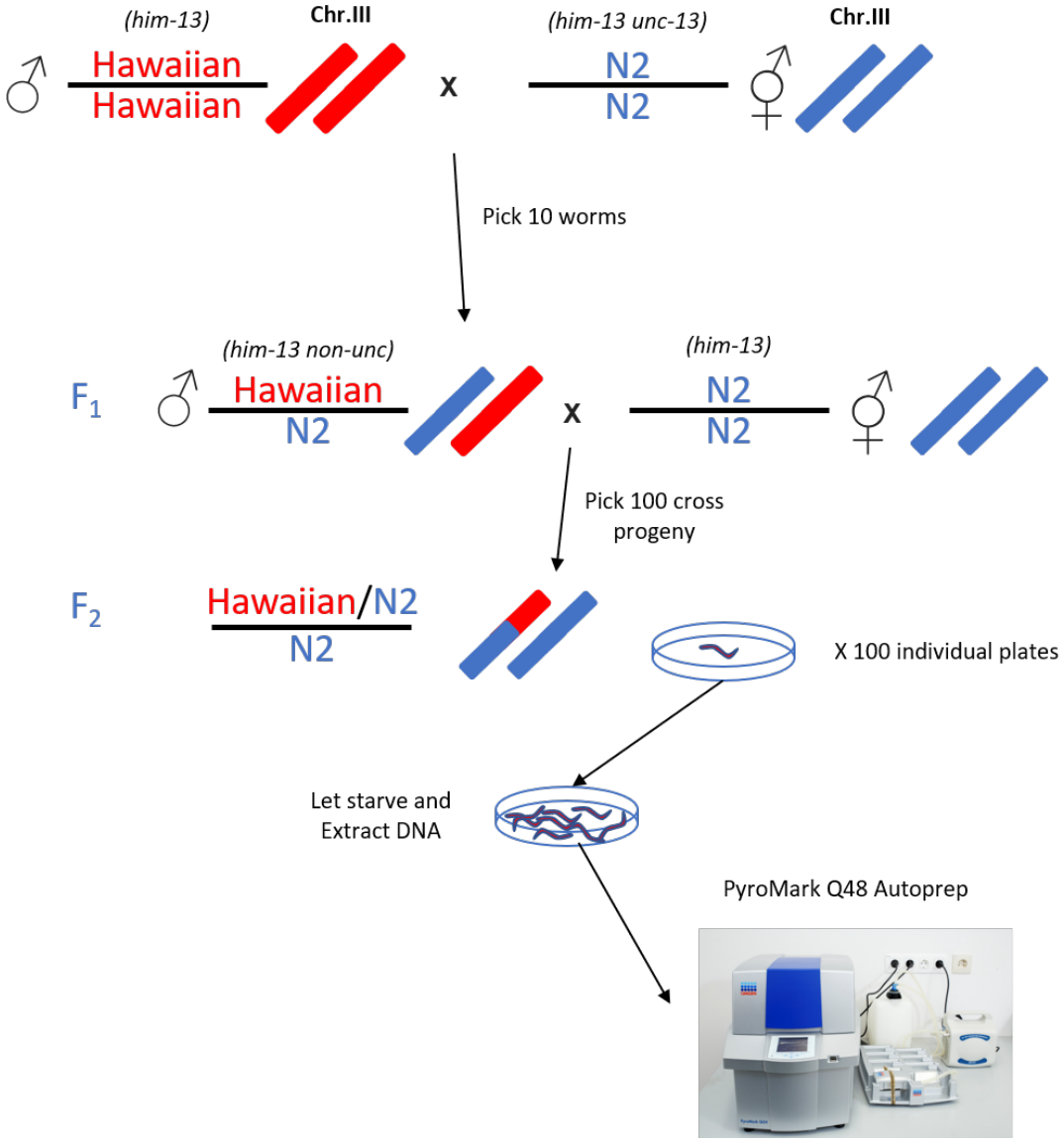
(him-13)
Chr.III
Hawaiian
Hawaiian
x
(him-13 unc-13)
Chr.III
N2
N2
Pick 10 worms
F1
(him-13 non-unc)
Hawaiian
N2
x
(him-13)
N2
N2
Pick 100 cross progeny
F2
Hawaiian/N2
N2
X 100 individual plates
Let starve and Extract DNA
PyroMark Q48 Autoprep

Figure 37. Genetic mapping confirms that CO distribution is altered on Chr. III in *him-13* mutants

A - Genetic and Physical maps of chromosome III, comparing positions of the six SNPs used for the genetic mapping. The six SNPs define the genetic intervals for the mapping experiment, being the first SNP1 located on the genetic left end (*H10E21*) and the sixth SNP6 on the genetic right end (*T28A8*). Genetic positions are given in centimorgans, while physical positions are indicated in megabase pairs.

B - Bar chart representing wild type CO distribution obtained in the genetic mapping, against the expected CO distribution calculated from the genetic intervals on Wormbase. Both distributions were statistically different (0.025, Chi-square test) (n = 36 recombinants).

C - Bar chart representing *him-13* CO distribution obtained in the genetic mapping, against the expected CO distribution calculated from the genetic intervals on Wormbase. Both distributions were statistically the same (0.104, Chi-square test) (n = 37).

D - Bar chart representing *him-13* and wild type CO distributions obtained in the genetic mapping. Both distributions were statistically different (0.0012, Chi-square test).

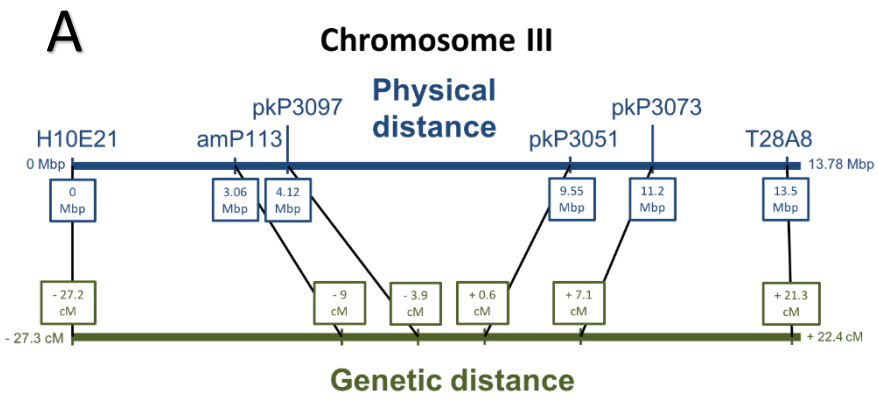
A
Chromosome III
Physical distance
H10E21
pkP3097
amP113
pkP3051
pkP3073
T28A8
0 Mbp
13.78 Mbp
0 Mbp
3.06 Mbp
4.12 Mbp
9.55 Mbp
11.2 Mbp
13.5 Mbp
- 27.2 cM
- 9 cM
- 3.9 cM
+ 0.6 cM
+ 7.1 cM
+ 21.3 cM
- 27.3 cM
+ 22.4 cM
Genetic distance

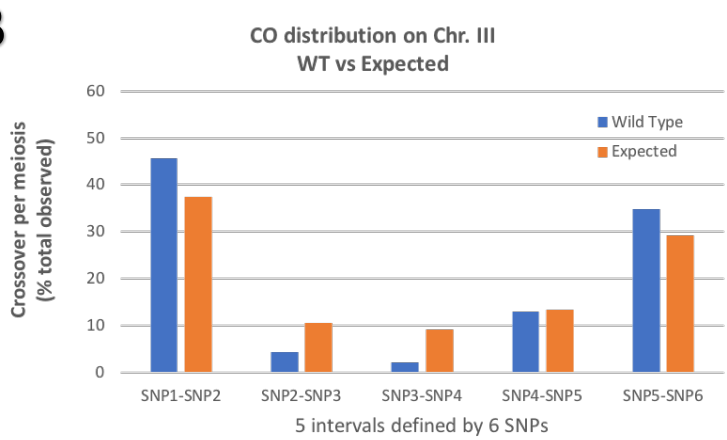
B
CO distribution on Chr. III
WT vs Expected
Crossover per meiosis (% total observed)
Wild Type
Expected
SNP1-SNP2
SNP2-SNP3
SNP3-SNP4
SNP4-SNP5
SNP5-SNP6
5 intervals defined by 6 SNPs

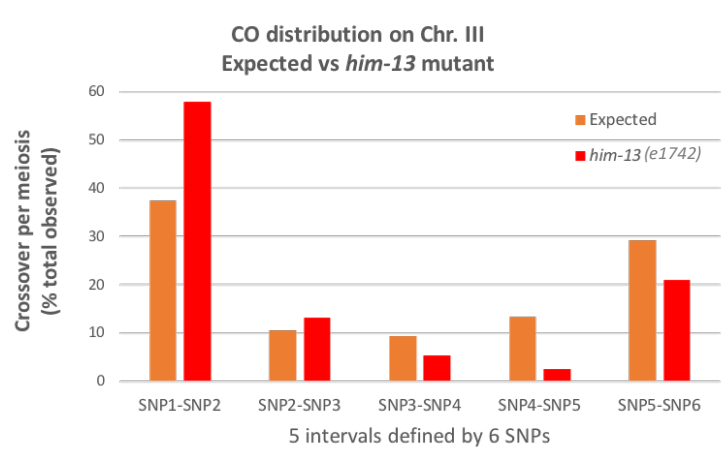
C
CO distribution on Chr. III
Expected vs him-13 mutant
Crossover per meiosis (% total observed)
Expected
him-13 (e1742)
SNP1-SNP2
SNP2-SNP3
SNP3-SNP4
SNP4-SNP5
SNP5-SNP6
5 intervals defined by 6 SNPs

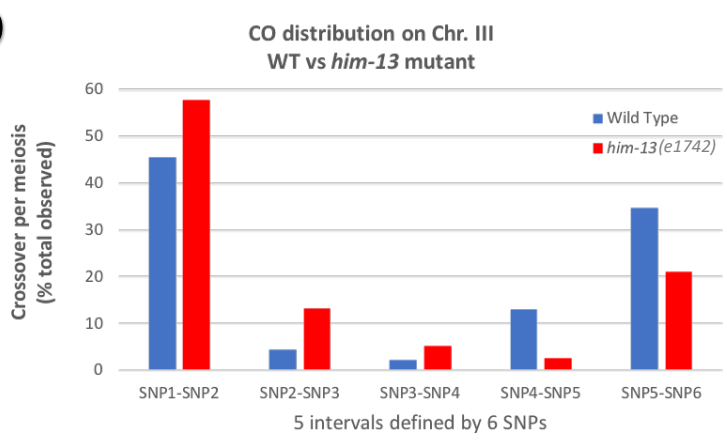
D
CO distribution on Chr. III
WT vs him-13 mutant
Crossover per meiosis (% total observed)
Wild Type
him-13 (e1742)
SNP1-SNP2
SNP2-SNP3
SNP3-SNP4
SNP4-SNP5
SNP5-SNP6
5 intervals defined by 6 SNPs

Figure 38. CO distribution is shifted to the left on Chr. X in *mei-2(fq37[E131K])* mutants

A - Table containing physical and genetic positions used to calculate the expected CO distribution. To do this, the total length of Chr. X (17.7Mbp) was divided into four regions. Then, genes that were around those positions were chosen and their corresponding genetic position were used to calculate the expected map. Genetic position data was obtained from Wormbase.

B - Graph indicating the expected COSA-1 foci distribution among four equal-length intervals along Chr. X.

C - Graph indicating the wild type COSA-1 foci distribution among four equal-length intervals along Chr. X. Both wild type and expected distributions were statistically similar (0.7109, chi-square test) (n=181 chromosomes).

D - Graph indicating the *him-13* COSA-1 foci distribution among four equal-length intervals along Chr. X (n = 203).

E - Graph indicating the *mei-2(fq37[E131K])* COSA-1 foci distribution among four equal-length intervals along Chr. X (n= 187 chromosomes).

F - Accumulative frequency plot comparing COSA-1 foci position along Chr. X from wild type and *him-13* germ lines. Wild type and him-13 distributions were statistically significant (0.045, Kolmogorov-Smirnov test).

G - Accumulative frequency plot comparing COSA-1 foci position along Chr. X from wild type and *mei-2(fq37[E131K])* germ lines. Wild type and *mei-2(fq37[E131K])* distributions were statistically significant (0.007, Kolmogorov-Smirnov test).

H - Accumulative frequency plot comparing COSA-1 foci position along Chr. X from *mei-2(fq37[E131K])* and *him-13* germ lines. *mei-2(fq37[E131K])* and *him-13* distributions were statistically significant (0.000, Kolmogorov-Smirnov test).

A

Physical Position (Mbp)	Gene Name	Physical Position (bp)	Genetic Position
0	cTel7X.3	151-263	-21.67
4.4	D1079.1	4403159-4407145	-7.70
8.8	R04E5.8	8801624-8806113	+0.41
13.2	F09D5.6	13200005-13200141	+10.23
17.7	cTel55X.1	17714968-17718720	+24.63

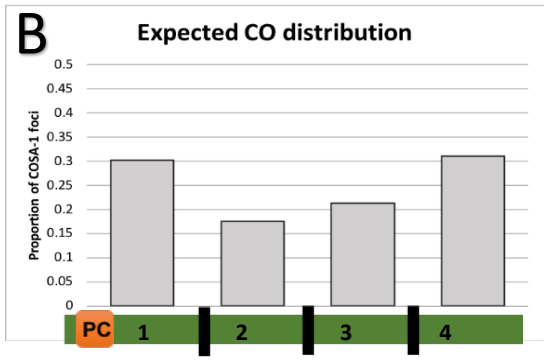

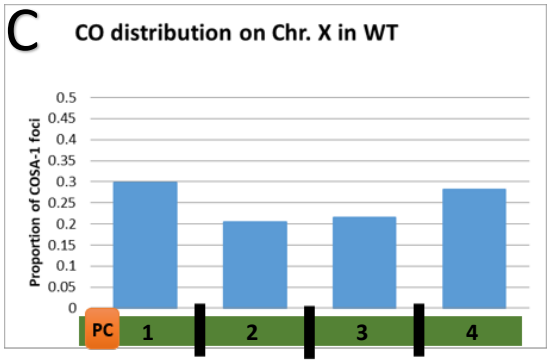

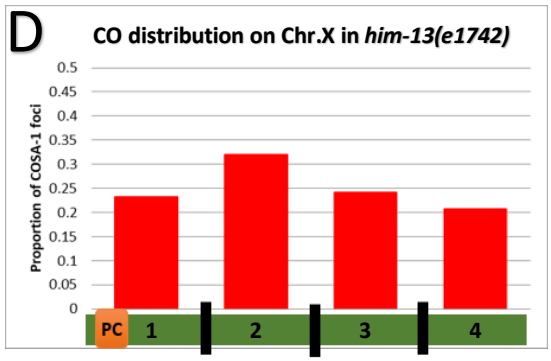

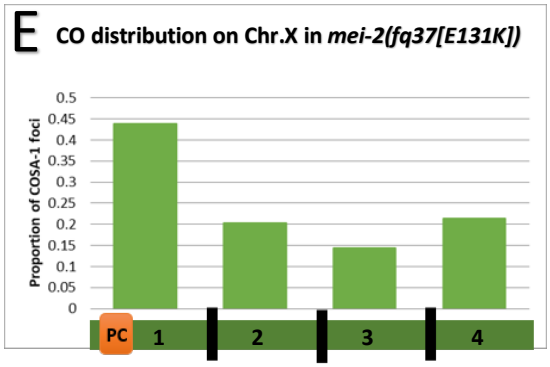

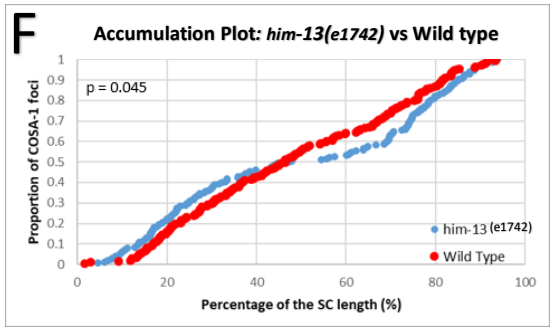

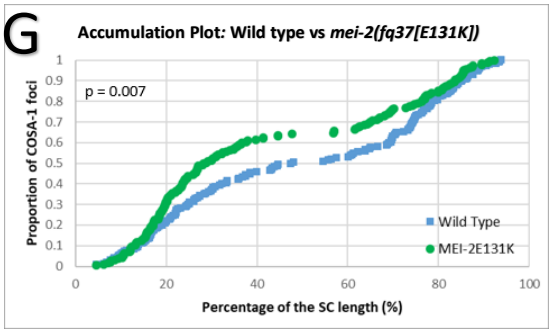

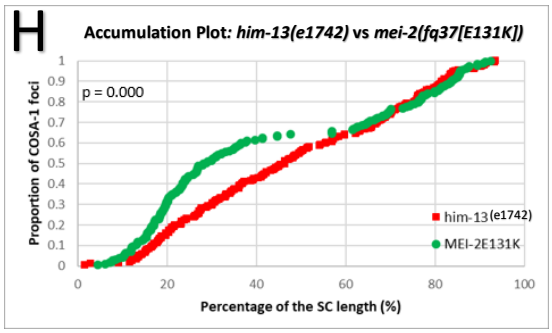

Figure 39. Depletion of MEI-2 protein affects CO distribution

A - Graph comparing the expected COSA-1 foci distribution against the untreated *mei-2::degron* distribution among four equal-length intervals along Chr. X. The expected distribution was generated by dividing the total length of Chr. X into four regions and calculating the frequency of recombination between those intervals using genetic recombination data from Wormbase. There was no difference between these two distributions (0.129, chi-squared test) (n= 196).

B - Graph comparing the expected COSA-1 foci distribution against the treated *mei-2::degron* distribution among four equal-length intervals along Chr. X. The differences between both distributions were statistically significant (0.000083, chi-squared test) (n= 195).

C - Graph comparing the treated *mei-2::degron* COSA-1 foci distribution against the untreated *mei-2::degron* distribution among four equal-length intervals along Chr. X.

D - Accumulative frequency plot comparing COSA-1 foci position along Chr. X from untreated *mei-2::degron* and auxin treated *mei-2::degron* germ lines. These distributions were statistically different (0.02, Kolmogorov-Smirnov test).

A

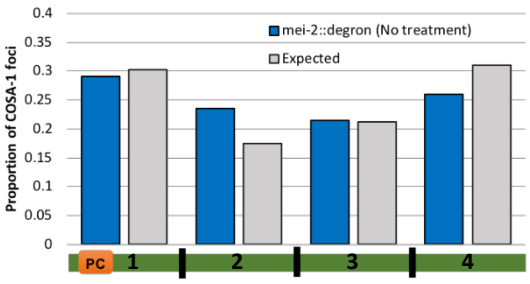
CO distribution on Chr. X
mei-2::degron (No treatment)
Expected
Proportion of COSA-1 foci
0.4
0.35
0.3
0.25
0.2
0.15
0.1
0.05
0
PC
1
2
3
4

B

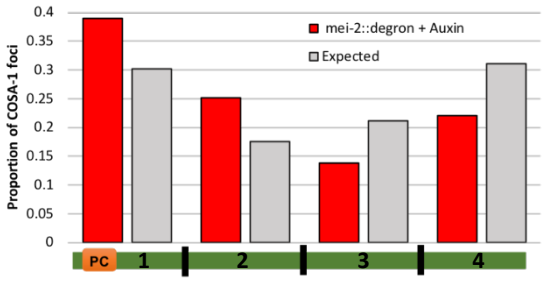
CO distribution on Chr. X
mei-2::degron + Auxin
Expected
Proportion of COSA-1 foci
0.4
0.35
0.3
0.25
0.2
0.15
0.1
0.05
0
PC
1
2
3
4

C

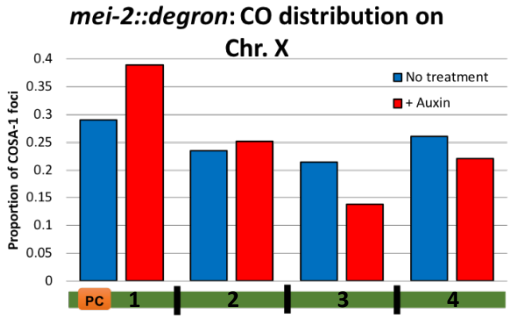
mei-2::degron: CO distribution on Chr. X
No treatment
+ Auxin
Proportion of COSA-1 foci
0.4
0.35
0.3
0.25
0.2
0.15
0.1
0.05
0
PC
1
2
3
4

D

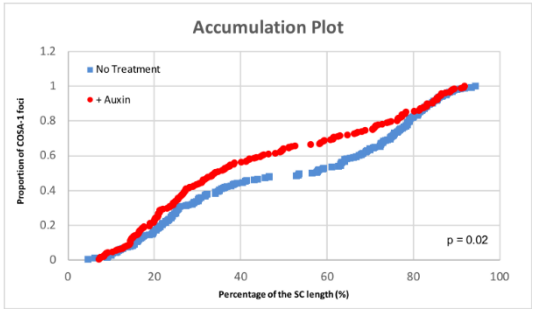
Accumulation Plot
No Treatment
+ Auxin
Proportion of COSA-1 foci
1.2
1
0.8
0.6
0.4
0.2
0
p = 0.02
0
20
40
60
80
100
Percentage of the SC length (%)

Figure 40. CO interference is not affected in *mei-2::degron* worms treated with auxin

A - Diagrammatic representation of *mnT12* fusion chromosome. The arrowheads represent the chromosome ends.

B - Double CO percentage does not vary in auxin-treated *mei-2::degron* germ lines.

C - Single CO distribution graph comparing the untreated *mei-2::degron* COSA-1 foci against the untreated *mei-2::degron* distribution among four equal-length intervals along *mnT12* chromosome (n = 89, n= 93 respectively).

D - Single CO accumulative frequency plot comparing COSA-1 foci position along *mnT12* from untreated and treated *mei-2::degron* germ lines. Although not statistically significant (0.053, Kolmogorov-Smirnov), there was a tendency indicating these distributions could be different.

E - Double CO distribution graph comparing the untreated *mei-2::degron* COSA-1 foci against the untreated *mei-2::degron* distribution among four equal-length intervals along *mnT12* chromosome (n = 24, n= 21 respectively).

F - Double CO accumulative frequency plot comparing COSA-1 foci position along *mnT12* from untreated and treated *mei-2::degron* germ lines. These distributions were equal (0.968, Kolmogorov-Smirnov).

A

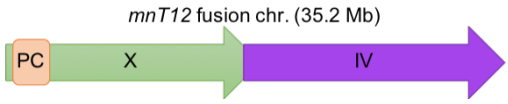
mnT12 fusion chr. (35.2 Mb)
PC
X
IV

B

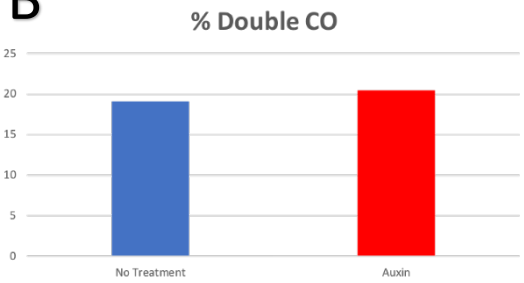
% Double CO
25
20
15
10
5
0
No Treatment
Auxin

C

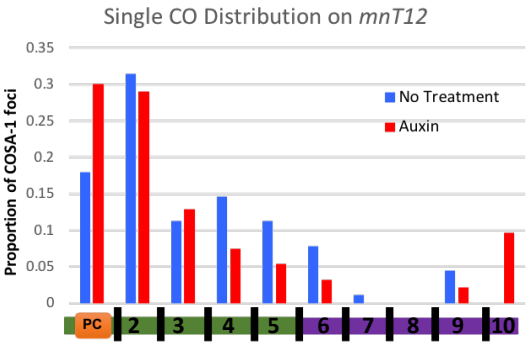
Single CO Distribution on mnT12
Proportion of COSA-1 foci
0.35
0.3
0.25
0.2
0.15
0.1
0.05
0
No Treatment
Auxin
PC
2
3
4
5
6
7
8
9
10

D

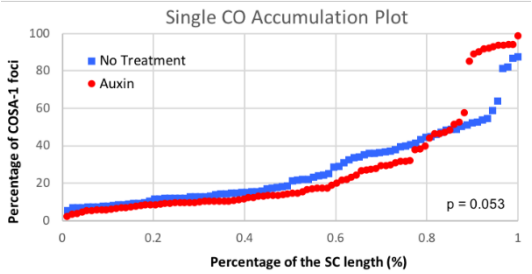
Single CO Accumulation Plot
Percentage of COSA-1 foci
100
80
60
40
20
0
No Treatment
Auxin
p = 0.053
0
0.2
0.4
0.6
0.8
1
Percentage of the SC length (%)

E

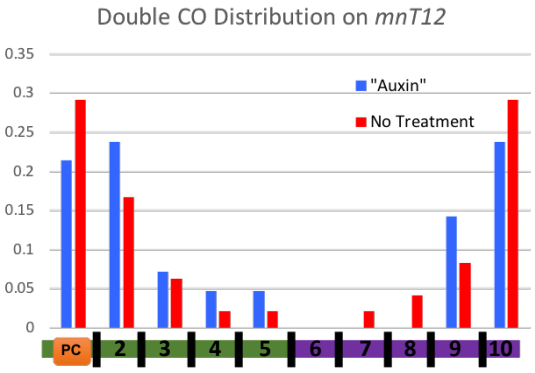
Double CO Distribution on mnT12
0.35
0.3
0.25
0.2
0.15
0.1
0.05
0
"Auxin"
No Treatment
PC
2
3
4
5
6
7
8
9
10

F

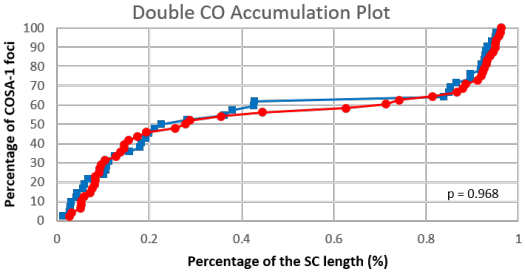
Double CO Accumulation Plot
Percentage of COSA-1 foci
100
90
80
70
60
50
40
30
20
10
0
p = 0.968
0
0.2
0.4
0.6
0.8
1
Percentage of the SC length (%)

CHAPTER 6: RESULTS.

USING SRM TECHNIQUES TO INVESTIGATE EARLY MEIOTIC CHROMOSOME STRUCTURE

6.1 Objectives and background

In chapter 3, I developed a method to measure CO position relative to the length of pachytene chromosomes that allows measurement of chromosome length in three-dimensionally intact nuclei. The study of meiotic chromosome length has always been challenging given the three-dimensional organization of chromosomes within the nucleus. Most cytological studies that measure chromosome length and CO position have been performed in two dimensional samples. For example, mouse pachytene nuclei are spread on the surface of slides to flatten chromosomes, however, this mechanical process is quite aggressive and could potentially affect chromosome structure (Peters et al., 1997). In *C. elegans*, X chromosome length has previously been measured in three-dimensionally intact pachytene nuclei using a Deltavision microscope followed by in silico "chromosome stretching" (Mets and Meyer, 2009). I decided to use the method that I developed to measure chromosome length variability of different chromosomes in wild type nuclei at different stages of meiotic prophase I, allowing me to investigate if chromosome axis length is coordinated among chromosomes within the same nucleus or each chromosome behaves independently from each other. Furthermore, I also started performing experiments to address how different known regulators of meiotic chromosome affect the organisation of pachytene chromosomes.

Below, before describing my results, I will explain what we know about chromosome length regulation in meiosis, focusing on two SMC protein complexes which are major players in chromosome length regulation: cohesin and condensin. I also mention other proteins known to participate in regulating meiotic chromosome structure.

6.1.1 Structural Maintenance Chromosome (SMC) proteins regulate chromosome organization

During the cell cycle, eukaryotic cells need to replicate, repair, and segregate their DNA, a process that involves extensive compaction of DNA within the nucleus. To achieve this, chromosomes must undergo morphological and topological changes that are largely mediated by conserved structural maintenance of chromosomes (SMC) proteins in an ATP-dependent manner (Jeppsson et al., 2014).

This family of proteins includes cohesin and condensin. Although cohesin complexes are mainly known for their role in sister chromatid cohesion during mitosis and meiosis, they also participate in homologous recombination, transcription regulation, chromosome condensation, and genome organisation in interphase and non-dividing cells (Mehta et al., 2013). On the other hand, condensin complexes mainly participate in chromosome condensation in preparation for cell division (Csankovszki et al., 2009a), and in *C. elegans* a variant of condensin, the dosage compensation complex, down regulates transcription of the X chromosomes in hermaphrodites (Chuang et al., 1994).

6.1.1.2 Cohesin

Cohesin complexes that provide sister chromatid cohesion (SCC) until anaphase must be loaded during S-phase and are essential to avoid chromosome missegregation in mitosis and meiosis (see section 1.2.4.1) (figure 4). *C. elegans* also has additional meiosis-specific kleisins beyond REC-8. These are COH-3 and COH-4, two highly identical and functionally redundant proteins that are required for CO formation, SC assembly, and meiotic chromosome structure (Crawley et al., 2016; Pasierbek et al., 2001; Severson and Meyer, 2014; Severson et al., 2009). REC-8 and COH-3/4 show differences in their loading to chromosomes, with REC-8 associating with chromosomes during S-phase and COH-3/4 cohesin only associating with chromosomes after S-phase (Severson and Meyer 2014). REC-8 and COH-3/4 display important functional differences, such as their sensitivity to WAPL-1-mediated removal during meiotic prophase, which is largely restricted to COH-3/4 complexes (Crawley et al., 2016).

WAPL-1 is a cohesin removal factor that participates in both mitosis and meiosis to limit the quantity of cohesin that is found associated with chromosomes (Crawley et al., 2016; Tedeschi et al., 2013). Interestingly, *C. elegans wapl-1* mutants display shortening of axial elements, demonstrating that regulating cohesin binding is key for controlling the length of pachytene chromosomes (Crawley et al., 2016). In yeast, the same effect has been observed in *wpl1* (also known as *Rad61*) meiotic mutants, demonstrating the conserved function of cohesin in regulating the structure of pachytene chromosomes (Challa et al., 2016).

6.1.1.3 Condensin

Condensin also plays a crucial role in regulating mitotic and mitotic chromosome structure (see section 1.2.4.1) (figure 5). In *C. elegans*, condensin I is composed of SMC-4, SMC-2, DPY-28 (kleisin) and two CAP proteins, CAPG-1 and DPY-26, whereas Condensin II is composed of HCP-6 kleisin and two CAP proteins, KLE-2 and HCP-2 (Csankovszki et al., 2009a). *C. elegans* also has a subtype of condensin I (condensin I^{DC}) that participates in dosage compensation of the X chromosome in hermaphrodites by condensing its chromatin structure (Chuang et al., 1994; Csankovszki et al., 2009a). Heterozygous worms carrying a mutated copy of any condensin I or II subunit were shown to have an axial extension in pachytene nuclei, increasing the number of DSBs and altering CO distribution (Mets and Meyer, 2009). Similar to this, removal of condensin from metaphase I mouse oocytes demonstrated that condensin plays a key role in promoting the longitudinal rigidity of mitotic chromosomes (Houlard et al., 2015).

6.1.2 Topoisomerase II and CENPA

In addition to SMC proteins, there are other proteins that control chromosome organization during the cell cycle. Topoisomerase II is known to participate in chromosome condensation and topology (Nitiss, 2009). On the other hand, the centromere protein A (CENP-A) is a histone H3 protein that has been found to have a role the elongation of axial elements in the holocentric mitotic chromosomes of *C. elegans* (Ladouceur et al., 2017).

6.1.2.1 Topoisomerase II

DNA Type II topoisomerases are conserved among eukaryotes and participate in chromosome fidelity by relieving the tensions generated within chromosomes (Nitiss, 2009). To achieve this, a dsDNA is cut and another unbroken molecule of DNA is passed, then the previous broken DNA molecule is religated, releasing topological stresses (Nitiss, 2009). Topoisomerase II enzymes are essential to resolve topological problems originated during mitosis, showing defects in chromosome condensation when topoisomerase II activity is impaired. In human cells, depletion of topoisomerase II causes an increment in length of mitotic chromosomes (Farr et al., 2014). Topoisomerase II is located along chromosome axes in mammals, yeast and *Drosophila* during mitosis (Mengoli et al., 2014; Uemura et al., 1987; Xu and Manley, 2007).

Similar to mitosis, Topoisomerase II is associated with meiotic chromosome axes in mammals, plants and budding yeast (Guturi et al., 2016; Klein et al., 1992; Liang et al., 2015). Topoisomerase II inhibitors produce problems in meiotic chromosome condensation and segregation (Gómez et al., 2014). Moreover, Topoisomerase II activity is essential to remove some interlock structures, being chromosome movement also necessary for others in *A. thaliana* (Martinez-Garcia et al., 2018).

6.1.2.2 Centromere protein A (CENP-A)

CENP-A replaces histone H3 during mitosis and it is located in centromeric regions (Sullivan et al., 2001). However, *C. elegans* has holocentric chromosomes and CENP-A-containing nucleosomes are distributed along the length of mitotic chromosomes, creating a surface where kinetochores can be established and spindle microtubules can be attached (Maddox et al., 2004). Interestingly, depletion of CENP-A decreases chromosome length in *C. elegans*, implying that CENP-A could potentially modify chromosome surface during mitosis (Heald and Gibeaux, 2018; Ladouceur et al., 2017). This mechanism could be specific of *C. elegans* holocentric chromosomes, given that CENP-A can be diminished significantly without affecting mitosis in human cells (Black et al., 2007).

6.2 Variability of X Chromosome length in pachytene nuclei

Using Imaris and the SIM system to map COs in nuclei where I had labelled the X chromosomes with anti-HIM-8 antibodies, I obtained a data set of X chromosome lengths as a by-product. This analysis revealed that the average length of the X chromosomes in late pachytene nuclei was 4.69 µm ± 0.77(SD) (n= 50). The X chromosomes displayed a relatively high level of length variability in wild type nuclei at pachytene, showing a two-fold difference between the shortest and the longest X chromosomes (figure 41). The average length that I found was comparable to a previous study performed in *C. elegans* where X chromosomes were straightened computationally, displaying an average length of 4.5 µm (Mets and Meyer, 2009). This suggests that this method is a valid tool to measure chromosome length along pachytene and it could be used to understand molecular processes that regulate chromosome length.

6.3 Generation of strains carrying LacO insertions in autosomes

Given that the X chromosome is more condensed than the autosomes (Chuang et al., 1994), I wondered if the changes in chromosome length that I observed on the X chromosomes were also occurring in autosomal chromosomes. The reason why I had studied the length of the X chromosome before the length of the autosomes was because X chromosome can easily be labelled by using the αHIM-8 antibody (Phillips et al., 2005), which marks the pairing center of the X chromosome. Labelling specific autosomes in pachytene nuclei is much more challenging as the pairing center binding proteins of the autosomes are removed at early pachytene (Phillips and Dernburg, 2006). A classical method to label autosomal chromosomes in *C. elegans* is FISH, which allows labelling of specific locus and identifying exact chromosomes at any meiotic stage (Martinez-Perez and Villeneuve, 2005). However, this technique requires DNA denaturation to hybridise the DNA with probes to label specific locus, altering chromosome structure in the process.

Another possibility to label chromosomes is to use LacO arrays. Insertion of *lacO* repeats at specific regions allows visualization of these chromosome positions when the arrays

are bound by the *LacI::GFP* represor (Robinett et al., 1996). Ideally, using this method I aimed to distinguish at least two autosomal chromosomes (III and V), while the X chromosomes could still be labelled using αHIM-8 antibodies. This approach is possible in *C. elegans* because the Jorgensen's laboratory has created several strains carrying a single *LacO* array (Frøkjær-Jensen et al., 2014). The positions of these *LacO* arrays are described and using this information, I planned to create a strain carrying one *LacO* position at the left end of chromosome III and four different LacO insertions on chromosome V. The chosen *LacO* positions were strategically selected to distinguish the direction of the chromosomes (figure 42A). Moreover, this "*LacO* strain" needed to carry the *cosa-1::HA* allele created by CRISPR to study CO distribution in several chromosomes within the same nucleus.

This "LacO strain" was successfully created by crossing the *cosa-1::HA* strain with strains carrying the chosen *LacO* positions, until achieving the final strain (figure 42A). Then, I established the staining conditions to measure chromosome length and CO distribution (see Material and Methods). Firstly, CO sites were labelled using an αHA antibody to visualize COSA-1::HA. Secondly, αHTP-3 antibody was used to mark the axial elements of the SC, which labels the whole length of the axial elements at all pachytene stages (Goodyer et al., 2008), therefore allowing measurement of chromosome length. Thirdly, αHIM-8 antibodies were used to mark the pairing center of X chromosome (Phillips et al., 2005), providing the orientation of the X chromosome. Finally, LacI::GFP protein was used to label *LacO* positions and the signal was amplified by using and αGFP primary antibody conjugated with Alexa488 (figure 42B). These slides were acquired with the Zeiss ELYRA S1 and then, the SIM stacks were processed with Imaris.

6.3.1 Chromosome length variability between early and late pachytene

The next step after creating the LacO strain was to measure the length of chromosomes III, V and X. The first question I wanted to address was if the previous differences in length variability found in the X chromosome were because early-mid pachytene and late pachytene chromosomes show different length as it occurs in mice (Vranis et al., 2010). Furthermore, it has been proposed that CO formation expands the axis length of chromosomes locally in *C. elegans* (Libuda et al., 2013). As the differences between

early-mid and late pachytene nuclei are not always clear in the germ line, I created a classification based on the number of COSA-1 foci. Only chromosomes coming from nuclei without any COSA-1 foci were considered as early-mid pachytene chromosomes. At the same time, only chromosomes coming from nuclei with 6 COSA-1 foci were considered as late pachytene chromosomes, as this indicates one CO per chromosome pair. Late pachytene X chromosomes were longer than early-mid pachytene chromosomes (figure 43A and D). Simultaneously, I measured the length of chromosomes III and V to check whether these changes in length between early-mid pachytene and late pachytene chromosomes could be visualised in autosomal chromosomes. As expected, early-mid pachytene autosomes were shorter than late pachytene chromosomes (figure 43B, C and D). Moreover, a ratio between chromosome size in megabase pairs (Mbp) and chromosome length in microns (µm) was created to evaluate chromosome condensation levels (figure 43E). The X chromosome showed the highest ratio (3.74), indicating that it is more condensed than the autosomes, as expected (figure 43E). Although the X chromosome was more condensed than the autosomes, there were differences between chromosomes III (2.06) and V (2.88) in condensation levels at pachytene, indicating that there might be differences in chromosome condensation among autosomes (figure 43E). These results demonstrate that chromosome length is regulated along pachytene in *C. elegans*, suggesting that conserved molecular mechanisms regulate chromosome length during pachytene.

6.3.2 Chromosome length is coordinated within individual nuclei

Once I found that chromosome length was varied as pachytene progressed in *C. elegans*, I wondered whether chromosome length was coordinated among chromosomes within the same nucleus, or the length of each chromosome was independent of one another. To test this, the length of chromosomes III, V and X of each nucleus was measured and represented in a plot XY graph. First, I compared the lengths of the autosomes (Chr. III and Chr. V) within the same nucleus (figure 44B). If there was a relationship between these two chromosomes, a direct correlation would be expected to be seen between the lengths of both chromosomes. Interestingly, this was the case (0.88), suggesting that a mechanism to control chromosome size may operate at this point.

After this, I also compared the length of the X chromosomes with chromosome III (figure 44A) and V (figure 44C). The same trend was observed, with the X chromosomes displaying a high correlation with both chromosomes III (0.88) and V (0.89), demonstrating interconnection of the three chromosomes (figure 44A and C). These results indicate that chromosome length is coordinated among chromosomes within the same nuclei.

6.3.3 Synaptonemal complex disassembly starts from the most distal end from the CO site

CO formation triggers asymmetrical disassembly of the SC at the end of late pachytene in *C. elegans* (Martinez-Perez et al., 2008; Nabeshima et al., 2005). This remodelling involves chromosome condensation and a redistribution of SC central elements components and specific axial element components (HTP-1/2 and LAB-1) to separate opposite sides of the single CO site (Bhalla et al., 2008; De Carvalho et al., 2008; Martinez-Perez et al., 2008). This process concludes with the formation of diakinesis bivalents in which central region components are limited to the short arm, while HTP-1/2 and LAB-1 are only found on the long arms. As HTP-1/2 and LAB-1 determine the pattern of SCC release during anaphase I, their correct redistribution during late-prophase chromosome remodelling is essential to ensure accurate chromosome segregation (De Carvalho et al., 2008; Ferrandiz et al., 2018; Gao and Colaiácovo, 2018).

Given that Imaris and SIM microscopy gave the opportunity of visualising structural changes in chromosomes that are challenging to observe in two dimensions, I decided to look at nuclei in late pachytene undergoing the early steps of the chromosome remodelling process. To achieve this, I used the *cosa-1::HA* strain and performed immunostaining to label CO sites (HA antibodies) and axial elements by using HTP-3 antibodies (figure 45). Interestingly, I observed that SC disassembly, as indicated by the separation of axial elements belonging to homologous chromosomes, always starts from the furthest telomere from the CO site. This result suggests that a molecular mechanism should transmit the signal from the CO to the long arm end to start the disassembly of the SC.

6.4 Investigating the contribution of SMC complexes to chromosome structure

After creating the LacO strain and using Imaris to visualise meiotic chromosome structures in three dimensions, I thought that I could use this method to visualise chromosome structure in situations where SMC function is altered. As previously mentioned, SMC proteins are essential for meiotic chromosome structure, participating in processes such as chromosome condensation, sister chromatid cohesion, and crucially axial element morphogenesis. For this reason, I decided to investigate situations in which SMC function is altered, but without compromising the integrity of axial elements. Thus, I investigated condensin by using a *dpy-26::degron* strain available in the lab, which should allow removal of condensing I complexes from late pachytene nuclei, and the contribution of cohesin by studying *wapl-1* mutants, in which axial elements are formed but contain an excess amount of COH-3/4 cohesin (Crawley et al. 2016).

6.4.1 *wapl-1* mutant

As mentioned above, WAPL-1 cohesin factor removes and restricts the amount of COH-3/4 cohesin that is associated with chromosomes throughout meiotic prophase (Crawley et al., 2016). Although chromosome structure is not as affected as the structure of other cohesin mutants, such as *rec-8* or *coh-3/4* mutants (Severson and Meyer, 2014), *wapl-1* mutants have chromosomes with shorter axial elements during pachytene, demonstrating that WAPL-1 and therefore cohesin are major players in controlling meiotic chromosome length (Crawley et al., 2016). The same phenotype has been observed in yeast (Challa et al., 2016), suggesting that this meiotic role of WAPL is conserved across eukaryotes. This mutant is particularly interesting to study how an increased amount of cohesin contributes to meiotic chromosome structure. Differences in length between late and early pachytene chromosomes was first reported in mice (Vranis et al., 2010). The authors of this study proposed that cohesin removal was the cause of the shortening of axial elements that can be observed between early and late pachytene stages. Moreover, cohesin removal mechanism in meiosis by WAPL seems to be conserved in eukaryotes (Brieño-Enríquez et al., 2016; Challa et al., 2016; Crawley et al., 2016; De et al., 2014). Therefore, I decided to investigate whether differences in

length between early-mid and late pachytene chromosomes could be observed in a *wapl-1* mutant, or if excess cohesin binding interferes with this process.

To perform this experiment, I crossed the *wapl-1* mutant with the LacO strain to be able to identify chromosomes III, V and X. This new strain was used to perform a staining using αHTP-3 antibody to label the axial elements, αHA antibody against COSA-1::HA to mark CO sites, αHIM-8 antibody label the pairing center of the X chromosome, and purified LacI::GFP protein to label *LacO* positions. These slides were acquired with the Zeiss ELYRA S1 and then, the SIM stacks were processed with Imaris. Moreover, as mentioned above, only chromosomes coming from nuclei without any COSA-1 foci were considered as early-mid pachytene chromosomes. At the same time, only chromosomes coming from nuclei with 6 COSA-1 foci were considered as late pachytene chromosomes. The analysis demonstrated that late pachytene chromosomes were longer than early-mid chromosomes, with this trend seen on the X chromosome (figure 46A), chromosome III (figure 46 B) and chromosome V (figure 46C) (figure 46D). As expected, *wapl-1* chromosomes were shorter in both early-mid and late pachytene stages compared to wild type (figure 47A and B). However, an interesting feature was the variability in chromosome length found in *wapl-1* mutants. Wild-type chromosomes showed a two-fold increment between the shortest and the longest chromosomes along pachytene (figure 43A, B and C), whereas in the *wapl-1* mutant there was a three-fold increment between the shortest and the longest along pachytene in chromosome III, V and X (figure 46A, B and C). These results demonstrate that the chromosomes of the *wapl-1* mutant are shorter than the wild type chromosomes, but they behave in the same way in terms of size variation, being shorter at early-mid pachytene and longer at late pachytene.

6.4.1.1 WAPL-1 and cohesin could have a role coordinating chromosome length

After observing that *wapl-1* mutant chromosomes also increase their length from early pachytene to late pachytene, I wondered whether chromosome length was also coordinated among chromosomes within the same nuclei as it occurs in the wild type. To validate this hypothesis, the length of chromosomes III, V and X of each nucleus was measured and represented in a plot XY graph. First, I compared the lengths of the

autosomes (Chr. III and Chr. V) within the same nucleus (figure 48B). A direct correction between the length of these two chromosomes was observed (0.81) (figure 48B). However, this correlation between Chr. III and V was reduced in *wapl-1* chromosomes compared to the wild type (0.81 and 0.91 respectively) (figure 48B and 44B). Afterwards, I compared the length of the X chromosomes with chromosomes III and V in the *wapl-1* mutant (figure 48A and C). The coefficients of determination between the X chromosome and chromosomes III (0.69) (figure 48A) and V (0.80) (figure 48C) in *wapl-1* chromosomes were also reduced in comparison to the wild type (Chr.III = 0.88 and Chr V = 0.89 in wild type chromosomes) (figure 44A and C), showing the same trend and suggesting that WAPL-1, and therefore cohesin, could have a role in coordinating the length of chromosomes through pachytene.

6.4.1.2 CO distribution is not affected in *wapl-1* mutants

After corroborating that the *wapl-1* mutant had shorter axial elements compared to the wild type, I wondered if CO distribution could also be affected in this mutant. This hypothesis emerged from the fact that heterozygous condensin mutants, another SMC protein, showed an elongation in the chromosome axis and, simultaneously, they also display an alteration in the CO distribution (Mets and Meyer, 2009). To address this question, I used the slides acquired in the previous experiment and I measured the CO distribution of each chromosome (III, V and X) in the wild type and *wapl-1* mutant (figure 49A, C and E). Kolmogorov Smirnoff tests confirmed that CO distributions were the same for chromosome X (0.381), III (0.496) and V (0.106) (figure 49B, D and F), rejecting the idea that WAPL-1 could have a role in regulating CO distribution, at least when detected by measuring CO distribution along the physical distance of late pachytene chromosomes.

6.4.2 *dpy-26::degron* strain

As previously indicated, condensin complexes play a role in regulating chromosome condensation and organisation (Hirano, 2016). *C. elegans* has two types of condensin, condensin I and condensin II, and a subtype of condensin I that participates in a mechanism of dosage compensation of chromosome X in hermaphrodites by

condensing its structure (Csankovszki et al., 2009a). It has been demonstrated that condensin complexes regulate DSB formation, and therefore CO distribution by using heterozygous worms carrying a mutated copy of any subunit of condensin I or II (Mets and Meyer, 2009). Moreover, these heterozygous mutants display longer chromosomes, demonstrating how condensin contributes to meiotic chromatin structure. However, these heterozygous mutants start from a situation where they do not have the same amount of condensin than wild type worms. Ongoing studies in our laboratory have seen that temporally-controlled depletion of cohesin complexes from axial elements that were normally formed during early meiosis affect chromosome structure in a rapid way. For this reason, I hypothesised that a depletion of Condensin I after axial element assembly could affect chromosome length and help to understand if condensin complexes participate in CO designation, apart from DSB formation.

To understand better the interplay between chromosome structure and condensin I, I crossed the *dpy-26::degron* CRISPR strain available in the lab with the LacO strain. Then, I did a quadruple immunostaining using αHIM-8, αHA and αHTP-3 antibodies together with LacI::GFP protein. To perform this staining, I picked L4 worms and allowed them grow in a NGM plate for 20 hours until they were young adults. The next day, I divided them into two different plates, one with 1mM of auxin and another one without auxin, both seeded with OP50 bacteria. After 7 hours, these worms were dissected, slides were acquired with the Zeiss ELYRA S1 and SIM images were processed using Imaris. As nuclei move around 1 row per hour in the *C. elegans* germline, during the 7 hours of auxin-induced depletion used in this experiment nuclei will have progressed little through meiotic prophase (pachytene lasts about 35 hours).

5.4.3 Chromosome length is not affected in auxin-treated *dpy-26::degron* germlines

The first question that I wanted to address was whether the depletion of DPY-26 would extend the length of the chromosome axis as it was observed with the heterozygous condensin mutants. Thus, I measured the length of chromosomes III, V and X within the same nuclei at early-mid pachytene and late pachytene in auxin treated and untreated *dpy-26::degron* germ lines. Early-mid pachytene chromosomes were longer than late pachytene chromosomes in both conditions (figure 50A and B), observing the same

tendency that occurs in the wild type. Moreover, auxin-treated and untreated chromosomes were compared, not showing any differences when DPY-26 was depleted (figure 50C and D). These preliminary data suggest that depletion of DPY-26 from properly assembled axial elements does not affect chromosome length under these conditions. However, further experiments need to be done to clarify the timing of this process and in particular to carefully evaluate the level of DPY-26 depletion obtained under the experimental conditions used here.

6.4.4 CO distribution is not affected in in auxin-treated *dpy-26::degron* germlines

One of the advantages of using the auxin-degron system is that it allows to separate subsequent processes. For example, heterozygous cohesin mutants display an altered CO distribution because DSB formation is affected during early prophase (Mets and Meyer, 2009). Nevertheless, using these mutants, it is almost impossible to address whether they also have defects in CO designation at later stages, given that if you make DSBs at different locations, COs will be made at different positions as well. The auxin-degron system allows this question to be answered. For example, if CO distribution is altered in a degron strain after 7 hours, it is because CO designation is being disturbed, given that for a nucleus to get from transition zone, where DSBs are made, to late pachytene, a nucleus needs at least 35 hours. To address this, chromosomes III, V and X were tracked for each condition, obtaining the relative position of each CO within the chromosome (figure 51A, C and E). Kolmogorov Smirnoff tests confirmed that CO distributions were the same for chromosome X (0.200) (figure 51B), chromosome III (0.133) (figure 51D) and chromosome V (0.672) (figure 51F), confirming that depletion of DPY-26 protein does not affect CO designation under these conditions. However, as mentioned above, additional controls are needed to carefully address the level of protein depletion.

6.5 Summary of results

In this chapter, I have explored the different possibilities that SIM microscopy and Imaris combined offered to study meiotic chromosome structure. First, using a non-aggressive fixation protocol, I have demonstrated that X chromosomes show variability in length during pachytene. Then, by using the LacO strain, I have also been able to quantify chromosome length variability in two autosomal chromosomes (III and V) within the same nuclei, confirming that the chromosome length variability occurs in autosomal chromosomes as well. Moreover, I have validated that this chromosome length variability along pachytene is somehow controlled, given that early pachytene chromosomes are shorter than late pachytene chromosomes for all three chromosomes investigated. Another question that the SIM-Imaris system has allowed me to address is how the SC starts to be disassembled after the CO is made, suggesting that this process starts from the most distal telomere to the CO site.

I also exploited the 3D chromosome measurement method to start investigating how SMC complexes regulate chromosome structure. I initially focused on *wapl-1* mutants, which were known to have shorter axial elements during pachytene due to excess cohesin binding. First, I confirmed that *wapl-1* mutants have shorter axial elements. Then, I also observed that *wapl-1* chromosomes are more variable in length than wild type chromosomes, an unexpected finding. Nonetheless, early-mid pachytene chromosomes were shorter than late pachytene chromosomes, similar to what I observed in wild-type nuclei, confirming that proteins other than WAPL-1 must be regulating this process. A correlation between different chromosome lengths within the same nucleus was also observed in this mutant, although interestingly the correlation was reduced in *wapl-1* chromosomes compared with wild type chromosomes. Preliminary observations show that CO distribution was not altered in *wapl-1* mutants, however, more numbers need to be acquired to confirm this result.

Finally, I used the 3D tracking method to study if rapid depletion of condensin I using the auxin-degron system affected the organization of pachytene chromosomes, as this system allows temporally-resolved depletion of the tagged protein. However, neither chromosome length nor CO distribution seemed to be affected when condensin I was depleted.

In conclusion, these early functional studies using the 3D tracking of meiotic chromosomes demonstrate that this method is a powerful tool to investigate the organization of meiotic chromosomes with single chromosome resolution.

Figure 41. X Chromosome length in pachytene nuclei

Distribution of X chromosome length between early and late pachytene (n = 86). Chromosomes were binned in 5 μm intervals along the X axis, while the Y axis depicts the frequency of chromosomes of each indicated size. Note the two-fold difference between the shortest and the longest X chromosomes.

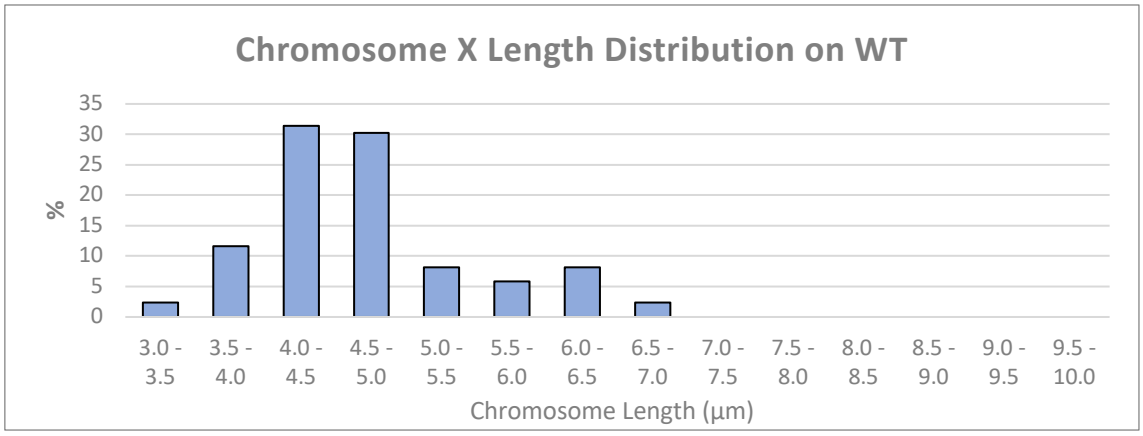
Chromosome X Length Distribution on WT
35
30
25
20
15
10
5
0
%
3.0 - 3.5
3.5 - 4.0
4.0 - 4.5
4.5 - 5.0
5.0 - 5.5
5.5 - 6.0
6.0 - 6.5
6.5 - 7.0
7.0 - 7.5
7.5 - 8.0
8.0 - 8.5
8.5 - 9.0
9.0 - 9.5
9.5 - 10.0
Chromosome Length (µm)

Figure 42. *LacO* insertions allows measurement of autosomal chromosomes

A - Diagrammatic representation of *LacO* positions within the LacO strain. *LacO* positions are indicated in purple and position of pairing centers in red. Note that HIM-8 is the specific pairing center of chromosome X. The LacO strain also carries the *cosa-1::HA* CRISPR allele to allow visualization of CO sites in late pachytene nuclei.

B - Visualisation of LacO strain on Imaris. Axial elements were labelled using αHTP-3 (green), COSA-1::HA was labelled using αHA (blue), LacO positions were marked by using LacI::GFP (purple) and HIM-8 was labelled by using an αHIM-8 (red).

A

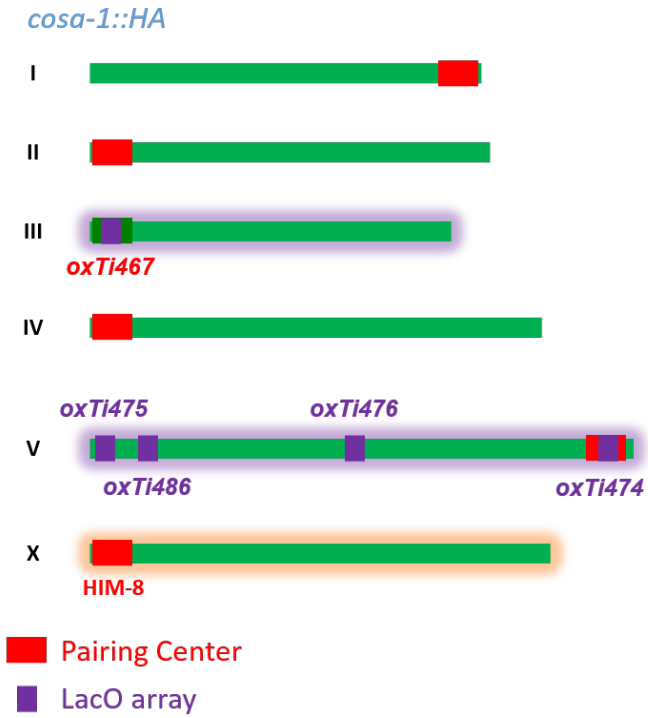
cosa-1::HA
I
II
III
oxTi467
IV
oxTi475
oxTi476
V
oxTi486
oxTi474
X
HIM-8
Pairing Center
LacO array

B

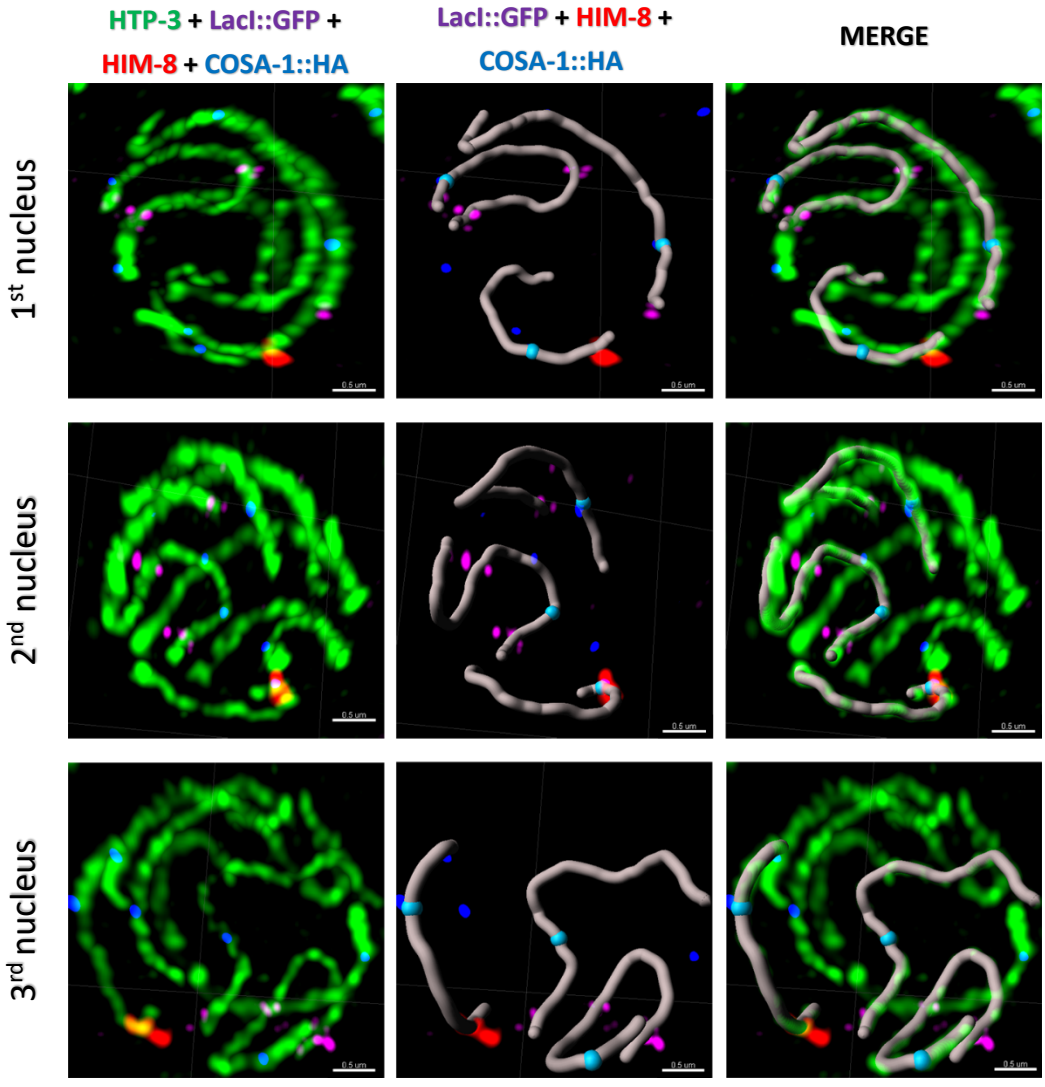
HTP-3 + LacI::GFP +
HIM-8 + COSA-1::HA
LacI::GFP + HIM-8 +
COSA-1::HA
MERGE
1st nucleus
2nd nucleus
3rd nucleus

Figure 43. Chromosomes increase in length from early-mid pachytene to late pachytene

A - Distribution of X chromosome lengths at early-mid and late pachytene (n = 41 and n=45 respectively). Late pachytene chromosomes are longer than early pachytene chromosomes.

B - Distribution of chromosome III lengths at early-mid and late pachytene (n = 41 and n=45 respectively). Late pachytene chromosomes are longer than early-mid pachytene chromosomes.

C - Distribution of chromosomes V lengths at early-mid and late pachytene (n = 41 and n=45 respectively). Late pachytene chromosomes are longer than early-mid pachytene chromosomes.

D - Comparison of chromosome length average between the three chromosomes. Note that the same trend is observed in all of them: early-mid chromosomes are shorter than late pachytene chromosomes.

E - Comparison of chromosome length in megabase pairs (Mbp) with chromosome length in microns (μm). The table below the graph represents the ratio between the chromosome size (Mbp) and the chromosome length (μm). Note that X chromosomes are more condensed than chromosomes III and V. Nonetheless, this graph also shows how chromosome V is more condensed than chromosome III proportionally, indicating than these two autosomal chromosomes might behave differently.

A

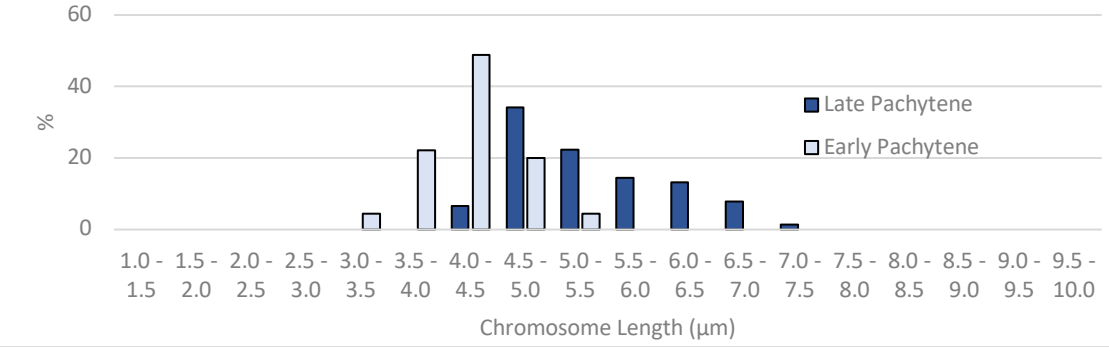

B

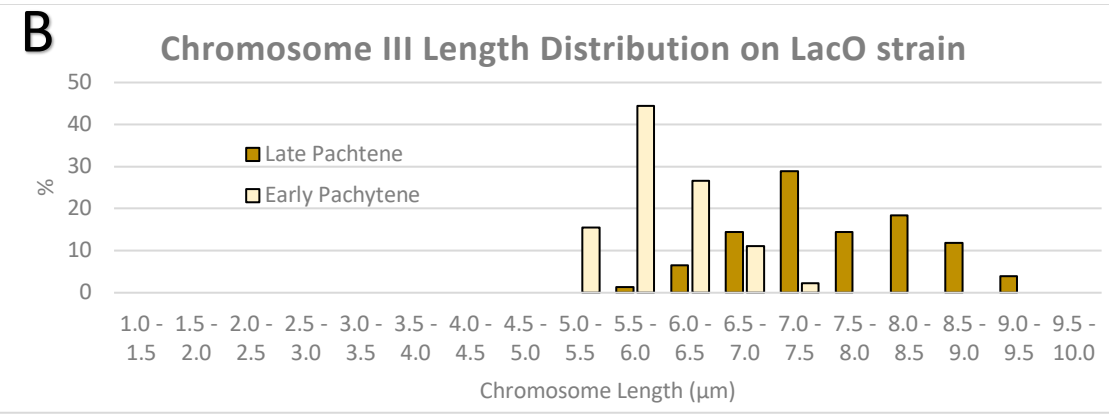

C

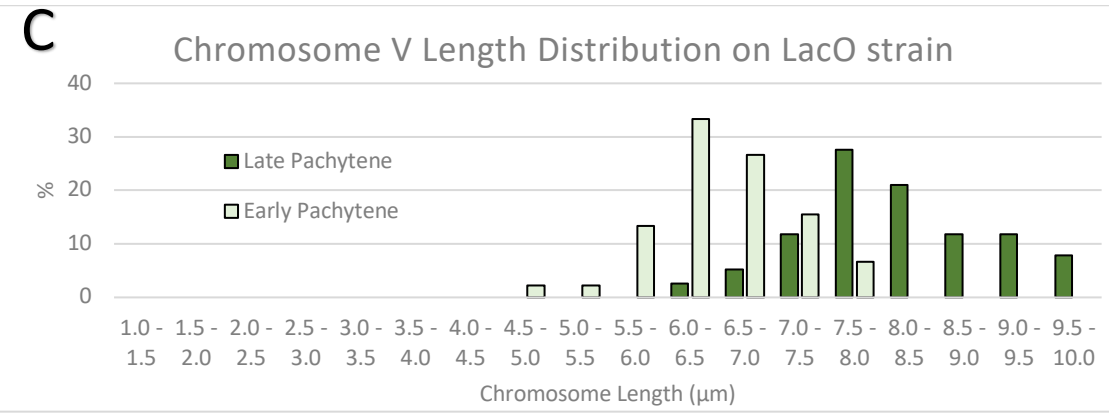

D

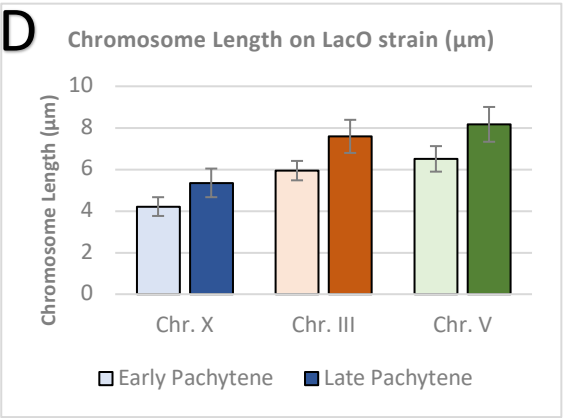

E

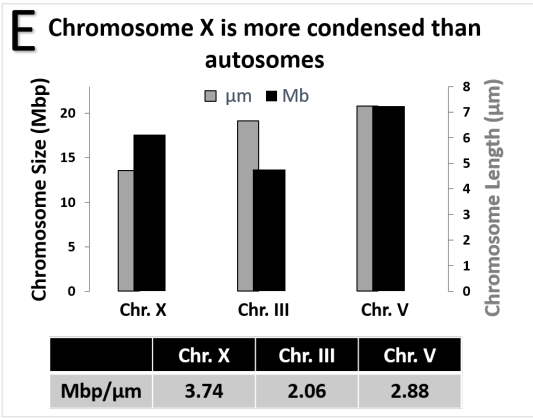

	Chr. X	Chr. III	Chr. V
Mbp/µm	3.74	2.06	2.88

Figure 44. Chromosome length is coordinated along pachytene within nuclei

A - XY plot graph representing pachytene chromosome length of chromosomes III and X withing the same nuclei. Early-mid pachytene chromosomes (n =41) were indicated in green, whereas late pachytene chromosomes (n = 45) were indicated in orange. Linear regression was 0.88.

B - XY plot graph representing pachytene chromosome length of chromosomes III and V withing the same nuclei. Early-mid pachytene chromosomes (n = 41) were indicated in green, whereas late pachytene chromosomes (n = 45) were indicated in orange. Linear regression was 0.91.

C - XY plot graph representing pachytene chromosome length of chromosomes V and X withing the same nuclei. Early-mid pachytene chromosomes (n = 41) were indicated in green, whereas late pachytene chromosomes (n = 45) were indicated in orange. Linear regression was 0.89.

Plots were made by Amalia Martinez-Segura.

A

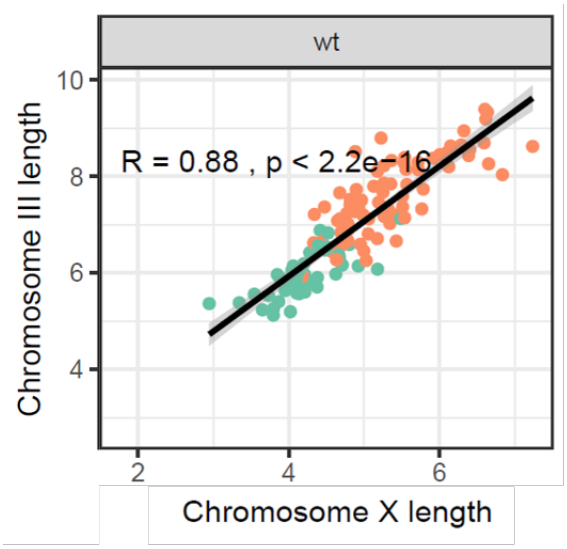
wt
R = 0.88 , p < 2.2e−16
Chromosome III length
Chromosome X length
10
8
6
4
2
4
6

B

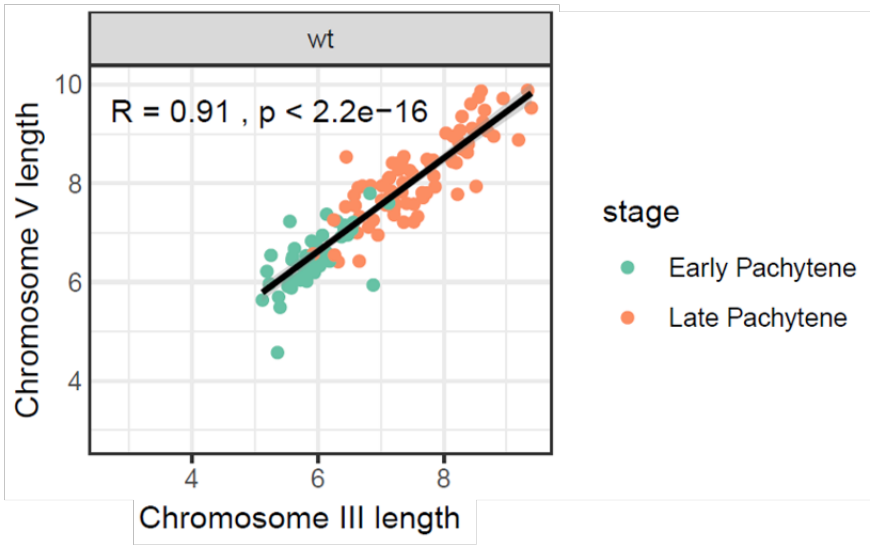
wt
R = 0.91 , p < 2.2e−16
Chromosome V length
Chromosome III length
stage
Early Pachytene
Late Pachytene
10
8
6
4
4
6
8

C

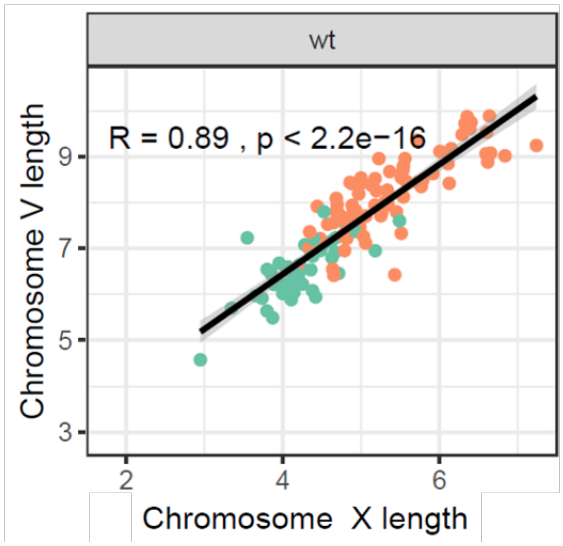
wt
R = 0.89 , p < 2.2e−16
Chromosome V length
Chromosome X length
9
7
5
3
2
4
6

Figure 45. Synaptonemal complex disassembly starts from the most distal end from the CO site

Visualisation of SC disassembly, inferred from separating axial elements, using Imaris. Axial elements were labelled using αHTP-3 (green) and COSA-1::HA was labelled using αHA (blue) to identify CO positions. Red arrows indicate the site of separating axial elements. Note that SC disassembly is initiated from the telomere which is the furthest away from the CO site.

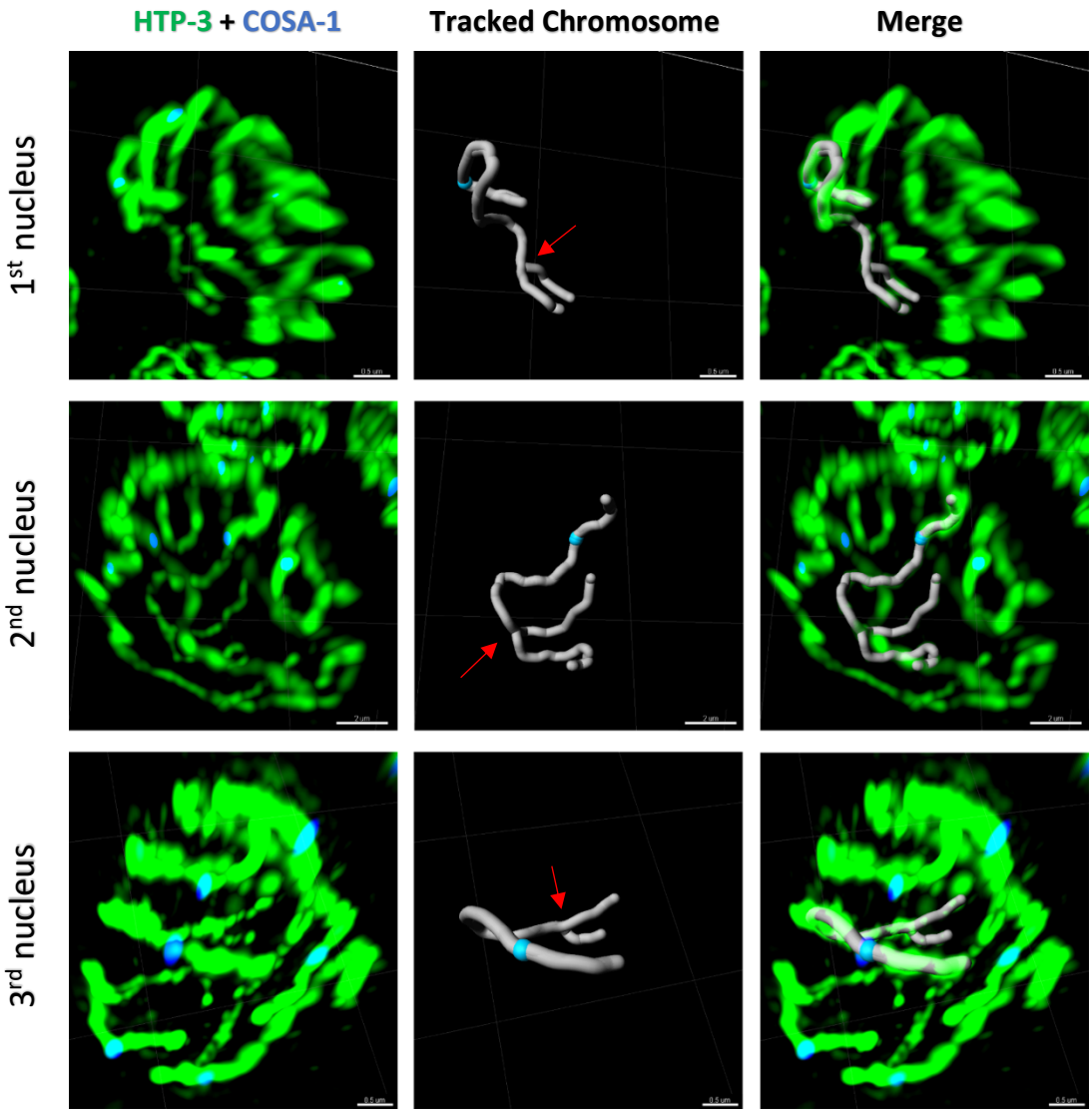
HTP-3 + COSA-1
Tracked Chromosome
Merge
1st nucleus
2nd nucleus
3rd nucleus

Figure 46. *wapl-1* mutant chromosomes, although smaller than wild type chromosomes, increase in length from early-mid pachytene to late pachytene

A - Distribution of chromosomes X length in *wapl-1* mutant at early-mid and late pachytene (n = 50 and n=44 respectively). Late pachytene chromosomes are clearly longer than early pachytene chromosomes.

B - Distribution of chromosomes III length in *wapl-1* mutant at early-mid and late pachytene (n = 50 and n=44 respectively). Autosomal chromosomes behave as the X chromosome, being late pachytene chromosomes longer than early-mid pachytene chromosomes.

C - Distribution of chromosomes V length in *wapl-1* mutant at early-mid and late pachytene (n = 50 and n=44 respectively). Autosomal chromosomes behave as the X chromosome, being late pachytene chromosomes longer than early-mid pachytene chromosomes.

D - Comparison of chromosome length averages in wapl-*1* mutant between the three chromosomes. Note the same trend is observed, early-mid chromosomes are shorter than late pachytene chromosomes.

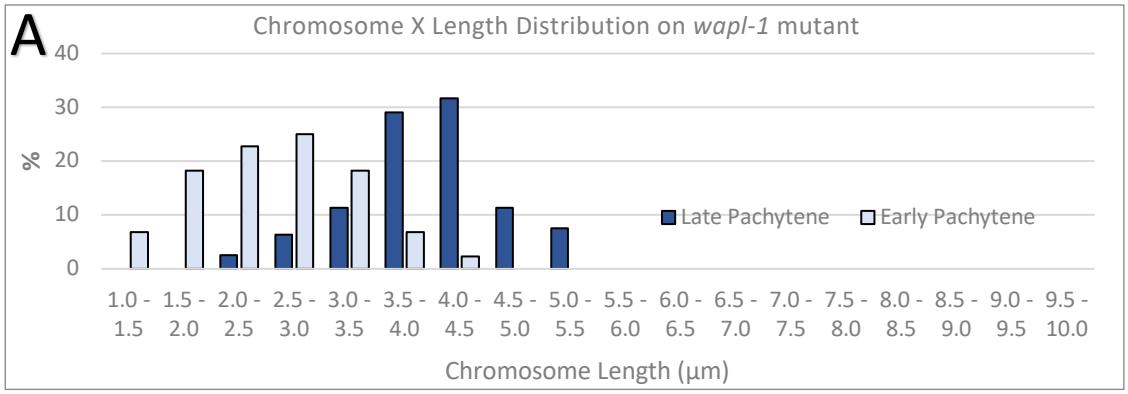
A
Chromosome X Length Distribution on wapl-1 mutant
%
40
30
20
10
0
Late Pachytene
Early Pachytene
1.0 - 1.5
1.5 - 2.0
2.0 - 2.5
2.5 - 3.0
3.0 - 3.5
3.5 - 4.0
4.0 - 4.5
4.5 - 5.0
5.0 - 5.5
5.5 - 6.0
6.0 - 6.5
6.5 - 7.0
7.0 - 7.5
7.5 - 8.0
8.0 - 8.5
8.5 - 9.0
9.0 - 9.5
9.5 - 10.0
Chromosome Length (µm)

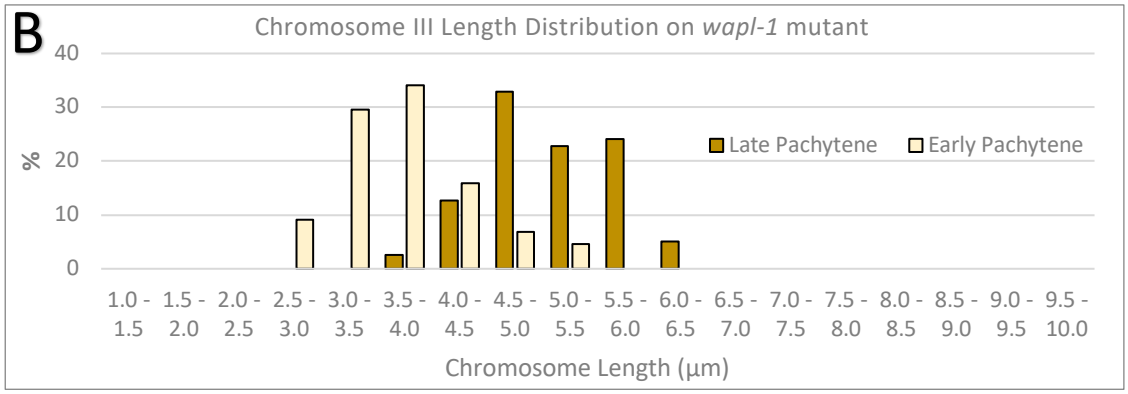
B
Chromosome III Length Distribution on wapl-1 mutant
%
40
30
20
10
0
Late Pachytene
Early Pachytene
1.0 - 1.5
1.5 - 2.0
2.0 - 2.5
2.5 - 3.0
3.0 - 3.5
3.5 - 4.0
4.0 - 4.5
4.5 - 5.0
5.0 - 5.5
5.5 - 6.0
6.0 - 6.5
6.5 - 7.0
7.0 - 7.5
7.5 - 8.0
8.0 - 8.5
8.5 - 9.0
9.0 - 9.5
9.5 - 10.0
Chromosome Length (µm)

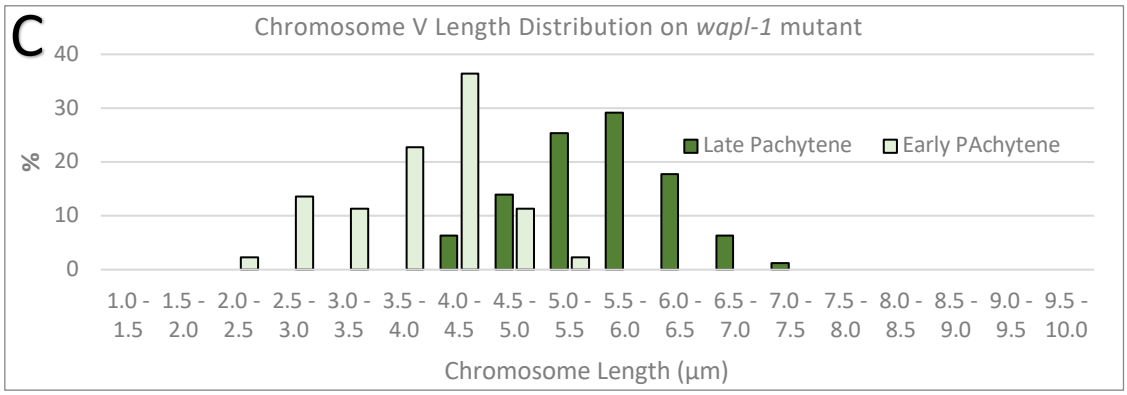
C
Chromosome V Length Distribution on wapl-1 mutant
%
40
30
20
10
0
Late Pachytene
Early PAchytene
1.0 - 1.5
1.5 - 2.0
2.0 - 2.5
2.5 - 3.0
3.0 - 3.5
3.5 - 4.0
4.0 - 4.5
4.5 - 5.0
5.0 - 5.5
5.5 - 6.0
6.0 - 6.5
6.5 - 7.0
7.0 - 7.5
7.5 - 8.0
8.0 - 8.5
8.5 - 9.0
9.0 - 9.5
9.5 - 10.0
Chromosome Length (µm)

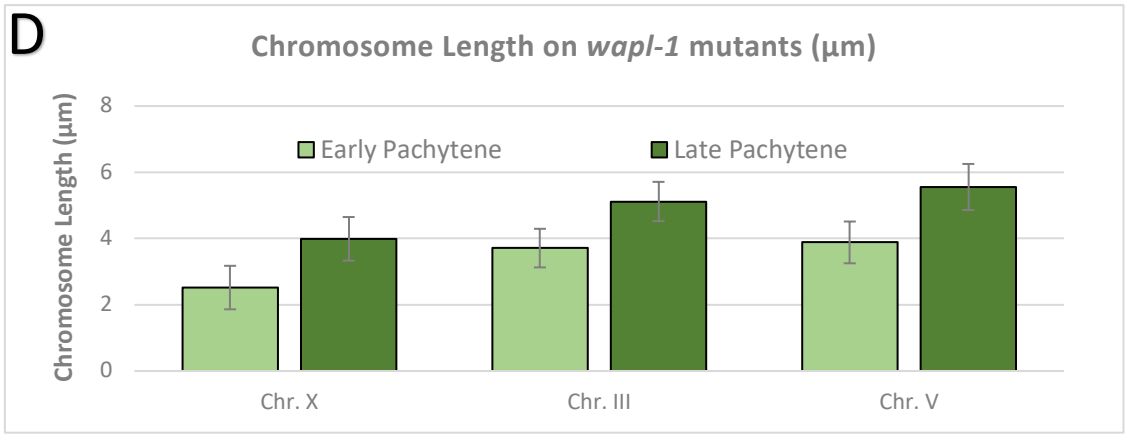
D
Chromosome Length on wapl-1 mutants (µm)
Chromosome Length (µm)
8
6
4
2
0
Early Pachytene
Late Pachytene
Chr. X
Chr. III
Chr. V

Figure 47. *wapl-1* mutant chromosomes are shorter than wild type chromosomes at both early-mid and late pachytene

A - Comparison of early-mid pachytene chromosome length averages between wild type and *wapl-1* mutant. Note that *wapl-1* mutant chromosomes are shorter than wild type chromosomes.

B - Comparison of late pachytene chromosome length averages between wild type and *wapl-1* mutant. Note the same trend is observed, *wapl-1* mutant chromosomes are shorter than wild type chromosomes.

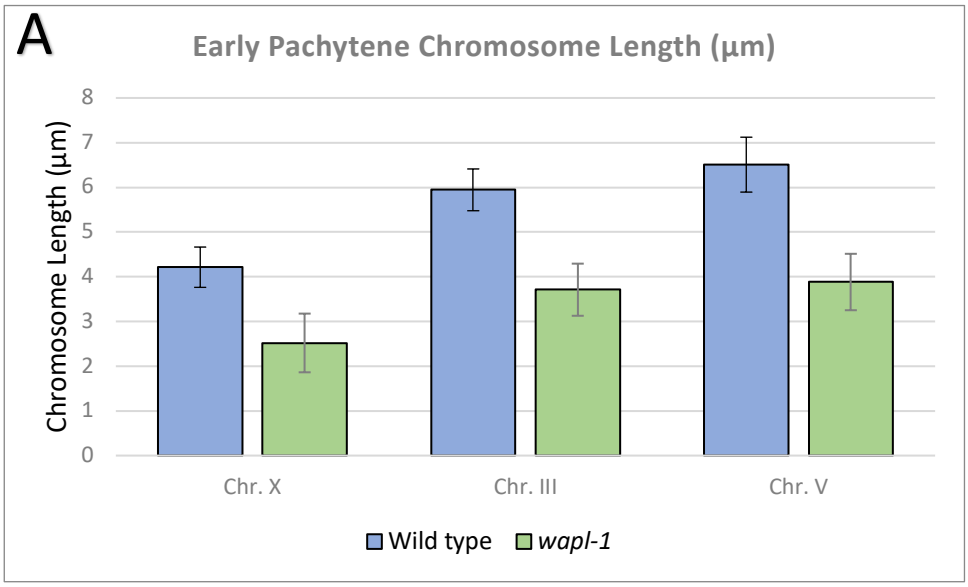
A
Early Pachytene Chromosome Length (µm)
Chromosome Length (µm)
8
7
6
5
4
3
2
1
0
Chr. X
Chr. III
Chr. V
Wild type
wapl-1

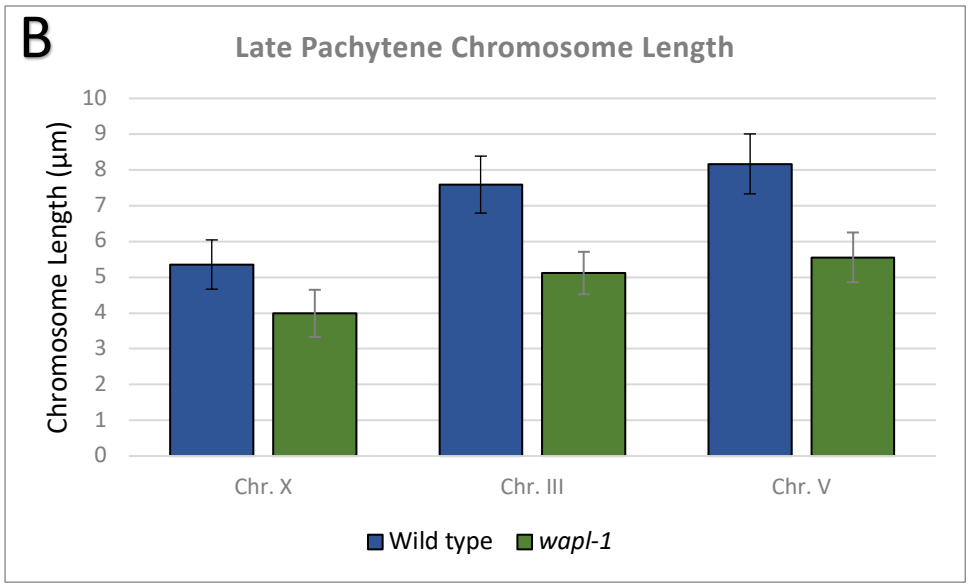
B
Late Pachytene Chromosome Length
Chromosome Length (µm)
10
9
8
7
6
5
4
3
2
1
0
Chr. X
Chr. III
Chr. V
Wild type
wapl-1

Figure 48. WAPL-1 may participate in coordinating chromosome length

XY plot graphs show how chromosome lengths are coordinated within the same nucleus in the *wapl-1* mutant.

A - XY plot graph representing pachytene chromosome length of chromosomes III and X withing the same nuclei. Early-mid pachytene chromosomes (n = 50) were indicated in green, whereas late pachytene chromosomes (n = 44) were indicated in orange. Linear regression was 0.69.

B - XY plot graph representing pachytene chromosome length of chromosomes III and V withing the same nuclei. Early-mid pachytene chromosomes (n = 50) were indicated in green, whereas late pachytene chromosomes (n = 44) were indicated in orange. Linear regression was 0.81.

C - XY plot graph representing pachytene chromosome length of chromosomes V and X withing the same nuclei. Early-mid pachytene chromosomes (n = 50) were indicated in green, whereas late pachytene chromosomes (n = 44) were indicated in orange. Linear regression was 0.80.

Plots were made by Amalia Martinez-Segura.

A

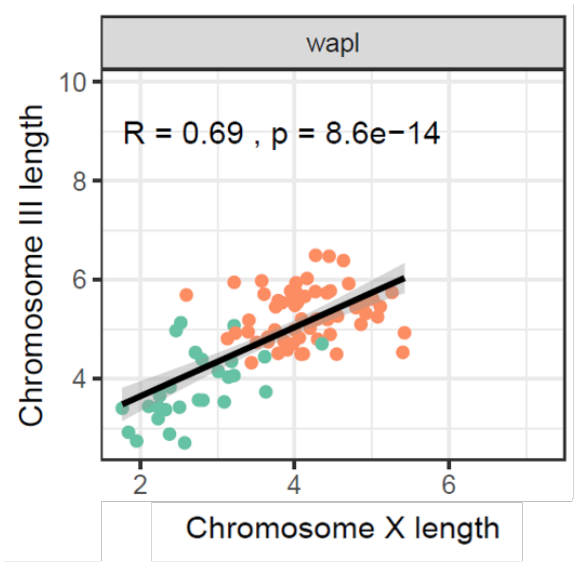
wapl
R = 0.69 , p = 8.6e−14
Chromosome III length
Chromosome X length
10
8
6
4
2
4
6

B

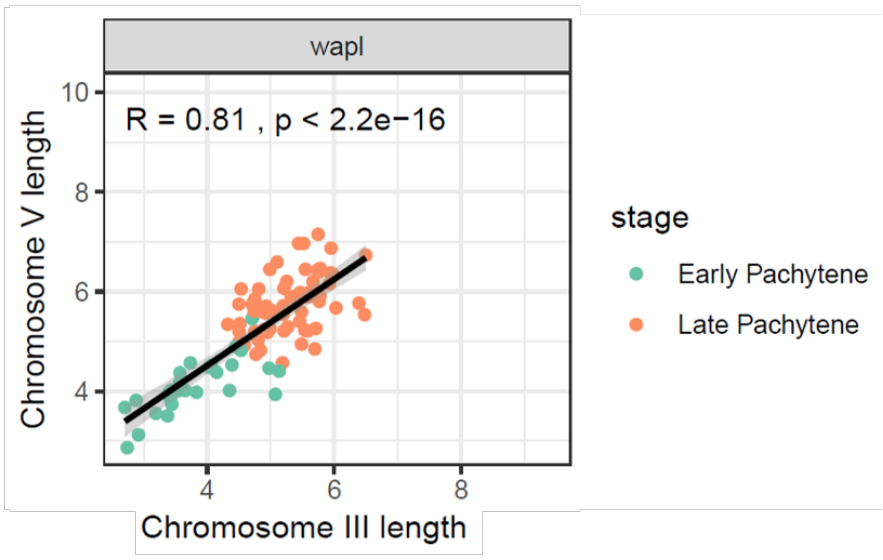
wapl
R = 0.81 , p < 2.2e−16
Chromosome V length
Chromosome III length
stage
Early Pachytene
Late Pachytene
10
8
6
4
4
6
8

C

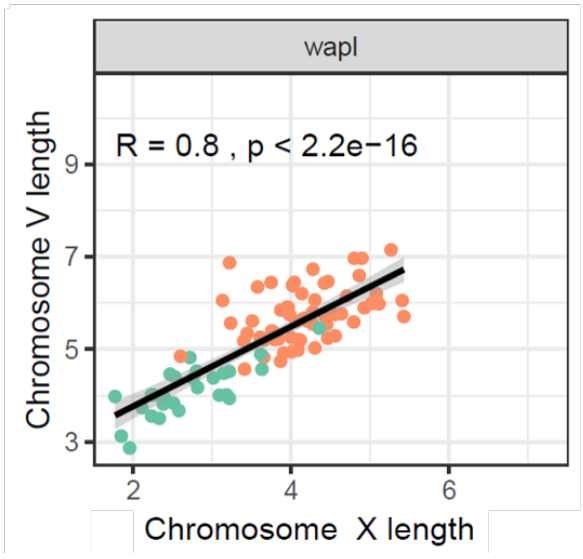
wapl
R = 0.8 , p < 2.2e−16
Chromosome V length
Chromosome X length
9
7
5
3
2
4
6

Figure 49. Analysis of CO distribution in *wapl-1* mutants using SIM

A - Graph comparing the wild type COSA-1 foci distribution against the *wapl-1* distribution among four equal-length intervals along Chr. X (n = 41 and n = 50 respectively).

B - Accumulative frequency plot comparing COSA-1 foci position along Chr. X from wild type and *wapl-1* mutant germ lines. These distributions were statistically equal (0.381, Kolmogorov-Smirnov test).

C - Graph comparing the wild type COSA-1 foci distribution against the *wapl-1* distribution among four equal-length intervals along Chr. III (n = 41 and n = 50 respectively).

D - Accumulative frequency plot comparing COSA-1 foci position along Chr. X from wild type and *wapl-1* mutant germ lines. These distributions were statistically equal (0.496, Kolmogorov-Smirnov test).

E - Graph comparing the wild type COSA-1 foci distribution against the *wapl-1* distribution among four equal-length intervals along Chr. V (n = 41 and n = 50 respectively).

F - Accumulative frequency plot comparing COSA-1 foci position along Chr. X from wild type and *wapl-1* mutant germ lines. These distributions were statistically equal (0.106, Kolmogorov-Smirnov test).

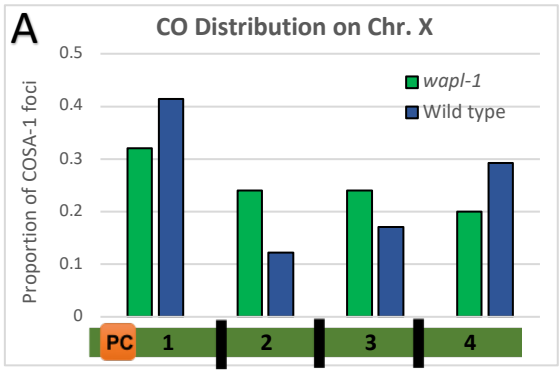
A
CO Distribution on Chr. X
Proportion of COSA-1 foci
0.5
0.4
0.3
0.2
0.1
0
wapl-1
Wild type
PC
1
2
3
4

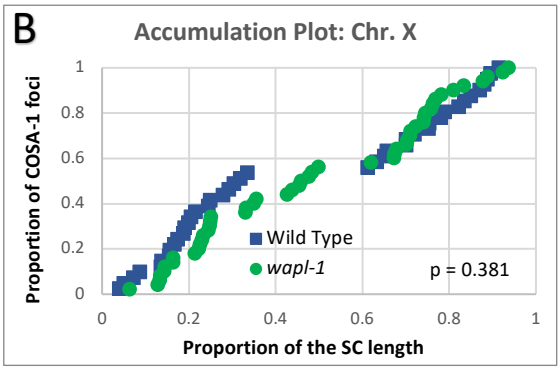
B
Accumulation Plot: Chr. X
Proportion of COSA-1 foci
1
0.8
0.6
0.4
0.2
0
0
0.2
0.4
0.6
0.8
1
Wild Type
wapl-1
p = 0.381
Proportion of the SC length

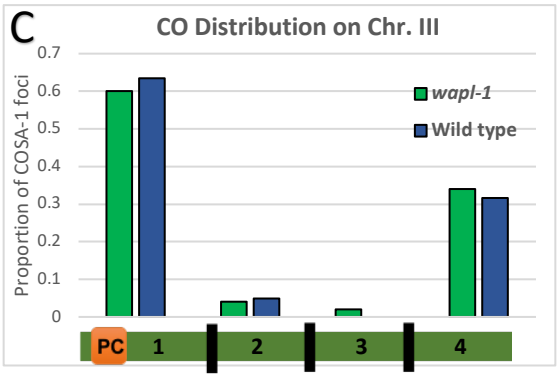
C
CO Distribution on Chr. III
Proportion of COSA-1 foci
0.7
0.6
0.5
0.4
0.3
0.2
0.1
0
wapl-1
Wild type
PC
1
2
3
4

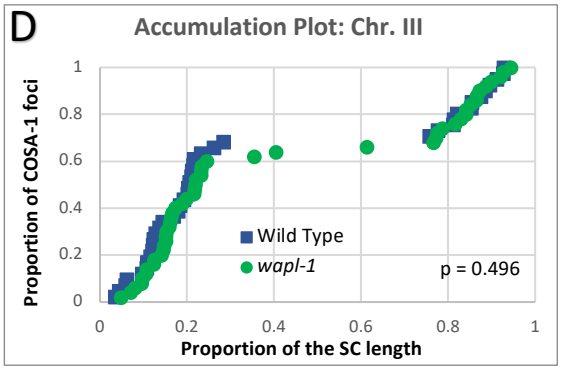
D
Accumulation Plot: Chr. III
Proportion of COSA-1 foci
1
0.8
0.6
0.4
0.2
0
0
0.2
0.4
0.6
0.8
1
Wild Type
wapl-1
p = 0.496
Proportion of the SC length

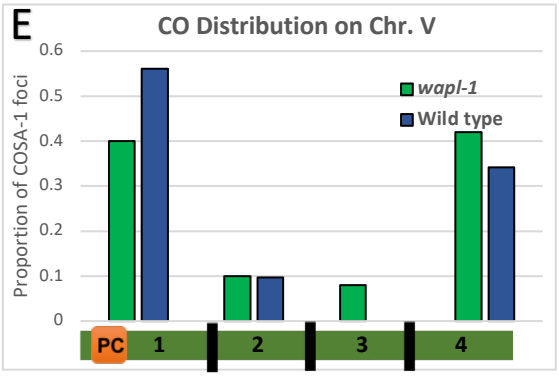
E
CO Distribution on Chr. V
Proportion of COSA-1 foci
0.6
0.5
0.4
0.3
0.2
0.1
0
wapl-1
Wild type
PC
1
2
3
4

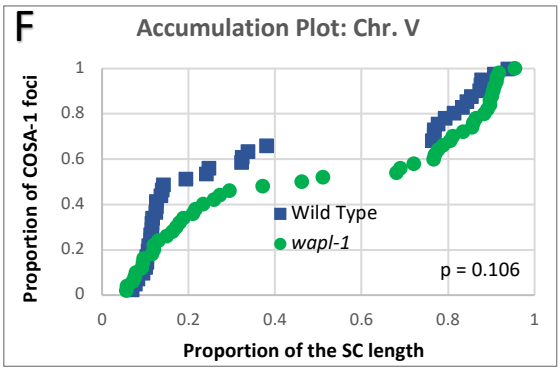
F
Accumulation Plot: Chr. V
Proportion of COSA-1 foci
1
0.8
0.6
0.4
0.2
0
0
0.2
0.4
0.6
0.8
1
Wild Type
wapl-1
p = 0.106
Proportion of the SC length

Figure 50. No differences in length observed between treated and untreated *dpy-26::degron* chromosomes

A - Graph comparing untreated *dpy-26::degron* early pachytene chromosomes against the untreated *dpy-26::degron* late pachytene chromosomes. Note that the same trend is observed, early-mid chromosomes are shorter than late pachytene chromosomes.

B - Graph comparing auxin treated *dpy-26::degron* early pachytene chromosomes against the auxin treated *dpy-26::degron* late pachytene chromosomes. Note that the same trend is observed, early-mid chromosomes are shorter than late pachytene chromosomes.

C - Graph comparing untreated *dpy-26::degron* early pachytene chromosomes against the auxin treated *dpy-26::degron* early pachytene chromosomes. No differences were observed between treated and untreated *dpy-26::degron* early pachytene chromosomes.

C - Graph comparing untreated *dpy-26::degron* late pachytene chromosomes against the auxin treated *dpy-26::degron* late pachytene chromosomes. No differences were observed between treated and untreated *dpy-26::degron* late pachytene chromosomes.

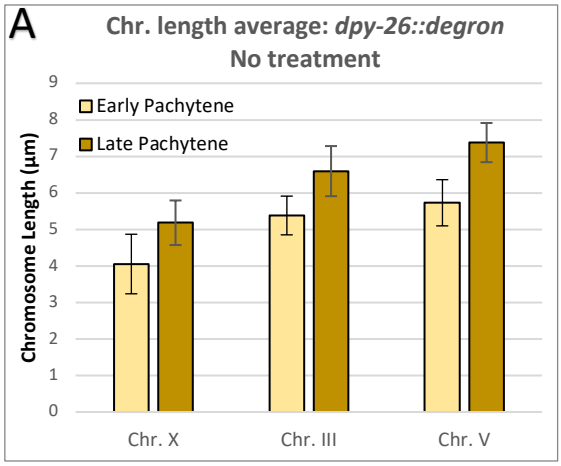
A
Chr. length average: dpy-26::degron
No treatment
Early Pachytene
Late Pachytene
Chromosome Length (µm)
0
1
2
3
4
5
6
7
8
9
Chr. X
Chr. III
Chr. V

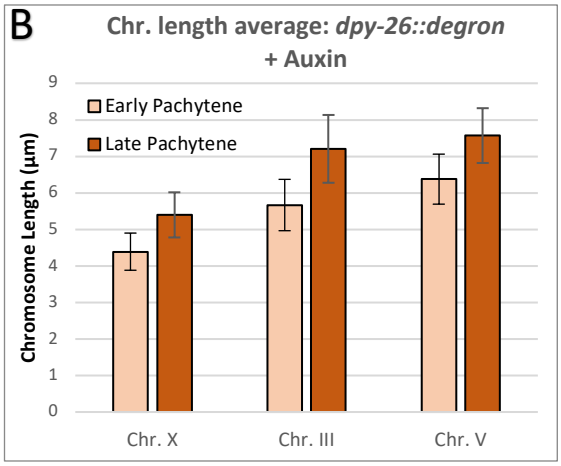
B
Chr. length average: dpy-26::degron
+ Auxin
Early Pachytene
Late Pachytene
Chromosome Length (µm)
0
1
2
3
4
5
6
7
8
9
Chr. X
Chr. III
Chr. V

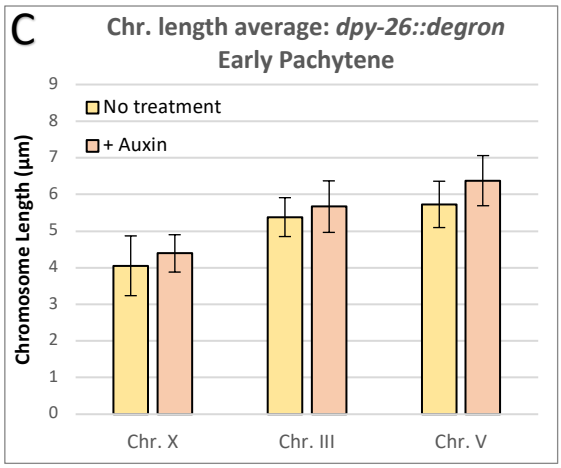
C
Chr. length average: dpy-26::degron
Early Pachytene
No treatment
+ Auxin
Chromosome Length (µm)
0
1
2
3
4
5
6
7
8
9
Chr. X
Chr. III
Chr. V

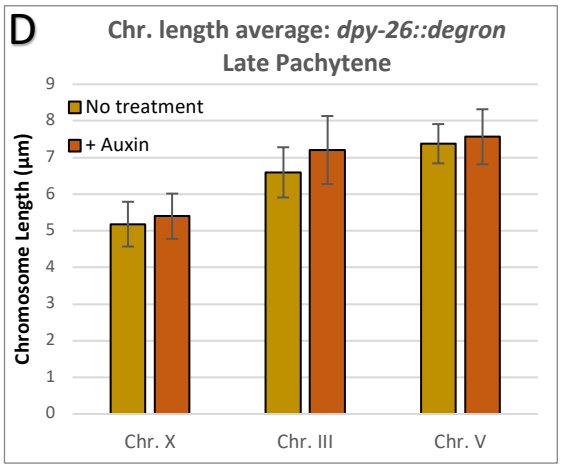
D
Chr. length average: dpy-26::degron
Late Pachytene
No treatment
+ Auxin
Chromosome Length (µm)
0
1
2
3
4
5
6
7
8
9
Chr. X
Chr. III
Chr. V

Figure 51. Preliminary data indicates that depletion of DPY-26 protein does not affect CO distribution

A - Graph comparing the auxin treated *dpy-26::degron* COSA-1 foci distribution against the untreated *mei-2::degron* distribution among four equal-length intervals along Chr. X (n = 49 and n = 49 respectively).

B - Accumulative frequency plot comparing COSA-1 foci position along Chr. X from untreated *dpy-26::degron* and auxin treated *dpy-26::degron* germ lines. These distributions were the same (0.200, Kolmogorov-Smirnov test).

C - Graph comparing the auxin treated *dpy-26::degron* COSA-1 foci distribution against the untreated *mei-2::degron* distribution among four equal-length intervals along Chr. III (n = 49 and n = 49 respectively).

D - Accumulative frequency plot comparing COSA-1 foci position along Chr. III from untreated *dpy-26::degron* and auxin treated *dpy-26::degron* germ lines. These distributions were the same (0.133, Kolmogorov-Smirnov test).

E - Graph comparing the auxin treated *dpy-26::degron* COSA-1 foci distribution against the untreated *mei-2::degron* distribution among four equal-length intervals along Chr. V (n = 49 and n = 49 respectively).

F - Accumulative frequency plot comparing COSA-1 foci position along Chr. V from untreated *dpy-26::degron* and auxin treated *dpy-26::degron* germ lines. These distributions were the same (0.672, Kolmogorov-Smirnov test).

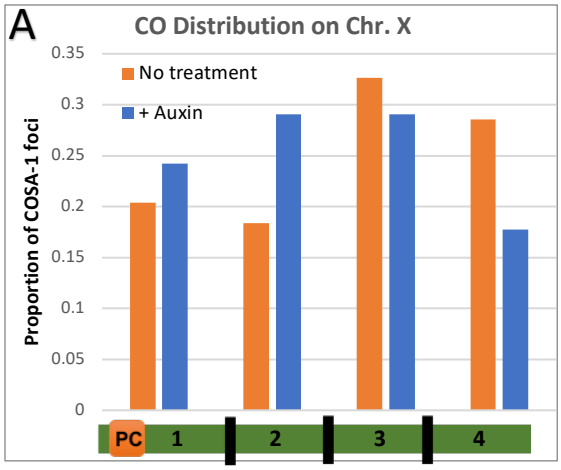
A
CO Distribution on Chr. X
Proportion of COSA-1 foci
0.35
0.3
0.25
0.2
0.15
0.1
0.05
0
No treatment
+ Auxin
PC
1
2
3
4

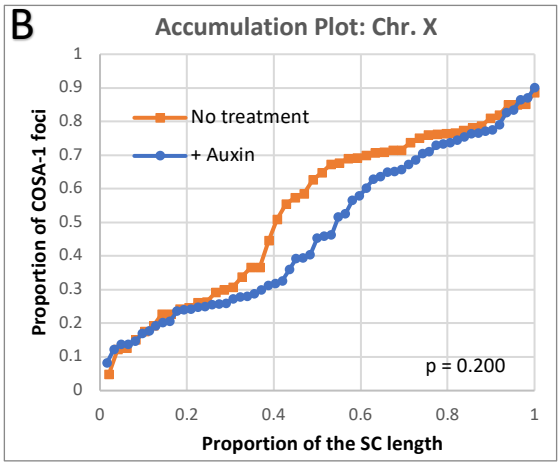
B
Accumulation Plot: Chr. X
Proportion of COSA-1 foci
1
0.9
0.8
0.7
0.6
0.5
0.4
0.3
0.2
0.1
0
No treatment
+ Auxin
p = 0.200
0
0.2
0.4
0.6
0.8
1
Proportion of the SC length

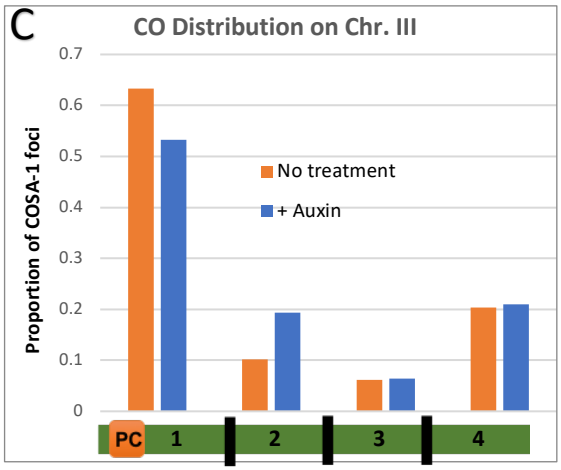
C
CO Distribution on Chr. III
Proportion of COSA-1 foci
0.7
0.6
0.5
0.4
0.3
0.2
0.1
0
No treatment
+ Auxin
PC
1
2
3
4

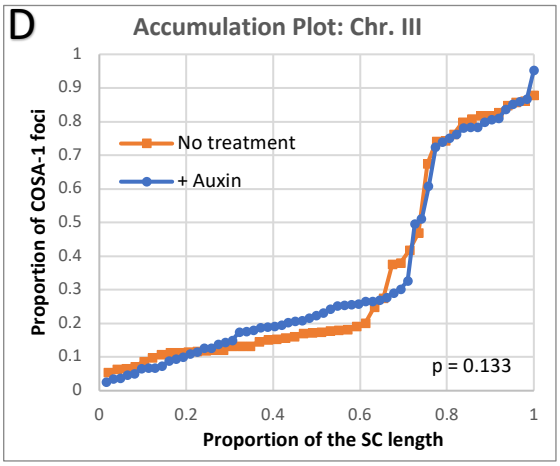
D
Accumulation Plot: Chr. III
Proportion of COSA-1 foci
1
0.9
0.8
0.7
0.6
0.5
0.4
0.3
0.2
0.1
0
No treatment
+ Auxin
p = 0.133
0
0.2
0.4
0.6
0.8
1
Proportion of the SC length

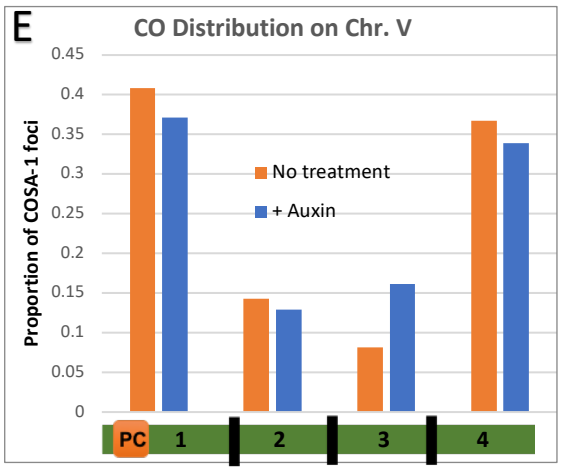
E
CO Distribution on Chr. V
Proportion of COSA-1 foci
0.45
0.4
0.35
0.3
0.25
0.2
0.15
0.1
0.05
0
No treatment
+ Auxin
PC
1
2
3
4

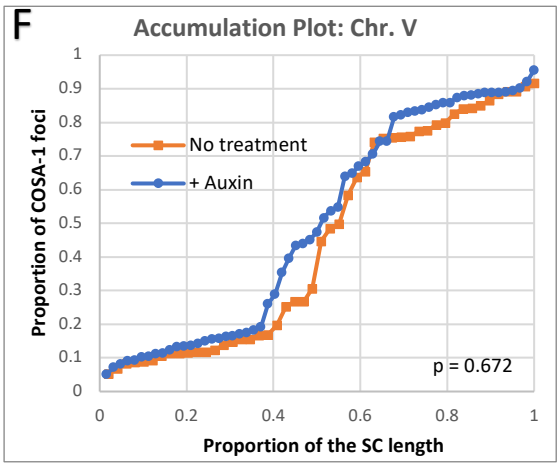
F
Accumulation Plot: Chr. V
Proportion of COSA-1 foci
1
0.9
0.8
0.7
0.6
0.5
0.4
0.3
0.2
0.1
0
No treatment
+ Auxin
p = 0.672
0
0.2
0.4
0.6
0.8
1
Proportion of the SC length

CHAPTER 7: DISCUSSION

7.1 Summary of findings

The first goal of my PhD was to use SRM to investigate the structural changes that meiotic chromosomes undergo during meiosis, focusing on the process of crossover formation during meiotic prophase. I demonstrated that both SIM and STED systems can resolve the axial elements from homologous chromosomes, which in pachytene nuclei are separated by a distance of around 120nm. Therefore, the methods used here provided a lateral resolution of at least 120 nm, well beyond the 200 nm limit of conventional wide-field microscopy. Then, I developed a method to map CO distribution in three-dimensionally intact meiotic nuclei by combining Imaris image software analysis with the SIM system to image CRISPR-generated strains in which CO sites were followed by tagging the COSA-1 protein. Tracking and orientation of individual chromosomes allows the detailed measurement of chromosome length throughout meiotic prophase, while in late pachytene nuclei this approach allows accurate identification of CO position along homologous axial elements. Using this method to analyse CO distribution on the X chromosomes, I observed striking similarities between the physical distribution of CO along late pachytene nuclei and the known genetic map of the X chromosome. Thus, mapping COs in three-dimensionally intact pachytene nuclei using SIM and Imaris image software analysis offers a powerful tool to investigate the regulation of CO distribution.

Besides mapping CO distribution, this technology offers further possibilities to investigate meiotic chromosome structure that I exploited in later sections of the thesis. First, I demonstrated that X chromosomes show a surprising level of variability in length between different pachytene nuclei. Then, I confirmed that this was also the case for the autosomes (chromosomes III and V). After this, I demonstrated under the experimental conditions employed that early pachytene chromosomes are shorter than late pachytene chromosomes, both in autosomes and the X chromosomes, suggesting that the transition to late pachytene involves a regulated extension of chromosomes. Moreover, I demonstrated that chromosome length was coordinated among

chromosomes within the same nucleus, indicating the presence of nucleus-autonomous mechanisms that regulate chromosome length.

I also exploited the SIM-Imaris method to start investigating how SMC complexes regulate chromosome structure during meiotic prophase. I began these functional studies by imaging meiotic chromosomes in *wapl-1* mutants, which were known to display shorter axial elements due to an excess in cohesin binding. First, I confirmed that *wapl-1* mutant chromosomes were shorter than wild type chromosomes. Moreover, *wapl-1* chromosomes were unexpectedly more variable in length than wild type chromosomes. Nonetheless, early-mid pachytene chromosomes were shorter than late pachytene chromosomes, similar to what I observed in wild-type nuclei, confirming that proteins other than WAPL-1 must be regulating this process. Preliminary results suggested that CO distribution was not altered in *wapl-1* mutants, however, more nuclei need to be acquired to confirm this result. The potential role of condensin I to prophase chromosome length was also investigated using the SIM-Imaris method and the auxin-degron system, which allows a rapid depletion of the tagged protein. However, depletion of condensin I using this approach did not affect chromosome length or CO distribution and is likely that larger depletion times are needed. Another possibility could be that the DPY-26::degron protein could not be degraded by the AID system. In conclusion, these studies confirmed that this three-dimensional method to measure chromosome length is a powerful tool that can be used for functional studies. Future studies will focus on investigating how different SMC complexes, including different cohesin, as well as Topo II, regulate chromosome structure during meiotic prophase.

The second goal of my PhD was to elucidate how the *him-13(e1742)* mutation, whose molecular identity was unknown, affects CO distribution and to determine if these changes in CO distribution were due to altered chromosome structure. In order to identify the molecular identity of the *him-13(e1742)* mutation I took several genetic approaches, which together confirmed that a mutation that results in a single amino acid substitution (E131K) in the *mei-2* gene is the responsible for the *him-13* phenotypes. MEI-2 is the *C. elegans* orthologue of p80, the non-catalytic subunit of the microtubule severing complex katanin. Thus, MEI-2, which had previously been shown to play a role

in the assembly of the meiotic spindle, appears to play an unexpected role in regulating CO distribution during meiotic prophase.

Following the identification of *him-13(e1742)* as *mei-2,* I started a functional characterisation of this mutant to understand why they display altered CO distribution. This demonstrated that early prophase stages were affected in *him-13(e1742)* mutants. Analysis of RAD-51 recombination intermediates suggested that DSB formation and/or the processing of these DSBs was delayed in *him-13* mutants. Supporting this idea, *him-13* mutants also displayed extension of the period when SPO-11 can make DSBs, as indicated by persistence of several CHK-2-dependent markers (DSB-2, PLK-2 on PCs, HIM-3 pS13, and HIM-8 pT64) in mid pachytene nuclei. These results evidenced a delay in early meiotic progression, which were likely due to an impairment in the early steps of recombination, as synaptonemal complex assembly appeared largely normal in *him-13* mutants. Crucially, delayed meiotic progression was also observed in CRISPR-generated *mei-2(fq37[E131K])* mutants and in auxin treated *mei-2::degron* germ lines, confirming that MEI-2 contributes to early prophase events. Moreover, using the SIM-Imaris method for CO mapping, I confirmed that MEI-2 is involved in regulating CO distribution and that CO interference remained unaffected. Initial analysis of the microtubule network surrounding early prophase nuclei failed to identify obvious defects, however, further experiments need to be performed to confirm this and to elucidate how MEI-2 promotes normal CO distribution.

7.2 SIM-Imaris method allows three-dimensional study of chromosome structure

When I started my project, one of the initial goals was to use SRM techniques to investigate meiotic chromosome structure. Since then, several studies using SRM have described different aspects of meiotic chromosome structure. For example, the SC has been studied in detail using SIM and PALM/STORM microscopy in *C. elegans* and *Drosophila* (Cahoon et al., 2017; Köhler et al., 2017; Woglar and Villeneuve, 2018). However, the methods used in these studies have clear differences in terms of acquisition and/or sample preparation compared to the method developed here. In the first *C. elegans* study, the authors studied the structure of the SC, obtaining a lateral

resolution of 10nm using a PALM/STORM system (Köhler et al., 2017). Nevertheless, this system does not allow the acquisition of whole three-dimensional intact nuclei, as imaging can only be done a few microns into the sample. In the second *C. elegans* study, the authors used a SIM system in combination with a nuclear spreading protocol that allows the visualization of recombination complexes in relationship with the SC (Woglar and Villeneuve, 2018). Although this protocol improves the visualisation of recombination complexes, the spreading process alters overall chromosome structure. In the *Drosophila* study, the SC was studied using a SIM system and a new technology called expansion microscopy (ExM)(Cahoon et al., 2017). Using this ExM gel, the biological sample is expanded, which makes it possible to resolve structures that without this procedure would be under the limit of resolution. Similar to the previous study, it enhances the visualisation of the structure by altering the sample.

In this study, I have developed a new method to investigate meiotic chromosome structure by combining SIM microscopy and a three-dimensional visualisation software (Imaris). Although the resolution that I obtained with this method is not as good as the resolution obtained with the methods of the studies described above, it has several advantages. First, the sample does not suffer any major disruption, allowing imaging of three-dimensional intact nuclei in relatively large numbers. Second, this method allows deeper imaging into the sample, making it possible to acquire two layers of whole-depth nuclei. Finally, this method allows the visualisation and tracking of three-dimensional linear structures, such as pachytene chromosomes, and to determine the position of specific events, such as CO sites, along chromosomes.

7.3 Differences in chromosome length between early-mid and late pachytene

Tracking and measurement of three different chromosomes (X, III, V) during meiotic prophase has revealed that chromosomes become longer as nuclei progress from early to late pachytene (figure 43D). Interestingly, a similar difference between early and late pachytene chromosomes have been described in mice (Vranis et al., 2010). In this study, the authors proposed that this difference in length could be explained by different levels of cohesin. However, I also observe chromosome elongation between early-mid and late

pachytene *wapl-1* mutants, which display overall increase in cohesin binding from the onset of meiosis (Crawley et al., 2016) (figure 46D). Although this result does not discard the possibility that regulation of cohesin binding is involved in chromosome elongation during late pachytene, it implies that players other than WAPL-1 must regulate this process. Interestingly, it has been proposed that CO formation expands chromosome axis locally in *C. elegans* (Libuda et al., 2013), suggesting that CO formation could be the responsible for increasing chromosome length in late pachytene. However, this conclusion was reached by measuring late pachytene chromosomes length in situations with different CO numbers (COSA-1 foci), and also the length of a specific interval on the X chromosome in the presence and absence of COs in that region. Comparisons with early pachytene nuclei were not possible as the measurements required the presence of COSA-1 foci at CO sites, which are only present in late pachytene. Therefore, whether CO-triggered axis extension is responsible for the global increase in chromosome length that I report here, or whether this is caused by a different mechanism remains to be elucidated. One way of addressing this will be to compare early and late pachytene nuclei of *spo-11* mutants. If chromosomes still show elongation at late pachytene this will suggest that the process is independent of recombination. On the other hand, if *spo-11* mutants do not undergo chromosome extension at late pachytene this will suggest that DSBs or COs intermediates are required for the global extension. Analysis of chromosome length in *cosa-1* mutants, which make DSBs but fail to form COs (Yokoo et al., 2012), should clarify this point. I plan to perform these experiments in the near future.

7.4 Chromosome length control during pachytene

I have confirmed that the WAPL-1 cohesin removal factor plays an important role in regulating chromosome size during early prophase, demonstrating the key role that cohesin plays in meiotic chromosome structure. However, cohesin is not thought to be the only player controlling chromosome architecture. For this reason, I decided to investigate condensin, another well-known regulator of chromosome length (Mets and Meyer, 2009). In the Mets and Meyer´s study, heterozygous condensin mutants were studied, showing that a partial reduction in condensin I or II from the onset of meiosis

caused expansion of chromosome axis. I wanted to investigate if rapid removal of condensin I from pachytene chromosomes that had undergone normal morphogenesis at the onset of meiosis would impact chromosome length. However, no clear differences were detected in these preliminary experiments. Larger times of condensin I depletion will need to be used in the future to clarify the timing of condensin I action during meiotic prophase in *C. elegans*.

Both condensin and cohesin appear to affect chromosome length by condensing chromosomes. For example, *wapl-1* mutants, which have an excess of cohesin associated with chromosomes, display shorter axial elements (Crawley et al., 2016), while heterozygous condensin mutants, which have lower amount of condensin loaded onto the chromosomes, show longer axial elements (Mets and Meyer, 2009). A recent study shows that condensin shields cohesin complexes from WAPL-1 removal during meiosis in *C. elegans* (Hernandez et al., 2018). This surprising finding could explain why both complexes behave in the same way. It could also mean that the shortening of axial elements observed in heterozygous condensin mutants may be caused by an indirect loss of cohesin. Further experiments would help to understand the differences between both SMC complexes regarding chromosome structure and the functional relationship between them.

In addition to condensin and cohesin, there are other potential candidates that are expected to regulate chromosome structure during meiotic prophase, including topoisomerase II and CENPA. In mammals, topoisomerase II is associated with meiotic chromosome axes, and defects in topoisomerase II cause problems in chromosome condensation and segregation (Gómez et al., 2014). Importantly, ongoing experiments in our laboratory with the auxin-degron system have demonstrated that topoisomerase II has a role in shortening chromosomes during diplotene. Moreover, a similar role for topoisomerase II in promoting chromosome shortening during the mitotic divisions of the *C. elegans* embryo has recently been reported (Ladouceur et al., 2017). This study also identified the histone H3 variant CENPA as a factor that regulates mitotic chromosome length, as depletion led to shorter chromosomes (Ladouceur et al., 2017). CENPA starts associating with meiotic chromosome during diplotene in *C. elegans* (Monen et al., 2005), suggesting that the interplay between CENPA and topoisomerase

II observed in mitosis may also occur during late meiotic prophase. I plan to perform these experiments in the future using the SIM-Imaris method.

7.5 How does MEI-2 regulate CO distribution?

As MEI-2 is a component of the microtubule severing complex katanin, the simplest way of explaining how a mutation in MEI-2 can affect CO distribution is through disrupting microtubule architecture in the germ line, which could affect chromosome movement during early prophase. Microtubules are essential for the chromosome movement that promote pairing and synapsis (Sato et al., 2009). Moreover, *sun-1* mutants, which have major problems in chromosome movement due to a failure in connecting chromosomes to the cytoskeleton, have defects in CO formation, demonstrating that chromosome movement promotes recombination (Penkner et al., 2007, 2009). These chromosome movements are conserved across species and they have been proposed to shape CO landscape by generating waves along homologous chromosomes that facilitate CO formation (Hultén, 2011), and in yeast functional interplay between chromosome movement and recombination has been demonstrated (Conrad et al., 2008; Koszul et al., 2008).

Therefore, it would be important to investigate both chromosome movement and the microtubule network in *mei-2* mutants. To do this, I crossed *mei-2* mutants with a strain carrying the SUN-1::GFP transgene (Penkner et al., 2007). This strain can be used to record chromosome movement *in vivo* and analyse if there was any difference between the *mei-2* mutant and the wild type. Unfortunately, due to time constrains I could not perform this experiment before writing the thesis. Another important point will be to determine how the E131K mutation affects the activity of MEI-2 on microtubules, which could be achieved using biochemical methods to measure katanin activity as described in (Joly et al., 2016). Furthermore, it would be interesting to investigate the reason why CO distribution appear to be different in *him-13(e1742)* and *mei-2(fq37[E131K])* mutant strains. One possible explanation for this phenotype would be that the protein levels of MEI-2 were different in both strains, despite being the same mutated protein. Another possibility would be that katanin had different levels of activity in each strain, for

example if the *him-13(e1742)* strain had accumulated other mutations in the background that could affect the activity of katanin. Both hypotheses would imply that variations in the levels of activity/expression of Katanin modulate CO distribution. If this is correct, it should be possible to find mutations in other microtubule-severing enzymes or microtubule-associated proteins that affect CO distribution.

Based on the known function of MEI-2 (p80) as part of katanin in different organisms, it seems unlikely that MEI-2 affects CO distribution in *C. elegans* by a non-canonical role. Determining if impairing MEI-1 (catalytic subunit of katanin) function causes altered CO distribution should help clarifying this point. However, experiments described here can not formally rule out that MEI-2 affects CO distribution independently of its role in Katanin. Interestingly, several cytoskeletal proteins have been found in the nucleus performing different roles compared to their known cytoplasmatic activity (Spichal and Fabre, 2017). For example, FIDGETIN-LIKE-1 (FIGNL1), a paralogous protein of fidgetin, has been shown to participate with RAD51 in homologous recombination in mammals (Yuan and Chen, 2013). In *A. thaliana*, it has also been shown that FIGL1 regulates dynamics of DMC1 and RAD51 recombinases in meiosis (Fernandes et al., 2018; Girard et al., 2015). This is a surprising result because it shows that FIGL1, a severing-microtubule enzyme as katanin, has a role not related with its canonical function. Similar to the *him-13(e1742)* mutant, CO distribution and RAD-51 numbers are affected in the *figl1* mutant. Nevertheless, the *figl1* mutant also displays an increase in the number of COs, a phenotype that is not observed in the *him-13(e1742)* (Fernandes et al., 2018; Girard et al., 2015). However, it is important to considerate that *C. elegans* shows complete CO interference, making it more difficult to reproduce this phenotype in this animal model.

An important question to address that would help to clarify the role of MEI-2 in CO distribution is to identify the specific recombination step affected by MEI-2. Based on my functional analysis of *mei-2* mutants, this step is likely to be either DSB formation or CO designation. Inducing artificial DSBs in a *spo-11* mutant background (no endogenous DSBs) will help to distinguish between these possibilities (Yokoo et al., 2012). If irradiated *mei-2; spo-11* double mutants show the same CO distribution as irradiated

spo-11 single mutants, this would suggest that MEI-2 is not involved in CO designation and is more likely to affect DSB formation by altering DSB number and/or location.

REFERENCES

- Abbe, E. (1873). Beiträge zur Theorie des Mikroskops und der mikroskopischen Wahrnehmung: I. Die Construction von Mikroskopen auf Grund der Theorie. Arch. Für Mikroskopische Anat.
- Agostinho, A., Meier, B., Sonneville, R., Jagut, M., Woglar, A., Blow, J., Jantsch, V., and Gartner, A. (2013). Combinatorial Regulation of Meiotic Holliday Junction Resolution in C. elegans by HIM-6 (BLM) Helicase, SLX-4, and the SLX-1, MUS-81 and XPF-1 Nucleases. PLoS Genet. *9*, 1–19.
- Ahmad, F.J., Yu, W., McNally, F.J., and Baas, P.W. (2000). An essential role for katanin in severing microtubules in the neuron. J. Cell Biol. *145*, 305–315.
- Alexandratos, N., and Bruinsma, J. (2012). World agriculture towards 2030/2050.
- Alpi, A., Pasierbek, P., Gartner, A., and Loidl, J. (2003). Genetic and cytological characterization of the recombination protein RAD-51 in Caenorhabditis elegans. Chromosoma *112*, 6–16.
- Anderson, E.L., Baltus, A.E., Roepers-Gajadien, H.L., Hassold, T.J., de Rooij, D.G., van Pelt, A.M.M., and Page, D.C. (2008). Stra8 and its inducer, retinoic acid, regulate meiotic initiation in both spermatogenesis and oogenesis in mice. Proc. Natl. Acad. Sci. *105*, 14976–14980.
- Anderson, L.K., Reeves, A., Webb, L.M., and Ashley, T. (1999). Distribution of crossing over on mouse synaptonemal complexes using immunofluorescent localization of MLH1 protein. Genetics.
- Aravind, L., and Koonin, E. V. (1998). The HORMA domain: a common structural denominator in mitotic checkpoints, chromosome synapsis and DNA repair. Trends Biochem. Sci. *23*, 284–286.
- Arribere, J.A., Bell, R.T., Fu, B.X.H., Artiles, K.L., Hartman, P.S., and Fire, A.Z. (2014). Efficient marker-free recovery of custom genetic modifications with CRISPR/Cas9 in Caenorhabditis elegans. Genetics *198*, 837–846.
- Baddeley, D., and Bewersdorf, J. (2017). Biological Insight from Super-Resolution Microscopy: What We Can Learn from Localization-Based Images. Annu. Rev. Biochem.
- Baltus, A.E., Menke, D.B., Hu, Y.C., Goodheart, M.L., Carpenter, A.E., De Rooij, D.G., and Page, D.C. (2006). In germ cells of mouse embryonic ovaries, the decision to enter meiosis precedes premeiotic DNA replication. Nat. Genet. *38*, 1430–1434.
- Barber, L.J., Youds, J.L., Ward, J.D., McIlwraith, M.J., O'Neil, N.J., Petalcorin, M.I.R., Martin, J.S., Collis, S.J., Cantor, S.B., Auclair, M., et al. (2008). RTEL1 Maintains Genomic Stability by Suppressing Homologous Recombination. Cell *135*, 261–271.
- Barnes, T.M., Kohara, Y., Coulson, A., and Hekimi, S. (1995). Meiotic recombination, noncoding DNA and genomic organization in Caenorhabditis elegans. Genetics *141*, 159–179.
- Baudat, F., and Nicolas, A. (1997). Clustering of meiotic double-strand breaks on yeast chromosome III. Proc. Natl. Acad. Sci. U. S. A. *94*, 5213–5218.
- Baudat, F., Buard, J., Grey, C., Fledel-Alon, A., Ober, C., Przeworski, M., Coop, G., and de Massy, B. (2010). PRDM9 is a major determinant of meiotic recombination hotspots in humans and mice. Science *327*, 836–840.
- Beadle, G.W., and Ker, W.G. (1931). A possible influence of the spindle fibre on crossing-over in Drosophila. Proc. Natl. Acad. Sci. *18*, 160–165.
- Beard, S.M., Smit, R.B., Chan, B.G., and Mains, P.E. (2016). Regulation of the MEI-1/MEI-2 Microtubule-

Severing Katanin Complex in Early Caenorhabditis elegans Development. G3: Genes|Genomes|Genetics.

- Berchowitz, L.E., and Copenhaver, G.P. (2010). Genetic interference: don't stand so close to me. Curr. Genomics *11*, 91–102.
- Berchowitz, L.E., Francis, K.E., Bey, A.L., and Copenhaver, G.P. (2007). The role of AtMUS81 in interference-insensitive crossovers in A. thaliana. PLoS Genet. *3*, 1355–1364.
- Bergerat, A., De Massy, B., Gadelle, D., Varoutas, P.C., Nicolas, A., and Forterre, P. (1997). An atypical topoisomerase II from archaea with implications for meiotic recombination. Nature *386*, 414–417.
- Bhalla, N., Wynne, D.J., Jantsch, V., and Dernburg, A.F. (2008). ZHP-3 acts at crossovers to couple meiotic recombination with synaptonemal complex disassembly and bivalent formation in C. elegans. PLoS Genet. *4*.
- Biggins, S., and Walczak, C.E. (2003). Captivating capture: How microtubules attach to kinetochores. Curr. Biol. *13*.
- Bishop, D.K., and Zickler, D. (2004). Early decision: Meiotic crossover interference prior to stable strand exchange and synapsis. Cell *117*, 9–15.
- Bishop, D.K., Park, D., Xu, L., and Kleckner, N. (1992). DMC1: A meiosis-specific yeast homolog of E. coli recA required for recombination, synaptonemal complex formation, and cell cycle progression. Cell *69*, 439–456.
- Black, Brock, Bédard, Woods, and Cleveland (2007). An epigenetic mark generated by the incorporation of CENP-A into centromeric nucleosomes. Proc. Natl. Acad. Sci. U. S. A.
- Blary, A., and Jenczewski, E. (2019). Manipulation of crossover frequency and distribution for plant breeding. Theor. Appl. Genet.
- Boateng, K.A., Bellani, M.A., Gregoretti, I. V., Pratto, F., and Camerini-Otero, R.D. (2013). Homologous Pairing Preceding SPO11-Mediated Double-Strand Breaks in Mice. Dev. Cell *24*, 196–205.
- Bolaños-Villegas, P., De, K., Pradillo, M., Liu, D., and Makaroff, C.A. (2017). In Favor of Establishment: Regulation of Chromatid Cohesion in Plants. Front. Plant Sci. *8*.
- Borde, V., and de Massy, B. (2013). Programmed induction of DNA double strand breaks during meiosis: Setting up communication between DNA and the chromosome structure. Curr. Opin. Genet. Dev. *23*, 147–155.
- Borde, V., Goldman, A.S.H., and Lichten, M. (2000). Direct coupling between meiotic DNA replication and recombination initiation. Science (80-.). *290*, 806–809.
- Borde, V., Robine, N., Lin, W., Bonfils, S., Géli, V., and Nicolas, A. (2009). Histone H3 lysine 4 trimethylation marks meiotic recombination initiation sites. EMBO J. *28*, 99–111.
- Börner, G.V., Kleckner, N., and Hunter, N. (2004). Crossover/noncrossover differentiation, synaptonemal complex formation, and regulatory surveillance at the leptotene/zygotene transition of meiosis. Cell *117*, 29–45.
- Bowles, J., Knight, D., Smith, C., Wilhelm, D., Richman, J., Mamiya, S., Yashiro, K., Chawengsaksophak, K., Wilson, M.J., Rossant, J., et al. (2006). Retinoid signaling determines germ cell fate in mice. Science *312*, 596–600.
- Brenner, S. (1974). The genetics of Caenorhabditis elegans. Genetics *77*, 71–94.
- Brick, K., Smagulova, F., Khil, P., Camerini-Otero, R.D., and Petukhova, G. V. (2012). Genetic recombination is directed away from functional genomic elements in mice. Nature *485*, 642–645.

- Brieño-Enríquez, M.A., Moak, S.L., Toledo, M., Filter, J.J., Gray, S., Barbero, J.L., Cohen, P.E., and Holloway, J.K. (2016). Cohesin Removal along the Chromosome Arms during the First Meiotic Division Depends on a NEK1-PP1γ-WAPL Axis in the Mouse. Cell Rep.
- Broman, K.W., Rowe, L.B., Churchill, G.A., and Paigen, K. (2002). Crossover interference in the mouse. Genetics *160*, 1123–1131.
- Buard, J., Barthès, P., Grey, C., and De Massy, B. (2009). Distinct histone modifications define initiation and repair of meiotic recombination in the mouse. EMBO J. *28*, 2616–2624.
- Burkhardt, S., Borsos, M., Szydlowska, A., Godwin, J., Williams, S.A., Cohen, P.E., Hirota, T., Saitou, M., and Tachibana-Konwalski, K. (2016). Chromosome Cohesion Established by Rec8-Cohesin in Fetal Oocytes is Maintained without Detectable Turnover in Oocytes Arrested for Months in Mice. Curr. Biol.
- Bzymek, M., Thayer, N.H., Oh, S.D., Kleckner, N., and Hunter, N. (2010). Double holliday junctions are intermediates of DNA break repair. Nature *464*, 937–941.
- Cahoon, C.K., and Hawley, R.S. (2016). Regulating the construction and demolition of the synaptonemal complex. Nat. Struct. Mol. Biol. *23*, 369–377.
- Cahoon, C.K., Yu, Z., Wang, Y., Guo, F., Unruh, J.R., Slaughter, B.D., and Hawley, R.S. (2017). Superresolution expansion microscopy reveals the three-dimensional organization of the *Drosophila* synaptonemal complex. Proc. Natl. Acad. Sci. 201705623.
- Cai, X. (2003). The Arabidopsis SYN1 cohesin protein is required for sister chromatid arm cohesion and homologous chromosome pairing. J. Cell Sci.
- Callan, H.G. (1973). Replication of dna in eukaryotic chromosomes. Br. Med. Bull. *29*, 192–195.
- Carlton, P.M. (2008). Three-dimensional structured illumination microscopy and its application to chromosome structure. Chromosom. Res.
- Carlton, P.M. (2013). Application of advanced fluorescence microscopy to the structure of meiotic chromosomes. Biophys. Rev.
- De Carvalho, C.E., Zaaijer, S., Smolikov, S., Gu, Y., Schumacher, J.M., and Colaiácovo, M.P. (2008). LAB-1 antagonizes the Aurora B kinase in C. elegans. Genes Dev.
- Cha, R.S., Weiner, B.M., Keeney, S., Dekker, J., and Kleckner, N. (2000). Progression of meiotic DNA replication is modulated by interchromosomal interaction proteins, negatively by Spo11p and positively by Rec8p. Genes Dev. *14*, 493–503.
- Challa, K., Lee, M.S., Shinohara, M., Kim, K.P., and Shinohara, A. (2016). Rad61/Wpl1 (Wapl), a cohesin regulator, controls chromosome compaction during meiosis. Nucleic Acids Res.
- Checchi, P.M., Lawrence, K.S., Van, M. V., Larson, B.J., and Engebrecht, J. (2014). Pseudosynapsis and decreased stringency of meiotic repair pathway choice on the hemizygous sex chromosome of Caenorhabditis elegans males. Genetics *197*, 543–560.
- Cheng, C.H., Lo, Y.H., Liang, S.S., Ti, S.C., Lin, F.M., Yeh, C.H., Huang, H.Y., and Wang, T.F. (2006). SUMO modifications control assembly of synaptonemal complex and polycomplex in meiosis of Saccharomyces cerevisiae. Genes Dev. *20*, 2067–2081.
- Chin, G.M., and Villeneuve, A.M. (2001). C. elegans mre-11 is required for meiotic recombination and DNA repair but is dispensable for the meiotic G2 DNA damage checkpoint. Genes Dev. *15*, 522–534.
- Chuang, P.T., Albertson, D.G., and Meyer, B.J. (1994). DPY-27: A chromosome condensation protein homolog that regulates C. elegans dosage compensation through association with the X chromosome. Cell.

- Colaiácovo, M.P., MacQueen, A.J., Martinez-Perez, E., McDonald, K., Adamo, A., La Volpe, A., and Villeneuve, A.M. (2003). Synaptonemal complex assembly in C. elegans is dispensable for loading strand-exchange proteins but critical for proper completion of recombination. Dev. Cell *5*, 463–474.
- Cole, F., Kauppi, L., Lange, J., Roig, I., Wang, R., Keeney, S., and Jasin, M. (2012). Homeostatic control of recombination is implemented progressively in mouse meiosis. Nat. Cell Biol. *14*, 424–430.
- Conrad, M.N., Lee, C.Y., Chao, G., Shinohara, M., Kosaka, H., Shinohara, A., Conchello, J.A., and Dresser, M.E. (2008). Rapid Telomere Movement in Meiotic Prophase Is Promoted By NDJ1, MPS3, and CSM4 and Is Modulated by Recombination. Cell.
- Couteau, F., and Zetka, M. (2005). HTP-1 coordinates synaptonemal complex assembly with homolog alignment during meiosis in C. elegans. Genes Dev. *19*, 2744–2756.
- Crawley, O., Barroso, C., Testori, S., Ferrandiz, N., Silva, N., Castellano-Pozo, M., Jaso-Tamame, A.L., and Martinez-Perez, E. (2016a). Cohesin-interacting protein WAPL-1 regulates meiotic chromosome structure and cohesion by antagonizing specific cohesin complexes. Elife *5*, 1–44.
- Crittenden, S.L., Eckmann, C.R., Wang, L., Bernstein, D.S., Wickens, M., and Kimble, J. (2003). Regulation of the mitosis/meiosis decision in the Caenorhabditis elegans germline. Philos. Trans. R. Soc. B Biol. Sci. *358*, 1359–1362.
- Cromie, G.A., Hyppa, R.W., Taylor, A.F., Zakharyevich, K., Hunter, N., and Smith, G.R. (2006). Single Holliday Junctions Are Intermediates of Meiotic Recombination. Cell *127*, 1167–1178.
- Csankovszki, G., Collette, K., Spahl, K., Carey, J., Snyder, M., Petty, E., Patel, U., Tabuchi, T., Liu, H., McLeod, I., et al. (2009a). Three Distinct Condensin Complexes Control C. elegans Chromosome Dynamics. Curr. Biol. *19*, 9–19.
- Csankovszki, G., Petty, E.L., and Collette, K.S. (2009b). The worm solution: A chromosome-full of condensin helps gene expression go down. Chromosom. Res. *17*, 621–635.
- Dan, D., Yao, B., and Lei, M. (2014). Structured illumination microscopy. In Optical Nanoscopy and Novel Microscopy Techniques, p.
- Daniel, K., Lange, J., Hached, K., Fu, J., Anastassiadis, K., Roig, I., Cooke, H.J., Stewart, A.F., Wassmann, K., Jasin, M., et al. (2011). Meiotic homologue alignment and its quality surveillance are controlled by mouse HORMAD1. Nat. Cell Biol. *13*, 599–610.
- De, K., Sterle, L., Krueger, L., Yang, X., and Makaroff, C.A. (2014). Arabidopsis thaliana WAPL Is Essential for the Prophase Removal of Cohesin during Meiosis. PLoS Genet.
- Dernburg, A.F., McDonald, K., Moulder, G., Barstead, R., Dresser, M., and Villeneuve, A.M. (1998). Meiotic recombination in C. elegans initiates by a conserved mechanism and is dispensable for homologous chromosome synapsis. Cell *94*, 387–398.
- Dong, F., Cai, X., and Makaroff, C.A. (2001). Cloning and characterization of two Arabidopsis genes that belong to the RAD21/REC8 family of chromosome cohesin proteins. Gene.
- Dutrillaux, B., Couturier, J., Richer, C.L., and Viegas-Péquignot, E. (1976). Sequence of DNA replication in 277 R- and Q-bands of human chromosomes using a BrdU treatment. Chromosoma *58*, 51–61.
- Dymek, E.E., Lefebvre, P.A., and Smith, E.F. (2004). PF15p is the Chlamydomonas homologue of the katanin p80 subunit and is required for assembly of flagellar central microtubules. Eukaryot. Cell *3*, 870–879.
- Farr, C.J., Antoniou-Kourounioti, M., Mimmack, M.L., Volkov, A., and Porter, A.C.G. (2014). The α isoform of topoisomerase II is required for hypercompaction of mitotic chromosomes in human cells. Nucleic Acids

Res. *42*, 4414–4426.

- Fernandes, J.B., Duhamel, M., Seguéla-Arnaud, M., Froger, N., Girard, C., Choinard, S., Solier, V., De Winne, N., De Jaeger, G., Gevaert, K., et al. (2018). FIGL1 and its novel partner FLIP form a conserved complex that regulates homologous recombination. PLoS Genet.
- Ferrandiz, N., Barroso, C., Telecan, O., Shao, N., Kim, H.M., Testori, S., Faull, P., Cutillas, P., Snijders, A.P., Colaiácovo, M.P., et al. (2018). Spatiotemporal regulation of Aurora B recruitment ensures release of cohesion during C. Elegans oocyte meiosis. Nat. Commun. *9*.
- Forsburg, S.L. (2002). Only connect: Linking meiotic DNA replication to chromosome dynamics. Mol. Cell *9*, 703–711.
- Foss, E., Lande, R., Stahl, F.W., and Steinberg, C.M. (1993). Chiasma interference as a function of genetic distance. Genetics *133*, 681–691.
- Fox, P.M., Vought, V.E., Hanazawa, M., Lee, M.-H., Maine, E.M., and Schedl, T. (2011). Cyclin E and CDK-2 regulate proliferative cell fate and cell cycle progression in the C. elegans germline. Development *138*, 2223–2234.
- Fraune, J., Schramm, S., Alsheimer, M., and Benavente, R. (2012). The mammalian synaptonemal complex: Protein components, assembly and role in meiotic recombination. Exp. Cell Res. *318*, 1340–1346.
- Frickey, T., and Lupas, A.N. (2004). Phylogenetic analysis of AAA proteins. In Journal of Structural Biology, pp. 2–10.
- Fridkin, A., Mills, E., Margalit, A., Neufeld, E., Lee, K.K., Feinstein, N., Cohen, M., Wilson, K.L., and Gruenbaum, Y. (2004). Matefin, a Caenorhabditis elegans germ line-specific SUN-domain nuclear membrane protein, is essential for early embryonic and germ cell development. Proc. Natl. Acad. Sci. U. S. A. *101*, 6987–6992.
- Friedland, A.E., Tzur, Y.B., Esvelt, K.M., Colaiácovo, M.P., Church, G.M., and Calarco, J.A. (2013). Heritable genome editing in C. elegans via a CRISPR-Cas9 system. Nat. Methods *10*, 741–743.
- Frøkjær-Jensen, C., Wayne Davis, M., Hopkins, C.E., Newman, B.J., Thummel, J.M., Olesen, S.P., Grunnet, M., and Jorgensen, E.M. (2008). Single-copy insertion of transgenes in Caenorhabditis elegans. Nat. Genet. *40*, 1375–1383.
- Frøkjær-Jensen, C., Davis, M.W., Ailion, M., and Jorgensen, E.M. (2012). Improved Mos1-mediated transgenesis in C. elegans. Nat. Methods *9*, 117–118.
- Frøkjær-Jensen, C., Davis, M.W., Sarov, M., Taylor, J., Flibotte, S., LaBella, M., Pozniakovsky, A., Moerman, D.G., and Jorgensen, E.M. (2014). Random and targeted transgene insertion in Caenorhabditis elegans using a modified Mos1 transposon. Nat. Methods *11*, 529–534.
- Gaillard, P.H.L., Noguchi, E., Shanahan, P., and Russell, P. (2003). The endogenous Mus81-Eme1 complex resolves Holliday junctions by a nick and counternick mechanism. Mol. Cell *12*, 747–759.
- Gao, J., and Colaiácovo, M.P. (2018). Zipping and Unzipping: Protein Modifications Regulating Synaptonemal Complex Dynamics. Trends Genet. *34*, 232–245.
- Garcia, V., Gray, S., Allison, R.M., Cooper, T.J., and Neale, M.J. (2015). Tel1ATM-mediated interference suppresses clustered meiotic double-strand-break formation. Nature *520*, 114–118.
- Gerton, J.L., DeRisi, J., Shroff, R., Lichten, M., Brown, P.O., and Petes, T.D. (2000). Global mapping of meiotic recombination hotspots and coldspots in the yeast Saccharomyces cerevisiae. Proc. Natl. Acad. Sci. *97*, 11383–11390.
- Ghosh, D.K., Dasgupta, D., and Guha, A. (2012). Models, Regulations, and Functions of Microtubule

Severing by Katanin. ISRN Mol. Biol. *2012*, 1–14.

- Girard, C., Chelysheva, L., Choinard, S., Froger, N., Macaisne, N., Lehmemdi, A., Mazel, J., Crismani, W., and Mercier, R. (2015). AAA-ATPase FIDGETIN-LIKE 1 and Helicase FANCM Antagonize Meiotic Crossovers by Distinct Mechanisms. PLoS Genet.
- Goldfarb, T., and Lichten, M. (2010). Frequent and efficient use of the sister chromatid for DNA double-strand break repair during budding yeast meiosis. PLoS Biol. *8*.
- Gómez, R., Viera, A., Berenguer, I., Llano, E., Pendás, A.M., Barbero, J.L., Kikuchi, A., and Suja, J.A. (2014). Cohesin removal precedes topoisomerase IIα-dependent decatenation at centromeres in male mammalian meiosis II. Chromosoma.
- Goodson, H. V., and Jonasson, E.M. (2018). Microtubules and Microtubule-Associated Proteins. Cold Spring Harb. Perspect. Biol. *10*, a022608.
- Goodyer, W., Kaitna, S., Couteau, F., Ward, J.D., Boulton, S.J., and Zetka, M. (2008a). HTP-3 Links DSB Formation with Homolog Pairing and Crossing Over during C. elegans Meiosis. Dev. Cell *14*, 263–274.
- Görlitz, F., Guldbrand, S., Runcorn, T.H., Murray, R.T., Jaso-Tamame, A.L., Sinclair, H.G., Martinez-Perez, E., Taylor, J.R., Neil, M.A.A., Dunsby, C., et al. (2018). easySLM-STED: stimulated emission depletion microscopy with aberration correction, extended field of view and multiple beam scanning. J. Biophotonics e201800087.
- Gray, S., and Cohen, P.E. (2016). Control of Meiotic Crossovers: From Double-Strand Break Formation to Designation. Annu. Rev. Genet. *50*, 175–210.
- Guillon, H., Baudat, F., Grey, C., Liskay, R.M., and De Massy, B. (2005). Crossover and noncrossover pathways in mouse meiosis. Mol. Cell *20*, 563–573.
- Guturi, K.K.N., Bohgaki, M., Bohgaki, T., Srikumar, T., Ng, D., Kumareswaran, R., El Ghamrasni, S., Jeon, J., Patel, P., Eldin, M.S., et al. (2016). RNF168 and USP10 regulate topoisomerase IIα function via opposing effects on its ubiquitylation. Nat. Commun.
- Harper, L. (2004). A bouquet of chromosomes. J. Cell Sci. *117*, 4025–4032.
- Harper, N.C., Rillo, R., Jover-Gil, S., Assaf, Z.J., Bhalla, N., and Dernburg, A.F. (2011). Pairing centers recruit a polo-like kinase to orchestrate meiotic chromosome dynamics in C. elegans. Dev. Cell *21*, 934–947.
- Hartmann, M.A., and Sekelsky, J. (2017). The absence of crossovers on chromosome 4 in Drosophila melanogaster: Imperfection or interesting exception? Fly (Austin). *11*, 253–259.
- Hartsuiker, E., Mizuno, K., Molnar, M., Kohli, J., Ohta, K., and Carr, A.M. (2009). Ctp1CtIP and Rad32Mre11 Nuclease Activity Are Required for Rec12Spo11 Removal, but Rec12Spo11 Removal Is Dispensable for Other MRN-Dependent Meiotic Functions. Mol. Cell. Biol. *29*, 1671–1681.
- Hassold, T., and Hunt, P. (2001). To err (meiotically) is human: The genesis of human aneuploidy. Nat. Rev. Genet. *2*, 280–291.
- Hassold, T.J., and Jacobs, P.A. (1984). Trisomy in Man. Annu. Rev. Genet. *18*, 69–97.
- Hauf, S., and Watanabe, Y. (2004). Kinetochore orientation in mitosis and meiosis. Cell *119*, 317–327.
- Hayashi, M., Chin, G.M., and Villeneuve, A.M. (2007). C. elegans germ cells switch between distinct modes of double-strand break repair during meiotic prophase progression. PLoS Genet. *3*, 2068–2084.
- Heald, R., and Gibeaux, R. (2018). Subcellular scaling: does size matter for cell division? Curr. Opin. Cell Biol.
- Henderson, K.A., Kee, K., Maleki, S., Santini, P.A., and Keeney, S. (2006). Cyclin-Dependent Kinase Directly Regulates Initiation of Meiotic Recombination. Cell *125*, 1321–1332.

- Herbert, M., Kalleas, D., Cooney, D., Lamb, M., and Lister, L. (2015). Meiosis and maternal aging: Insights from aneuploid oocytes and trisomy births. Cold Spring Harb. Perspect. Biol.
- Herman, R.K., and Kari, C.K. (1989). Recombination between small X chromosome duplications and the X chromosome in Caenorhabditis elegans. Genetics *121*, 723–737.
- Hernandez, M.R., Davis, M.B., Jiang, J., Brouhard, E.A., Severson, A.F., and Csankovszki, G. (2018). Condensin I protects meiotic cohesin from WAPL-1 mediated removal. PLoS Genet. *14*.
- Herrán, Y., Gutiérrez-Caballero, C., Sánchez-Martín, M., Hernández, T., Viera, A., Barbero, J.L., De Álava, E., De Rooij, D.G., Suja, J.Á., Llano, E., et al. (2011). The cohesin subunit RAD21L functions in meiotic synapsis and exhibits sexual dimorphism in fertility. EMBO J. *30*, 3091–3105.
- Higgins, J.D., Perry, R.M., Barakate, A., Ramsay, L., Waugh, R., Halpin, C., Armstrong, S.J., and Franklin, F.C.H. (2012). Spatiotemporal Asymmetry of the Meiotic Program Underlies the Predominantly Distal Distribution of Meiotic Crossovers in Barley. Plant Cell *24*, 4096–4109.
- Hillers, K.J., and Villeneuve, A.M. (2003). Chromosome-wide control of meiotic crossing over in C. elegans. Curr. Biol. *13*, 1641–1647.
- Hirano, T. (2016). Condensin-Based Chromosome Organization from Bacteria to Vertebrates. Cell *164*, 847–857.
- Hiraoka, Y. (1998). Meiotic telomeres: A matchmaker for homologous chromosomes. Genes to Cells *3*, 405–413.
- Ho, J.W.K., Jung, Y.L., Liu, T., Alver, B.H., Lee, S., Ikegami, K., Sohn, K.A., Minoda, A., Tolstorukov, M.Y., Appert, A., et al. (2014). Comparative analysis of metazoan chromatin organization. Nature *512*, 449–452.
- Hodgkin, J., Horvitz, H.R., and Brenner, S. (1979). Nondisjunction Mutants of the Nematode CAENORHABDITIS ELEGANS. Genetics *91*, 67–94.
- Holliday, R. (1964). A mechanism for gene conversion in fungi. Genet. Res. *5*, 282–304.
- Hollingsworth, R.E., and Sclafani, R.A. (1993). Yeast pre-meiotic DNA replication utilizes mitotic origin ARS1 independently of CDC7 function. Chromosoma *102*, 415–420.
- Hollingsworth, N.M., Goetsch, L., and Byers, B. (1990). The HOPI Gene Encodes a Meiosis- Specific Component of Yeast Chromosomes. Cell *61*, 73–84.
- Hollingsworth, N.M., Ponte, L., and Halsey, C. (1995). MSH5, a novel MutS homolog, facilitates meiotic reciprocal recombination between homologs in Saccharomyces cerevisiae but not mismatch repair. Genes Dev. *9*, 1728–1739.
- Holloway, J.K., Booth, J., Edelmann, W., McGowan, C.H., and Cohen, P.E. (2008). MUS81 generates a subset of MLH1-MLH3-independent crossovers in mammalian meiosis. PLoS Genet. *4*.
- Holloway, J.K., Sun, X., Yokoo, R., Villeneuve, A.M., and Cohen, P.E. (2014). Mammalian CNTD1 is critical for meiotic crossover maturation and deselection of excess precrossover sites. J. Cell Biol. *205*, 633–641.
- Holmquist, G., Gray, M., Porter, T., and Jordan, J. (1982). Characterization of Giemsa dark- and light-band DNA. Cell *31*, 121–129.
- Houlard, M., Godwin, J., Metson, J., Lee, J., Hirano, T., and Nasmyth, K. (2015). Condensin confers the longitudinal rigidity of chromosomes. Nat. Cell Biol. *17*, 771–781.
- Huang, B., Babcock, H., and Zhuang, X. (2010). Breaking the diffraction barrier: Super-resolution imaging of cells. Cell *143*, 1047–1058.
- Hultén, M.A. (2011). On the origin of crossover interference: A chromosome oscillatory movement (COM) model. Mol. Cytogenet. *4*, 10.

- Hunter, N. (2015). Meiotic recombination: The essence of heredity. Cold Spring Harb. Perspect. Biol.
- Interthal, H., and Heyer, W.D. (2000). MUS81 encodes a novel helix-hairpin-helix protein involved in the response to UV- and methylation-induced DNA damage in Saccharomyces cerevisiae. Mol. Gen. Genet. *263*, 812–827.
- Ishiguro, K.I., Kim, J., Shibuya, H., Hernández-Hernández, A., Suzuki, A., Fukagawa, T., Shioi, G., Kiyonari, H., Li, X.C., Schimenti, J., et al. (2014). Meiosis-specific cohesin mediates homolog recognition in mouse spermatocytes. Genes Dev.
- Jaramillo-Lambert, A., Ellefson, M., Villeneuve, A.M., and Engebrecht, J.A. (2007). Differential timing of S phases, X chromosome replication, and meiotic prophase in the C. elegans germ line. Dev. Biol. *308*, 206–221.
- Jeppsson, K., Kanno, T., Shirahige, K., and Sjögren, C. (2014). The maintenance of chromosome structure: Positioning and functioning of SMC complexes. Nat. Rev. Mol. Cell Biol. *15*, 601–614.
- Jiang, L., Xia, M., Strittmatter, L.I., and Makaroff, C.A. (2007). The Arabidopsis cohesin protein SYN3 localizes to the nucleolus and is essential for gametogenesis. Plant J.
- Joly, N., Martino, L., Gigant, E., Dumont, J., and Pintard, L. (2016). Microtubule-severing activity of the AAA+ ATPase Katanin is essential for female meiotic spindle assembly. Development *143*, 3604–3614.
- Jordan, P., Copsey, A., Newnham, L., Kolar, E., Lichten, M., and Hoffmann, E. (2009). Ipl1/Aurora B kinase coordinates synaptonemal complex disassembly with cell cycle progression and crossover formation in budding yeast meiosis. Genes Dev. *23*, 2237–2251.
- Jordan, P.W., Karppinen, J., and Handel, M.A. (2012). Polo-like kinase is required for synaptonemal complex disassembly and phosphorylation in mouse spermatocytes. J. Cell Sci. *125*, 5061–5072.
- JS, K., and AM, R. (1987). The effect of gamma radiation on recombination frequency in C. elegans. Genome *29*, 457–462.
- Kadyk, L.C., and Hartwell, L.H. (1992). Sister chromatids are preferred over homologs as substrates for recombinational repair in Saccharomyces cerevisiae. Genetics *132*, 387–402.
- Kaur, T., and Rockman, M. V. (2014). Crossover heterogeneity in the absence of hotspots in Caenorhabditis elegans. Genetics *196*, 137–148.
- Keeney, S., Giroux, C.N., and Kleckner, N. (1997). Meiosis-specific DNA double-strand breaks are catalyzed by Spo11, a member of a widely conserved protein family. Cell *88*, 375–384.
- Kelly, K.O., Dernburg, A.F., Stanfield, G.M., and Villeneuve, A.M. (2000). Caenorhabditis elegans msh-5 is required for both normal and radiation-induced meiotic crossing over but not for completion of meiosis. Genetics *156*, 617–630.
- Kepinski, S., and Leyser, O. (2005). The Arabidopsis F-box protein TIR1 is an auxin receptor. Nature *435*, 446–451.
- Kim, S.K. (2001). A Gene Expression Map for Caenorhabditis elegans. Science (80-.). *293*, 2087–2092.
- Kim, Y., Kostow, N., and Dernburg, A.F. (2015). The Chromosome Axis Mediates Feedback Control of CHK-2 to Ensure Crossover Formation in C. elegans. Dev. Cell *35*, 247–261.
- Kimble, J. (2007). The Mysteries of Sexual Identity : The Germ Cell ' s Perspective. Science (80-.). *400*, 400–401.
- King, J.S., and Mortimer, R.K. (1990). A polymerization model of chiasma interference and corresponding computer simulation. Genetics *126*, 1127–1138.
- Kitagawa, K., and Hieter, P. (2001). Evolutionary conservation between budding yeast and human

kinetochores. Nat. Rev. Mol. Cell Biol. *2*, 678–687.

- Kleckner, N., Zickler, D., Jones, G.H., Dekker, J., Padmore, R., Henle, J., and Hutchinson, J. (2004). A mechanical basis for chromosome function. Proc. Natl. Acad. Sci. *101*, 12592–12597.
- Klein, F., Laroche, T., Cardenas, M.E., Hofmann, J.F.X., Schweizer, D., and Gasser, S.M. (1992). Localization of RAP1 and topoisomerase II in nuclei and meiotic chromosomes of yeast. J. Cell Biol.
- Kogo, H., Tsutsumi, M., Inagaki, H., Ohye, T., Kiyonari, H., and Kurahashi, H. (2012). HORMAD2 is essential for synapsis surveillance during meiotic prophase via the recruitment of ATR activity. Genes to Cells *17*, 897–912.
- Köhler, S., Wojcik, M., Xu, K., and Dernburg, A.F. (2017). Superresolution microscopy reveals the three-dimensional organization of meiotic chromosome axes in intact *Caenorhabditis elegans* tissue. Proc. Natl. Acad. Sci.
- Koszul, R., and Kleckner, N. (2009). Dynamic chromosome movements during meiosis: a way to eliminate unwanted connections? Trends Cell Biol.
- Koszul, R., Kim, K.P., Prentiss, M., Kleckner, N., and Kameoka, S. (2008). Meiotic Chromosomes Move by Linkage to Dynamic Actin Cables with Transduction of Force through the Nuclear Envelope. Cell.
- Kuliev, A., Cieslak, J., Ilkevitch, Y., and Verlinsky, Y. (2003). Chromosomal abnormalities in a series of 6733 human oocytes in preimplantation diagnosis for age-related aneuploidies. Reprod. Biomed. Online *6*, 54–59.
- Labella, S., Woglar, A., Jantsch, V., and Zetka, M. (2011). Polo kinases establish links between meiotic chromosomes and cytoskeletal forces essential for homolog pairing. Dev. Cell *21*, 948–958.
- Ladouceur, A.M., Ranjan, R., Smith, L., Fadero, T., Heppert, J., Goldstein, B., Maddox, A.S., and Maddox, P.S. (2017). CENP-A and topoisomerase-II antagonistically affect chromosome length. J. Cell Biol.
- Lee, J., and Hirano, T. (2011). RAD21L, a novel cohesin subunit implicated in linking homologous chromosomes in mammalian meiosis. J. Cell Biol. *192*, 263–276.
- Liang, Z., Zickler, D., Prentiss, M., Chang, F.S., Witz, G., Maeshima, K., and Kleckner, N. (2015). Chromosomes progress to metaphase in multiple discrete steps via global compaction/expansion cycles. Cell *161*, 1124–1137.
- Libuda, D.E., Uzawa, S., Meyer, B.J., and Villeneuve, A.M. (2013). Meiotic chromosome structures constrain and respond to designation of crossover sites. Nature *502*, 703–706.
- Lightfoot, J., Testori, S., Barroso, C., and Martinez-Perez, E. (2011). Loading of meiotic cohesin by SCC-2 is required for early processing of DSBs and for the DNA damage checkpoint. Curr. Biol. *21*, 1421–1430.
- Lim, J.G.Y., Stine, R.R.W., and Yanowitz, J.L. (2008). Domain-specific regulation of recombination in Caenorhabditis elegans in response to temperature, age and sex. Genetics *180*, 715–726.
- De los Santos, T., Hunter, N., Lee, C., Larkin, B., Loidl, J., and Hollingsworth, N.M. (2003). The MUS81/MMS4 endonuclease acts independently of double-holliday junction resolution to promote a distinct subset of crossovers during meiosis in budding yeast. Genetics *164*, 81–94.
- Lu, C., and Mains, P.E. (2007). The C. elegans anaphase promoting complex and MBK-2/DYRK kinase act redundantly with CUL-3/MEL-26 ubiquitin ligase to degrade MEI-1 microtubule-severing activity after meiosis. Dev. Biol. *302*, 438–447.
- Lui, D.Y., and Colai??covo, M.P. (2013). Meiotic development in Caenorhabditis elegans. Adv. Exp. Med. Biol. *757*, 133–170.
- Luis Royo, J., Hidalgo, M., and Ruiz, A. (2007). Pyrosequencing protocol using a universal biotinylated

primer for mutation detection and snp genotyping. Nat. Protoc. *2*, 1734–1739.

- Lukinavičius, G., Blaukopf, C., Pershagen, E., Schena, A., Reymond, L., Derivery, E., Gonzalez-Gaitan, M., D'Este, E., Hell, S.W., Gerlich, D.W., et al. (2015). SiR-Hoechst is a far-red DNA stain for live-cell nanoscopy. Nat. Commun. *6*, 1–2.
- Lynn, A., Soucek, R., and Börner, G.V. (2007). ZMM proteins during meiosis: Crossover artists at work. Chromosom. Res. *15*, 591–605.
- MacQueen, A.J., and Villeneuve, A.M. (2001). Nuclear reorganization and homologous chromosome pairing during meiotic prophase require C. elegans chk-2. Genes Dev. *15*, 1674–1687.
- MacQueen, A.J., Colaiácovo, M.P., McDonald, K., and Villeneuve, A.M. (2002). Synapsis-dependent and -independent mechanisms stabilize homolog pairingduring meiotic prophase in C.elegans. Genes Dev. *16*, 2428–2442.
- MacQueen, A.J., Phillips, C.M., Bhalla, N., Weiser, P., Villeneuve, A.M., and Dernburg, A.F. (2005). Chromosome sites play dual roles to establish homologous synapsis during meiosis in C. elegans. Cell *123*, 1037–1050.
- Maddox, P.S., Oegema, K., Desai, A., and Cheeseman, I.M. (2004). "Holo"er than thou: Chromosome segregation and kinetochore function in C. elegans. Chromosom. Res.
- Mains, P.E., Kemphues, K.J., Sprunger, S.A., Sulston, I.A., and Wood, W.B. (1990). Mutations affecting the meiotic and mitotic divisions of the early Caenorhabditis elegans embryo. Genetics *126*, 593–605.
- Malone, C.J., Misner, L., Le Bot, N., Tsai, M.C., Campbell, J.M., Ahringer, J., and White, J.G. (2003). The C. elegans Hook Protein, ZYG-12, Mediates the Essential Attachment between the Centrosome and Nucleus. Cell *115*, 825–836.
- Martinez-Garcia, M., Schubert, V., Osman, K., Darbyshire, A., Sanchez-Moran, E., and Franklin, F.C.H. (2018). TOPII and chromosome movement help remove interlocks between entangled chromosomes during meiosis. J. Cell Biol.
- Martinez-Perez, E., and Villeneuve, A.M. (2005). HTP-1-dependent constraints coordinate homolog pairing and synapsis and promote chiasma formation during C. elegans meiosis. Genes Dev. *19*, 2727–2743.
- Martinez-Perez, E., Schvarzstein, M., Barroso, C., Lightfoot, J., Dernburg, A.F., and Villeneuve, A.M. (2008). Crossovers trigger a remodeling of meiotic chromosome axis composition that is linked to two-step loss of sister chromatid cohesion. Genes Dev. *22*, 2886–2901.
- Martini, E., Diaz, R.L., Hunter, N., and Keeney, S. (2006). Crossover Homeostasis in Yeast Meiosis. Cell *126*, 285–295.
- Martini, E., Borde, V., Legendre, M., Audic, S., Regnault, B., Soubigou, G., Dujon, B., and Llorente, B. (2011). Genome-wide analysis of heteroduplex DNA in mismatch repair-deficient yeast cells reveals novel properties of meiotic recombination pathways. PLoS Genet. *7*.
- McMahill, M.S., Sham, C.W., and Bishop, D.K. (2007). Synthesis-dependent strand annealing in meiosis. PLoS Biol. *5*, 2589–2601.
- McNally, F.J., and Vale, R.D. (1993). Identification of katanin, an ATPase that severs and disassembles stable microtubules. Cell *75*, 419–429.
- McNally, K.P., and McNally, F.J. (2011). The spindle assembly function of Caenorhabditis elegans katanin does not require microtubule-severing activity. Mol. Biol. Cell *22*, 1550–1560.
- McNally, K., Audhya, A., Oegema, K., and McNally, F.J. (2006). Katanin controls mitotic and meiotic spindle length. J. Cell Biol. *175*, 881–891.

- Mehta, G.D., Kumar, R., Srivastava, S., and Ghosh, S.K. (2013). Cohesin: Functions beyond sister chromatid cohesion. FEBS Lett.
- Meneely, P.M., Farago, A.F., and Kauffman, T.M. (2002). Crossover distribution and high interference for both the X chromosome and an autosome during oogenesis and spermatogenesis in Caenorhabditis elegans. Genetics *162*, 1169–1177.
- Mengoli, V., Bucciarelli, E., Lattao, R., Piergentili, R., Gatti, M., and Bonaccorsi, S. (2014). The Analysis of Mutant Alleles of Different Strength Reveals Multiple Functions of Topoisomerase 2 in Regulation of Drosophila Chromosome Structure. PLoS Genet.
- Mets, D.G., and Meyer, B.J. (2009a). Condensins Regulate Meiotic DNA Break Distribution, thus Crossover Frequency, by Controlling Chromosome Structure. Cell *139*, 73–86.
- Mézard, C., Tagliaro Jahns, M., and Grelon, M. (2015). Where to cross? New insights into the location of meiotic crossovers. Trends Genet. *31*, 393–401.
- Minn, I., Rolls, M.M., Hanna-Rose, W., and Malone, C.J. (2009). SUN-1 and ZYG-12, Mediators of Centrosome-Nucleus Attachment, Are a Functional SUN/KASH Pair in Caenorhabditis elegans. Mol. Biol. Cell *20*, 4586–4595.
- Mohibullah, N., and Keeney, S. (2017). Numerical and spatial patterning of yeast meiotic DNA breaks by Tel1. Genome Res. *27*, 278–288.
- Monen, J., Maddox, P.S., Hyndman, F., Oegema, K., and Desai, A. (2005). Differential role of CENP-A in the segregation of holocentric C. elegans chromosomes during meiosis and mitosis. Nat. Cell Biol.
- Moores, C.A., Perderiset, M., Kappeler, C., Kain, S., Drummond, D., Perkins, S.J., Chelly, J., Cross, R., Houdusse, A., and Francis, F. (2006). Distinct roles of doublecortin modulating the microtubule cytoskeleton. EMBO J. *25*, 4448–4457.
- Moose, S.P., and Mumm, R.H. (2008). Molecular Plant Breeding as the Foundation for 21st Century Crop Improvement. PLANT Physiol.
- Morrical, S.W. (2015). DNA-pairing and annealing processes in homologous recombination and homology-directed repair. Cold Spring Harb. Perspect. Biol. *7*.
- Moses, M.J. (1969). Structure and function of the synaptonemal complex. Genetics *61*.
- Müller-Reichert, T., Greenan, G., O'Toole, E., and Srayko, M. (2010). The elegans of spindle assembly. Cell. Mol. Life Sci. *67*, 2195–2213.
- Müller, T., Schumann, C., and Kraegeloh, A. (2012). STED microscopy and its applications: New insights into cellular processes on the nanoscale. ChemPhysChem.
- Murakami, H., and Nurse, P. (2001). Regulation of premeiotic S phase and recombination- related double-strand DNA breaks during meiosis in fission yeast. Cancer Res. *28*, 290–293.
- De Muyt, A., Zhang, L., Piolot, T., Kleckner, N., Espagne, E., and Zickler, D. (2014). E3 ligase Hei10: A multifaceted structure-based signaling molecule with roles within and beyond meiosis. Genes Dev. *28*, 1111–1123.
- Myers, S., Spencer, C.C.A., Auton, A., Bottolo, L., Freeman, C., Donnelly, P., and McVean, G. (2006). The distribution and causes of meiotic recombination in the human genome. Biochem. Soc. Trans. *34*, 526–530.
- Myers, S., Freeman, C., Auton, A., Donnelly, P., and McVean, G. (2008). A common sequence motif associated with recombination hot spots and genome instability in humans. Nat. Genet. *40*, 1124–1129.
- Nabeshima, K., Villeneuve, A.M., and Colaiácovo, M.P. (2005). Crossing over is coupled to late meiotic

prophase bivalent differentiation through asymmetric disassembly of the SC. J. Cell Biol. *168*, 683–689.

- Nagaoka, S.I., Hassold, T.J., and Hunt, P.A. (2012). Human aneuploidy: mechanisms and new insights into an age-old problem. Nat. Rev. Genet. *13*, 493–504.
- Nasmyth, K., and Haering, C.H. (2009). Cohesin: Its Roles and Mechanisms. Annu. Rev. Genet. *43*, 525–558.
- Neale, M.J., Pan, J., and Keeney, S. (2005). Endonucleolytic processing of covalent protein-linked DNA double-strand breaks. Nature *436*, 1053–1057.
- Nel-Themaat, L., Gonzalez, G., Akiyama, H., and Behringer, R.R. (2010). Illuminating testis morphogenesis in the mouse. J. Androl. *31*, 5–10.
- Nitiss, J.L. (2009). DNA topoisomerase II and its growing repertoire of biological functions. Nat. Rev. Cancer.
- Niu, H., Wan, L., Baumgartner, B., Schaefer, D., Loidl, J., and Hollingsworth, N.M. (2005). Partner Choice during Meiosis Is Regulated by Hop1-promoted Dimerization of Mek1 Hengyao. Mol. Biol. Cell *16*, 5804–5818.
- Ohta, K., Wu, T.C., Lichten, M., and Shibata, T. (1999). Competitive inactivation of a double-strand DNA break site involves parallel suppression of meiosis-induced changes in chromatin configuration. Nucleic Acids Res. *27*, 2175–2180.
- Ono, T., Fang, Y., Spector, D.L., and Hirano, T. (2004). Spatial and Temporal Regulation of Condensins I and II in Mitotic Chromosome Assembly in Human Cells. Mol. Biol. Cell *15*, 3296–3308.
- Ortiz, R., Kouznetsova, A., Echeverría-Martínez, O.M., Vázquez-Nin, G.H., and Hernández-Hernández, A. (2016). The width of the lateral element of the synaptonemal complex is determined by a multilayered organization of its components. Exp. Cell Res. *344*, 22–29.
- Ottolini, C.S., Newnham, L.J., Capalbo, A., Natesan, S.A., Joshi, H.A., Cimadomo, D., Griffin, D.K., Sage, K., Summers, M.C., Thornhill, A.R., et al. (2015). Genome-wide maps of recombination and chromosome segregation in human oocytes and embryos show selection for maternal recombination rates. Nat. Genet. *47*, 727–735.
- Oulad-Abdelghani, M., Bouillet, P., Décimo, D., Gansmuller, A., Heyberger, S., Dollé, P., Bronner, S., Lutz, Y., and Chambon, P. (1996). Characterization of a premeiotic germ cell-specific cytoplasmic protein encoded by Stra8, a novel retinoic acid-responsive gene. J. Cell Biol. *135*, 469–477.
- Paix, A., Folkmann, A., Rasoloson, D., and Seydoux, G. (2015). High efficiency, homology-directed genome editing in Caenorhabditis elegans using CRISPR-Cas9ribonucleoprotein complexes. Genetics.
- Paix, A., Schmidt, H., and Seydoux, G. (2016). Cas9-assisted recombineering in C. elegans: Genome editing using in vivo assembly of linear DNAs. Nucleic Acids Res. *44*, e128.
- Parra, M.T. (2003). Dynamic relocalization of the chromosomal passenger complex proteins inner centromere protein (INCENP) and aurora-B kinase during male mouse meiosis. J. Cell Sci. *116*, 961–974.
- Parvanov, E.D., Petkov, P.M., and Paigen, K. (2010). Prdm9 controls activation of mammalian recombination hotspots. Science (80-.). *327*, 835.
- Pasierbek, P., Jantsch, M., Melcher, M., Schleiffer, A., Schweizer, D., and Loidl, J. (2001). A Caenorhabditis elegans cohesion protein with functions in meiotic chromosome pairing and disjunction. Genes Dev. *15*, 1349–1360.
- Pellestor, F., Andréo, B., Arnal, F., Humeau, C., and Demaille, J. (2003). Maternal aging and chromosomal abnormalities: new data drawn from in vitro unfertilized human oocytes. Hum. Genet. *112*, 195–203.

- Penkner, A., Tang, L., Novatchkova, M., Ladurner, M., Fridkin, A., Gruenbaum, Y., Schweizer, D., Loidl, J., and Jantsch, V. (2007). The Nuclear Envelope Protein Matefin/SUN-1 Is Required for Homologous Pairing in C. elegans Meiosis. Dev. Cell *12*, 873–885.
- Penkner, A.M., Fridkin, A., Gloggnitzer, J., Baudrimont, A., Machacek, T., Woglar, A., Csaszar, E., Pasierbek, P., Ammerer, G., Gruenbaum, Y., et al. (2009). Meiotic Chromosome Homology Search Involves Modifications of the Nuclear Envelope Protein Matefin/SUN-1. Cell *139*, 920–933.
- Perry, J.J., Kleckner, N.N., and Börner, G.V.G. V (2005). Bioinformatic analyses implicate the collaborating meiotic crossover/chiasma proteins Zip2, Zip3, and Spo22/Zip4 in ubiquitin labeling. Proc. Natl. Acad. Sci. U. S. A. *102*, 17594–17599.
- Peters, A.H.F.M., Plug, A.W., Van Vugt, M.J., and De Boer, P. (1997). A drying-down technique for the spreading of mammalian melocytes from the male and female germline. Chromosom. Res.
- Petronczki, M., Siomos, M.F., and Nasmyth, K. (2003). Un ménage à quatre: The molecular biology of chromosome segregation in meiosis. Cell.
- Phillips, C.M., and Dernburg, A.F. (2006). A Family of Zinc-Finger Proteins Is Required for Chromosome-Specific Pairing and Synapsis during Meiosis in C. elegans. Dev. Cell *11*, 817–829.
- Phillips, C.M., Wong, C., Bhalla, N., Carlton, P.M., Weiser, P., Meneely, P.M., and Dernburg, A.F. (2005). HIM-8 binds to the X chromosome pairing center and mediates chromosome-specific meiotic synapsis. Cell *123*, 1051–1063.
- Phillips, C.M., Meng, X., Zhang, L., Chretien, J.H., Urnov, F.D., and Dernburg, A.F. (2009). Identification of chromosome sequence motifs that mediate meiotic pairing and synapsis in C. elegans. Nat. Cell Biol. *11*, 934–942.
- Rasmussen, S.W., and Holm, P.B. (1984). The synaptonemal complex, recombination nodules and chiasmata in human spermatocytes. Symp Soc Exp Biol *38*, 271–292.
- Ray, D.K., Ramankutty, N., Mueller, N.D., West, P.C., and Foley, J.A. (2012). Recent patterns of crop yield growth and stagnation. Nat. Commun.
- Ray, D.K., Mueller, N.D., West, P.C., and Foley, J.A. (2013). Yield Trends Are Insufficient to Double Global Crop Production by 2050. PLoS One.
- Ren, H., Ferguson, K., Kirkpatrick, G., Vinning, T., Chow, V., and Ma, S. (2016). Altered crossover distribution and frequency in spermatocytes of infertile men with azoospermia. PLoS One *11*.
- Robert, T., Vrielynck, N., Mézard, C., de Massy, B., and Grelon, M. (2016a). A new light on the meiotic DSB catalytic complex. Semin. Cell Dev. Biol.
- Robert, T., Nore, A., Brun, C., Maffre, C., Crimi, B., Bourbon, H.M., and De Massy, B. (2016b). The Topo VIB-Like protein family is required for meiotic DNA double-strand break formation. Science (80-.).
- Robinett, C.C., Straight, A., Li, G., Willhelm, C., Sudlow, G., Murray, A., and Belmont, A.S. (1996). In vivo localization of DNA sequences and visualization of large-scale chromatin organization using lac operator/repressor recognition. J. Cell Biol.
- Rockman, M. V., and Kruglyak, L. (2009). Recombinational landscape and population genomics of caenorhabditis elegans. PLoS Genet. *5*.
- Roll-Mecak, A., and McNally, F.J. (2010). Microtubule-severing enzymes. Curr. Opin. Cell Biol. *22*, 96–103.
- Roll-Mecak, A., and Vale, R.D. (2006). Making more microtubules by severing: A common theme of noncentrosomal microtubule arrays? J. Cell Biol. *175*, 849–851.
- Roll-Mecak, A., and Vale, R.D. (2008). Structural basis of microtubule severing by the hereditary spastic

paraplegia protein spastin. Nature *451*, 363–367.

- Rosu, S., Zawadzki, K.A., Stamper, E.L., Libuda, D.E., Reese, A.L., Dernburg, A.F., and Villeneuve, A.M. (2013). The C. elegans DSB-2 Protein Reveals a Regulatory Network that Controls Competence for Meiotic DSB Formation and Promotes Crossover Assurance. PLoS Genet. *9*.
- Saito, T.T., and Colaiácovo, M.P. (2017a). Regulation of Crossover Frequency and Distribution during Meiotic Recombination. Cold Spring Harb. Symp. Quant. Biol. *LXXXII*, 034132.
- Saito, T.T., Lui, D.Y., Kim, H.M., Meyer, K., and Colai??covo, M.P. (2013a). Interplay between Structure-Specific Endonucleases for Crossover Control during Caenorhabditis elegans Meiosis. PLoS Genet. *9*.
- Sandalinas, M., Marquez, C., Bahce, M., Escudero, T., Cohen, J., and Munné, S. (2000). Spectral Karyotyping of Unfertilized and Noninseminated Oocytes. Fertil. Steril. *74*, S2.
- Sanford, C., and Perry, M.D. (2001). Asymmetrically distributed oligonucleotide repeats in the Caenorhabditis elegans genome sequence that map to regions important for meiotic chromosome segregation. Nucleic Acids Res. *29*, 2920–2926.
- Sato, A., Isaac, B., Phillips, C.M., Rillo, R., Carlton, P.M., Wynne, D.J., Kasad, R.A., and Dernburg, A.F. (2009a). Cytoskeletal Forces Span the Nuclear Envelope to Coordinate Meiotic Chromosome Pairing and Synapsis. Cell *139*, 907–919.
- Schermelleh, L., Heintzmann, R., and Leonhardt, H. (2010). A guide to super-resolution fluorescence microscopy. J. Cell Biol. *190*, 165–175.
- Scherthan, H. (2001). A bouquet makes ends meet. Nat. Rev. Mol. Cell Biol. *2*, 621–627.
- K Schild-Prüfert, K., Saito, T.T., Smolikov, S., Gu, Y., Hincapie, M., Hill, D.E., Vidal, M., McDonald, K., and Colaiácovo, M.P. (2011). Organization of the synaptonemal complex during meiosis in Caenorhabditis elegans. Genetics *189*, 411–421.
- Schwacha, A., and Kleckner, N. (1994). Identification of joint molecules that form frequently between homologs but rarely between sister chromatids during yeast meiosis. Cell *76*, 51–63.
- Sears, D.D., Hegemann, J.H., Shero, J.H., and Hieter, P. (1995). Cis-acting determinants affecting centromere function, sister-chromatid cohesion and reciprocal recombination during meiosis in Saccharomyces cerevisiae. Genetics *139*, 1159–1173.
- Sehorn, M.G., Sigurdsson, S., Bussen, W., Unger, V.M., and Sung, P. (2004). Human meiotic recombinase Dmc1 promotes ATP-dependent homologous DNA strand exchange. Nature *429*, 433–437.
- Severson, A.F., and Meyer, B.J. (2014). Divergent kleisin subunits of cohesin specify mechanisms to tether and release meiotic chromosomes. Elife *3*, e03467.
- Severson, A.F., Ling, L., Van Zuylen, V., and Meyer, B.J. (2009). The axial element protein HTP-3 promotes cohesin loading and meiotic axis assembly in C. elegans to implement the meiotic program of chromosome segregation. Genes Dev. *23*, 1763–1778.
- Sharma, N., Bryant, J., Wloga, D., Donaldson, R., Davis, R.C., Jerka-Dziadosz, M., and Gaertig, J. (2007). Katanin regulates dynamics of microtubules and biogenesis of motile cilia. J. Cell Biol. *178*, 1065–1079.
- Sharp, D.J., and Ross, J.L. (2012). Microtubule-severing enzymes at the cutting edge. J. Cell Sci. *125*, 2561–2569.
- Shin, Y.H., Choi, Y., Erdin, S.U., Yatsenko, S.A., Kloc, M., Yang, F., Wang, P.J., Meistrich, M.L., and Rajkovic, A. (2010). Hormad1 mutation disrupts synaptonemal complex formation, recombination, and chromosome segregation in mammalian meiosis. PLoS Genet. *6*.
- Shinohara, A., Ogawa, H., and Ogawa, T. (1992). Rad51 protein involved in repair and recombination in S.

cerevisiae is a RecA-like protein. Cell *69*, 457–470.

- Shinohara, M., Oh, S.D., Hunter, N., and Shinohara, A. (2008). Crossover assurance and crossover interference are distinctly regulated by the ZMM proteins during yeast meiosis. Nat. Genet. *40*, 299–309.
- Silva, N., Ferrandiz, N., Barroso, C., Tognetti, S., Lightfoot, J., Telecan, O., Encheva, V., Faull, P., Hanni, S., Furger, A., et al. (2014). The fidelity of synaptonemal complex assembly is regulated by a signaling mechanism that controls early meiotic progression. Dev. Cell *31*, 503–511.
- Simchen, G., and Hirschberg, J. (1977). Effects of the mitotic cell-cycle mutation cdc4 on yeast meiosis. Genetics *86*, 57–72.
- Smith, A. V., and Roeder, G.S. (1997). The yeast Red1 protein localizes to the cores of meiotic chromosomes. J. Cell Biol. *136*, 957–967.
- Smith, G.R., Boddy, M.N., Shanahan, P., and Russell, P. (2003). Fission Yeast Mus81·Eme1 Holliday Junction Resolvase Is Required for Meiotic Crossing over but Not for Gene Conversion. Genetics *165*, 2289–2293.
- Smolikov, S., Eizinger, A., Schild-Prufert, K., Hurlburt, A., McDonald, K., Engebrecht, J., Villeneuve, A.M., and Colaiácovo, M.P. (2007). SYP-3 restricts synaptonemal complex assembly to bridge paired chromosome axes during meiosis in Caenorhabditis elegans. Genetics *176*, 2015–2025.
- Smolikov, S., Schild-Prüfert, K., and Colaiácovo, M.P. (2008). CRA-1 uncovers a double-strand break-dependent pathway promoting the assembly of central region proteins on chromosome axes during C. elegans meiosis. PLoS Genet.
- Smolikov, S., Schild-Prüfert, K., and Colaiácovo, M.P. (2009). A yeast two-hybrid screen for SYP-3 interactors identifies SYP-4, a component required for synaptonemal complex assembly and chiasma formation in Caenorhabditis elegans meiosis. PLoS Genet. *5*.
- Sourirajan, A., and Lichten, M. (2008). Polo-like kinase Cdc5 drives exit from pachytene during budding yeast meiosis. Genes Dev. *22*, 2627–2632.
- Spichal, M., and Fabre, E. (2017). The emerging role of the cytoskeleton in chromosome dynamics. Front. Genet.
- Srayko, M., Buster, D.W., Bazirgan, O.A., McNally, F.J., and Mains, P.E. (2000). MEI-1/MEI-2 katanin-like microtubule severing activity is required for Caenorhabditis elegans meiosis. Genes Dev. *14*, 1072–1084.
- Srayko, M., O'Toole, E.T., Hyman, A.A., and Müller-Reichert, T. (2006). Katanin Disrupts the Microtubule Lattice and Increases Polymer Number in C. elegans Meiosis. Curr. Biol. *16*, 1944–1949.
- Stambrook, P.J., and Flickinger, R.A. (1970). Changes in chromosomal DNA replication patterns in developing frog embryos. J. Exp. Zool. *174*, 101–113.
- Stamper, E.L., Rodenbusch, S.E., Rosu, S., Ahringer, J., Villeneuve, A.M., and Dernburg, A.F. (2013). Identification of DSB-1, a Protein Required for Initiation of Meiotic Recombination in Caenorhabditis elegans, Illuminates a Crossover Assurance Checkpoint. PLoS Genet. *9*.
- Starr, D.A., and Han, M. (2002). Role of ANC-1 in tethering nuclei to the actin cytoskeleton. Science (80-.). *298*, 406–409.
- Sturtevant, A.H. (1915). Castle and wright on crossing over in rats. Science (80-.). *42*, 342.
- Subramanian, V. V., and Hochwagen, A. (2014). The meiotic checkpoint network: Step-by-step through meiotic prophase. Cold Spring Harb. Perspect. Biol.
- Sullivan, B.A., Blower, M.D., and Karpen, G.H. (2001). Determining centromere identity: Cyclical stories and forking paths. Nat. Rev. Genet.

- Sun, F., and Handel, M.A. (2008). Regulation of the meiotic prophase I to metaphase I transition in mouse spermatocytes. Chromosoma *117*, 471–485.
- Sun, H., Treco, D., Schultes, N.P., and Szostak, J.W. (1989). Double-strand breaks at an initiation site for meiotic gene conversion. Nature *338*, 87–90.
- Sung, W.K., Van't Hof, J., and Jagiello, G. (1986). DNA synthesis studies in pre-meiotic mouse oogenesis. Exp. Cell Res. *163*, 370–380.
- Sym, M., Engebrecht, J., and Roeder, G.S. (1993). ZIP1 is a synaptonemal complex protein required for meiotic chromosome synapsis. Cell *72*, 365–378.
- Szostak, J.W., Orr-Weaver, T.L., Rothstein, R.J., and Stahl, F.W. (1983). The double-strand-break repair model for recombination. Cell *33*, 25–35.
- Tachibana-Konwalski, K., Godwin, J., Van Der Weyden, L., Champion, L., Kudo, N.R., Adams, D.J., and Nasmyth, K. (2010). Rec8-containing cohesin maintains bivalents without turnover during the growing phase of mouse oocytes. Genes Dev.
- Tan, X., Calderon-Villalobos, L.I.A., Sharon, M., Zheng, C., Robinson, C. V., Estelle, M., and Zheng, N. (2007). Mechanism of auxin perception by the TIR1 ubiquitin ligase. Nature *446*, 640–645.
- Taylor, A.I. (1968). Autosomal trisomy syndromes: a detailed study of 27 cases of Edwards'syndrome and 27 cases of Patau's syndrome. J. Med. Genet. *5*, 227–252.
- Tedeschi, A., Wutz, G., Huet, S., Jaritz, M., Wuensche, A., Schirghuber, E., Davidson, I.F., Tang, W., Cisneros, D.A., Bhaskara, V., et al. (2013). Wapl is an essential regulator of chromatin structure and chromosome segregation. Nature.
- Tsai, C.J., Mets, D.G., Albrecht, M.R., Nix, P., Chan, A., and Meyer, B.J. (2008). Meiotic crossover number and distribution are regulated by a dosage compensation protein that resembles a condensin subunit. Genes Dev. *22*, 194–211.
- Tsubouchi, H., and Ogawa, H. (2000). Exo1 roles for repair of DNA double-strand breaks and meiotic crossing over in Saccharomyces cerevisiae. Mol Biol Cell *11*, 2221–2233.
- Tsubouchi, H., and Roeder, G.S. (2002). The Mnd1 protein forms a complex with hop2 to promote homologous chromosome pairing and meiotic double-strand break repair. Mol Cell Biol *22*, 3078–3088.
- Uemura, T., Ohkura, H., Adachi, Y., Morino, K., Shiozaki, K., and Yanagida, M. (1987). DNA topoisomerase II is required for condensation and separation of mitotic chromosomes in S. pombe. Cell.
- Vale, R.D. (1991). Severing of stable microtubules by a mitotically activated protein in xenopus egg extracts. Cell *64*, 827–839.
- Varas, J., Sánchez-Morán, E., Copenhaver, G.P., Santos, J.L., and Pradillo, M. (2015). Analysis of the Relationships between DNA Double-Strand Breaks, Synaptonemal Complex and Crossovers Using the Atfas1-4 Mutant. PLoS Genet. *11*.
- Vranis, N.M., van der Heijden, G.W., Malki, S., and Bortvin, A. (2010). Synaptonemal complex length variation in wild-type male mice. Genes (Basel).
- Vrielynck, N., Chambon, A., Vezon, D., Pereira, L., Chelysheva, L., De Muyt, A., Mézard, C., Mayer, C., and Grelon, M. (2016). A DNA topoisomerase VI-like complex initiates meiotic recombination. Science (80-.).
- Wan, L., de los Santos, T., Zhang, C., Shokat, K., and Hollingsworth, N.M. (2004). Mek1 kinase activity functions downstream of RED1 in the regulation of meiotic double strand break repair in budding yeast. Mol. Biol. Cell *15*, 11–23.
- Wan, L., Niu, H., Futcher, B., Zhang, C., Shokat, K.M., Boulton, S.J., and Hollingsworth, N.M. (2008). Cdc28-

Clb5 (CDK-S) and Cdc7-Dbf4 (DDK) collaborate to initiate meiotic recombination in yeast. Genes Dev. *22*, 386–397.

- Watanabe, Y., Yokobayashi, S., Yamamoto, M., and Nurse, P. (2001). Pre-meiotic S phase is linked to reductional chromosome segregation and recombination. Nature *409*, 359–363.
- Wegel, E., Göhler, A., Lagerholm, B.C., Wainman, A., Uphoff, S., Kaufmann, R., and Dobbie, I.M. (2016). Imaging cellular structures in super-resolution with SIM, STED and Localisation Microscopy: A practical comparison. Sci. Rep.
- White, S.R., Evans, K.J., Lary, J., Cole, J.L., and Lauring, B. (2007). Recognition of C-terminal amino acids in tubulin by pore loops in Spastin is important for microtubule severing. J. Cell Biol. *176*, 995–1005.
- Williamson, D.H., Johnston, L.H., Fennell, D.J., and Simchen, G. (1983). The timing of the S phase and other nuclear events in yeast meiosis. Exp. Cell Res. *145*, 209–217.
- Woglar, A., and Villeneuve, A.M. (2018). Dynamic Architecture of DNA Repair Complexes and the Synaptonemal Complex at Sites of Meiotic Recombination. Cell *173*, 1678-1691.e16.
- Wojtasz, L., Daniel, K., Roig, I., Bolcun-Filas, E., Xu, H., Boonsanay, V., Eckmann, C.R., Cooke, H.J., Jasin, M., Keeney, S., et al. (2009). Mouse HORMAD1 and HORMAD2, two conserved meiotic chromosomal proteins, are depleted from synapsed chromosome axes with the help of TRIP13 AAA-ATPase. PLoS Genet. *5*.
- Wyatt, H.D.M., and West, S.C. (2014). Holliday junction resolvases. Cold Spring Harb. Perspect. Biol. *6*.
- Xu, Y.X., and Manley, J.L. (2007). The Prolyl Isomerase Pin1 Functions in Mitotic Chromosome Condensation. Mol. Cell.
- Yancey-Wrona, J.E., and Camerini-Otero, R.D. (1995). The search for DNA homology does not limit stable homologous pairing promoted by RecA protein. Curr. Biol. *5*, 1149–1158.
- Yanowitz, J. (2010). Meiosis: Making a break for it. Curr. Opin. Cell Biol. *22*, 744–751.
- Yelina, N.E., Choi, K., Chelysheva, L., Macaulay, M., de Snoo, B., Wijnker, E., Miller, N., Drouaud, J., Grelon, M., Copenhaver, G.P., et al. (2012). Epigenetic Remodeling of Meiotic Crossover Frequency in Arabidopsis thaliana DNA Methyltransferase Mutants. PLoS Genet. *8*.
- Yin, Y., and Smolikove, S. (2013). Impaired resection of meiotic double-strand breaks channels repair to nonhomologous end joining in Caenorhabditis elegans. Mol. Cell. Biol. *33*, 2732–2747.
- Yokoo, R., Zawadzki, K.A., Nabeshima, K., Drake, M., Arur, S., and Villeneuve, A.M. (2012a). COSA-1 reveals robust homeostasis and separable licensing and reinforcement steps governing meiotic crossovers. Cell *149*, 75–87.
- Youds, J.L., Mets, D.G., McIlwraith, M.J., Martin, J.S., Ward, J.D., Oneil, N.J., Rose, A.M., West, S.C., Meyer, B.J., and Boulton, S.J. (2010). RTEL-1 enforces meiotic crossover interference and homeostasis. Science (80-.). *327*, 1254–1258.
- Yu, Z., Kim, Y., and Dernburg, A.F. (2016). Meiotic recombination and the crossover assurance checkpoint in Caenorhabditis elegans. Semin. Cell Dev. Biol. *54*, 106–116.
- Yuan, J., and Chen, J. (2013). FIGNL1-containing protein complex is required for efficient homologous recombination repair. Proc. Natl. Acad. Sci.
- Zakharyevich, K., Ma, Y., Tang, S., Hwang, P.Y.H., Boiteux, S., and Hunter, N. (2010). Temporally and Biochemically Distinct Activities of Exo1 during Meiosis: Double-Strand Break Resection and Resolution of Double Holliday Junctions. Mol. Cell *40*, 1001–1015.
- Zakharyevich, K., Tang, S., Ma, Y., and Hunter, N. (2012). Delineation of joint molecule resolution pathways in meiosis identifies a crossover-specific resolvase. Cell *149*, 334–347.

- Zalevsky, J., MacQueen, A.J., Duffy, J.B., Kemphues, K.J., and Villeneuve, A.M. (1999). Crossing over during Caenorhabditis elegans meiosis requires a conserved MutS-based pathway that is partially dispensable in budding yeast. Genetics *153*, 1271–1283.
- Zetka, M.C., Kawasaki, I., Strome, S., and Müller, F. (1999). Synapsis and chiasma formation in Caenorhabditis elegans require HIM-3, a meiotic chromosome core component that functions in chromosome segregation. Genes Dev. *13*, 2258–2270.
- Zhang, D., Rogers, G.C., Buster, D.W., and Sharp, D.J. (2007). Three microtubule severing enzymes contribute to the "Pacman- flux" machinery that moves chromosomes. J. Cell Biol. *177*, 231–242.
- Zhang, L., Liang, Z., Hutchinson, J., and Kleckner, N. (2014). Crossover Patterning by the Beam-Film Model: Analysis and Implications. PLoS Genet.
- Zhang, L., Ward, J.D., Cheng, Z., and Dernburg, A.F. (2015). The auxin-inducible degradation (AID) system enables versatile conditional protein depletion in C. elegans. Development *142*, 4374–4384.
- Zhao, D., Yang, X., Quan, L., Timofejeva, L., Rigel, N.W., Ma, H., and Makaroff, C.A. (2006). ASK1, a SKP1 homolog, is required for nuclear reorganization, presynaptic homolog juxtaposition and the proper distribution of cohesin during meiosis in Arabidopsis. Plant Mol. Biol.
- Zhou, K., Rolls, M.M., Hall, D.H., Malone, C.J., and Hanna-Rose, W. (2009). A ZYG-12-dynein interaction at the nuclear envelope defines cytoskeletal architecture in the C. elegans gonad. J. Cell Biol. *186*, 229–241.
- Zickler, D., and Kleckner, N. (1998). The leptotene-zygotene transition of meiosis. Annu. Rev. Genet. *32*, 619–697.
- Zickler, D., and Kleckner, N. (1999). Meiotic Chromosomes: Integrating Structure and Function. Annu. Rev. Genet. *33*, 603–754.
- Zierhut, C., Berlinger, M., Rupp, C., Shinohara, A., and Klein, F. (2004). Mnd1 is required for meiotic interhomolog repair. Curr. Biol. *14*, 752–762.